UNIVERSIDADE DE LISBOA
FACULDADE DE CIÊNCIAS

New ZnO-based core-shell nanostructures for perovskite solar cells

"Documento Definitivo"

Doutoramento em Química
Especialidade de Química Física

Tânia Cristina Antunes Frade Costa

Tese orientada por:
Doutor Jorge Manuel Palma Correia
Doutor Killian Paulo Kiernan Lobato
Doutor Ramón Tena-Zaera

Documento especialmente elaborado para a obtenção do grau de doutor

2021

UNIVERSIDADE DE LISBOA

FACULDADE DE CIÊNCIAS

New ZnO-based core-shell nanostructures for perovskite solar cells

Doutoramento em Química

Especialidade de Química Física

Tânia Cristina Antunes Frade Costa

Tese orientada por:

Doutor Jorge Manuel Palma Correia

Doutor Killian Paulo Kiernan Lobato

Doutor Ramón Tena-Zaera

Júri:

Presidente:

- Doutor Manuel Eduardo Ribeiro Minas da Piedade, Professor Catedrático e Presidente do Departamento de Química e Bioquímica da Faculdade de Ciências da Universidade de Lisboa

Vogais:

- Doutora Luísa Manuela Madureira Andrade Silva, Professora Auxiliar da Faculdade de Engenharia da Universidade do Porto;
- Doutora Ana Maria Carreira Lopes, Professora Associada da Faculdade de Ciências da Universidade da Beira Interior;
- Doutor Manuel João de Moura Dias Mendes, Professor Auxiliar da Faculdade de Ciências e Tecnologia da Universidade Nova de Lisboa;
- Doutora Alda Maria Pereira Simões, Professora Associada com Agregação do Instituto Superior Técnico da Universidade de Lisboa;
- Doutor Killian Paulo Kiernan Lobato, Professor Auxiliar da Faculdade de Ciências da Universidade de Lisboa (orientador).

Documento especialmente elaborado para a obtenção do grau de doutor

Fundação para a Ciência e Tecnologia (FCT) no âmbito do uma Bolsa Individual de Doutoramento (SFRH/BD/84669/2012)

2021

To my husband and son,

In memory of my supervisor Doctor Anabela Gomes Boavida (perished in 2018)

Acknowledgements

First and foremost, I would like to thank my supervisor Dr. Anabela Boavida, to whom I dedicate this thesis, for all the support, guidance, and friendship, who unfortunately did not have the opportunity to see this cycle completed. This is for you.

My special thanks to my supervisor Dr. Jorge Correia for accepting the guidance of my thesis and for their support in the final stages of completion. I am also grateful to both of my supervisors Dr. Killian Lobato and Dr. Ramón Tena-Zaera, for their support and guidance throughout the PhD.

I would like to thank the members of CIDETEC, especially Dr. Ivet Kosta and Sandra Rodríguez, for their supervision, collaboration in the research studies, and friendship during my entire stay in CIDETEC.

I thank Prof. Teresa Monteiro and her team from Universidade de Aveiro for the Photoluminescence measurements and scientific contributions in the published articles.

I must also thank all the members and colleagues of the Solid State Group for their kind support, help, and cooperation whenever required, particularly to Prof. Helena Mendonça, Prof. Estrela Jorge, and Daniel Siopa for their assistance on countless occasions. It was a pleasure to work and be part of this group, which provided me with the skills that I believe have made me the researcher I am today.

I must thank the Fundação para a Ciência e Tecnologia for funding my PhD Grant.

I want to thank my parents for their support, love, for always being there for me, and for giving me strength and for not letting me give up.

Especially, I want to express my deepest gratitude to Rui for his endless patience and support. He was always there for me since the beginning, and his kindness and love gave me the strength to overcome all the adversities that arise over time.

Finally, to Rodrigo, my baby boy, thanks for all the smiles, hugs, love, and fun that we share.

Abstract

Perovskite solar cells are the emerging thin-film photovoltaics that has been most studied in the last decade, reaching record power conversion efficiencies close to those exhibited by silicon solar cells, which means a considerable breakthrough in photovoltaic technology. However, it has been found that in methylammonium lead halide perovskite devices, $MAPbX_3$, either the electron transport material or hole transport material, affects the perovskite material's stability, compromising the perovskite device performance. Therefore, other alternatives should be considered to avoid the perovskite layer's degradation, namely, the electron transport material employed in the perovskite solar cells.

This PhD project aimed to develop nanostructures alternatives to the standard titanium dioxide (TiO_2) through ZnO-based nanostructures, using a low-cost and versatile technique such as pulsed electrodeposition, and applying them as the electron transport layer within perovskite solar cells.

Well-aligned arrays of ZnO nanorods were produced by pulsed potentiostatic electrodeposition in aqueous media, under mild reaction conditions. Several modified substrates were evaluated for the growth of nanorods to optimise the nanorod diameter and vertical orientation. Using a TiO_2 intermediate layer as a template for the ZnO nanorods growth successfully allowed a decrease of the nanorod diameter, increased their spatial density, and increased the ZnO films' chemical stability with time and under illumination. Also, it was verified that the pulsed electrodeposition conditions at which the nanorods grow, namely the pulse operational parameters, had a very appreciable impact on its optoelectronic properties.

Several ZnO thin films prepared using different deposition media were studied to assess the influence of ZnO nature on the thermal stability of the $MAPbI_3$ perovskite. Some chemical groups attached to the ZnO surface affected the crystallization of the perovskite layer and accelerated its thermal degradation at the ZnO/perovskite interface.

The ZnO@TiO_2 core-shell nanostructures were considered to prevent the perovskite instability issues when in intimate contact with ZnO. Despite the slight improvement in device performance using ZnO@TiO_2 core-shell nanorods, compared to ZnO nanorods, the morphological reproducibility of a TiO_2 shell that completely covers the ZnO surface is crucial to obtain higher photovoltaic performances.

Keywords: ZnO nanorods, pulsed electrodeposition, perovskite solar cells, $MAPbI_3$ perovskite, ZnO@TiO_2 core-shell nanorods.

Resumo

As células solares de perovskita são os sistemas fotovoltaicos emergentes de filmes finos que têm vindo a ser mais estudados na última década, alcançando valores de eficiência de conversão energética muito próximos dos valores obtidos para células solares de silício, o que significa um grande avanço na tecnologia fotovoltaica. Os dispositivos de perovskitas de halogenetos de chumbo e metilamónio, $MAPbX_3$, têm sido intensivamente estudados, no sentido de otimizar o seu desempenho e obter elevadas conversões energéticas. No entanto, a camada de $MAPbI_3$, que em células solares de perovskita tem revelado altas eficiências energéticas, tem demonstrado alguns problemas de estabilidade, nomeadamente em termos de instabilidade térmica, sob condições ambientais (humidade, raios ultravioleta (UV)), e quando em contato com alguns materiais usados como transportadores de eletrões ou de lacunas, comprometendo a performance dos dispositivos. No sentido de evitar a degradação da camada de perovskita outras alternativas têm sido consideradas, focadas nomeadamente nos materiais transportadores de eletrões.

Este projeto de doutoramento teve como objetivo desenvolver nanoestruturas alternativas ao típico dióxido de titânio (TiO_2), tais como as nanoestruturas (nanopilares) de base óxido de zinco (ZnO), usando uma técnica de deposição versátil e de baixo custo, como a eletrodeposição pulsada, e aplicá-las como camada transportadora de eletrões no interior de células solares de perovskita.

O ZnO tem sido muito estudado como alternativa ao TiO_2 devido à semelhança de propriedade óticas, mas com a vantagem de apresentar uma mobilidade eletrónica bastante superior. Considerando a sua aplicabilidade em dispositivos solares, as nanoestruturas unidimensionais (1D) permitem um caminho direto para o transporte de carga e um aumento da área superficial capaz de captar a luz solar. No desenvolver deste projeto de doutoramento, nanopilares de ZnO, bem alinhados, foram produzidos por eletrodeposição potenciostática pulsada em meio aquoso sob moderadas condições de reação. A electrodeposição pulsada tem a vantagem de promover a nucleação, através do ajuste dos parâmetros da onda pulsada, que permitirá uma melhoria na difusão das espécies reativas, uma importante etapa da eletrodeposição, e assim proporcionar a formação de cristais finos. A utilização de um eletrólito aquoso à base de iões nitrato tem a vantagem de reduzir a necessidade de convecção e da utilização de um oxidante adicional.

Primeiramente, vários substratos modificados foram testados, tendo como base o substrato condutor de óxido de estanho dopado com flúor (FTO), no sentido de otimizar o crescimento

dos nanopilares e, subsequentemente, controlar o diâmetro dos nanopilares e a sua orientação vertical. Primeiramente, e através de um estudo voltamétrico analisou-se o processo de deposição do ZnO em substratos modificados e não modificados de FTO, e avaliou-se quais as melhores condições a aplicar na eletrodeposição pulsada. Técnicas de caraterização morfológica e estrutural, como microscopia eletrónica de varrimento (SEM), difração de raios-X (XRD) e espectroscopia de Raman, permitiram acompanhar as diferenças que cada substrato modificado originava no crescimento dos nanopilares de ZnO. As propriedades óticas e fotoeletroquímicas dos filmes de ZnO eletrodepositados, foram acompanhadas através da técnica de fotoluminescência (PL) e por fotovoltametria linear. O uso de uma camada de TiO_2 intermédia como matriz suporte para o crescimento dos nanopilares de ZnO, permitiu uma diminuição do seu diâmetro, um aumento da sua densidade espacial e um aumento da estabilidade química dos filmes de ZnO ao longo do tempo e sob irradiação.

Posteriormente, avaliou-se as condições da eletrodeposição pulsada em que os nanopilares crescem, mais precisamente os parâmetros da onda pulsada utilizados, através do controlo da percentagem do tempo total de um ciclo, também conhecido como *duty cycle*, da frequência definida com sendo recíproca do ciclo de tempo, e do ciclo de tempo aplicado. As técnicas espetroscópicas de fotoluminescência (PL) e de impedância eletroquímica (EIS), permitiram verificar que a modelação destes parâmetros tem um grande impacto nas propriedades optoelectrónicas dos filmes de ZnO. Por EIS foi possível verificar que a concentração de portadores de carga e a altura da barreira (V_{FB}) nas regiões de fronteira de grão do ZnO parecem estar relacionadas com as condições de pulso aplicadas. A combinação de diferentes técnicas espectroscópicas permitiu comprovar que, aplicando um tratamento térmico aos nanopilares de ZnO, promove a qualidade ótica, sendo esta evidenciada através da nitidez dos limites de absorção e pelo estreitamento da largura à meia-altura do máximo da emissão ultravioleta (UV).

Antes de aplicar os nanopilares de ZnO em dispositivos de perovskita, vários filmes finos de ZnO preparados utilizando diferentes meios de deposição, nomeadamente em meio aquoso, orgânico e líquido iónico, foram estudados no sentido de avaliar a influência do meio de síntese do ZnO nas suas propriedades, e como estas afetavam a estabilidade térmica da perovskita de $MAPbI_3$. Mediante o meio de deposição utilizado, foi necessário utilizar diferentes técnicas de deposição, nomeadamente a técnica de spray pirólise para filmes de ZnO preparados a partir de meio aquoso, a técnica de *spin-coating* para os filmes obtidos a partir de meio orgânico, e a técnica de eletrodeposição para os filmes obtidos em meio de líquido iónico. As técnicas de caracterização morfológica e estrutural permitiram acompanhar

a cristalização da perovskita $MAPbI_3$ sobre os diferentes filmes de ZnO estudados, bem como a sua degradação térmica ao longo do tempo, quando aplicada em células de perovskita. Por espectroscopia fotoeletrónica de raios-X (XPS) foi possível detetar a presença de alguns grupos químicos ligados à superfície do ZnO, mais propriamente dos filmes obtidos em meio de líquido iónico e em meio orgânico acidificado, que afetaram a cristalização da camada de perovskita e acelerou a sua degradação térmica na interface ZnO/perovskita.

No sentido de evitar os problemas de instabilidade da perovskita quando em contato direto com o ZnO, foi considerada a alternativa de formar uma camada de TiO_2 que funcionasse como concha sobre os nanopilares de ZnO que funcionariam como núcleo, criando assim nanoestruturas *core-shell* de ZnO@TiO_2. Dois métodos de deposição da *shell* de TiO_2 foram considerados, nomeadamente a técnica de *spin-coating* e o método solvotérmico. O método solvotérmico foi considerado o indicado para a preparação da *shell* de TiO_2, pois permitiu formar uma camada de TiO_2 aderente às nanoestruturas de ZnO aparentemente intactas após o processo de deposição. Por forma a otimizar a sua morfologia e uniformidade no recobrimento individualizado dos nanopilares de ZnO, foram estudados diferentes parâmetros de síntese, tais como a temperatura, o tempo de reação e a adição de aditivos, mais propriamente, de acetilacetona. A temperatura de 150 °C foi considerada a indicada para a obtenção de TiO_2 na fase pura de anatase sem ocorrer uma formação exacerbada da camada de TiO_2. A caraterização morfológica das nanoestruturas *core-shell* de ZnO@TiO_2 obtidas com uma solução percursora envelhecida revelou que ao longo do tempo de reação, as nanoestruturas de ZnO sofriam dissolução devido ao pH ácido da solução após o tratamento solvotérmico, não sendo considerado uma etapa viável para a obtenção das nanoestruturas *core-shell*. A adição de acetilacetona à solução percursora teve como intuito controlar a formação de TiO_2 através da supressão da reação de hidrólise, sendo necessário apenas uma pequena porção para que a *shell* de TiO_2 formada fosse mais uniformemente distribuída sobre os nanopilares de ZnO. Um estudo preliminar, permitiu averiguar que apesar da ligeira melhoria no desempenho dos dispositivos usando os nanopilares *core-shell* de ZnO@TiO_2, comparativamente aos dispositivos utilizando os nanopilares de ZnO, a reprodutibilidade morfológica da camada de TiO_2 que deverá cobrir na totalidade a superfície do ZnO parece ser determinante para o sucesso destas estruturas alternativas na obtenção de melhores desempenhos fotovoltaicos.

Palavras-chave: nanopilares de ZnO, electrodeposição pulsada, células solares de perovskita, perovskita de $MAPbI_3$, nanopilares core-shell de ZnO@TiO_2.

Declaration of Authorship

All work presented in this thesis, except where explicitly indicated below, is of my authorship. The experimental work and interpretation of the results performed in collaboration with other researchers are as follows:

Chapter 3, Section 3.3 and 3.4: The Raman spectra and Photoluminescence experiments were performed by José F.C. Carreira, of the Departamento de Física from Universidade de Aveiro. All the interpretation and discussion reported within this chapter was part of a collaboration with Professor Teresa Monteiro and her team from Departamento de Física and I3N from Universidade de Aveiro.

Chapter 4, Section 4.2: The Raman, Absorption, and all the Photoluminescence spectra (including PLE and TRPL) were performed by José F.C. Carreira and Joana Rodrigues of the Departamento de Física from Universidade de Aveiro. As in Chapter 3, all the interpretations and discussions reported with this chapter resulted from a collaboration with Professor Teresa Monteiro and her team from Departamento de Física and I3N from Universidade de Aveiro.

Table of Contents

List of figures

List of tables

Nomenclature

Abbreviations

PCBM	[6,6]phenyl-C61-butyric acid methyl ester
MEA	2-(2-methoxyethoxy)acetic acid
Spiro-OMeTAD	2,2’,7,7’-tetrakis(N,N’-di-4-methoxyphenylamino)-9,9’-spirobifluorene
TBP	4-tert-butylpyridine
ACAC	Acetylacetone
AM	Air mass coefficient
AZO	Al-doped zinc oxide
AC	Alternating current
AFM	Atomic force microscopy
ALD	Atomic layer deposition
BCP	Bathocuproine
BE	Binding energy
CBD	Chemical bath deposition
N3	cis-bis(isothiocyanato)bis(2,2’-bipyridyl-4,4’-dicarboxylato)ruthenium (II)
c-TiO_2	Compact titanium dioxide
CIGS	Copper indium gallium selenide
CZTSSe	Cupper zinc tin sulfide/selenide absorber
CV	Cyclic voltammetry
DMF	Dimethylformamide
DMSO	Dimethylsulfoxide
DC	Direct current
N719	di-tetrabutylammonium cis-bis(isothiocyanato)bis(2,2’-bipyridyl-4,4’-dicarboxylato) ruthenium (II) dye
DSSC	Dye-sensitized solar cell
EIS	Electrochemical Impedance Spectroscopy
ETM	Electron transport material
ETL	Electron Transporting Layer
EDS	Energy dispersive spectroscopy
ETA	Extremely thin absorber
FESEM	Field-emission scanning electron microscopy
FTO	Fluorine-doped tin oxide
FAI	Formamidinium iodide
FA^+	Formamidinium ion

FB	Forward bias
FRA	Frequency response analyser
FWHM	Full width half maximum
GBL	g-butylrolactone
HMT	Hexamethylenetetramine
HOMO	Highest occupied molecular orbital
HTM	Hole transport material
HTL	Hole transporting layer
ITO	Indium-doped tin oxide
IPA	isopropanol
JCPDS	Joint Committee for Powder Standards
LO	Longitudinal optical vibration
LUMO	Lowest unoccupied molecular orbital
mp-TiO_2	Mesoporous titanium dioxide
MOCVD	Metal-organic chemical vapour deposition
MAI	Methylammonium iodide
MA^+	Methylammonium ion
$MAPbX_3$	Methylammonium lead halide perovskite
MS	Mott-Schottky
NRs	Nanorods
NREL	National Renewable Energy Laboratory
NBE	Near band edge emission
OPSC	Organic and polymeric solar cell
OHP	Outer Helmholtz plane
PSC	Perovskite solar cell
PL	Photoluminescence
PLE	Photoluminescence excitation
PV	Photovoltaic
PECVD	Plasma enhanced chemical vapour deposition
PEDOT	Poly(3,4-ethylenedioxythiophene)
P3HT	Poly(3-hexylthiophene)
PSS	Poly(styrene sulfonate)
PANI	Polyaniline
PTAA	Polytriarylamine
XRD	Powder X-Ray Diffraction
PCE	Power conversion efficiency

QDs	Quantum dots
QDSSC	Quantum dot-sensitized solar cell
Ref.	Reference electrode
RTC	Relative texture coefficient
r.p.m.	Revolutions per minute
RT	Room temperature
SD	Sample delay
SEM	Scanning electron microscopy
SL	Seed-layer
SC	Short circuit
TRPL	Time-resolved photoluminescence
TTIP	Titanium (IV) isopropoxide
TEM	Transmission electron microscopy
TCO	Transparent conductive oxide
TO	Transverse optical vibration
UV	Ultraviolet
UV-Vis	Ultraviolet-Visible Spectroscopy
1D	Unidimensional
VASP	Vapour-assisted solution process
VLS	Vapour-liquid-solid deposition
XPS	X-ray photoelectron spectroscopy

Symbols and Constants

T	Absolute temperature
Abs	Absorptance
V	Applied potential
E_g	Bandgap energy
L	Bond length
R_{ct}	Charge transfer resistance
E_{CB}	Conduction band edge
Z_{CPA}	Constant phase angle element
I	Current
i	Current density
J	Current density
ε_{ZnO}	Dielectric constant of ZnO
D^0X	Donor bound excitons

N_D	Donor density
Θ	Effective phonon temperature
e^-	Electron
q	Electron charge
e_{cb}^-	Electron on the conduction band
E_g	Energy gap
E_{co}	Equilibrium potential
FF	Fill factor
V_{FB}	Flatband potential
e.g.	For example
FX	Free bound excitons
f	Frequency
h^+	Hole
$h\nu$	Incident photon energy
Zn_i	Intrinsic point defect of Zn
a, b, and c	Lattice constants
P_{max}	Maximum power
hkl	Miller indices
E_h	Nucleation overpotential
V_{oc}	Open-circuit voltage
α	Optical absorption coefficient
V_o	Oxygen vacancies
ε_0	Permittivity of free space
E	potential
η	Power conversion efficiency
t_{on}	Pulse deposition time
E_{on}	Pulse potential
R (%)	Reflectance
E_{off}	Rest potential
t_{off}	Rest time
J_{sc}	Short circuit current density
P_{in}	Solar incident power
R_s	Solution resistance
C	Space charge capacitance
sq	square
ε	Strain

σ	Stress
Δ	Temperature
$T\ (\%)$	transmittance
E_{VB}	Valence band edge
λ	Wavelength

Chapter I

Introduction

The climate crisis has become mainstream in the last few years and is, arguably, the primary global concern. Greenhouse gas emissions have had a considerable impact, and their levels have become critical to the point that new measures must be taken to minimise the impacts of climate change.

Renewable energies are considered the most viable alternative energy sources since they are sustainable, non-pollutant, produce zero emissions, and now cost-effective. Thus, by 2023, the renewable energies, according to the IEA "are forecast to meet more than 70 % of the global electricity generation growth, led by solar" [1].

Solar energy used as photovoltaic (PV) technology allows direct production of high-quality electric power from the Sun's radiation via the photovoltaic effect [2]. This effect, discovered in 1839 by the physicist Alexandre-Edmond Becquerel, occurs in semiconductor materials. They are simply characterized as having electrical conductivity values between those typically exhibited by a conductor and an insulator [3]. Briefly, when the light reaches the semiconducting material, it causes the excitation of an electron to a higher energy state, providing the photons have sufficient energy to overcome the potential barrier for excitation; this phenomenon leads to the creation of an electron-hole pair, and this charge separation process produces a voltage (photopotential); upon application of an electric field or by means of the built-in electric field of the depletion region, the charge carriers are swept in opposite directions, generating an electrical current (photocurrent) [4].

Photovoltaic systems are environmentally friendly, which means that no gas emissions are generated, can operate autonomously with almost no maintenance, and do not generate any noise or disturbance, being a perfect solution for urban areas and residential applications. However, like other renewable energy technologies, the energy supply is intermittent, requiring additional equipment to store the energy and convert direct current (DC) to alternating current (AC) to deliver a stable energy supply and be used on the power network. Additionally, the costs linked to the production and materials used during the manufacture of the panels increases the investment for conventional PV panels considerably.

Many different photovoltaic technologies have been developed to provide affordable renewable energy to replace fossil fuels and can be grouped into three generations of devices. The first-generation is wafer-based cells using thick crystalline films, namely silicon (Si) and

gallium arsenide (GaAs), which are the most widely used for commercial solar panels. This PV architecture operates according to the principle of the p-n junction, Figure 1.1, which is formed by joining p-type (an excess of positive charges, called holes) and n-type (an excess of electrons) semiconductors. When the sunlight's photons reach the solar cell, the electrons absorb its energy, producing excited hole-electron pairs. These charge carriers are separated by an electrical field in the depletion region and conducted through the p-n junction. If an external circuit is connected to the cell terminals, these charges flow in as an electric current, which means electricity. The use of crystalline silicon in photovoltaic technology has many advantages becoming hard to compete with. Considering the availability of the raw material, it has the advantage of being the second most abundant element in the earth's crust [5], which means that it is unlikely to face issues related to abundance, stability and toxicity. It also benefits of more than half a century of knowledge on these devices, being now produced at a record PCE of 26.7 % [6], which is very close to the maximum theoretical efficiency of ~33 % for a single p-n junction solar cell, also known as the Shockley-Queisser limit [7]. Despite these advantageous characteristics, all the costs associated with silicon modules' manufacturing are still very expensive.

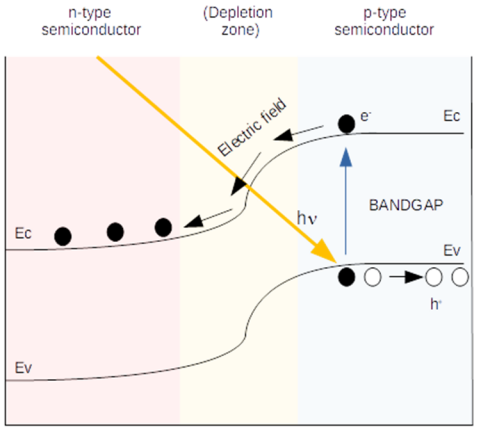

Figure 1.1 – Band diagram of p-n junction in a standard solar cell.

The second-generation PV cells were developed to reduce the high costs associated with the first-generation devices by using a lower amount of material, thin films down to only ~1 µm layer thickness. Cells based on amorphous Si (*a*-Si), cadmium telluride (CdTe), and copper indium gallium selenide (CIGS), Figure 1.2, are included in this generation [8]. These

PV technologies are cheaper than crystalline Si-solar cells because the used materials present higher absorption coefficients than crystalline Si enabling the use of thinner films [9]. However, the record efficiencies for these PV cells are lower than those obtained for Si solar cells [10]. Also, the toxicity, abundance and outdoor instability of some of the employed materials has significant concerns when their widespread use are questioned [9].

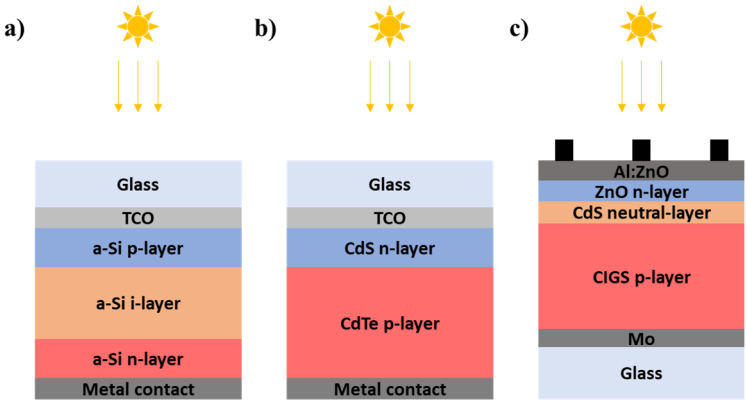

Figure 1.2 - Schematic cross-section representation of typical second-generation photovoltaic cells: ***a)*** *amorphous silicon (a-Si),* ***b)*** *Cadmium Telluride (CdTe), and* ***c)*** *Copper Indium Gallium Selenide (CIGS). TCO is transparent conductive oxide. (Adapted from* [11]*).*

The third-generation PV cells are considered the emerging technologies that can overcome many of the limitations of the previous generations. It aims to develop highly efficient devices using low-cost thin layer deposition techniques with abundant non-toxic raw materials, with mechanical robustness and suitable for large-scale production [12]. This generation includes several device architectures as inorganic solar cells, organic and polymeric solar cells (Figure 1.3), dye-sensitized solar cells (DSSCs) (Figure 1.4), and quantum dot-sensitized solar cells (QDSSCs). However, despite the efforts to achieve higher efficiencies with these PV devices, their record power efficiencies are still far from the accomplished efficiencies for Silicon devices [10].

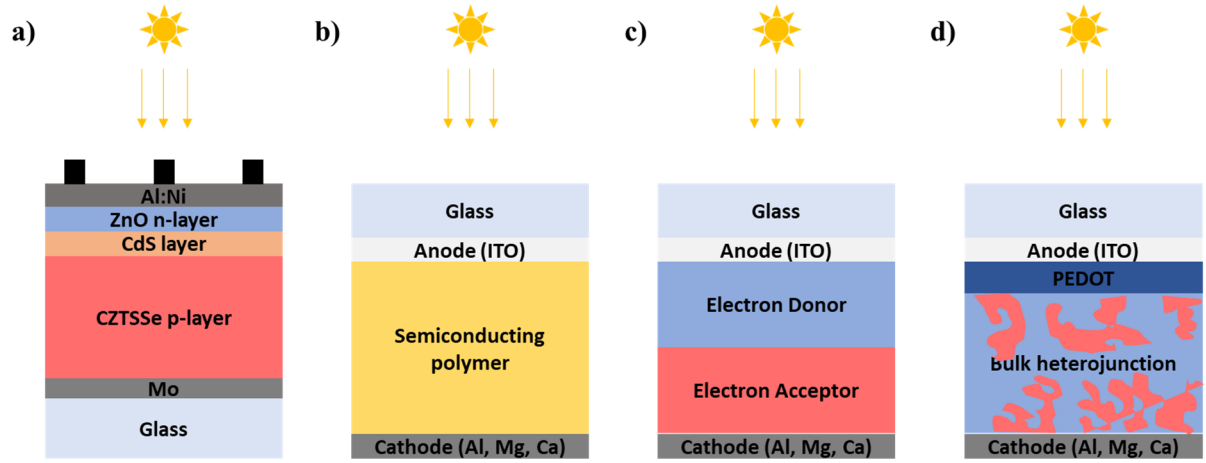

Figure 1.3 - Schematic cross-section representation of some of third-generation photovoltaic cells, namely ***a)*** *Copper Zinc Tin Sulfur-Selenium (CZTSSe) solar cells, and organic and polymeric solar cells (OPSCs):* ***b)*** *single layer,* ***c)*** *bilayer, and* ***d)*** *bulk heterojunction. (Adapted from* [11]*).*

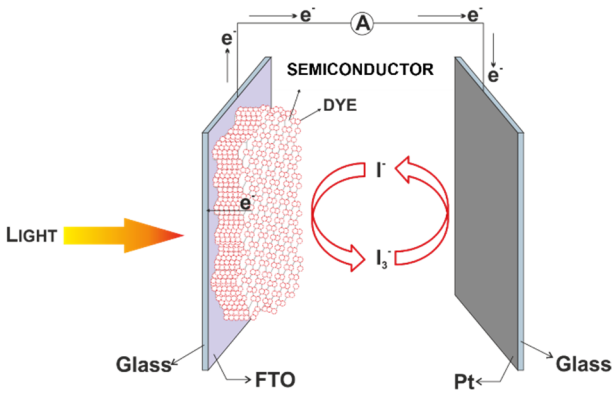

Figure 1.4 - Schematic representation of the mechanism of a DSSC.

In 2009, with the aim of combining organic and inorganic photosensitive materials, Miyasaka et al. used for the first time perovskite materials, more precisely a hybrid organic-inorganic lead halide-based materials, as sensitizers in a liquid electrolyte based dye-sensitized solar cell, presenting an initial efficiency value of 3.8 % [13]. Through optimization of the perovskite coating solution, TiO_2 film thickness and electrolyte formulation, Park *et al.* reached a higher PCE of 6.5 % using a lead iodide-based perovskite quantum dot sensitizer [14]. However, despite the increase in PCE values, the liquid electrolyte was still an issue in terms of the lack of stability of the perovskite material [14]. In 2012, this instability problem was solved by replacing the liquid electrolyte with a solid hole-transporting material, the first solid-state mesoscopic perovskite solar cell that was highly efficient [15]. Therefore,

perovskite solar cells (PSCs) are a new class of photovoltaic devices that have gained the attention of the solar energy research community. Since the beginning of the application of perovskite materials in PV devices, a significant improvement in cell efficiencies has been accomplished in just ten years, reaching a certified value of 25.2 % [10], putting this PV technology in direct competition with crystalline silicon technology.

There has been a great deal of interest in perovskite solar cells following these significant improvements, with over 20,000 peer-reviewed research papers on perovskite solar cells published in the last decade (based on Web of Science data), Figure 1.5.

Since perovskite solar cells is the area of application of the materials developed in this thesis, it will be covered in more detail in the next section.

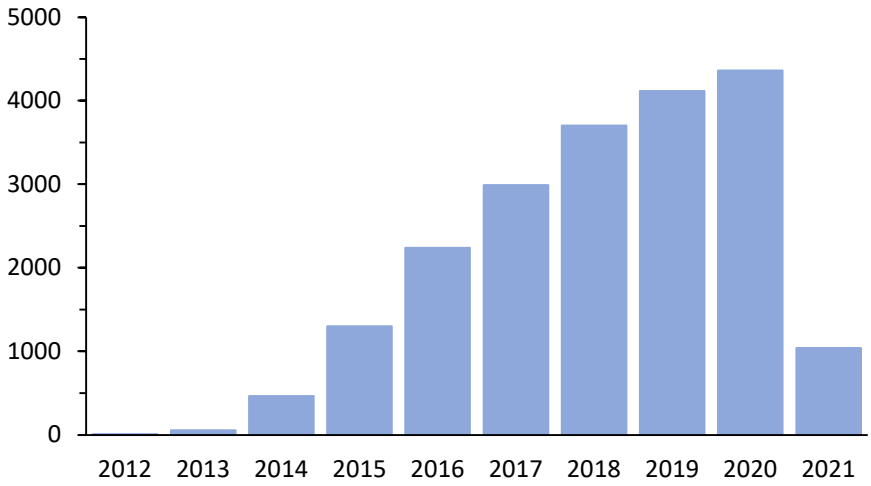

Figure 1.5 - Number of publications on perovskite solar cells in the last decade, based on Web of Science data (24/04/2021).

Figure 1.6 shows a compilation of the PV technologies developed up to nowadays, with the certified cells efficiencies values from NREL [10].

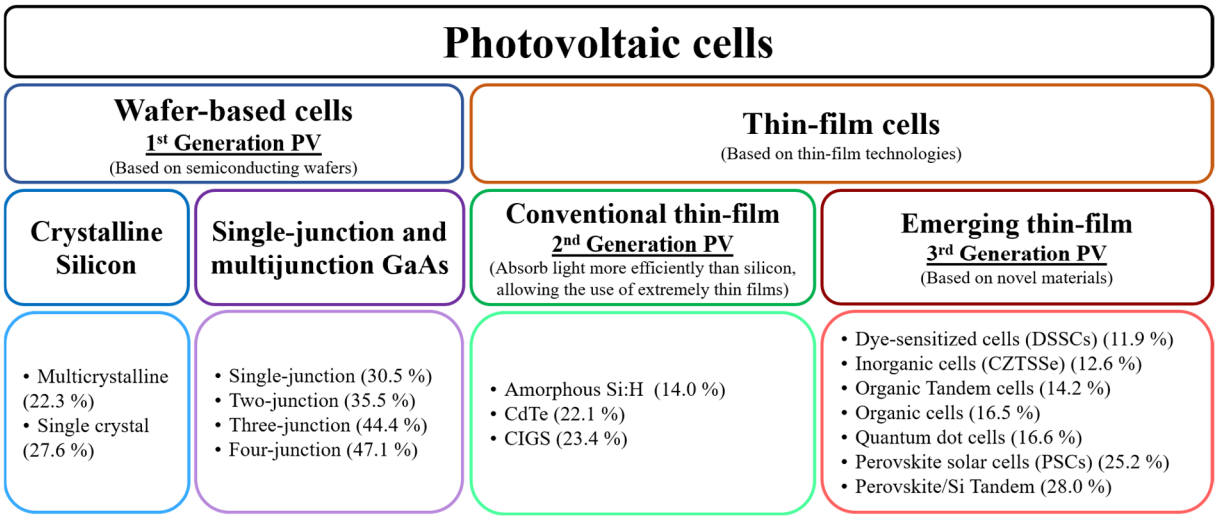

Figure 1.6 - Scheme of photovoltaic technologies developed up to the present, with the respective best-certified cell efficiencies from NREL [10].

1.1. Perovskite solar cells (PSCs)

1.1.1. PSC working principle

The working principle of PSC devices also involves light absorption, charge separation, charge transport, and charge collection [16]. Figure 1.7 shows the band diagram and the operation principle of a general PSC. First, the perovskite layer absorbs light, and electron-hole pairs are generated (equation 1.1) [17]. The charge separation can then occur through two possible reactions, namely by the injection of photogenerated electrons into the electron-transporting layer (ETL) (equation 1.2 and 1.3) and/or by the injection of holes into a hole-transporting layer (HTL) (equation 1.4 and 1.5) [17]:

- Photoexcitation of perovskite:

$$Perovskite + h\nu \rightarrow (e^- \cdots h^+)_{perovskite} \quad (1.1)$$

- followed by electron injection:

$$(e^- \cdots h^+)_{perovskite} \rightarrow e^-_{cb}(ETL) + h^+(perovskite) \quad (1.2)$$

$$h^+(perovskite) \rightarrow h^+(HTL) \quad (1.3)$$

- or followed by hole injection:

$$(e^- \cdots h^+)_{perovskite} \rightarrow h^+(HTL) + e^-(perovskite) \quad (1.4)$$

$$e^-(perovskite) \rightarrow e^-_{cb}(ETL) \quad (1.5)$$

However, it is still unclear which processes (electron or hole injection) occur first. Meanwhile, to achieve high PCE, the charge generation and transport rate should be faster than the undesired recombination reactions, such as photoluminescence, non-radiative recombination, and recombination of the charge carriers at the three interfaces [17,18].

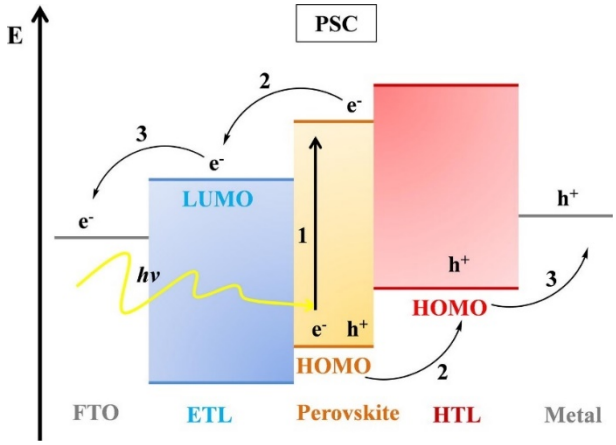

Figure 1.7 - Band diagram and operation principle of perovskite solar cell: 1)Absorption of photon and free charge generation; 2) Charge transport; 3) Charge extraction (Taken from [19]*). LUMO is the lowest occupied molecular orbital, and HOMO is the highest occupied molecular orbital, also known as conduction band level (E_{cb}) and valence band level (E_{vb}), respectively.*

1.1.2. PSC architecture and their components

The PSC architecture includes a material with a perovskite structure (Figure 1.8), a class of materials with a generic structure ABX_3, where both A and B are cations, and X is an anion, and it acts as the light-harvesting active layer. This layer is placed between the electron transport material (ETM) and the hole transport material (HTM) (Figure 1.9). In a standard device configuration, the negative terminal is a transparent conductive electrode, usually a FTO slide, and the positive terminal is a thermally-evaporated gold layer.

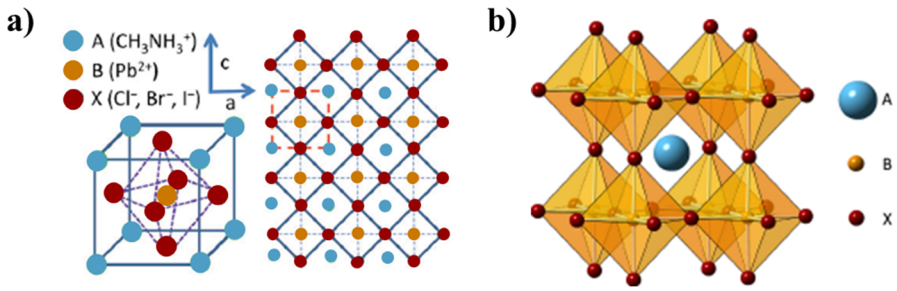

Figure 1.8 - Perovskite structure: ***a)*** *the perovskite cubic crystal structure* [20] *and* ***b)*** *three-dimensional crystal* [19]. *In hybrid organic-inorganic perovskite materials the (A)is an organic cation (as $CH_3NH_3^+$), (B)is generally lead cation (Pb^{2+}), and (C) is a halide anion such as chloride (Cl^-), bromide (Br^-) or iodide (I^-).*

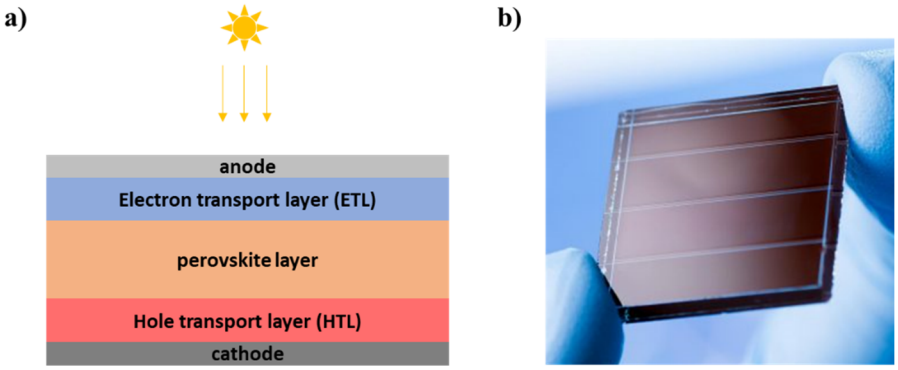

Figure 1.9 - ***a)*** *Schematic representation of a cross-section perovskite solar cell and* ***b)*** *a real PSC device (Taken from* [21]*).*

1.1.2.1. PSC components

The main components of a perovskite solar cell are a perovskite layer between electron transport layers (ETLs) and hole transport layers (HTLs). Generally, the ETLs and HTLs are used to extract the charges selectively and to maximise the solar cells' open circuit voltage [22]. Additionally, the highest occupied molecular orbital (HOMO) energy level of the HTM should be well aligned with the valence band (E_{VB}) of the perovskite, while the conduction band (E_{CB}) of the perovskite should be aligned with the lowest unoccupied molecular orbital (LUMO) energy level of the ETM, to minimise energy losses [23]. Figure 1.10 shows the energy levels of the most common perovskite, electron transport and hole transport materials used in PSCs.

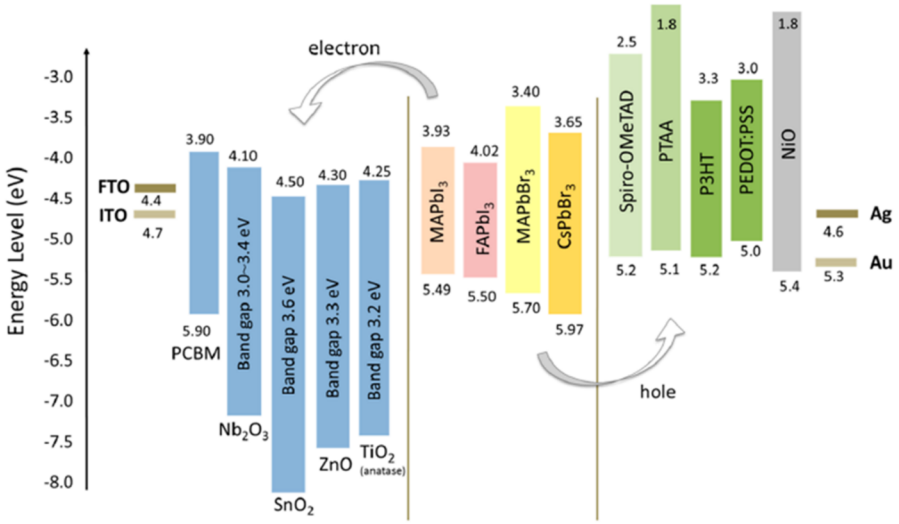

Figure 1.10 - Energy levels of lead halide perovskite materials and the electron transport materials (ETMs) and hole transport materials (HTMs) most employed in solar cell devices (taken from [24]*).*

Perovskite materials

The perovskite materials which have shown a greater potential to be used in PV devices are the hybrid organic-inorganic perovskite materials, especially the organometal halide perovskites with ABX_3 structure, where A is the organic fragment such as methylammonium ($CH_3NH_3^+$ or MA^+) or formamidinium ($NH_2CH{=}NH_2^+$ or FA^+), B is a divalent metal cation as Pb^{2+}, Cu^{2+}, Co^{2+}, and X is a halide (I^-, Cl^-, Br^-) [25]. Among all the possible combinations, the methylammonium lead iodide ($CH_3NH_3PbI_3$, $MAPbI_3$) proved to be a promising material due to its properties, namely high light absorption coefficients (~10^5 cm^{-1} in the visible region) [26,27], direct bandgap [28,29], ambipolar charge carrier [30], high intrinsic carrier mobility [31], and long electron-hole diffusion lengths [32].

In recent years, considering improvements of the PCEs and long-term stability of the devices, perovskite compositional engineering has been applied through distinct combinations of A-site cations and X-sites halides, resulting in published NREL certified cell efficiencies [24].

The inorganic perovskite materials have emerged to improve the long-term stability of the devices since the organic part is believed to be responsible for the poor thermal and environmental stability of these materials [33]. Caesium-based perovskite structures like $CsPbX_3$ (X = Cl, Br, I) have been considered a model compound among all inorganic

perovskites that Wells first studied in 1893 [34]. However, despite its superior stability against heat, the effective application of $CsPbX_3$ in PSCs has been complex for several reasons. Therefore, the progress in PCE of these cells has been slow [35,36].

Electron transport materials (ETM)

The electron transport layers (ETLs) applied in PSCs can be organic or inorganic. The inorganic charge transport materials are commonly n-type oxide semiconductors, such as titanium oxide (TiO_2), zinc oxide (ZnO) or tin oxide (SnO_2). Depending on the type of cell architecture to be applied, the ETL can either be a compact layer (*e.g.* TiO_2 compact layer, c-TiO_2) when used in a planar configuration [37] or a mesoporous/nanostructured layer (*e.g.* mesoporous TiO_2 layer, mp-TiO_2) when applied in a mesoscopic design [38]. The main goal of using nanostructured ETLs in PSC is to improve the charge collection [39].

TiO_2 remains the most prevalent inorganic ETM used in PSCs due to its attractive energy levels Figure 1.10, high optical transparency and environmental stability, which has resulted in the highest reported efficiencies [40,41]. However, it suffers from several drawbacks, namely the need for high deposition temperature to obtain pure anatase phase [42], its low electron mobility (0.1 – 4 $cm^2\ V\ s^{-1}$ [43]) resulting in an inefficient charge extraction from the perovskite, and its photocatalytic properties which can contribute to the perovskite degradation under UV light [44]. Despite the several efforts that have been made to obtain high efficiencies of PSCs with TiO_2 ETL, alternative ETLs that could be processed at lower temperatures have been considered. ZnO has been pointed out as an alternative to TiO_2 ETL due to its similar bandgap, high electron mobility (200-300 $cm^2\ V\ s^{-1}$ for bulk material and ~ 1000 $cm^2\ V\ s^{-1}$ for single-crystal nanowires [43]), and can be synthesised at low temperatures [45]. Liu *et al.* [46] were the first to report using ZnO nanoparticle layers as a compact ETL on planar PSCs with efficiencies approaching 15.7 % and on flexible perovskite solar cells with performances exceeding 10 %. Another alternative material to TiO_2 that gained popularity in recent years is SnO_2, which is more conductive than TiO_2, allowing to achieve high efficient and stable devices [47]. Table 1.1 compares some physical properties of TiO_2, ZnO, and SnO_2 [48].

Table 1.1 - A comparison of some physical properties of TiO_2, ZnO, and SnO_2 (taken from [48]*).*

Physical property	**TiO_2**	**ZnO**	**SnO_2**
Crystal structure	Rutile, anatase, and brookite	Rocksalt, zinc blende, and wurtzite	Rutile and tetragonal
Energy band gap (eV)	3.0-3.2	3.2-3.3	3.6
Electron mobility (cm^2 V s^{-1})	0.1-0.4 (bulk TiO_2)	205-300 (bulk ZnO)	200 (bulk SnO_2)

The organic ETLs have been used due to the possibility of being processable at low temperatures. The most commonly used organic ETLs in PSCs are fullerene derivatives, such as 6,6-phenyl-C_{61}(or C_{71})-butyric acid methyl ester (known as PCBM), which possess sufficiently high electron mobility, well-defined energy levels, and good energy alignment with the perovskite [40]. The organic ETLs are often used in inverted perovskite devices reporting PCE between 16-18% [49–51].

Hole transport materials (HTM)

Similar to ETLs, the hole transport layers (HTLs) can be organic or inorganic materials. The most commonly used HTLs are organic materials, such as 2,2',7,7'-tetrakis(*N*,*N*-di-4-methoxyphenylamino)-9,9'-spirobifluorene (Spiro-OMeTAD), which is the most used in devices with oxide ETL, poly(3,4-ethylenedioxythiophene) doped with polystyrene sulfonate (PEDOT:PSS) is the most used in devices with organic hole transport layers, polytriarylamine (PTAA) or poly(3-hexylthiophene) (P3HT) [52].

While most of the reported HTLs have been organic materials, inorganic HTLs have also been used for stability improvements. However, it should be noted that the use of inorganic HTLs can result in potential operational difficulties related to the layer deposition process, namely deposition temperature limitations or the nature of the solvents used for materials processing that dissolves the perovskite material. These limitations are only effective in a conventional architecture with the HTL on top of perovskite, which could be circumvented in an inverted device architecture, with the HTM layer deposited directly on the substrate. The inorganic materials most reported are nickel oxide (NiO) [53], copper thiocyanate (CuSCN) [54], and copper iodide (CuI) [55].

1.1.2.2. Evolution of PSC architecture

In the last decade, there has been significant focus on research of perovskite solar cells, consistently to achieve devices with high efficiencies and excellent stability. Accordingly, several PSC architectures have been developed, from the simple application of perovskite QDs as a sensitizer in DSSC structure to the PSC planar structure (Figure 1.11 [56]).

The cell architecture is one of the parameters that strongly affects the final cell efficiency. Indeed, depending on the combination of the main components, it is possible to optimize the device's performance.

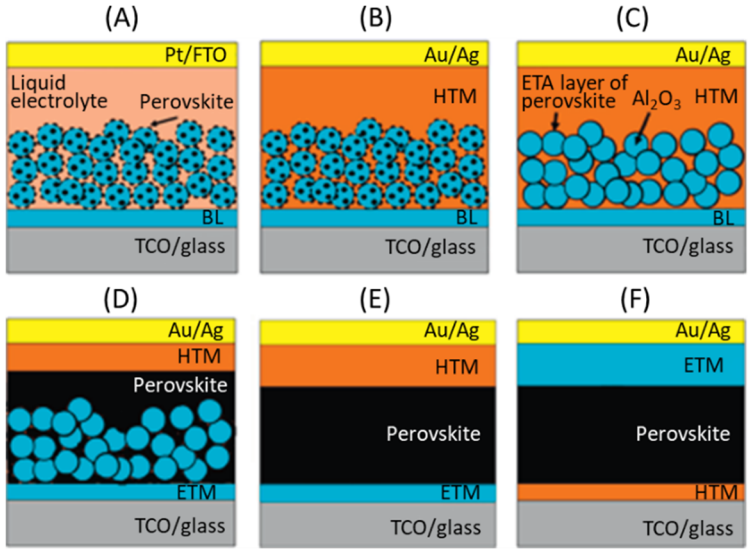

Figure 1.11 - Schematic of perovskite solar cell architecture evolution: (A) liquid electrolyte DSSC structure with perovskite QDs, (B) Solid-state mesoscopic structure, (C) meso-superstructured structure, (D) mesoporous structure, (E) planar structure, and (F) inverted planar structure (Taken from [56]*). BL is the blocking layer, ETA is an extremely thin absorber, and the blue particles on (A), (B) and (D) are mp-TiO_2.*

(A) Liquid electrolyte DSSC structure

The hybrid organic-inorganic perovskite devices were initially fabricated in the conventional DSSC structure, where an organometal halide perovskite material replaced the organic dye. In 2009, Kojima *et al.* reported using $MAPbI_3$ and $MAPbBr_3$ perovskite nanocrystalline particles onto mp-TiO_2/c-TiO_2/FTO substrate [13]. Table 1.2 shows the PV characteristics of the perovskite-sensitized photovoltaic cells tested. Despite having a very similar overall performance, assessed by the fill factor (*FF*) of the characteristic curve, essential differences of the systems may be depicted. For example, the highest PCE of 3.8 %

was reached by the $MAPbI_3$ devices, with a short circuit current density (J_{sc}) twice higher than $MAPbBr_3$ devices.

In contrast, $MAPbI_3$ devices showed a low open-circuit voltage (V_{oc}) of 0.61 V, while the $MAPbBr_3$ device yielded a higher V_{oc} of 0.96 V. The higher J_{sc} of the $MAPbI_3$ devices is justified by the lower bandgap value of this perovskite (1.5 eV) in comparison with $MAPbBr_3$ (2.3 eV), allowing photoconversion at longer light wavelengths [56]. However, lower values of V_{oc} were recorded for $MAPbI_3$ devices due to the slight difference between the energy levels of the conduction band of the perovskite and the redox potential of the triiodide/iodide (I_3^-/I^-) mediator (Figure 1.12) [13]. This work demonstrated the potential of the hybrid organic-inorganic perovskite materials in photovoltaic applications, despite the low logged efficiencies.

Table 1.2 - Photovoltaic characteristics of perovskite-based cells, measured with an effective incident area of 0.24 cm^2 under 100 $mW.cm^{-2}$ AM 1.5 simulated sunlight irradiation (adapted from [13]*).*

Perovskite sensitizer	J_{sc} **(mA.cm^{-2})**	V_{oc} **(V)**	***FF***	η **(%)**
$MAPbBr_3$	5.57	0.96	0.59	3.13
$MAPbI_3$	11.0	0.61	0.57	3.81

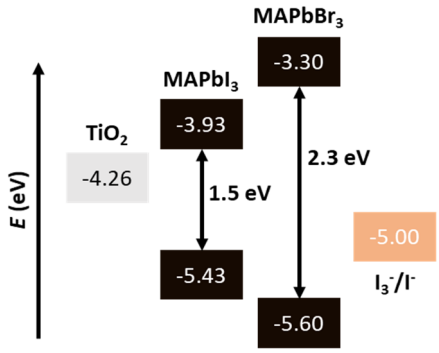

Figure 1.12 - Energy level diagram of a liquid-electrolyte DSSC with perovskite sensitizers (adapted from [56]*).*

Interested in this type of material for DSSCs applications, Im *et al.* manufactured perovskite-sensitized DSSCs using $MAPbI_3$ QDs on a mp-TiO_2 layer (Figure 1.11A), showing a significant improvement in PCE, obtaining a record of 6.54 % [14]. However, although this work revealed the high light absorption coefficient of the hybrid perovskite materials, the

instability of this device limits their applicability, since, in just 10 min of continuous illumination, the performance of the device dropped 80% due to, according to the authors, the dissolution of the perovskite QDs in the liquid electrolyte.

(B) Solid-state mesoscopic structure

To overcome the instability issue of the perovskite devices with a liquid electrolyte, Kim *et al.* developed the first solid-state PSC by replacing the liquid electrolyte with Spiro-OMeTAD, a solid HTM [15]. This device configuration is very similar to the perovskite-sensitized DSSCs (Figure 1.11B), although the thickness of the mp-TiO_2 layer is much smaller (~ 0.6 μm). By penetrating the pores of the mp-TiO_2 layer, the HTM makes direct contact with the perovskite QDs, and the remaining material creates a dense layer that covers the mp-TiO_2 layer preventing the electron transfer to the anode. The use of Spiro-OMeTAD allowed a better hole-transfer efficiency achieving a record PCE of 9.7 %, a marked enhancement in the device stability, remaining stable after 500 h under illumination, and an improvement of V_{oc} values due to a better alignment of the HOMO level of Spiro-OMeTAD with the valence band of $MAPbI_3$, allowing an effective hole extraction from the perovskite (Figure 1.13) [56].

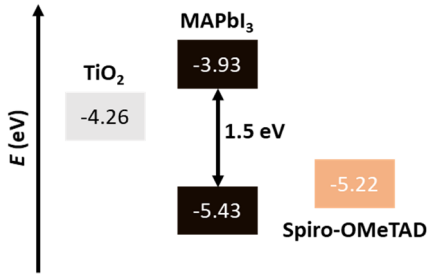

Figure 1.13 - Energy level diagram of a perovskite solar cell in solid-state mesoscopic structure (adapted from [56]*).*

(C) Meso-superstructured structure

Lee *et al.* developed the meso-superstructure architecture based on the mesoscopic configuration by replacing the mp-TiO_2 layer with a porous insulating layer of Al_2O_3 and by employing an extremely thin absorber (ETA) layer strategy, a continuous and highly tinny $MAPbI_2Cl$ perovskite layer on the porous metal oxide surface were used (Figure 1.11C) [57].

Interesting results were obtained when Al_2O_3 was used, achieving a PCE of 10.9 % (for mp-TiO_2, the best device obtained a PCE of 7.6 %), and significantly high V_{oc} values of approximately 1.1 V, which indicates low non-radiative recombination and long carrier diffusion lengths of the mixed halide perovskite [32].

The charge transport on meso-superstructured cells is slightly different than in mesoscopic cells. Whereas in mesoscopic devices, the photoexcited electrons from the perovskite absorber are injected into the conduction band of the mp-TiO_2 layer, this injection is energetically unfavourable when an Al_2O_3 layer is used due to the higher energy level of the conduction band of Al_2O_3 relative to the mixed halide perovskite absorber (Figure 1.14) [57,58]. In this device architecture, the electrons are transported to the c-TiO_2 blocking layer through the ETA perovskite layer, which means that the PSCs could be manufactured without the mesoporous layer.

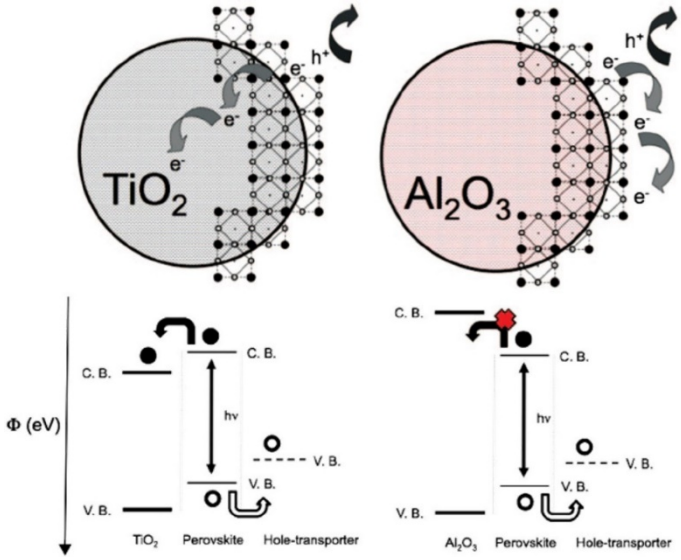

Figure 1.14 - Schematic diagram illustrating the charge transfer and charge transport of PSCs using a mp-TiO_2 layer (left) and an insulating Al_2O_3 layer (right), and a representation of the energy level diagrams (below) (taken from [57]*).*

(D) Mesoporous structure

Several researchers dedicated to the study of the perovskites and discovered that these materials have a low trap state density and long carrier diffusion lengths [32,59], which means that thicker perovskite films can be used instead of ETA layers on PSCs. In this sense, the

mesoporous structure, also known as the regular structure, was developed based on the meso-superstructure architecture but used a thicker and dense perovskite layer (Figure 1.11D). This structure allowed the researchers to fabricate high-efficiency PSCs since increasing the thickness of the perovskite layer can improve the absorption of large wavelength photons and prevent the possibility of a short circuit between electrodes. However, if the thickness of the perovskite layer is greater than the carrier diffusion length, the generated carriers will recombine before reaching the ETL [60]. Therefore, mesoporous ETMs are deposited over a hole-blocking layer to avoid this recombination, allowing the photogenerated electrons to flow through it, reaching the collecting electrode before recombining [61].

Heo *et al.* fabricated PSCs with this structure using $MAPbI_3$ perovskite to fill the pores of a mp-TiO_2 layer and form a pillar-shaped perovskite capping layer (Figure 1.15a) [62]. The PCE of the best cell was 12 % for a 600 nm mp-TiO_2 layer with 200-300 nm of $MAPbI_3$ overlayer on top of mp-TiO_2, which allowed the optimal trade-off between TiO_2/$MAPbI_3$ interface area and hole path length, avoiding the probability of recombination [62]. However, it was also observed that due to the roughness and discontinuous morphology of the $MAPbI_3$ overlayer, an improvement in device performance was limited.

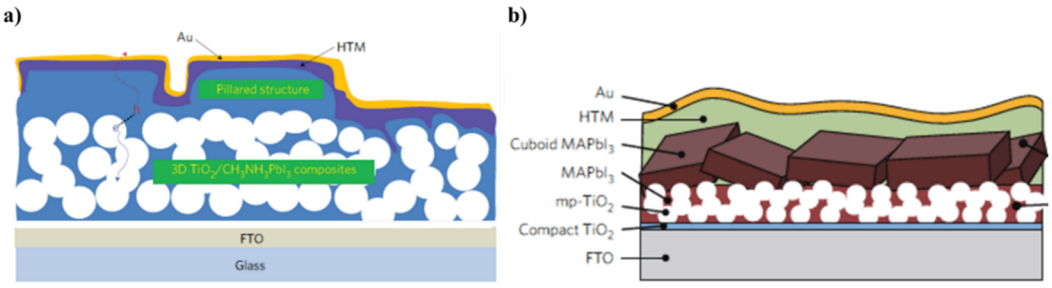

Figure 1.15 - Schematic of PSC device architectures: ***a)*** *with pillar-shaped (taken from* [62]*) and* ***b)*** *with cuboid-shaped $MAPbI_3$ capping layer (taken from* [63]*).*

The advances in the perovskite film deposition techniques enabled us to overcome some previous limitations and made it possible to obtain thick and dense perovskite films deposited on top of thin mp-TiO_2 layers. Im *et al.* used a two-step sequential deposition method (described in detail in subsection 1.1.3) to prepare PSCs, obtaining a dense perovskite capping layer in cuboid shape on a thin mp-TiO_2 layer (~100 nm) (Figure 1.15b) [63]. The formation

of a dense and uniform perovskite layer allowed Im *et al.* to improve the values of J_{sc} (21.64 mA/cm^2), V_{oc} (1.056 V), and efficiency (17 %) of the devices [56,63].

(E) Planar structure

The planar configuration (Figure 1.11E) emerged from the fact that the mesoporous layer has become so thin up to the point that eventually, it was no longer needed. The complete device structure usually comprises a TCO current collector electrode, an n-type ETM, a thick perovskite layer, a p-type HTM, and a current metal collector.

The first attempt to apply the $MAPbI_{3-x}Cl_x$ perovskite to a planar architecture was made by Lee *et al.* [57], achieving only 1.8 % efficiency, most likely due to an incomplete film coverage that led to electric shunts in the device. Several efforts have been made to improve the PCE by optimizing the processing conditions, such as the annealing temperature and film thickness. However, due to the porosity and high surface defect density of the obtained perovskite films, PCEs of only 11 % were achieved [64].

To improve the uniformity of the perovskite film, Liu *et al.* prepared a uniform $MAPbI_{3-x}Cl_x$ on the c-TiO_2 layer (Figure 1.16) using an optimized thermal vapour deposition technique, reaching PCEs of 15 %, with V_{oc} of 1.07 V and J_{sc} of 21.5 mA/cm^2 [65].

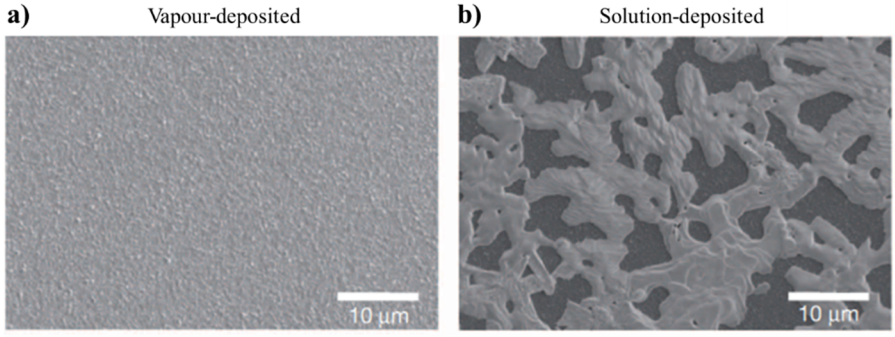

*Figure 1.16 - SEM top-views of **a)** a vapour-deposited and **b)** a solution-deposited $MAPbI_{3-x}Cl_x$ perovskite film (Taken from* [65]*).*

The optimization in the perovskite film deposition through different techniques allowed a present state-of-the-art for mesoporous and planar PSCs with PCE around 20 % [66,67].

(F) Inverted planar structure

The inverted planar structure appeared as an alternative to mesoporous and planar PSC architectures. This structure has an opposite sequence of HTM and ETM than the regular configuration (Figure 1.11F), comprised of a TCO substrate, a p-type HTM, an intrinsic perovskite layer, an n-type ETM, and a metal electrode.

The first attempt to prototype an inverted planar PSC was reported by Jeng *et al.*, where the hybrid methylammonium lead iodide/fullerene ($MAPbI_3/C_{60}$) layer was used as a planar heterojunction and a thin layer of bathocuproine (BCP) and PEDOT:PSS as ETM and HTM, respectively (Figure 1.17a) [68]. By replacing the C_{60} with phenyl-C_{61}-butyric acid methyl ester (PCBM), the PCE of the devices improved from 1.6 % to 3.9 %, due to more considerable energy offset between the HOMO of $MAPbI_3$ and the LUMO of PCBM, and consequently a more efficient electron injection into the metal cathode (Figure 1.17b) [56,68].

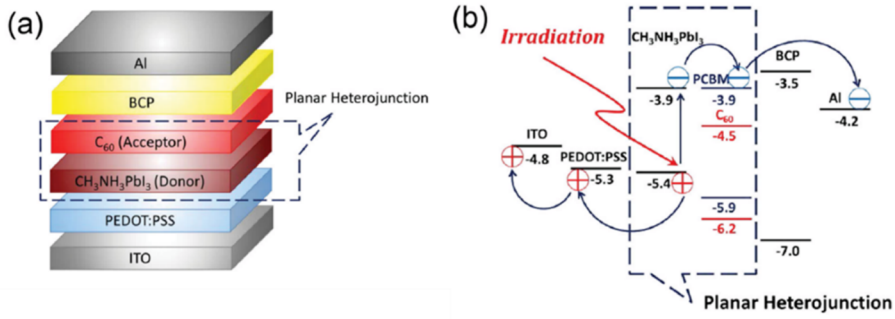

Figure 1.17 - ***a)*** *Representation of a configuration of an inverted planar perovskite solar cell and* ***b)*** *the scheme of the energy levels of each layer in the device (taken from* [68]*).*

Several combinations of planar heterojunctions have been made to improve the efficiencies of PSCs, which allowed Liu *et al.* to achieve a remarkable PCE of 20.7 % with the structure ITO/ poly(triarylamine) (PTAA) / $Cs_{0.05}(FA_{0.85}MA_{0.85})_{0.95}Pb(I_{0.85}Br_{0.15})_3$ (CsFAMA) / C_{60} / BCP / Ag [69].

1.1.3. Perovskite layer deposition methods

The advances in the PSCs architecture design required optimising the perovskite layer's manufacturing techniques to obtain devices with high efficiencies. Therefore, it is essential to

control stoichiometry, crystallographic phase, and the grain size of the perovskite material. According to different preparation procedures, the perovskite layer fabrication can be processed by four approaches: one-step solution method, two-steps solution method, vapour-assisted solution method, and thermal evaporation method (Figure 1.18) [56].

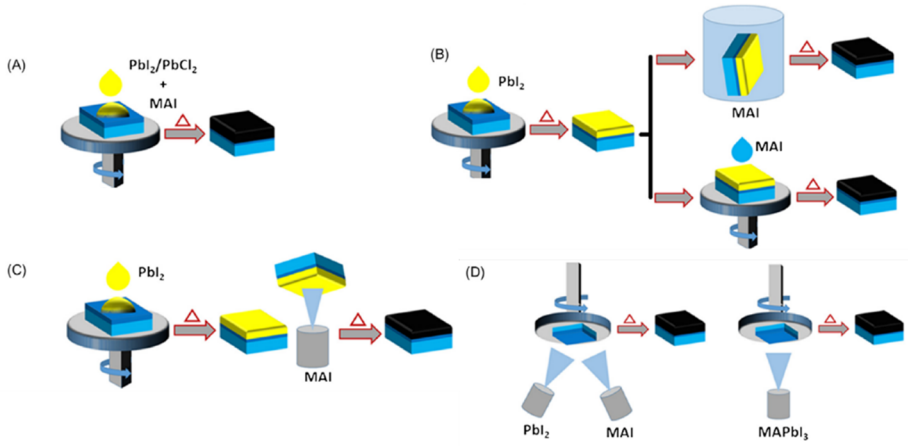

Figure 1.18 - Perovskite film deposition processes: ***(A)*** *one-step,* ***(B)*** *two-steps,* ***(C)*** *vapour-assisted, and* ***(D)*** *thermal evaporation (taken from* [56]*). *PbI_2 is lead iodide, $PbCl_2$ is lead chloride, MAI is methylammonium iodide, and $MAPbI_3$ is methylammonium lead iodide perovskite.*

➢ One-Step Solution Method

The one-step deposition method was used primarily to prepare the PSC due to its greater simplicity, and it is still the most widely used processing technique for preparing the perovskite films. This method employs as perovskite precursor solution, a mixture of an organic halide MAX (*e.g.* methylammonium iodide (MAI), formamidinium iodide (FAI)) and a metal halide PbX_2 (*e.g.* lead iodide (PbI_2), lead chloride ($PbCl_2$)) dissolved in an aprotic polar solvent, such as γ-butyrolactone (GBL), dimethylformamide (DMF), dimethylsulfoxide (DMSO) or even a combination of solvents. This precursor solution is then spin-coated on a substrate followed by annealing at temperatures ranging 80 to 150 °C to form a pure-phase, pinhole-free and dense perovskite layer (Figure 1.18A) [70]. Therefore, selecting the appropriate post-deposition annealing temperature and time is crucial to obtain high-quality perovskite films based on the precursor composition. Moreover, the environmental conditions, the roughness of the substrates, and some processing parameters such as rotation

speed and time influence perovskite film properties, namely crystallinity, morphology and uniformity [71–75].

Lee *et al.* [57] were the first to report using a one-step approach to synthesise $MAPbI_2Cl$ perovskite. Using a 3:1 molar ratio of MAI:$PbCl_2$ in DMF, the formation of the perovskite layer were accomplished after 30 s of spin-coating and 100 °C of post-annealing, and the devices displayed a V_{oc} of more than 1 V. Since then, several one-step coating solution-based approaches have been developed to control the formation of larger grain sizes, the roughness and the uniformity of perovskite film morphology, which may suppress the charge carrier extraction processes that lead to poor device PCE [76].

- **Two-Steps Solution Method**

The two-steps solution deposition were developed to overcome the poor-surface coverage of perovskite films [62]. Liang *et al.* [77] and Burschka *et al.* [78] developed the two-steps solution deposition method to prepare uniform hybrid organic-inorganic perovskite films. In this method, a PbX_2 layer is first deposited on a substrate, dried by annealing, and subsequently reacted with MAX in isopropanol (IPA) solution by dipping [79] or spin-coating [80] to form $MAPbX_3$ (Figure 1.18B). This process involves diffusion of the MA^+ cations into the PbX_2 matrix to create the perovskite material, confirmed by changing the film's colour from yellowish to dark brown [76].

In the two-steps solution method, improving the morphologic features and overall quality of perovskite films is possible by adjusting the operational parameters in either step. Im *et al.* investigated the relationship between the grain size of perovskite and the MAI concentration and found that the grain size decreased with increasing MAI concentration [63]. However, several drawbacks to this method have been found, namely the surface smoothness related to the perovskite grain size. An increase in surface roughness leads to higher surface recombination and leakage current. On the other hand, smooth films with small grains suffer from low carrier lifetime and short diffusion length. Another drawback is the incomplete conversion of PbX_2, which decreases the total light absorption, and blocks the efficient charge carrier transport to the selective contacts, resulting in reduced V_{oc} and J_{sc} [56]. These handicaps were circumvented by using some advanced film deposition engineering, namely,

using additives [82] or passing small amounts of solvent vapour during the annealing of perovskite films [81].

➢ Vapour-Assisted Solution Method (VASP)

The vapour-assisted solution method was developed as a modified two-steps deposition procedure. Vaporised MAX reacts with the PbX_2 layer during the second step to form the perovskite phase after further film annealing (Figure 1.18C). Chen *et al.* developed this method to fabricate highly pure and uniform $MAPbI_3$ films, using as-synthesised MAI vapour applied on spin-coated PbI_2 precursor at 150 °C in an inert environment [82]. The perovskite films prepared by this method showed complete conversion of PbI_2 and exhibited a smooth surface of a uniform phase formed by large grains up to the micrometre scale. Furthermore, the large grain size substantially reduces the length of grain-boundaries, which act as traps and promote charge-carrier scattering, therefore contributing to decrease charge recombination and to enhance device performance [83]. The only disadvantage of this perovskite preparation approach is that the process of MAX incorporation into the PbX_2 matrix needs several hours to accomplish, being much slower than the solution deposition, limiting the practical application of this method.

➢ Thermal Vapour Deposition

Thermal vapour deposition consists of evaporation from a single source of a hybrid material or a dual-source of organic and inorganic materials and post-annealing of the deposited perovskite films (Figure 1.18D). The first reference of using thermal vapour deposition to produce perovskite films was reported by Mitzi *et al.* [84], but Liu *et al.* [65] improved this method by using the dual co-evaporation to fabricate planar PSCs. Employing the co-evaporation of MAI and $PbCl_2$ sources on a rotated substrate followed by annealing, they prepared a smooth, conformal, and uniform $MAPbI_{3-x}Cl_x$ perovskite film, achieved a record PCE of 15.4 % when integrated into a planar structure PSC [65]. This method allows for more uniform and pinhole-free perovskite films than solution-processed films. However, the low thermal stability of both the precursor sources and the products and the difficulty of controlling the temperature during deposition often results in off-stoichiometric films [85].

1.1.4. Main challenges of PSCs

The scaling up of the perovskite devices to a large area is imminent. First, however, it is necessary to overcome some challenges regarding stability, the *J-V* curve hysteresis, and environmental concerns.

Stability

The stability of perovskite materials has been identified as one of the most significant problems affecting PSCs' performance. For example, it is known that the hybrid organic-inorganic lead halide perovskite materials suffer degradation when exposed to high temperatures [86–88], ultraviolet (UV) light [89], and under environmental conditions (water, oxygen, and moisture [90–92]).

The possible degradation mechanisms, triggered by environmental conditions, can be synthesized in equations 1.6 and 1.7 shown below [70,93]:

$$CH_3NH_3PbI_3\ (s) \overset{H_2O}{\rightleftharpoons} PbI_2\ (s) + CH_3NH_3^+(aq.) + I^-(aq) \quad (1.6)$$

$$CH_3NH_3I\ (aq.) \rightleftharpoons CH_3NH_2\ (aq.) + HI\ (aq.) \quad (1.7)$$

Several previous studies concluded that $MAPbI_3$ degradation in humid air occurs mainly by the hydrolysis of $CH_3NH_3PbI_3$, resulting in CH_3NH_3I, PbI_2, and HI after a few hours of humidity conditions [94,95].

On a laboratory scale, highly efficiency devices are generally produced in a glove box that allows humidity control. Although, at a larger scale, the encapsulation of the devices has been common practice to improve the stability of perovskite solar cells [96].

It has been reported that the degradation of the perovskite under UV light irradiation when PSCs are subjected to long-term stability tests under simulated sunlight. It seems that the TiO_2 layer is responsible for the perovskite material's poor stability [44]. According to Ito *et al.* [97], exposing $CH_3NH_3PbI_3$ perovskite devices, with TiO_2 as ETL, to sunlight simulator,

could lead to perovskite decomposition as a consequence of the formation of PbI_2 and evaporation of CH_3NH_2 and HI (equation 1.8):

$$CH_3NH_3PbI_3\ (s) \overset{UV}{\rightleftharpoons} PbI_2\ (s) + CH_3NH_2 \uparrow + HI \uparrow \quad (1.8)$$

Due to TiO_2 ability to extract electrons from iodide (I^-) electrodes in DSSCs, the decomposition of $MAPbI_3$ may be the result of electron extraction by TiO_2 surface from an iodide anion (equation 1.9 to 1.11 and Figure 1.19) [97]:

$$2I^- \rightleftharpoons I_2 + 2e^- \quad (1.9)$$

$$3CH_3NH_3^+ \rightleftharpoons 3CH_3NH_2 \uparrow + 3H^+ \quad (1.10)$$

$$I^- + I_2 + 3H^+ + 2e^- \rightleftharpoons 3HI \uparrow \quad (1.11)$$

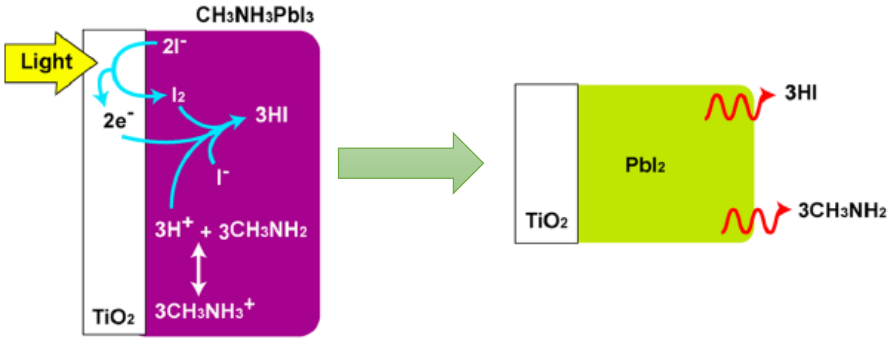

Figure 1.19 - Degradation scheme of $CH_3NH_3PbI_3$ perovskite solar cells during light exposure (Adapted from [97]*).*

To overcome this issue, the replacement of TiO_2 with alternative electron selective contacts [44,98] and the insertion of interlayers [97,99] have been reported.

Reports of thermal instability and consequent degradation of the perovskite have also been appeared [100–102]. The thermal degradation of $MAPbI_3$ perovskite films results in the formation of PbI_2 within the film, which can cause adverse effects on the device performance. The ability to withstand high temperatures during prolonged sun exposure is one of the requirements to be a promising solar cell material, so this is a critical issue that needs to be resolved. According to what has been reported, it appears that the thermal instability is closely

related to the chemistry between the perovskite and the contact layer, rather than an inherent problem of the perovskite [103]. Therefore, the simplest way to solve this problem is through the correct choice of materials.

J-V curve hysteresis

The measurement of a *J-V* curve typically evaluates the performance of a solar cell. This *J-V* curve is obtained by sweeping the applied voltage whilst the current under a standard light source, such as 1 Sun AM 1.5, is measured. This measurement gives the steady-state power output of a cell at any given bias and should not be dependent on the scan rate or scan direction. The term hysteresis is related to differences monitored in the current measured during the forward scan (from short circuit (SC) to forward bias (FB)) and the reverse scan (from FB to SC).

Hysteresis between forward and backward scans of *J-V* measurements have been observed on perovskite solar cells (Figure 1.20) as well as on DSSCs and silicon solar cells [104–106]. However, unlike in the case of DSSCs and silicon solar cells, where hysteresis appears when high scan rates are employed as a result of the capacitive charging at forward bias, for PSCs, this hysteresis increases upon reducing the potential sweep rate, revealing that the capacitive charging is not the source of the hysteresis, and led to termed as “anomalous hysteresis” [104]. Furthermore, Snaith *et al.* found that this type of hysteresis is more pronounced for planar cell structures than for mesoporous cell structures. Additionally, it has been more or less evident for cells featuring mesoporous films, depending on the selective electron material used, which can be related to the different routes of charge transport within the cells [104].

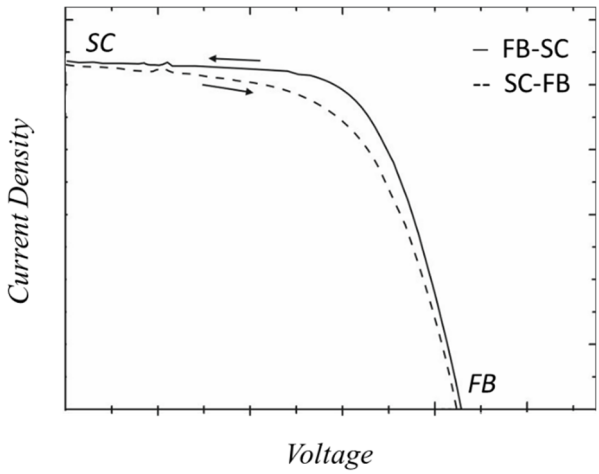

Figure 1.20 - A typical J-V curve hysteresis behaviour in a mesoporous TiO_2-based perovskite solar cell. The measurement is undertaken backwards from forward bias (FB) to short circuit (SC) and forwards from SC to FB, under stimulated AM 1.5 sunlight (based on [104]*).*

Several hypotheses had been proposed to explain this phenomenon, namely based on ferroelectric polarization [107], ion migration [108], charge trapping [109], and capacitive effects [110]. The most recent works suggested that both ion migration and charge trapping could be the reasons for the *J-V* hysteresis of perovskite solar cells [111] but, for a better appraisal, the improvement of the PCE measurement technique is needed [112].

Lead toxicity

One of the main concerns of using lead in the composition of the organometal halide perovskites is the potential risk of lead leaching into the environment at the waste treatment stage of the large-scale fabrication. The serious health effects of exposure to lead compounds are well known [113], so it is crucial to guarantee an effective device encapsulation to prevent lead leaching. Hailegnaw *et al.* found that the perovskite films suffer decomposition into lead iodide (PbI_2) when exposed to water without any encapsulation of the perovskite layer [114].

Although the simulations show that possible lead contamination from perovskite would be relatively insignificant compared with other sources of lead pollution [115], several studies have been made to develop lead-free perovskite structures that can be used in photovoltaics. The tin-based perovskites have been demonstrated to be the most viable material, with higher efficiency results compared to other novel perovskite materials based on different elements

[116–118]. Even so, their efficiencies are still below those of lead-based perovskites [119,120], likely due to the instability of the valence state Sn^{2+} in the ambient atmosphere, requiring encapsulation under an inert atmosphere.

Therefore, the lead-based perovskite appears to be the only viable technology to date without a technological breakthrough. Still, the disposal of the devices must be taken into consideration and the recycling of some components, namely the ETMs and FTO substrates [121,122].

1.2. ZnO-based nanostructures as ETM in PSCs

ZnO has been one of the most commonly explored alternatives to TiO_2 as an ETL in perovskite solar cells, as expected due to the similarity of bandgap and energy levels of these materials and the high bulk electron mobility of ZnO [48].

The first reports that mention the use of ZnO within perovskite solar cells involved using ZnO nanorods with different lengths. Bi *et al.* [123] used ZnO nanorods grown on FTO coated glass substrates and applied them within perovskite solar cells, using Spiro-OMeTAD and gold as hole conductor and metal contact, respectively [123]. They found that the maximum power conversion efficiency of 5.0 % was attained for nanorods with 1000 nm in length. The lower performance of ZnO-based perovskite solar cells comparatively with TiO_2-based PSCs was assigned to increased recombination losses within this cell structure. Kumar *et al.* [124] employed a similar cell design but with shorter nanorods (around 500 nm in length) and obtained a conversion efficiency of 8.9 % for rigid substrates and 2.6 % for flexible substrates.

Further improvements have been made, and Son *et al.* produced a ZnO nanorod perovskite cell with a maximum PCE of 11 % with an average nanorod length of 1000 nm, as in the work of Bi *et al.* [123,125]. In addition, Son *et al.* found that ZnO nanorod PSCs gave significantly higher J_{sc} values than TiO_2 nanorod PSCs, suggesting that ZnO nanorods enhanced electron collection compared to TiO_2 being an effective charge collection system in PSCs.

Several deposition techniques can be used to prepare ZnO nanorods, namely vapour liquid-solid growth (VLS) [126], metal-organic chemical vapour deposition (MOCVD) [127], hydrothermal method [128], chemical bath deposition (CBD) [129], and electrodeposition [130]. Table 1.3 shows a list of performance parameters of several reported perovskite solar cells featuring ZnO nanorods, prepared by different deposition techniques.

Table 1.3 - The photovoltaic performance of different perovskite solar cells featuring ZnO nanorods reported in the literature. CBD = chemical bath deposition; PECVD = plasma-enhanced chemical vapour deposition. AZO substrates = Al-doped zinc oxide substrates

Cell structure	**Nanorod deposition technique**	**J_{sc} (mA.cm^{-2})**	**V_{oc} (V)**	**FF (%)**	**PCE (%)**	**Ref.**
FTO/ZnO/$MAPbI_3$/Spiro-OMeTAD/Au	CBD	16.98	1.02	51.11	8.90	[124]
FTO/ZnO/$MAPbI_3$/Spiro-OMeTAD/Au	Hydrothermal	20.08	0.99	56.00	11.13	[125]
FTO/TiO_2/ZnO/$MAPbI_3$/Spiro-OMeTAD/Au	PECVD	16.00	0.72	41.20	4.80	[131]
ITO/ZnO/$MAPbI_3$/Spiro-OMeTAD/MoO_3/Ag	Sputtering	22.40	1.04	57.40	13.40	[132]
FTO/ZnO/$MAPbI_3$/Spiro-OMeTAD/Au	Hydrothermal	19.44	1.06	69.80	14.35	[133]
FTO/ZnO/$MAPbI_3$/Graphite-coated FTO	Electrodeposition	1.50	0.47	23.00	0.16	[134]
FTO/ZnO/$MAPbI_3$/Spiro-OMeTAD/Au	Hydrothermal	22.70	0.99	68.00	15.30	[135]
ITO/ZnO/$MAPbI_3$/Spiro-OMeTAD/Ag	Hydrothermal	21.70	0.97	70.00	16.19	[136]
FTO/ZnO/$MAPbI_3$/Spiro-OMeTAD/Ag	Hydrothermal	21.39	0.71	43.0	6.63	[137]
FTO/ZnO/$MAPbI_3$/Spiro-OMeTAD/Au	CBD	21.56	0.68	62.3	9.06	[138]
AZO/ZnO/$MAPbI_xCl_{3-x}$/C	Hydrothermal	14.87	0.86	28.0	3.62	[139]
FTO/ZnO/Cs_2SnI_6/P3HT/Ag	CBD	3.20	0.52	51.20	0.86	[140]
FTO/ZnO/$MAPbI_3$/Spiro-OMeTAD/Au	Hydrothermal	17.80	0.957	53.7	9.15	[141]
FTO/ZnO/$MAPbI_3$/Spiro-OMeTAD/Au	Hydrothermal	20.9	1.07	77.58	17.3	[142]
FTO/ZnO/$MAPbI_3$/P3HT/Ag	Hydrothermal	10.96	0.562	49.7	3.05	[143]
FTO/ZnO/$MAPbI_{3-x}Cl_x$/Spiro-OMeTAD/Au	Electrodeposition	6.8	0.85	46	2.4	[144]
ITO/ZnO/$MAPbI_3$/Spiro-OMeTAD/Au	Hydrothermal	11.50	0.806	70.0	4.55	[145]

The sol-gel processes are more attractive due to the grown films' excellent homogeneity and optical properties, ease of composition control, use low processing temperatures, allow large area coatings, and use low-cost equipment. However, an additional annealing step is needed to achieve the film crystallization.

Electrodeposition is a viable alternative to sol-gel processes for the preparation of ZnO thin films since it is a low-cost technique that allows to easily control the thickness, morphology, and composition of the films, with the advantage of producing high purity and crystalline coatings at low temperatures [146–148].

1.2.1. Short concept of electrodeposition

Electrodeposition generally comprises an electrolysis process in which solids or condensed matter are deposited in different forms and shapes on a substrate. This technique has been applied over the years to prepare coatings of metals and alloys for functional, protective or decorative purposes. However, the spectrum of applications has been extended to all kinds of solid materials, from metals to composites or semiconductors, and polymer materials, in various dimensions from nano-scale to macro-sized structures [149].

The main components of an electrodeposition system consist of an electrolyte containing metal ions, an electrode or substrate, also known as working electrode, on which the deposition is desired, a counter electrode which is often used as a "soluble" electrode that allows keeping constant the concentration of the metal ion, a reference electrode that is essential to control the potential of the working electrode, and a power supply, which can either be at constant potential/current (potentiostatic or galvanostatic electrodeposition, respectively) or pulsed potential/current (Figure 1.21).

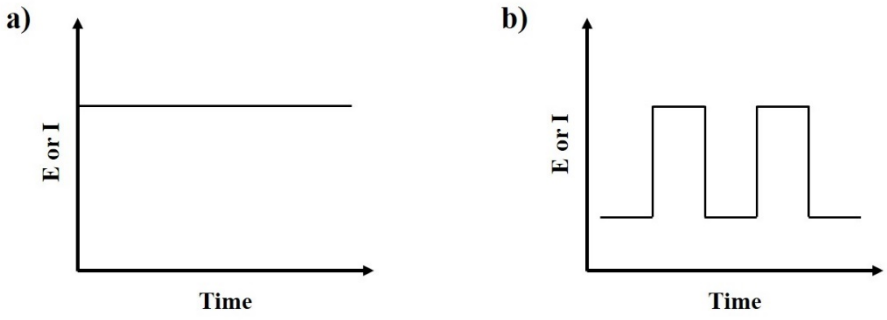

Figure 1.21 - Two different modes of electrodeposition: ***a)*** *constant potentiostatic/galvanostatic electrodeposition and* ***b)*** *pulsed potentiostatic/galvanostatic electrodeposition.*

Quite generally, a current flow passes through the electrolyte and the cations and anions diffuse and migrate towards the cathode and anode, respectively, and a deposit forms at the electrode surface upon a charge transfer reaction [149].

In general, to obtain an electrodeposited material, several steps are required. The different stages of the electrodeposition process are schematically shown in Figure 1.22 [150].

The first step (stage 1) refers to the transport of solvated ions (in aqueous electrolytes) from the bulk electrolyte to the interface region under mass transport control, namely diffusion, migration and convection. Upon approaching the substrate surface, the hydrated ions at the Helmholtz double-layer (stage 2) and partially dehydrate, releasing water molecules. At this point, a charge-transfer event takes place (eventually by tunnelling), and the partially hydrated ions attach onto the substrate surface in the form of ad-ions or ad-atoms (stage 3). The denomination of the transient species depends mainly on the number of hydration molecules that the ad-ion preserves. If a large number is kept and its net charge is close to that of the free ion oxidation number, it is called ad-ion; If the net charge is close to zero and, consequently, the number of water hydration molecules is significantly reduced, it is called ad-atom. These adsorbed transient species diffuse on the substrate surface from one site to another site energetically more favourable, lowering its energy and reducing its net charge while successively releasing hydration molecules (stage 4); eventually, the ad-atom ends up incorporated in the lattice, which results in the nucleation of stable clusters (stage 5). Depending on the category of growth sites, the irreversible incorporation of ad-atoms in the lattice establishes a crystallographic texture and morphology specific to the electrodeposited material (stage 6). This process is also known as electrocrystallisation [150].

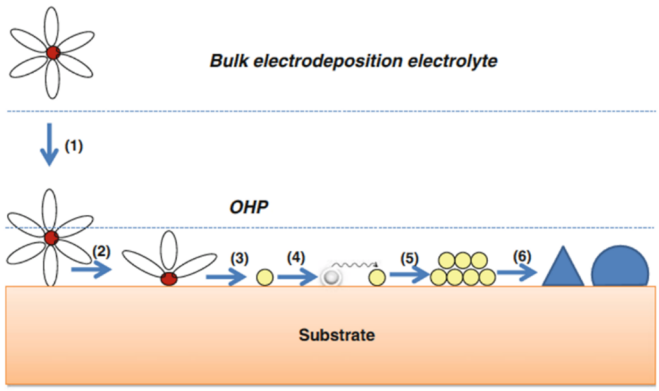

Figure 1.22 - Schematic picture of nucleation and growth during a typical electrodeposition process (Taken from [150]*). OHP is the outer Helmholtz plane.*

1.2.2. Electrodeposition of ZnO nanostructures

Considering the characteristics of ZnO, the main application areas are electronics and optoelectronics. Therefore, it is crucial to have a deposition technique suited to obtain homogeneous materials, at a large-scale, without affecting the ZnO fundamental physical properties. The electrodeposition technique allows to achieve these goals at low cost and using low-temperature growth processes of nanostructured ZnO [151].

Among the different morphologies that ZnO nanostructures can exhibit, the unidimensional (1D) vertically-oriented morphologies, such as nanotubes, nanowires and nanorods, that stand up, are ideal in DSSCs and PSCs applications [152]. The oriented 1D ZnO nanostructured arrays have been widely investigated as photoelectrodes in solar cells. They provide direct electrical pathways with a high interfacial area between the donor and the acceptor material, ensuring the rapid collection of carriers generated throughout the device [153].

The structural, optical, and electrical properties of these kinds of ZnO films can be tuned by the electrodeposition growth conditions, as will be discussed in detail in Chapters 3 and 4.

1.2.3. The instability of ZnO-based perovskite solar cells

In the literature, the thermal instability of perovskite has been highlighted as a major issue in using ZnO as a contact layer in PSCs. Annealing the perovskite layer after deposition is a standard procedure to improve crystallinity and ensure the complete conversion to the perovskite. However, it has been noticed that heating the perovskite layer on top of a ZnO layer results in the shifting of the dark brown colour of perovskite back to the yellow colour of PbI_2 [102]. This thermal degradation jeopardizes the long-term stability of ZnO-based perovskite solar cells, especially in situations where the units can reach temperatures above 80 °C of working conditions in warm climates. Yang *et al.* [101] started by studying the origin of this instability and found that even at temperatures as low as 100 °C, the annealed perovskite films on ZnO layers degraded to PbI_2, being confirmed by Ultraviolet-Visible Spectroscopy (UV-Vis) and Powder X-Ray Diffraction (XRD). ZnO's hygroscopic nature is pointed out as the main reason for this degradation since it leads to additional moisture into the cell, being the source of perovskite degradation.

The presence of hydroxyl groups on the ZnO surface can be depended on the type of synthesis technique used to prepare the ZnO films and will be discussed in more detail in Chapter 5.

1.2.4. ZnO-based core-shell nanostructures

An effective route that has been studied to reduce perovskite instability and prevent the recombination that occurs at the interface between ZnO and the perovskite is the production of core-shell nanostructures, where ZnO acts as the core, which is surrounded by another material acting as a shell.

Several approaches have been attempted in terms of shell material. Liu *et al.* used a CdS shell layer to provide additional absorption contribution, passivate ZnO surface defects, reduce interfacial recombination, and eliminate the perovskite decomposition on the ZnO surface [154]. Li *et al.* combined a ZnO core with high electron mobility offered by a SnO_2 shell that provided a match in the alignment of energy levels for electron injection, thereby increasing the PSC efficiency [155]. An Aluminium-doped ZnO layer (AZO material), with only 5 % of Al doping level, has also been found to be an effective shell material to suppress recombination, achieving an increase in PCE of the perovskite solar cell [156]. Nevertheless, the most commonly used shell material has been TiO_2 due to its known intrinsic properties and performance as an ETM in perovskite solar cells. Zhong *et al.* prepared PSCs based on ZnO@TiO_2 core-shell nanorods (NRs) in ambient atmosphere, using the sol-gel method to coat ZnO NRs surface with a TiO_2 shell layer [157]. They found that the performance of the PSCs can be improved when ZnO@TiO_2 core-shell NRs are used, compared to ZnO-based PSCs, and that the TiO_2 shell layer eliminates the direct contact between ZnO and the perovskite layer, suppressing the charge recombination at ZnO/perovskite interface (Figure 1.23).

Additionally, depending on the preparation technique and deposition parameters used to obtain the TiO_2 shell layer, it is possible to tune its structure, morphology and, consequently, the optical and electrical properties of the core-shell material to optimise the performance of the perovskite solar cells using core-shell nanostructures as ETL [158]. This approach will be discussed in more detail in Chapter 6.

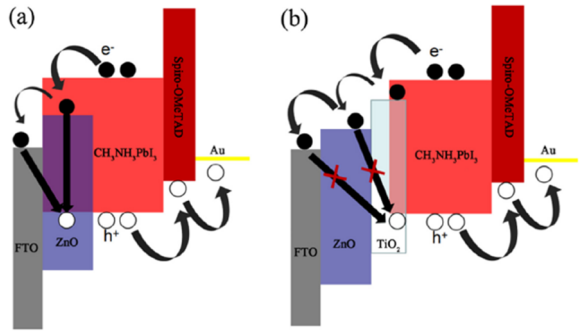

Figure 1.23 - Schematic diagrams of carrier transport and recombination processes in PSCs based on ***a)*** *ZnO NRs and* ***b)*** *ZnO@TiO_2 core-shell NRs (Taken from* [157]*).*

1.3. Aims and Scope

A large part of this thesis was focused on the synthesis of materials with the potential to be applied to perovskite solar cells. As mentioned before, the morphology of these materials is the key to producing high efficient devices, being the vertically-oriented 1D morphology the most promising. Fortunately, many different techniques are available for creating ZnO nanostructures with different morphologies. However, the main technique chosen to synthesize ZnO nanostructures within this thesis is the electrodeposition technique, which is a low cost and low-temperature methodology capable of producing a wide range at a large scale of ZnO nanostructures.

In particular, this thesis will focus on producing ZnO nanorods using pulsed electrodeposition since nanorods have attractive features for photovoltaic applications. The use of a ZnO seed layer or a TiO_2 template to obtain vertically oriented ZnO nanorods are some of the approaches explored in detail, and the effect of the electrodeposition pulse profile parameters on the enhancement of the optoelectronic properties of ZnO.

The second major goal of this thesis will focus on understanding how the synthesis method of ZnO ETLs can affect the performance of PSCs and, consequently, the instability of the perovskite layer. Finally, since the core-shell nanostructures, when applied to perovskite solar cells, reduce the recombination processes between the ETL and perovskite layer, an approach of core-shell nanostructures based on the electrodeposited ZnO NRs as the core will be presented, optimizing the deposition conditions of the TiO_2 shell layer.

Therefore, the aims of this thesis can be summarised as:

- to evaluate the effect of ZnO seeds and TiO_2 template layers on the nucleation step during the electrodeposition of ZnO crystals;

- to determine how a TiO_2 intermediate layer affects the photoelectronic properties of the ZnO NRs;
- to establish the factors that control the growth of ZnO nanorods during pulsed electrochemical deposition, and use this knowledge to tailor their optoelectronic properties towards application in perovskite solar cells;
- to understand the key elements that compromise the stability of the perovskite layer when in contact with ZnO ETL;
- to apply a TiO_2 layer on the electrodeposited ZnO nanorods surface, creating core-shell nanostructures suited to be employed as ETLs in perovskite solar cells.

1.4. Thesis Structure

The thesis is divided into seven chapters. After this introductory chapter, in Chapter 2, the full details of all the experimental procedures and characterisation methods will be documented. The results of these experiments are reported and discussed in Chapters 3 to 6.

The results presented in this thesis are very much split into three parts. Chapters 3 and 4 will focus on developing ZnO nanostructures, Chapter 5 will focus on the factors that affect the stability of the perovskite layer, and Chapter 6 will focus on an alternative ETL to suppress recombination processes and to avoid the decomposition of the perovskite layer during the annealing step.

In Chapter 3, a systematic study of the influence of the TiO_2 intermediate layer on ZnO nanorod growth conditions will be presented. Further characterisation of the nanorods is then performed to determine the most likely modified FTO substrate (with or without ZnO seed-layer on TiO_2-coated FTO substrates) for the study of the influence of pulse parameters on ZnO nanorod growth and how they affect the ZnO optoelectronic properties, being the results presented in Chapter 4. The results and discussion presented in Chapters 3 and 4 resulted in the publication of two papers: TiO_2 anatase intermediary layer acting as a template for ZnO pulsed electrodeposition [159] and Optoelectronic characterization of ZnO nanorod arrays obtained by pulsed electrodeposition [160], respectively.

In Chapter 5, several ZnO deposition methods will be evaluated on the perovskite formation process and their influence on material thermal stability. The performance of these perovskite devices is compared with that of the standard TiO_2 perovskite photovoltaic planar architecture.

The ZnO nanorods whose preparation and properties were discussed in Chapters 3 and 4 are then used as the core material on core-shell nanostructures as presented in Chapter 6. The influence of the deposition conditions of the TiO_2 shell layer is analysed, and a straightforward application of these core-shell materials as ETLs on perovskite solar cells is presented.

Finally, an overall assessment of the results of this thesis is summarized in Chapter 7 and suggestions for possible areas of future work are proposed.

1.5. References

[1] F. Birol, The International Energy Agency, Renewables 2018. (2018). https://www.iea.org/renewables2018/ (accessed 8 August 2019).

[2] B. Zaidi, Introductory Chapter: Introduction to Photovoltaic Effect, in: B. Zaidi (Ed.), Sol. Panels Photovolt. Mater., IntechOpen, Rijeka, 2018. doi:10.5772/intechopen.74389.

[3] W.W. Anderson, Y.G. Chai, Becquerel effect solar cell, Energy Convers. 15 (1976) 85–94. doi:10.1016/0013-7480(76)90020-6.

[4] J.A. Luceño-Sánchez, A.M. Díez-Pascual, R. Peña Capilla, Materials for Photovoltaics: State of Art and Recent Developments, Int. J. Mol. Sci. 20 (2019) 976 (1–42). doi:10.3390/ijms20040976.

[5] A.M. Kuhlmann, The Second Most Abundant Element in the Earth's Crust, JOM. 15 (1963) 502–505. doi:10.1007/BF03378936.

[6] M.A. Green, E.D. Dunlop, D.H. Levi, J. Hohl-Ebinger, M. Yoshita, A.W.Y. Ho-Baillie, Solar cell efficiency tables (version 54), Prog. Photovoltaics Res. Appl. 27 (2019) 565–575. doi:10.1002/pip.3171.

[7] W. Shockley, H.J. Queisser, Detailed Balance Limit of Efficiency of p-n Junction Solar Cells, J. Appl. Phys. 32 (1961) 510–519. doi:10.1063/1.1736034.

[8] K. Ranabhat, L. Patrikeev, A.A. evna Revina, K. Andrianov, V. Lapshinsky, E. Sofronova, An introduction to solar cell technology, J. Appl. Eng. Sci. 14 (2016) 481–491. doi:10.5937/jaes14-10879.

[9] M. Afzaal, P. O'Brien, Recent developments in II–VI and III–VI semiconductors and their applications in solar cells, J. Mater. Chem. 16 (2006) 1597–1602. doi:10.1039/B512182E.

[10] National Renewable Energy Laboratory (NREL), Best Research Cell Efficiencies, (2019). https://www.nrel.gov/pv/cell-efficiency.html (accessed 5 August 2019).

[11] D.O. Miles, Anodized ZnO Nanostructures for Next-Generation Photovoltaics, University of Bath, 2015.

[12] M.A. Green, Third generation photovoltaics: Ultra-high conversion efficiency at low cost, Prog. Photovoltaics Res. Appl. 9 (2001) 123–135. doi:10.1002/pip.360.

[13] A. Kojima, K. Teshima, Y. Shirai, T. Miyasaka, Organometal Halide Perovskites as Visible-Light Sensitizers for Photovoltaic Cells, J. Am. Chem. Soc. 131 (2009) 6050–

6051. doi:10.1021/ja809598r.

[14] J.-H. Im, C.-R. Lee, J.-W. Lee, S.-W. Park, N.-G. Park, 6.5% efficient perovskite quantum-dot-sensitized solar cell, Nanoscale. 3 (2011) 4088–4093. doi:10.1039/C1NR10867K.

[15] H.-S. Kim, C.-R. Lee, J.-H. Im, K.-B. Lee, T. Moehl, A. Marchioro, S.-J. Moon, R. Humphry-Baker, J.-H. Yum, J.E. Moser, M. Grätzel, N.-G. Park, Lead iodide perovskite sensitized all-solid-state submicron thin film mesoscopic solar cell with efficiency exceeding 9%, Sci. Rep. 2 (2012) 591 (1–7). doi:10.1038/srep00591.

[16] S. Emani, L. Andrade, A. Mendes, Recent progress in long-term stability of perovskite solar cells, U. Porto J. Eng. 1:2 (2015) 52–62. doi:10.24840/2183-6493_001.002_0007.

[17] A. Marchioro, J. Teuscher, D. Friedrich, M. Kunst, R. van de Krol, T. Moehl, M. Grätzel, J.-E. Moser, Unravelling the mechanism of photoinduced charge transfer processes in lead iodide perovskite solar cells, Nat. Photonics. 8 (2014) 250–255. doi:10.1038/nphoton.2013.374.

[18] E. Da Como, F. De Angelis, H. Snaith, A. Walker, eds., Unconventional Thin Film Photovoltaics, The Royal Society of Chemistry, Cambridge, UK, 2016. doi:10.1039/9781782624066.

[19] N. Marinova, S. Valero, J.L. Delgado, Organic and perovskite solar cells: Working principles, materials and interfaces, J. Colloid Interface Sci. 488 (2017) 373–389. doi:10.1016/J.JCIS.2016.11.021.

[20] S.D. Stranks, P.K. Nayak, W. Zhang, T. Stergiopoulos, H.J. Snaith, Formation of Thin Films of Organic–Inorganic Perovskites for High-Efficiency Solar Cells, Angew. Chemie Int. Ed. 54 (2015) 3240–3248. doi:10.1002/anie.201410214.

[21] N.U.O.S.A. TECHNOLOGY, SciTechDaily, Sol. Cell Effic. Increased with Innov. Two-Dimensional Mater. (2019). https://scitechdaily.com/solar-cell-efficiency-increased-with-innovative-two-dimensional-materials/ (accessed 22 November 2019).

[22] S. Ryu, J.H. Noh, N.J. Jeon, Y. Chan Kim, W.S. Yang, J. Seo, S. Il Seok, Voltage output of efficient perovskite solar cells with high open-circuit voltage and fill factor, Energy Environ. Sci. 7 (2014) 2614–2618. doi:10.1039/C4EE00762J.

[23] F. Hanusch, M. Petrus, P. Docampo, Towards Optimum Solution-processed Planar Heterojunction Perovskite Solar Cells, in: Unconv. Thin Film Photovoltaics, The Royal Society of Chemistry, 2016: pp. 32–56. doi:10.1039/9781782624066-00032.

[24] A.K. Jena, A. Kulkarni, T. Miyasaka, Halide Perovskite Photovoltaics: Background, Status, and Future Prospects, Chem. Rev. 119 (2019) 3036–3103. doi:10.1021/acs.chemrev.8b00539.

[25] F.F. Targhi, Y.S. Jalili, F. Kanjouri, MAPbI3 and FAPbI3 perovskites as solar cells: Case study on structural, electrical and optical properties, Results Phys. 10 (2018) 616–627. doi:10.1016/J.RINP.2018.07.007.

[26] S. De Wolf, J. Holovsky, S.-J. Moon, P. Löper, B. Niesen, M. Ledinsky, F.-J. Haug, J.-H. Yum, C. Ballif, Organometallic Halide Perovskites: Sharp Optical Absorption Edge and Its Relation to Photovoltaic Performance, J. Phys. Chem. Lett. 5 (2014) 1035–1039. doi:10.1021/jz500279b.

[27] S. Sun, T. Salim, N. Mathews, M. Duchamp, C. Boothroyd, G. Xing, T.C. Sum, Y.M. Lam, The origin of high efficiency in low-temperature solution-processable bilayer organometal halide hybrid solar cells, Energy Environ. Sci. 7 (2014) 399–407. doi:10.1039/C3EE43161D.

[28] A. Kojima, M. Ikegami, K. Teshima, T. Miyasaka, Highly Luminescent Lead Bromide Perovskite Nanoparticles Synthesized with Porous Alumina Media, Chem. Lett. 41 (2012) 397–399. doi:10.1246/cl.2012.397.

[29] J.H. Noh, S.H. Im, J.H. Heo, T.N. Mandal, S. Il Seok, Chemical Management for Colorful, Efficient, and Stable Inorganic–Organic Hybrid Nanostructured Solar Cells, Nano Lett. 13 (2013) 1764–1769. doi:10.1021/nl400349b.

[30] L. Etgar, P. Gao, Z. Xue, Q. Peng, A.K. Chandiran, B. Liu, M.K. Nazeeruddin, M. Grätzel, Mesoscopic CH3NH3PbI3/TiO2 Heterojunction Solar Cells, J. Am. Chem. Soc. 134 (2012) 17396–17399. doi:10.1021/ja307789s.

[31] Y. Wang, Y. Zhang, P. Zhang, W. Zhang, High intrinsic carrier mobility and photon absorption in the perovskite CH3NH3PbI3, Phys. Chem. Chem. Phys. 17 (2015) 11516–11520. doi:10.1039/C5CP00448A.

[32] S.D. Stranks, G.E. Eperon, G. Grancini, C. Menelaou, M.J.P. Alcocer, T. Leijtens, L.M. Herz, A. Petrozza, H.J. Snaith, Electron-Hole Diffusion Lengths Exceeding 1 Micrometer in an Organometal Trihalide Perovskite Absorber, Science (80-.). 342 (2013) 341–344. doi:10.1126/science.1243982.

[33] E. Smecca, Y. Numata, I. Deretzis, G. Pellegrino, S. Boninelli, T. Miyasaka, A. La Magna, A. Alberti, Stability of solution-processed MAPbI3 and FAPbI3 layers, Phys.

Chem. Chem. Phys. 18 (2016) 13413–13422. doi:10.1039/C6CP00721J.

[34] H.L. Wells, Über die Cäsium- und Kalium-Bleihalogenide, Zeitschrift Für Anorg. Chemie. 3 (1893) 195–210. doi:10.1002/zaac.18930030124.

[35] J. Duan, H. Xu, W.E.I. Sha, Y. Zhao, Y. Wang, X. Yang, Q. Tang, Inorganic perovskite solar cells: an emerging member of the photovoltaic community, J. Mater. Chem. A. 7 (2019) 21036–21068. doi:10.1039/C9TA06674H.

[36] Q. Tai, K.-C. Tang, F. Yan, Recent progress of inorganic perovskite solar cells, Energy Environ. Sci. 12 (2019) 2375–2405. doi:10.1039/C9EE01479A.

[37] Y. Wu, X. Yang, H. Chen, K. Zhang, C. Qin, J. Liu, W. Peng, A. Islam, E. Bi, F. Ye, M. Yin, P. Zhang, L. Han, Highly compact TiO2 layer for efficient hole-blocking in perovskite solar cells, Appl. Phys. Express. 7 (2014) 52301. doi:10.7567/apex.7.052301.

[38] D.G. Lee, M. Kim, B.J. Kim, D.H. Kim, S.M. Lee, M. Choi, S. Lee, H.S. Jung, Effect of TiO2 particle size and layer thickness on mesoscopic perovskite solar cells, Appl. Surf. Sci. 477 (2019) 131–136. doi:https://doi.org/10.1016/j.apsusc.2017.11.124.

[39] A. Fakharuddin, F. Di Giacomo, A.L. Palma, F. Matteocci, I. Ahmed, S. Razza, A. D'Epifanio, S. Licoccia, J. Ismail, A. Di Carlo, T.M. Brown, R. Jose, Vertical TiO2 Nanorods as a Medium for Stable and High-Efficiency Perovskite Solar Modules, ACS Nano. 9 (2015) 8420–8429. doi:10.1021/acsnano.5b03265.

[40] G. Yang, H. Tao, P. Qin, W. Ke, G. Fang, Recent progress in electron transport layers for efficient perovskite solar cells, J. Mater. Chem. A. 4 (2016) 3970–3990. doi:10.1039/C5TA09011C.

[41] B.J. Kim, S.L. Kwon, M. Kim, Y.U. Jin, D.G. Lee, J.B. Jeon, Y. Yun, M. Choi, G. Boschloo, S. Lee, H.S. Jung, High-Efficiency Flexible Perovskite Solar Cells Enabled by an Ultrafast Room-Temperature Reactive Ion Etching Process, ACS Appl. Mater. Interfaces. 12 (2020) 7125–7134. doi:10.1021/acsami.9b19030.

[42] Q. Zhang, C. Li, Pure Anatase Phase Titanium Dioxide Films Prepared by Mist Chemical Vapor Deposition, Nanomater. (Basel, Switzerland). 8 (2018) 827. doi:10.3390/nano8100827.

[43] A.K. Chandiran, M. Abdi-Jalebi, M.K. Nazeeruddin, M. Grätzel, Analysis of Electron Transfer Properties of ZnO and TiO2 Photoanodes for Dye-Sensitized Solar Cells, ACS Nano. 8 (2014) 2261–2268. doi:10.1021/nn405535j.

[44] T. Leijtens, G.E. Eperon, S. Pathak, A. Abate, M.M. Lee, H.J. Snaith, Overcoming ultraviolet light instability of sensitized TiO2 with meso-superstructured organometal tri-halide perovskite solar cells, Nat. Commun. 4 (2013) 2885. doi:10.1038/ncomms3885.

[45] J. Zhang, E.J. Juárez-Pérez, I. Mora-Seró, B. Viana, T. Pauporté, Fast and low temperature growth of electron transport layers for efficient perovskite solar cells, J. Mater. Chem. A. 3 (2015) 4909–4915. doi:10.1039/C4TA06416J.

[46] D. Liu, T.L. Kelly, Perovskite solar cells with a planar heterojunction structure prepared using room-temperature solution processing techniques, Nat. Photonics. 8 (2013) 133. https://doi.org/10.1038/nphoton.2013.342.

[47] E.H. Anaraki, A. Kermanpur, L. Steier, K. Domanski, T. Matsui, W. Tress, M. Saliba, A. Abate, M. Grätzel, A. Hagfeldt, J.-P. Correa-Baena, Highly efficient and stable planar perovskite solar cells by solution-processed tin oxide, Energy Environ. Sci. 9 (2016) 3128–3134. doi:10.1039/C6EE02390H.

[48] J. Luo, Y. Wang, Q. Zhang, Progress in perovskite solar cells based on ZnO nanostructures, Sol. Energy. (2018). doi:10.1016/j.solener.2018.01.035.

[49] C.J. Brabec, S. Gowrisanker, J.J.M. Halls, D. Laird, S. Jia, S.P. Williams, Polymer–Fullerene Bulk-Heterojunction Solar Cells, Adv. Mater. 22 (2010) 3839–3856. doi:10.1002/adma.200903697.

[50] J.-Y. Jeng, K.-C. Chen, T.-Y. Chiang, P.-Y. Lin, T.-D. Tsai, Y.-C. Chang, T.-F. Guo, P. Chen, T.-C. Wen, Y.-J. Hsu, Nickel Oxide Electrode Interlayer in CH3NH3PbI3 Perovskite/PCBM Planar-Heterojunction Hybrid Solar Cells, Adv. Mater. 26 (2014) 4107–4113. doi:10.1002/adma.201306217.

[51] J.H. Heo, H.J. Han, D. Kim, T.K. Ahn, S.H. Im, Hysteresis-less inverted CH3NH3PbI3 planar perovskite hybrid solar cells with 18.1% power conversion efficiency, Energy Environ. Sci. 8 (2015) 1602–1608. doi:10.1039/C5EE00120J.

[52] X. Zhao, M. Wang, Organic hole-transporting materials for efficient perovskite solar cells, Mater. Today Energy. 7 (2018) 208–220. doi:https://doi.org/10.1016/j.mtener.2017.09.011.

[53] W. Chen, Y. Wu, Y. Yue, J. Liu, W. Zhang, X. Yang, H. Chen, E. Bi, I. Ashraful, M. Grätzel, L. Han, Efficient and stable large-area perovskite solar cells with inorganic charge extraction layers, Science (80-.). 350 (2015) 944 LP – 948.

doi:10.1126/science.aad1015.

[54] P. Qin, S. Tanaka, S. Ito, N. Tetreault, K. Manabe, H. Nishino, M.K. Nazeeruddin, M. Grätzel, Inorganic hole conductor-based lead halide perovskite solar cells with 12.4% conversion efficiency, Nat. Commun. 5 (2014) 3834. doi:10.1038/ncomms4834.

[55] J.A. Christians, R.C.M. Fung, P. V Kamat, An Inorganic Hole Conductor for Organo-Lead Halide Perovskite Solar Cells. Improved Hole Conductivity with Copper Iodide, J. Am. Chem. Soc. 136 (2014) 758–764. doi:10.1021/ja411014k.

[56] S.C. Watthage, Z. Song, A.B. Phillips, M.J. Heben, Evolution of Perovskite Solar Cells, in: Perovskite Photovoltaics, Academic Press, 2018: pp. 43–88. doi:10.1016/B978-0-12-812915-9.00003-4.

[57] M.M. Lee, J. Teuscher, T. Miyasaka, T.N. Murakami, H.J. Snaith, Efficient Hybrid Solar Cells Based on Meso-Superstructured Organometal Halide Perovskites, Science (80-.). 338 (2012) 643–647. doi:10.1126/science.1228604.

[58] T. Leijtens, S.D. Stranks, G.E. Eperon, R. Lindblad, E.M.J. Johansson, I.J. McPherson, H. Rensmo, J.M. Ball, M.M. Lee, H.J. Snaith, Electronic Properties of Meso-Superstructured and Planar Organometal Halide Perovskite Films: Charge Trapping, Photodoping, and Carrier Mobility, ACS Nano. 8 (2014) 7147–7155. doi:10.1021/nn502115k.

[59] G. Xing, N. Mathews, S. Sun, S.S. Lim, Y.M. Lam, M. Grätzel, S. Mhaisalkar, T.C. Sum, Long-Range Balanced Electron- and Hole-Transport Lengths in Organic-Inorganic CH3NH3PbI3, Science (80-.). 342 (2013) 344–347. doi:10.1126/science.1243167.

[60] V. Manjunath, R. Krishna, S. Maniarasu, E. Ramasamy, S. Shanmugasundaram, G. Veerappan, Perovskite Solar Cell Architectures, Perovskite Photovoltaics. (2018) 89–121. doi:10.1016/B978-0-12-812915-9.00004-6.

[61] B. Parida, A. Singh, M. Oh, M. Jeon, J.-W. Kang, H. Kim, Effect of compact TiO2 layer on structural, optical, and performance characteristics of mesoporous perovskite solar cells, Mater. Today Commun. 18 (2019) 176–183. doi:https://doi.org/10.1016/j.mtcomm.2018.12.007.

[62] J.H. Heo, S.H. Im, J.H. Noh, T.N. Mandal, C.-S. Lim, J.A. Chang, Y.H. Lee, H. Kim, A. Sarkar, M.K. Nazeeruddin, M. Grätzel, S. Il Seok, Efficient inorganic–organic hybrid heterojunction solar cells containing perovskite compound and polymeric hole

conductors, Nat. Photonics. 7 (2013) 486–491. doi:10.1038/nphoton.2013.80.

[63] J.-H. Im, I.-H. Jang, N. Pellet, M. Grätzel, N.-G. Park, Growth of CH3NH3PbI3 cuboids with controlled size for high-efficiency perovskite solar cells, Nat. Nanotechnol. 9 (2014) 927–932. doi:10.1038/nnano.2014.181.

[64] G.E. Eperon, V.M. Burlakov, P. Docampo, A. Goriely, H.J. Snaith, Morphological Control for High Performance, Solution-Processed Planar Heterojunction Perovskite Solar Cells, Adv. Funct. Mater. 24 (2014) 151–157. doi:10.1002/adfm.201302090.

[65] M. Liu, M.B. Johnston, H.J. Snaith, Efficient planar heterojunction perovskite solar cells by vapour deposition, Nature. 501 (2013) 395–398. doi:https://doi.org/10.1038/nature12509.

[66] M. Wang, X. Jiang, J. Bian, Y. Feng, C. Wang, Y. Huang, Y. Zhang, Y. Shi, High-Performance and Stable Mesoporous Perovskite Solar Cells via Well-Crystallized FA0.85MA0.15Pb(I0.8Br0.2)3, ACS Appl. Mater. Interfaces. 11 (2019) 2989–2996. doi:10.1021/acsami.8b17833.

[67] Z. Liu, J. Chang, Z. Lin, L. Zhou, Z. Yang, D. Chen, C. Zhang, S. (Frank) Liu, Y. Hao, High-Performance Planar Perovskite Solar Cells Using Low Temperature, Solution–Combustion-Based Nickel Oxide Hole Transporting Layer with Efficiency Exceeding 20%, Adv. Energy Mater. 8 (2018) 1703432. doi:10.1002/aenm.201703432.

[68] J.-Y. Jeng, Y.-F. Chiang, M.-H. Lee, S.-R. Peng, T.-F. Guo, P. Chen, T.-C. Wen, CH3NH3PbI3 Perovskite/Fullerene Planar-Heterojunction Hybrid Solar Cells, Adv. Mater. 25 (2013) 3727–3732. doi:10.1002/adma.201301327.

[69] X. Liu, Y. Cheng, C. Liu, T. Zhang, N. Zhang, S. Zhang, J. Chen, Q. Xu, J. Ouyang, H. Gong, 20.7% highly reproducible inverted planar perovskite solar cells with enhanced fill factor and eliminated hysteresis, Energy Environ. Sci. 12 (2019) 1622–1633. doi:10.1039/C9EE00872A.

[70] Z. Shi, A.H. Jayatissa, Perovskites-Based Solar Cells: A Review of Recent Progress, Materials and Processing Methods, Materials (Basel). 11 (2018) 729 (1–34 p). doi:10.3390/ma11050729.

[71] Z. Song, S.C. Watthage, A.B. Phillips, B.L. Tompkins, R.J. Ellingson, M.J. Heben, Impact of Processing Temperature and Composition on the Formation of Methylammonium Lead Iodide Perovskites, Chem. Mater. 27 (2015) 4612–4619. doi:10.1021/acs.chemmater.5b01017.

[72] S.S. Shin, E.J. Yeom, W.S. Yang, S. Hur, M.G. Kim, J. Im, J. Seo, J.H. Noh, S. Il Seok, Colloidally prepared La-doped $BaSnO_3$ electrodes for efficient, photostable perovskite solar cells, Science (80-.). 356 (2017) 167 LP – 171. doi:10.1126/science.aam6620.

[73] X. Guo, C. McCleese, C. Kolodziej, A.C.S. Samia, Y. Zhao, C. Burda, Identification and characterization of the intermediate phase in hybrid organic–inorganic MAPbI3 perovskite, Dalt. Trans. 45 (2016) 3806–3813. doi:10.1039/C5DT04420K.

[74] Y. Zhang, G. Grancini, Y. Feng, A.M. Asiri, M.K. Nazeeruddin, Optimization of Stable Quasi-Cubic FAxMA1–xPbI3 Perovskite Structure for Solar Cells with Efficiency beyond 20%, ACS Energy Lett. 2 (2017) 802–806. doi:10.1021/acsenergylett.7b00112.

[75] A. Dualeh, N. Tétreault, T. Moehl, P. Gao, M.K. Nazeeruddin, M. Grätzel, Effect of Annealing Temperature on Film Morphology of Organic–Inorganic Hybrid Pervoskite Solid-State Solar Cells, Adv. Funct. Mater. 24 (2014) 3250–3258. doi:10.1002/adfm.201304022.

[76] P. Tonui, S.O. Oseni, G. Sharma, Q. Yan, G. Tessema Mola, Perovskites photovoltaic solar cells: An overview of current status, Renew. Sustain. Energy Rev. 91 (2018) 1025–1044. doi:10.1016/J.RSER.2018.04.069.

[77] K. Liang, D.B. Mitzi, M.T. Prikas, Synthesis and Characterization of Organic−Inorganic Perovskite Thin Films Prepared Using a Versatile Two-Step Dipping Technique, Chem. Mater. 10 (1998) 403–411. doi:10.1021/cm970568f.

[78] J. Burschka, N. Pellet, S.-J. Moon, R. Humphry-Baker, P. Gao, M.K. Nazeeruddin, M. Grätzel, Sequential deposition as a route to high-performance perovskite-sensitized solar cells, Nature. 499 (2013) 316–319. doi:10.1038/nature12340.

[79] D. Bi, A.M. El-Zohry, A. Hagfeldt, G. Boschloo, Improved Morphology Control Using a Modified Two-Step Method for Efficient Perovskite Solar Cells, ACS Appl. Mater. Interfaces. 6 (2014) 18751–18757. doi:10.1021/am504320h.

[80] M. Xiao, F. Huang, W. Huang, Y. Dkhissi, Y. Zhu, J. Etheridge, A. Gray-Weale, U. Bach, Y.-B. Cheng, L. Spiccia, A Fast Deposition-Crystallization Procedure for Highly Efficient Lead Iodide Perovskite Thin-Film Solar Cells, Angew. Chemie. 126 (2014) 10056–10061. doi:10.1002/ange.201405334.

[81] B.S. Tosun, H.W. Hillhouse, Enhanced Carrier Lifetimes of Pure Iodide Hybrid

Perovskite via Vapor-Equilibrated Re-Growth (VERG), J. Phys. Chem. Lett. 6 (2015) 2503–2508. doi:10.1021/acs.jpclett.5b00842.

[82] Q. Chen, H. Zhou, Z. Hong, S. Luo, H.-S. Duan, H.-H. Wang, Y. Liu, G. Li, Y. Yang, Planar Heterojunction Perovskite Solar Cells via Vapor-Assisted Solution Process, J. Am. Chem. Soc. 136 (2014) 622–625. doi:10.1021/ja411509g.

[83] H. Zhou, Q. Chen, Y. Yang, Vapor-assisted solution process for perovskite materials and solar cells, MRS Bull. 40 (2015) 667–673. doi:DOI: 10.1557/mrs.2015.171.

[84] D.B. Mitzi, M.T. Prikas, K. Chondroudis, Thin Film Deposition of Organic−Inorganic Hybrid Materials Using a Single Source Thermal Ablation Technique, Chem. Mater. 11 (1999) 542–544. doi:10.1021/cm9811139.

[85] M. Sessolo, C. Momblona, L. Gil-Escrig, H.J. Bolink, Photovoltaic devices employing vacuum-deposited perovskite layers, MRS Bull. 40 (2015) 660–666. doi:DOI: 10.1557/mrs.2015.170.

[86] H.-S. Kim, J.-Y. Seo, N.-G. Park, Material and Device Stability in Perovskite Solar Cells, ChemSusChem. 9 (2016) 2528–2540. doi:10.1002/cssc.201600915.

[87] T.J. Jacobsson, W. Tress, J.-P. Correa-Baena, T. Edvinsson, A. Hagfeldt, Room Temperature as a Goldilocks Environment for CH3NH3PbI3 Perovskite Solar Cells: The Importance of Temperature on Device Performance, J. Phys. Chem. C. 120 (2016) 11382–11393. doi:10.1021/acs.jpcc.6b02858.

[88] B. Conings, J. Drijkoningen, N. Gauquelin, A. Babayigit, J. D'Haen, L. D'Olieslaeger, A. Ethirajan, J. Verbeeck, J. Manca, E. Mosconi, F. De Angelis, H.-G. Boyen, Intrinsic Thermal Instability of Methylammonium Lead Trihalide Perovskite, Adv. Energy Mater. 5 (2015) 1500477. doi:10.1002/aenm.201500477.

[89] S.-W. Lee, S. Kim, S. Bae, K. Cho, T. Chung, L.E. Mundt, S. Lee, S. Park, H. Park, M.C. Schubert, S.W. Glunz, Y. Ko, Y. Jun, Y. Kang, H.-S. Lee, D. Kim, UV Degradation and Recovery of Perovskite Solar Cells, Sci. Rep. 6 (2016) 38150. doi:10.1038/srep38150.

[90] J. Huang, S. Tan, P.D. Lund, H. Zhou, Impact of H2O on organic–inorganic hybrid perovskite solar cells, Energy Environ. Sci. 10 (2017) 2284–2311. doi:10.1039/C7EE01674C.

[91] A. Senocrate, T. Acartürk, G.Y. Kim, R. Merkle, U. Starke, M. Grätzel, J. Maier, Interaction of oxygen with halide perovskites, J. Mater. Chem. A. 6 (2018) 10847–

10855. doi:10.1039/C8TA04537B.

[92] H.M. Cronin, K.D.G.I. Jayawardena, Z. Stoeva, M. Shkunov, S.R.P. Silva, Effects of ambient humidity on the optimum annealing time of mixed-halide Perovskite solar cells, Nanotechnology. 28 (2017) 114004. doi:10.1088/1361-6528/aa5bec.

[93] Q.-D. Dao, R. Tsuji, A. Fujii, M. Ozaki, Study on degradation mechanism of perovskite solar cell and their recovering effects by introducing CH3NH3I layers, Org. Electron. 43 (2017) 229–234. doi:https://doi.org/10.1016/j.orgel.2017.01.038.

[94] J. Bisquert, E.J. Juarez-Perez, The Causes of Degradation of Perovskite Solar Cells, J. Phys. Chem. Lett. 10 (2019) 5889–5891. doi:10.1021/acs.jpclett.9b00613.

[95] U.-G. Jong, C.-J. Yu, G.-C. Ri, A.P. McMahon, N.M. Harrison, P.R.F. Barnes, A. Walsh, Influence of water intercalation and hydration on chemical decomposition and ion transport in methylammonium lead halide perovskites, J. Mater. Chem. A. 6 (2018) 1067–1074. doi:10.1039/C7TA09112E.

[96] F. Matteocci, L. Cinà, E. Lamanna, S. Cacovich, G. Divitini, P.A. Midgley, C. Ducati, A. Di Carlo, Encapsulation for long-term stability enhancement of perovskite solar cells, Nano Energy. 30 (2016) 162–172. doi:https://doi.org/10.1016/j.nanoen.2016.09.041.

[97] S. Ito, S. Tanaka, K. Manabe, H. Nishino, Effects of Surface Blocking Layer of Sb2S3 on Nanocrystalline TiO2 for CH3NH3PbI3 Perovskite Solar Cells, J. Phys. Chem. C. 118 (2014) 16995–17000. doi:10.1021/jp500449z.

[98] A. Mei, X. Li, L. Liu, Z. Ku, T. Liu, Y. Rong, M. Xu, M. Hu, J. Chen, Y. Yang, M. Grätzel, H. Han, A hole-conductor–free, fully printable mesoscopic perovskite solar cell with high stability, Science (80-.). 345 (2014) 295 LP – 298. doi:10.1126/science.1254763.

[99] W. Li, W. Zhang, S. Van Reenen, R.J. Sutton, J. Fan, A.A. Haghighirad, M.B. Johnston, L. Wang, H.J. Snaith, Enhanced UV-light stability of planar heterojunction perovskite solar cells with caesium bromide interface modification, Energy Environ. Sci. 9 (2016) 490–498. doi:10.1039/C5EE03522H.

[100] J. Zhang, T. Pauporté, Effects of Oxide Contact Layer on the Preparation and Properties of CH3NH3PbI3 for Perovskite Solar Cell Application, J. Phys. Chem. C. 119 (2015) 14919–14928. doi:10.1021/acs.jpcc.5b02984.

[101] J. Yang, B.D. Siempelkamp, E. Mosconi, F. De Angelis, T.L. Kelly, Origin of the

Thermal Instability in CH3NH3PbI3 Thin Films Deposited on ZnO, Chem. Mater. 27 (2015) 4229–4236. doi:10.1021/acs.chemmater.5b01598.

[102] Y. Cheng, Q.-D. Yang, J. Xiao, Q. Xue, H.-W. Li, Z. Guan, H.-L. Yip, S.-W. Tsang, Decomposition of Organometal Halide Perovskite Films on Zinc Oxide Nanoparticles, ACS Appl. Mater. Interfaces. 7 (2015) 19986–19993. doi:10.1021/acsami.5b04695.

[103] T.T. Ava, A. Al Mamun, S. Marsillac, G. Namkoong, A Review: Thermal Stability of Methylammonium Lead Halide Based Perovskite Solar Cells, Appl. Sci. 9 (2019) 188. doi:10.3390/app9010188.

[104] H.J. Snaith, A. Abate, J.M. Ball, G.E. Eperon, T. Leijtens, N.K. Noel, S.D. Stranks, J.T.-W. Wang, K. Wojciechowski, W. Zhang, Anomalous Hysteresis in Perovskite Solar Cells, J. Phys. Chem. Lett. 5 (2014) 1511–1515. doi:10.1021/jz500113x.

[105] F. Wu, X. Li, Y. Tong, T. Zhang, Hysteresis analysis in dye-sensitized solar cells based on external bias field effects, J. Power Sources. 342 (2017) 704–708. doi:https://doi.org/10.1016/j.jpowsour.2017.01.002.

[106] M. Herman, M. Jankovec, M. Topič, Optimal I-V Curve Scan Time of Solar Cells and Modules in Light of Irradiance Level, Int. J. Photoenergy. 2012 (2012) 151452. doi:10.1155/2012/151452.

[107] H.-W. Chen, N. Sakai, M. Ikegami, T. Miyasaka, Emergence of Hysteresis and Transient Ferroelectric Response in Organo-Lead Halide Perovskite Solar Cells, J. Phys. Chem. Lett. 6 (2015) 164–169. doi:10.1021/jz502429u.

[108] J.M. Azpiroz, E. Mosconi, J. Bisquert, F. De Angelis, Defect migration in methylammonium lead iodide and its role in perovskite solar cell operation, Energy Environ. Sci. 8 (2015) 2118–2127. doi:10.1039/C5EE01265A.

[109] S. van Reenen, M. Kemerink, H.J. Snaith, Modeling Anomalous Hysteresis in Perovskite Solar Cells, J. Phys. Chem. Lett. 6 (2015) 3808–3814. doi:10.1021/acs.jpclett.5b01645.

[110] O. Almora, I. Zarazua, E. Mas-Marza, I. Mora-Sero, J. Bisquert, G. Garcia-Belmonte, Capacitive Dark Currents, Hysteresis, and Electrode Polarization in Lead Halide Perovskite Solar Cells, J. Phys. Chem. Lett. 6 (2015) 1645–1652. doi:10.1021/acs.jpclett.5b00480.

[111] C. Li, A. Guerrero, Y. Zhong, S. Huettner, Origins and mechanisms of hysteresis in organometal halide perovskites, J. Phys. Condens. Matter. 29 (2017) 193001.

doi:10.1088/1361-648X/aa626d.

[112] K. Domanski, E.A. Alharbi, A. Hagfeldt, M. Grätzel, W. Tress, Systematic investigation of the impact of operation conditions on the degradation behaviour of perovskite solar cells, Nat. Energy. 3 (2018) 61–67. doi:10.1038/s41560-017-0060-5.

[113] A. Babayigit, A. Ethirajan, M. Muller, B. Conings, Toxicity of organometal halide perovskite solar cells, Nat. Mater. 15 (2016) 247–251. doi:10.1038/nmat4572.

[114] B. Hailegnaw, S. Kirmayer, E. Edri, G. Hodes, D. Cahen, Rain on Methylammonium Lead Iodide Based Perovskites: Possible Environmental Effects of Perovskite Solar Cells, J. Phys. Chem. Lett. 6 (2015) 1543–1547. doi:10.1021/acs.jpclett.5b00504.

[115] D. Fabini, Quantifying the Potential for Lead Pollution from Halide Perovskite Photovoltaics, J. Phys. Chem. Lett. 6 (2015) 3546–3548. doi:10.1021/acs.jpclett.5b01747.

[116] W. Ming, H. Shi, M.-H. Du, Large dielectric constant, high acceptor density, and deep electron traps in perovskite solar cell material CsGeI3, J. Mater. Chem. A. 4 (2016) 13852–13858. doi:10.1039/C6TA04685A.

[117] T.J. Jacobsson, M. Pazoki, A. Hagfeldt, T. Edvinsson, Goldschmidt's Rules and Strontium Replacement in Lead Halogen Perovskite Solar Cells: Theory and Preliminary Experiments on CH3NH3SrI3, J. Phys. Chem. C. 119 (2015) 25673–25683. doi:10.1021/acs.jpcc.5b06436.

[118] J.I. Uribe, D. Ramirez, J.M. Osorio-Guillén, J. Osorio, F. Jaramillo, CH3NH3CaI3 Perovskite: Synthesis, Characterization, and First-Principles Studies, J. Phys. Chem. C. 120 (2016) 16393–16398. doi:10.1021/acs.jpcc.6b04207.

[119] W. Liao, D. Zhao, Y. Yu, C.R. Grice, C. Wang, A.J. Cimaroli, P. Schulz, W. Meng, K. Zhu, R.-G. Xiong, Y. Yan, Lead-Free Inverted Planar Formamidinium Tin Triiodide Perovskite Solar Cells Achieving Power Conversion Efficiencies up to 6.22%, Adv. Mater. 28 (2016) 9333–9340. doi:10.1002/adma.201602992.

[120] N.K. Noel, S.D. Stranks, A. Abate, C. Wehrenfennig, S. Guarnera, A.-A. Haghighirad, A. Sadhanala, G.E. Eperon, S.K. Pathak, M.B. Johnston, A. Petrozza, L.M. Herz, H.J. Snaith, Lead-free organic–inorganic tin halide perovskites for photovoltaic applications, Energy Environ. Sci. 7 (2014) 3061–3068. doi:10.1039/C4EE01076K.

[121] B.J. Kim, D.H. Kim, S.L. Kwon, S.Y. Park, Z. Li, K. Zhu, H.S. Jung, Selective dissolution of halide perovskites as a step towards recycling solar cells, Nat. Commun.

7 (2016) 11735. doi:10.1038/ncomms11735.

[122] L. Huang, Z. Hu, J. Xu, X. Sun, Y. Du, J. Ni, H. Cai, J. Li, J. Zhang, Efficient electron-transport layer-free planar perovskite solar cells via recycling the FTO/glass substrates from degraded devices, Sol. Energy Mater. Sol. Cells. 152 (2016) 118–124. doi:https://doi.org/10.1016/j.solmat.2016.03.035.

[123] D. Bi, G. Boschloo, S. Schwarzmüller, L. Yang, E.M.J. Johansson, A. Hagfeldt, Efficient and stable CH3NH3PbI3-sensitized ZnO nanorod array solid-state solar cells, Nanoscale. 5 (2013) 11686–11691. doi:10.1039/C3NR01542D.

[124] M.H. Kumar, N. Yantara, S. Dharani, M. Graetzel, S. Mhaisalkar, P.P. Boix, N. Mathews, Flexible, low-temperature, solution processed ZnO-based perovskite solid state solar cells, Chem. Commun. 49 (2013) 11089–11091. doi:10.1039/C3CC46534A.

[125] D.-Y. Son, J.-H. Im, H.-S. Kim, N.-G. Park, 11% Efficient Perovskite Solar Cell Based on ZnO Nanorods: An Effective Charge Collection System, J. Phys. Chem. C. 118 (2014) 16567–16573. doi:10.1021/jp412407j.

[126] S. Kumar, P.D. Sahare, S. Kumar, Optimization of the CVD parameters for ZnO nanorods growth: Its photoluminescence and field emission properties, Mater. Res. Bull. 105 (2018) 237–245. doi:10.1016/j.materresbull.2018.05.002.

[127] A. Ievtushenko, V. Karpyna, J. Eriksson, I. Tsiaoussis, I. Shtepliuk, G. Lashkarev, R. Yakimova, V. Khranovskyy, Effect of Ag doping on the structural, electrical and optical properties of ZnO grown by MOCVD at different substrate temperatures, Superlattices Microstruct. 117 (2018) 121–131. doi:10.1016/j.spmi.2018.03.029.

[128] A. Rivera, J. Zeller, A. Sood, M. Anwar, A Comparison of ZnO Nanowires and Nanorods Grown Using MOCVD and Hydrothermal Processes, J. Electron. Mater. 42 (2013) 894–900. doi:10.1007/s11664-012-2444-4.

[129] P. Gu, X. Zhu, D. Yang, Vertically aligned ZnO nanorods arrays grown by chemical bath deposition for ultraviolet photodetectors with high response performance, J. Alloys Compd. 815 (2020) 152346. doi:10.1016/j.jallcom.2019.152346.

[130] S.N. Sarangi, Controllable growth of ZnO nanorods via electrodeposition technique: towards UV photo-detection, J. Phys. D. Appl. Phys. 49 (2016) 355103. doi:10.1088/0022-3727/49/35/355103.

[131] F.J. Ramos, M.C. López-Santos, E. Guillén, M.K. Nazeeruddin, M. Grätzel, A.R. Gonzalez-Elipe, S. Ahmad, Perovskite Solar Cells Based on Nanocolumnar Plasma-

Deposited ZnO Thin Films, ChemPhysChem. 15 (2014) 1148–1153. doi:10.1002/cphc.201301215.

[132] L. Liang, Z. Huang, L. Cai, W. Chen, B. Wang, K. Chen, H. Bai, Q. Tian, B. Fan, Magnetron Sputtered Zinc Oxide Nanorods as Thickness-Insensitive Cathode Interlayer for Perovskite Planar-Heterojunction Solar Cells, ACS Appl. Mater. Interfaces. 6 (2014) 20585–20589. doi:10.1021/am506672j.

[133] D.-Y. Son, K.-H. Bae, H.-S. Kim, N.-G. Park, Effects of Seed Layer on Growth of ZnO Nanorod and Performance of Perovskite Solar Cell, J. Phys. Chem. C. 119 (2015) 10321–10328. doi:10.1021/acs.jpcc.5b03276.

[134] F.A. Cataño, L.W. Allende, H. Gómez, ELECTRODEPOSITION OF ZnO NANOROD ARRAYS FOR APPLICATION IN PEROVSKITE BASED SOLAR CELLS, J. Chil. Chem. Soc. 60 (2015) 2940–2943. doi:10.4067/s0717-97072015000200017.

[135] J. Dong, J. Shi, D. Li, Y. Luo, Q. Meng, Controlling the conduction band offset for highly efficient ZnO nanorods based perovskite solar cell, Appl. Phys. Lett. 107 (2015) 73507. doi:10.1063/1.4929435.

[136] K. Mahmood, B.S. Swain, A. Amassian, 16.1% Efficient Hysteresis-Free Mesostructured Perovskite Solar Cells Based on Synergistically Improved ZnO Nanorod Arrays, Adv. Energy Mater. 5 (2015) 1500568. doi:10.1002/aenm.201500568.

[137] M. Wang, S. Li, P. Zhang, Y. Wang, H. Li, Z. Chen, A modified sequential method used to prepare high quality perovskite on ZnO nanorods, Chem. Phys. Lett. 639 (2015) 283–288. doi:10.1016/j.cplett.2015.09.044.

[138] A. Dymshits, L. Iagher, L. Etgar, Parameters Influencing the Growth of ZnO Nanowires as Efficient Low Temperature Flexible Perovskite-Based Solar Cells, Materials (Basel). 9 (2016) 60. doi:10.3390/ma9010060.

[139] H. Wang, L. Yan, J. Liu, J. Li, H. Wang, Fabrication of well-aligned ZnO nanorod photoanodes for perovskite solar cells, J. Mater. Sci. Mater. Electron. 27 (2016) 6872–6880. doi:10.1007/s10854-016-4640-0.

[140] X. Qiu, Y. Jiang, H. Zhang, Z. Qiu, S. Yuan, P. Wang, B. Cao, Lead-free mesoscopic Cs2SnI6 perovskite solar cells using different nanostructured ZnO nanorods as electron transport layers, Phys. Status Solidi - Rapid Res. Lett. 10 (2016) 587–591.

doi:10.1002/pssr.201600166.

[141] Y. Xu, Tian Liu, Z. Li, B. Feng, S. Li, J. Duan, C. Ye, J. Zhang, H. Wang, Preparation and photovoltaic properties of perovskite solar cell based on ZnO nanorod arrays, Appl. Surf. Sci. 388 (2016) 89–96. doi:10.1016/j.apsusc.2016.03.079.

[142] S. Li, P. Zhang, H. Chen, Y. Wang, D. Liu, J. Wu, H. Sarvari, Z.D. Chen, Mesoporous PbI2 assisted growth of large perovskite grains for efficient perovskite solar cells based on ZnO nanorods, J. Power Sources. 342 (2017) 990–997. doi:10.1016/j.jpowsour.2017.01.024.

[143] P. Ruankham, D. Wongratanaphisan, A. Gardchareon, S. Phadungdhitidhada, S. Choopun, T. Sagawa, Full coverage of perovskite layer onto ZnO nanorods via a modified sequential two-step deposition method for efficiency enhancement in perovskite solar cells, Appl. Surf. Sci. 410 (2017) 393–400. doi:10.1016/j.apsusc.2017.03.096.

[144] A. Burgos, Electrodeposition of ZnO Nanorods as Electron Transport Layer in a Mixed Halide Perovskite Solar Cell, Int. J. Electrochem. Sci. (2018) 6577–6583. doi:10.20964/2018.07.25.

[145] M.F. Hossain, S. Naka, H. Okada, Fabrication of perovskite solar cells with ZnO nanostructures prepared on seedless ITO substrate, J. Mater. Sci. Mater. Electron. 29 (2018) 13864–13871. doi:10.1007/s10854-018-9518-x.

[146] M.R. Khelladi, L. Mentar, A. Beniaiche, L. Makhloufi, A. Azizi, A study on electrodeposited zinc oxide nanostructures, J. Mater. Sci. Electron. 24 (2013) 153–159. doi:10.1007/s10854-012-0973-5.

[147] H. Zeng, J. Cui, B. Cao, U. Gibson, Y. Bando, D. Golberg, Electrochemical Deposition of ZnO Nanowire Arrays: Organization, Doping, and Properties, Sci. Adv. Mater. 2 (2010) 336–358. doi:10.1166/sam.2010.1096.

[148] M. Skompska, K. Zarębska, Electrodeposition of ZnO Nanorod Arrays on Transparent Conducting Substrates–a Review, Electrochim. Acta. 127 (2014) 467–488. doi:https://doi.org/10.1016/j.electacta.2014.02.049.

[149] R.K. Pandey, S.N. Sahu, S. Chandr, Handbook of semiconductor electrodeposition, Applied Ph, New York, 1996.

[150] F. Nasirpouri, Fundamentals and Principles of Electrode-Position, in: Electrodepos. Nanostructured Mater., Springer International Publishing, Cham, 2017: pp. 75–121.

doi:10.1007/978-3-319-44920-3_3.

[151] M.A. Thomas, J. Cui, Electrodeposition of ZnO Nanostructures: Growth, Doping, and Physical Properties, in: M. Aliofkhazraei, A.S.H. Makhlouf (Eds.), Handb. Nanoelectrochemistry Electrochem. Synth. Methods, Prop. Charact. Tech., Springer International Publishing, Cham, 2016: pp. 647–679. doi:10.1007/978-3-319-15266-0_22.

[152] T. Kawano, H. Imai, Nanoscale morphological design of ZnO crystals grown in aqueous solutions, J. Ceram. Soc. Japan. 118 (2010) 969–976. doi:10.2109/jcersj2.118.969.

[153] Q. Peng, Y. Qi, ZnO Nanowires and Their Application for Solar Cells, in: Nanowires - Implementations Appl., InTech, 2011. doi:10.5772/17923.

[154] C. Liu, Z. Qiu, W. Meng, J. Chen, J. Qi, C. Dong, M. Wang, Effects of interfacial characteristics on photovoltaic performance in CH3NH3PbBr3-based bulk perovskite solar cells with core/shell nanoarray as electron transporter, Nano Energy. 12 (2015) 59–68. doi:10.1016/j.nanoen.2014.12.004.

[155] Z. Li, R. Wang, J. Xue, X. Xing, C. Yu, T. Huang, J. Chu, K.-L. Wang, C. Dong, Z. Wei, Y. Zhao, Z.-K. Wang, Y. Yang, Core–Shell ZnO@SnO2 Nanoparticles for Efficient Inorganic Perovskite Solar Cells, J. Am. Chem. Soc. 141 (2019) 17610–17616. doi:10.1021/jacs.9b06796.

[156] J. Dong, Y. Zhao, J. Shi, H. Wei, J. Xiao, X. Xu, J. Luo, J. Xu, D. Li, Y. Luo, Q. Meng, Impressive enhancement in the cell performance of ZnO nanorod-based perovskite solar cells with Al-doped ZnO interfacial modification, Chem. Commun. 50 (2014) 13381–13384. doi:10.1039/c4cc04908j.

[157] M. Zhong, L. Chai, Y. Wang, Core-shell structure of ZnO@TiO2 nanorod arrays as electron transport layer for perovskite solar cell with enhanced efficiency and stability, Appl. Surf. Sci. 464 (2019) 301–310. doi:10.1016/J.APSUSC.2018.09.080.

[158] I. Panžić, K. Juraić, N. Krstulović, A. Šantić, D. Belić, D. Blažeka, M. Plodinec, V. Mandić, J. Macan, A. Hammud, D. Ivanov, J. Plaisier, M.G. Willinger, D. Gracin, A. Gajović, ZnO@TiO2 Core Shell Nanorod Arrays with Tailored Structural, Electrical, and Optical Properties for Photovoltaic Application, Molecules. 24 (2019) 3965. doi:10.3390/molecules24213965.

[159] T. Frade, K. Lobato, J.F.C. Carreira, J. Rodrigues, T. Monteiro, A. Gomes, TiO2

anatase intermediary layer acting as template for ZnO pulsed electrodeposition, Mater. Des. 110 (2016) 18–26. doi:10.1016/j.matdes.2016.07.122.

[160] T. Frade, D. Siopa, A.F. Martins, J.F.C. Carreira, J. Rodrigues, N. Ben Sedrine, M.R. Correia, T. Monteiro, R. Tena-Zaera, A. Gomes, Optoelectronic Characterization of ZnO Nanorod Arrays Obtained by Pulse Electrodeposition, J. Electrochem. Soc. 165 (2018) D595–D603. doi:10.1149/2.0131813jes.

Chapter II

Materials and Methods

This chapter describes all the experimental details of the preparation of the nanomaterials and photovoltaic devices discussed throughout the thesis. The chapter is divided into five sections, with Sections 2.2 to 2.4 covering the experimental details associated with the results reported in Chapters 3 to 6. Chapter 2.1 details the materials and chemicals used. Chapter 2.2 details the experimental methods related to ZnO nanostructures preparation. Section 2.3 describes the methods used to obtain the ZnO-based core-shell nanostructures. The steps involved in the production of PSCs are described in Section 2.4. Finally, Section 2.5 will provide details of the characterisation techniques used throughout Chapters 3 to 6.

2.1. Chemicals

The chemicals used in this research were (listed in alphabetical order):

- Acetic acid glacial (CH_3CO_2H, Scharlab)
- Acetylacetone (ACAC, Sigma-Aldrich)
- 1-Butanol (BuOH, ≥ 99.5 %, Aldrich)
- 1-Butyl-1-methylpyrrolidinium bis(trifluoromethanesulfonyl)imide ($PYR_{14}TFSI$, 99.9 %, Solvionic)
- 4-*tert*-Butylpyridine (TBP, 96 %, Sigma-Aldrich)
- Chlorobenzene anhydrous (C_6H_5Cl, 99.8 %, Sigma-Aldrich)
- Dichloromethane (CH_2Cl_2, 99.5 %, Scharlab)
- *N*,*N*-dimethylformamide (DMF, extra pure, Scharlab)
- Ethanol absolute (EtOH, synthesis grade, Scharlab)
- Ethanol anhydrous (EtOH, Sigma-Aldrich)
- Lead(II) iodide (PbI_2, 99 %, Sigma-Aldrich)
- Lithium bis(trifluoromethane) sulfonimidate (LiTFSI, 99.9 %, Solvionic)
- Lithium perchlorate ($LiClO_4$, 99.99 %, Sigma-Aldrich)
- Methanol (CH_3OH, synthesis grade, Scharlab)
- 2-(2-Methoxyethoxy)acetic acid ($CH_3OCH_2CH_2OCH_2CO_2H$, MEA acid Sigma-Aldrich)
- Methylammonium iodide (MAI, CH_3NH_3I, Dyesol)
- Potassium chloride (KCl, ≥ 99.0 %, Sigma-Aldrich)
- Potassium hydroxide (KOH, Sigma-Aldrich)
- 2-Propanol (IPA, ≥ 99.5 %, ACS)
- Propylene carbonate anhydrous ($C_4H_6O_3$, 99.7 %, Aldrich)

- 2,2',7,7'-Tetrakis(*N*,*N*-di-p-methoxyphenylamine)-9,9-spirobifluorene (spiro-OMeTAD, 99 %, Feiming Chemicals Limited)
- Titanium diisopropoxide bis(acetylacetonate) ($Ti(acac)_2O\mathit{i}Pr_2$, 75wt. % in isopropanol, Aldrich)
- Titanium(IV) isopropoxide (TTIP, 97 %, Aldrich)
- Zinc acetate dehydrate ($Zn(CH_3COO)_2 \cdot 2H_2O$, 99.0 %, Sigma-Aldrich)
- Zinc(II) bis(trifluoromethanesulfonyl)imide ($Zn(TFSI)_2$, 99.5 %, Solvionic)
- Zinc nitrate hexahydrate ($Zn(NO_3)_2 \cdot 6H_2O$, 98.0 %, Sigma-Aldrich)

2.2. Cells and electrodes

ZnO nanostructures electrodeposition were carried out in a single compartment electrochemical glass cell. The working electrodes consisted of bare fluorine-doped tin oxide coated glass (FTO, Pilkington TEC 15, sheet resistance of 15 Ω/sq) or FTO modified substrate. Firstly, the FTO substrates were cleaned by ultra-sonication (Elma S30) sequentially for 15 min in neutral dishwashing liquid soap, acetone and ethanol absolute or 2-propanol. In between sonication, the substrates were rinsed in abundant deionised water (18.2 MΩ.cm). The substrates were then dried in nitrogen flux.

The electrode area in contact with the electrolyte was a square measuring 2.25 cm^2. A graphite foil with 9 cm^2 area was used as counter electrode and Ag/AgCl (KCl saturated) electrode, with low impedance (< 1000 Ω) as the reference in the case of aqueous electrolyte solutions, and a Pt wire and a Ti-Pt mesh were used as the pseudo reference and counter electrode, respectively, in the case of ionic liquid electrolyte solutions. The working and counter electrodes were placed facing each other, separated by a distance of 2 cm.

The voltammetric studies were performed in a three-compartment glass cell, with FTO or FTO-modified substrates as working electrode, Ag/AgCl as the reference electrode and a Pt wire as the counter electrode. From now on, the Ag/AgCl reference electrode will be referred to as Ref.

The photoelectrochemical characterization of the ZnO and ZnO-based core-shell nanostructures was performed using a three-electrode cell with a quartz window, a graphite bar as counter and Ag/AgCl as reference electrodes.

Mott-Schottky measurements were obtained using a three-electrode cell with a Pt foil as the counter electrode and an Ag/AgCl reference electrode. As-grown, heat-treated ZnO

nanorods and ZnO-based core-shell nanostructures were used as the working electrodes, with an exposed geometric area of 0.196 cm^2.

2.3. ZnO nanostructures: different approaches

2.3.1. Preparation of TiO_2 thin layers

In the following chapters, two types of TiO_2 thin layers are presented and studied. A TiO_2 intermediate layer (designated FTO/TiO_2) was used in the work discussed in Chapters 3, 4, and 6. A TiO_2 compact layer (designated c-TiO_2) was used in the work presented in Chapter 5.

The FTO/TiO_2 substrates were prepared by spin-coating a TiO_2 layer on FTO glass at 500 r.p.m. for 3 s and 2000 r.p.m. for 30 s using a solution of 0.15 M $Ti(acac)_2O$*i*Pr_2 in 1-butanol. Upon deposition, the samples were then moved into an oven and heated in air at 125 °C for 5 min. Upon cooling to room temperature (RT), the same spin-coating and heating process was repeated twice, however, with a more concentrated solution of 0.30 M $Ti(acac)_2O$*i*Pr_2 in 1-butanol. Finally, after rinsing with deionised water, the FTO/TiO_2 substrates were annealed in air at 500 °C for 15 min inside a muffle furnace. The heating rate was 5 °C.min^{-1} whilst cooling to RT occurred naturally within the furnace. The expected thickness of the TiO_2 thin layer is ~100 nm.

The TiO_2 compact films, c-TiO_2, were prepared by spin-coating on FTO glass substrates at 2000 r.p.m. for 30 s using a solution of 0.34 M TTIP in ethanol anhydrous, then were heated at 500 °C for 30 min with a heating rate of 10 °C.cm^{-1} and allowed to cool down naturally to RT. The resultant thickness of the TiO_2 compact films was ~70 nm.

2.3.2. Preparation of ZnO nanostructures by electrodeposition - Aqueous electrolyte

Before the ZnO nanorods electrodeposition, a ZnO seed-layer (< 100 nm thickness) was prepared electrochemically by applying -1.3 V vs Ref. for 30 s on FTO and FTO/TiO_2 substrates, using an aqueous solution of 10 mM $Zn(NO_3)_2$ and 5 mM KCl prepared with deionised water, as the electrolytic bath (solution pH 6.4). The temperature of the solution was maintained at 70 °C using a thermostatic bath. The samples prepared with

electrodeposited ZnO seed-layers on FTO and FTO/TiO_2 were named FTO/ZnO_SL and FTO/TiO_2/ZnO_SL samples, respectively.

The ZnO electrodeposition in pulse mode was applied on FTO and FTO modified electrodes. The electrolytic bath was the same as used for ZnO seed-layer electrodeposition. ZnO thin films were prepared by repetitive application of different potentiostatic square waves pulses, as exemplified in Figure 2.1 with the significant operational parameters detailed in Table 2.1. The different electrodeposition profiles were denoted as Profile A, B and C. The deposition charge density was fixed at approximately 425 mC.cm^{-2} (at 70 °C) to obtain a film thickness of ~300 nm. The ZnO nanorods presented in Chapter 3 were prepared by Profile C. Resultant film thickness varied between ca. 500 nm and 800 nm depending on the substrate used.

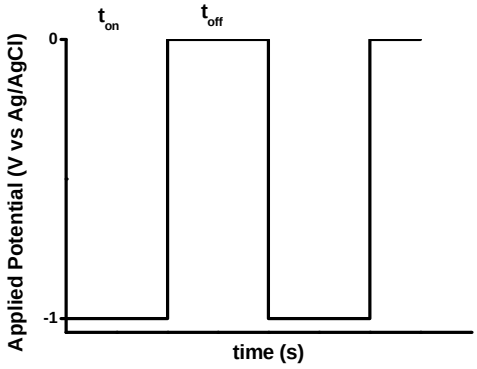

Figure 2.1 - Schematic illustration of the square wave used in potentiostatic pulse electrodeposition. t_{on} and t_{off} denote the pulse time and the rest time, respectively [1].

Table 2.1 - Pulse parameters of ZnO pulse electrodeposition [1]. *T is the cycle time.*

Profile	***E*$_{on}$ (V vs Ref.)**	***t*$_{on}$ (s)**	***E*$_{off}$ (V vs Ref.)**	***t*$_{off}$ (s)**	***T* (s)**	***f* (Hz)**	***Duty cycle* (%)**
A	-1.00	0.50	0.00	1.50	2.00	0.50	25.0
B		0.50		1.00	1.50	0.67	33.3
C		0.25		1.00	1.25	0.80	20.0

The as-deposited ZnO arrays obtained at a fixed potential (seed-layer) or pulsed electrodeposition (nanorods) were rinsed in deionized water and annealed in air at 450 °C for 1 h inside a muffle furnace, with a heating rate of 5 °C.min^{-1}, and then allowed to cool down naturally to RT. The obtained ZnO nanorods arrays were named ZnO NRs.

- Ionic liquid electrolyte

The electrodeposition of ZnO thin films was carried out in a 0.05 M $Zn(TFSI)_2$ solution in $PYR_{14}TFSI$, which was bubbled with oxygen before and during the experiment (Figure 2.2). The electrodeposition was performed at -1.6 V until a charge density of 0.03 $C.cm^{-2}$ was attained. The temperature during deposition was 150 °C. The samples were then rinsed with acetone and immersed in dichloromethane to remove the traces of the ionic liquid. The obtained ZnO thin films were named ZnOiL and will be analysed and discussed in Chapter 5.

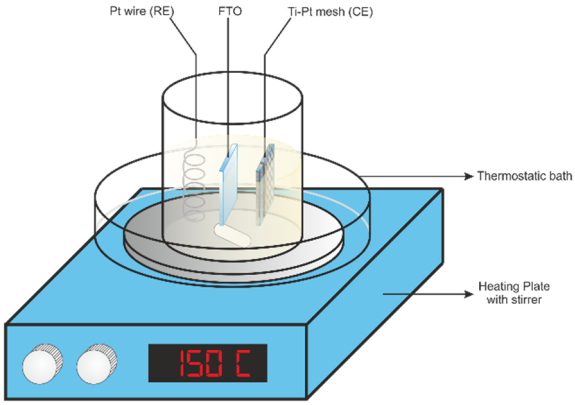

Figure 2.2 - Scheme of electrodeposition of ZnO thin films in ionic liquid electrolyte.

2.3.3. Preparation of ZnO nanostructures by spray pyrolysis

The ZnO thin films prepared by spray pyrolysis named as ZnOsp were prepared from a solution of $Zn(CH_3COO)_2 \cdot 2H_2O$ (1.778 g) dissolved in ethanol absolute (60 mL), deionised water (20 mL), and acetic acid (1 mL). The solution was sprayed onto heated FTO glass substrates at 350 °C (slides with 25 × 30 mm^2 area) using compressed air as carrier gas (at ~ 4 mbar pressure) (Figure 2.3). To obtain a film thickness of ~ 40 nm, the heated FTO slides were sprayed for 100 cycles (3 s spraying plus 7 s waiting). The FTO-sprayed slides were annealed at 450 °C for 60 min (10 $°C.min^{-1}$ heating rate) and then cooled down to RT within the tubular furnace.

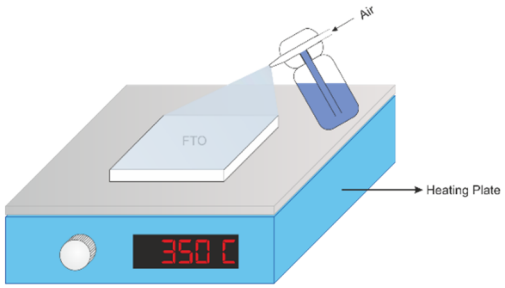

Figure 2.3 - Scheme of the preparation of ZnO thin films obtained by spray pyrolysis.

2.3.4. Preparation of ZnO nanostructures by spin-coating

Two different ZnO nanoparticles synthesis was used to produce thin films by spin-coating. The obtained ZnO thin films were named as $ZnOnp_{ac}$ and ZnOnp, for the ZnO nanoparticles suspension with the addition of MEA and without, respectively.

- ZnO nanoparticles suspension without the addition of acid (ZnOnp)

ZnOnp thin films were obtained by using a ZnO nanoparticles suspension, which was prepared by dissolving $Zn(CH_3COO)_2 \cdot 2H_2O$ (0.144 g) in methanol (66 mL) at 60 °C. Next, a KOH (0.057 g) solution in methanol (34 mL) at 60 °C was added dropwise to the previous solution under vigorous stirring. Before adding KOH solution, 100 μL of deionised water was added to avoid precipitation. After 2 h, the heater and stirrer were removed, allowing the suspension to cool down to RT.

- ZnO nanoparticles suspension with the addition of MEA acid ($ZnOnp_{ac}$)

$ZnOnp_{ac}$ thin films were obtained by using a ZnO nanoparticles suspension, which was prepared by dissolving $Zn(CH_3COO)_2 \cdot 2H_2O$ (1.558 g) in methanol (66 mL) at 60 °C. Next, a KOH (0.80 g) solution in methanol (34 mL) at 60 °C was added dropwise to the previous solution under vigorous stirring. After 3 h, the solution was centrifuged to obtain the precipitate that was washed with methanol (100 mL). To disperse the nanoparticles, the washed precipitate was treated with chlorobenzene (4.2 mL) and MEA acid (12.7 μL). The concentrated suspension was diluted in a 1:6 dilution ratio of chlorobenzene and MEA acid, obtaining a mass concentration of ~23 $g.L^{-1}$ of ZnO nanoparticles.

The ZnO nanoparticles suspensions were spin-coated onto FTO substrates at 2000 r.p.m. for 30 s. After spin-coating, the coated substrates were heated to 110 °C for 5 min (Figure 2.4). To obtain a film thickness of ~ 30-40 nm, this procedure was performed once for $ZnOnp_{ac}$ thin films and repeated four times for ZnOnp thin films, resulting in continuous smooth films.

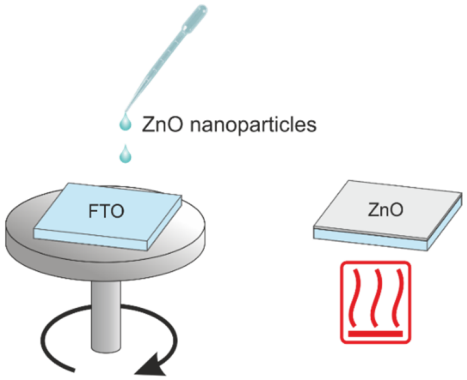

Figure 2.4 - Scheme of the preparation of ZnO thin films obtained by spin-coated ZnO nanoparticles.

2.4. ZnO-TiO_2 core-shell nanostructures

Chapter 6 will present the results of ZnO@TiO_2 core-shell nanostructures obtained by two different ways of synthesising the TiO_2 shell, namely by spin-coating and solvothermal method.

- TiO_2 shell prepared by spin-coating method

A TiO_2 layer was grown as a shell on FTO/ZnO_SL/ZnO NRs surface following a sol-gel process based on a procedure described elsewhere [2]. First, an amount of acetic acid glacial and water was added dropwise to the ethanolic solution of TTIP and 2-propanol, maintaining the concentration of TTIP:2-propanol:acetic acid:water :: 1:40 or 80:0.3:1 in molar ratio, followed by the stirring process at 500 r.p.m., for 60 min at room temperature.

The obtained sol-gel solution was used to coat a TiO_2 shell layer on the ZnO NRs surface using spin-coating technique using two different speed profiles, as shown in Figure 2.5. This was repeated three times with an evaporation step at 125 °C for 150 s between cycles. A pre-treatment with UV irradiation for 60 min was performed to improve the impregnation of

sol-gel solution into ZnO NRs. Finally, the samples were heated at 450 °C for 60 min (5 °C.min^{-1} heating rate) to form ZnO@TiO_2 core-shell nanostructures.

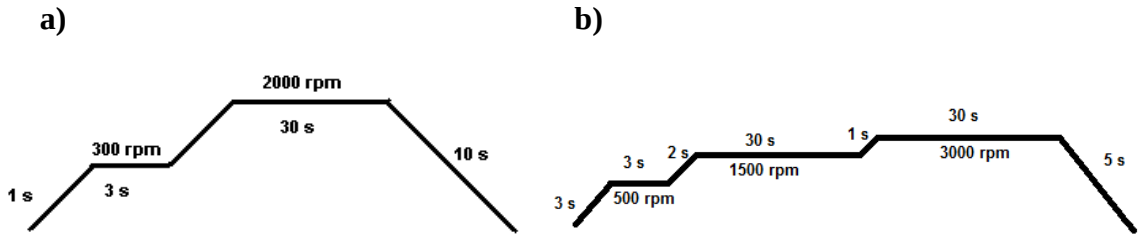

Figure 2.5 - Spin-coating speed profiles used for TiO_2 shell layer deposition on ZnO NRs surfaces: ***a)*** *Profile 1 and* ***b)*** *Profile 2.*

- TiO_2 shell prepared by solvothermal method

A TiO_2 layer was grown as a shell on FTO/ZnO_SL/ZnO NRs and FTO/TiO_2/ZnO_SL/ZnO NRs surfaces following a solvothermal method. The titanium precursor solution was prepared by stirring 50 mL of a 5 or 10 mM TTIP solution in 2-propanol for 2 h. Different amounts of ACAC were added to the previous solution (0 to 20 μL) while stirring for an additional 30 min. The titanium precursor solution was transferred into a Teflon-lined stainless-steel autoclave where the ZnO NRs samples were placed vertically, allowing complete immersion of the ZnO-coated areas. The autoclave was sealed and heated to 150 or 180 °C for 30 min to 24 h in a laboratory oven. After solvothermal synthesis, the autoclave was naturally cooled down to RT. The samples were washed carefully with ethanol to remove the residual solution and dried with nitrogen flux. Finally, the samples were annealed at 450 °C for 2 h (1 °C.min^{-1} heating rate) to form the TiO_2 crystal structure.

2.5. Solar cells application

$CH_3NH_3PbI_3$ was deposited on TiO_2, ZnO, and ZnO@TiO_2 thin films using a two-step coating method described elsewhere [3]. Briefly, the thin films were pre-heated at 100 ºC for 5 min. A 0.97 M PbI_2 solution in DMF was spun on the pre-heated thin films at 2300 r.p.m. for 60 s and dried at 100 ºC for 15 min. After cooling to room temperature, 0.315 M (50 mg.mL^{-1}) MAI solution in 2-propanol was loaded on the PbI_2-coated thin film substrate for 15 s (loading time), which was spun at 4000 r.p.m. for 20 s and heated at 100 ºC for 5 to 120 min, washed with 2-propanol and dried with air. All procedures were carried out in an argon-filled glovebox.

On top of the perovskite layer, the spiro-OMeTAD hole-selective contact was deposited from a solution that contained spiro-OMeTAD (108.4 mg) in chlorobenzene (953.43 μL), LiTFSI solution in acetonitrile (17.17 μL, 520 $mg.mL^{-1}$), and TBP (29.4 μL). A volume of 100 μL of spiro-OMeTAD solution was spin-coated on the $CH_3NH_3PbI_3$ perovskite layer at 3000 r.p.m. for 30 s. The samples were left for 16 h in a desiccator. Finally, an array of circular Au back contacts (~ 0.07 cm^2) was deposited by thermal evaporation at more than 5×10^{-6} Torr with a NANO38 (Kurt J. Lesker) apparatus with a shadow mask.

2.6. Characterisation Techniques

2.6.1. Materials characterisation

A. Electrochemical Analysis

Cyclic Voltammetry (CV)

Cyclic voltammetry is probably the most versatile electroanalytical technique in studying electroactive species, providing information on the electrochemical process and detecting intermediate reactions [4]. This technique, in this present work, is employed to understand the electrolytic bath and the substrate's effect on ZnO film growth. Furthermore, it also served to understand which are the best conditions for ZnO nanorod array electrodeposition.

Several voltammetric studies involving the formation of deposits have characteristic voltammograms, as shown in Figure 2.6.

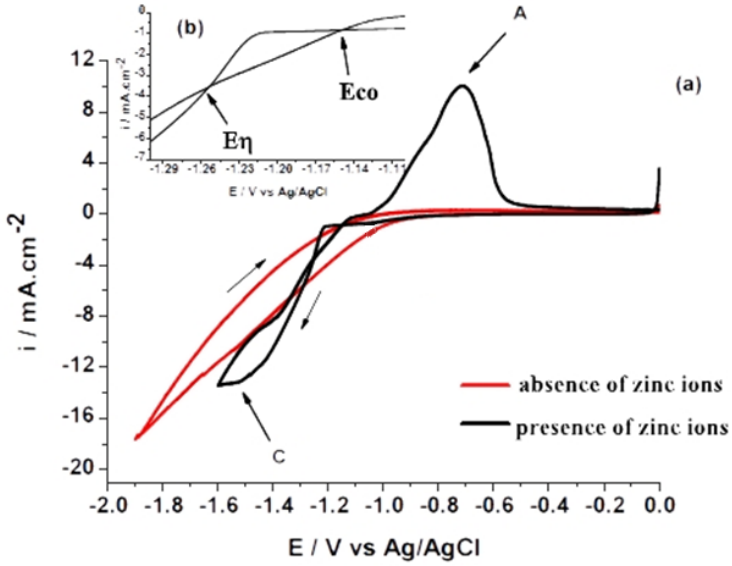

Figure 2.6 - ***a)*** *Cyclic voltammograms of steel electrode in 0.2 M $MgSO_4$ + 0.15 M H_3BO_3, with or without 0.1 M $ZnSO_4$, at pH 4. Scan rate of 10 mV.s^{-1}.* ***b)*** *Inset: Detail of the cyclic voltammogram in presence of zinc ions in the potential window -1,10 V to -1,30 V vs. Ag/AgCl. E_η is the nucleation overpotential, and E_{co} is the equilibrium potential.*

The cathodic peak (C) corresponds to the deposition of the reduced species. In the reverse sweep (anodic sweep from negative potentials to positive potentials), the deposition continues until the potential reaches a crossover potential, also known as equilibrium potential (E_{co}). Sometimes, a second crossover occurs at more negative overpotential than E_{co} indicating a formation of stable growing centres at the surface electrode named nucleation overpotential (E_η) [5]. An anodic peak (A) can be detected when the oxidation of the deposited species occurs. If the anodic current decreases to approximately zero after the oxidation step, it means that most of the deposited material was removed from the substrate.

The voltammetric studies were performed using a PC controlled Gamry R600 potentiostat (PHE200 software). The electrolyte composition, conditions and electrode setup, were identical to those used for pulsed electrodeposition. Voltammograms were acquired by potential scanning between the open-circuit potential (~ 0.2 V) and -1.3 V vs. Ref. and back three times. The scan rate was 10 mV.s^{-1}.

Mott-Schottky Method (MS)

The Mott-Schottky method is frequently used to measure the flatband potential and determine the charge carrier densities of semiconductor material in contact with electrolyte [6]. By varying the potential at the electrode/electrolyte interface, the space-charge capacitance within the semiconductor is measured, which gives the location of the energy

levels in the electrode/electrolyte junction, namely the flatband potential (V_{FB}), the conduction band edge (E_C) and the valence band edge (E_V) [7].

The Mott-Schottky (MS) analysis was performed with the samples held in the dark and at RT. The impedance was measured at a fixed frequency as a function of an applied DC potential. A 20 mV AC sinusoidal signal was superimposed on the applied potential interval (-0.8 V ≤ E ≤ 1.2 V vs. Ref.). The frequency was fixed in the range between 1 kHz – 10 kHz.

A 0.1 M $LiClO_4$ in propylene carbonate electrolyte (pH 7) was adopted [8] and degassed for 15 min before the experiments for oxygen removal.

The apparatus used for EIS measurements was a frequency response analyser (FRA) and PC controlled Gamry R600 potentiostat (EIS300 software). The acquired spectra were analysed by fitting them to equivalent circuit models. A series capacitor-resistor circuit model (Figure 2.7) was applied to calculate the capacitance of the ZnO/liquid interface. The series resistance R_s represents the resistance of the electrolyte solution and cables, R_{ct} is the charge transfer resistance that describes the electrochemical reaction that happens, and Z_{CPA} is the constant phase angle element that comprises the real and the imaginary part of the impedance Z [9]. After performing all the experiments under mentioned frequencies values, it was concluded that the MS plots obtained at 5 kHz better represent the ZnO nanorod arrays behaviour.

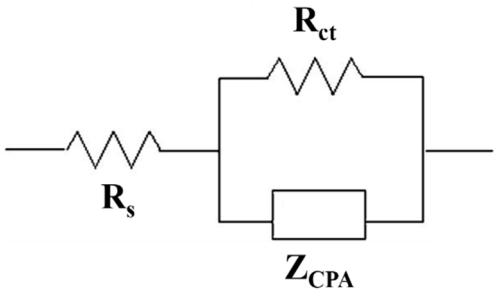

Figure 2.7 - Equivalent circuit model of electrode/electrolyte interface. R_s is solution resistance, R_{ct} is charge transfer resistance, and Z_{CPA} is constant phase angle impedance.

B. Morphological Analysis

Field-Emission Scanning Electron Microscopy with Energy Dispersive Spectroscopy (FESEM/EDS)

The morphology and elemental composition of ZnO and ZnO-based core-shell nanostructures were investigated by field-emission scanning electron microscopy using a FESEM/EDS JEOL JSM-7001F apparatus, with an electron beam voltage of 5, 15 or 25 kV.

The SEM micrographs were analysed to determine the ZnO nanorod size distribution, area coverage, diameter and spatial number density. The software used to analyse the micrographs was CorelDraw version 15 and ImageJ version 1.46.

Cross-section micrographs of the ZnO and perovskite samples were acquired with a FESEM ULTRA plus ZEISS microscope. The samples were cut with a Dremel multi-tool, with a cutting fibreglass disc.

Transmission Electron Microscopy (TEM)

The morphology of ZnO-based core-shell nanostructures was accessed using Transmission Electron Microscopy (TEM) using a Hitachi H8100. The nanostructures were scraped from the FTO substrates and dispersed via sonication in deionised water. They were then deposited onto TEM grids by pipetting and evaporating the solvent.

Atomic Force Microscopy (AFM)

The surface morphology of the TiO_2 films (FTO/TiO_2) was imaged by atomic force microscopy (Nanoscope IIIa multimode microscope Digital Instruments, Veeco). The acquisition was in tapping mode at a scan rate of 1.5 – 1.8 Hz in air using etched silicon cantilevers (TESP, Bruker) with a resonance frequency of ~ 300 kHz.

C. Surface Chemical Analysis

X-ray Photoelectron Spectroscopy (XPS)

The chemical groups attached to the ZnO thin films surface was analysed using X-ray photoelectron spectroscopy (XPS) [10]. XPS measurements were performed using a Phoibos photoelectron spectrometer equipped with an Al Kα X-ray source (16 mA, 12.5 kV) as the incident photon radiation. The overall resolution was approximately 0.9 eV. During the measurements, the chamber pressure was $< 1.0 \times 10^{-9}$ mBar. A tantalum foil was used to create an electrical contact between the sample surface and the sample holder to avoid charging effects. The binding energy (BE) scale calibration was performed by fixing the adventitious C1s peak at 284.8 eV. The analysis of the sample spectra was carried out using the CasaXPS software (version 2.3.23, © Casa software Ltd., 2020). To fit the individual components, a Shirley type baseline was employed, and Gaussian (70 %) – Lorentzian (30 %) (GL(30)) profiles were used. In addition, a ZnO single crystal reference extracted from previous experiments was used as a reference for Zn2p and O1s core levels.

D. Structural Analysis

X-ray Diffraction (XRD)

The structural characterisation of the films was carried out by X-ray diffraction (XRD) on a Philips Analytical PW 3050/60 X'Pert PRO (θ/2θ) equipped with X'Celerator detector with X'Pert Data Collector (v2.0b) software, using monochromatic Cu-K_α radiation as the incident beam, operating at 40 kV and 30 mA. XRD patterns were obtained by continuous scanning in the 2θ-range from 20 to 90 ° with a 2θ-step size of 0.017 ° and a scan step time of 10 s. In addition, a Bruker AXS-D8 Advance X-ray diffractometer with CuK_α was used for perovskite films.

The preferred orientation of the ZnO nanorods was estimated from the X-ray data according to the methodology developed by Bérubé et al. [11], considering the three Miller indexes of the four usually used to describe the hexagonal modified ZnO wurtzite structure, where the relative texture coefficient (*RTC*) is calculated by the expression described in equation 2.1.

$$RTC_{(hkl)} = \frac{R_{(hkl)}}{\sum R_{(hkl)}};\ \ R_{(hkl)} = \frac{I_{s(hkl)}}{I_{p(hkl)}} \tag{2.1}$$

$I_{s(hkl)}$ and $I_{p(hkl)}$ correspond to the diffraction intensities of the *(hkl)* planes measured for the films and the standard ZnO sample, respectively. Here the (100), (002), and (101) ZnO diffraction maxima were considered.

Raman Spectroscopy

Raman measurements, also conducted at RT, were performed in a Jobin Yvon HR800 spectrometer (1800 g.mm^{-1} diffraction grating) in backscattering geometry, using 442 nm wavelength radiation from a continuous waveform He-Cd laser and a × 100 magnification lens.

E. Optical Analysis

UV-Vis Spectroscopy

The optical absorption spectra of the ZnO samples were recorded on a UV-Vis spectrophotometer Shimadzu UV-2600 PC equipped with an ISR2600 plus integrating sphere.

Barium sulphate was used as a reference. The spectra were recorded at RT in the range of 200-1200 nm. The optical bandgap was determined via the Tauc method (neglecting band tail effects). For direct bandgap materials, a direct transition between the extreme points of the energy-momentum dispersion relation is expected, resulting in the following relationship between the optical absorption coefficient, α, and the incident photon energy $h\nu$ [12],

$$\alpha(h\nu) = A(h\nu - E_g)^{1/2} \quad (2.2)$$

where A is a proportionality constant, and E_g is the bandgap energy.

The perovskite absorptance spectra were obtained from the transmittance and reflectance spectra (equation 2.3), which were measured with a UV-VIS-NIR spectrophotometer JASCO V-570 with an integrating sphere.

$$Abs = 100 - T(\%) - R(\%) \quad (2.3)$$

where *Abs* is the absorptance, *T(%)* and *R(%)* are the transmittance and reflectance values in percentage, respectively.

Photoluminescence (PL)

The photoluminescence (PL) is a non-destructive optical characterization technique frequently used to determine the quality of semiconducting materials. A PL spectrum gives information about the processes that involve the intrinsic and extrinsic emissions of the studied material. In addition to these emissions, transitions associated with impurities and defects in ZnO can be interpreted based on the luminescence spectra analysis obtained under steady-state and transient conditions (time-resolved photoluminescence, TRPL) and photoluminescence excitation (PLE) spectra [13].

Steady-state RT photoluminescence (PL) and photoluminescence excitation (PLE) measurements were assessed in a Fluorolog-3 Horiba Scientific modular equipment with a double additive grating Gemini 180 scanning monochromator (2 × 180 mm, 1200 gr.mm^{-1}), in the excitation and a triple grating iHR550 spectrometer in the emission (550 mm, 1200 gr.mm^{-1}). A 450 W Xe lamp was used as the excitation source.

The PLE was assessed by setting the emission monochromator in the maxima of the optically active defects' emission band, and the excitation was scanned to higher energies. The measurements were performed using proper angle acquisition geometry, and the presented spectra were corrected to the optical components, photomultiplier detector and the Xe lamp spectral responses.

RT time-resolved photoluminescence (TRPL) spectra were acquired with the same Fluoroloh-3 system using a pulsed Xe lamp coupled to a monochromator.

Additionally, temperature-dependent PL analysis was performed using a dispersive system SPEX 1704 monochromator (1 m, 1200 $gr.mm^{-1}$) fitted with a cooled Hamamatsu R928 photomultiplier tube and exciting the samples with a 325 nm He-Cd laser line with a power density less than 0.6 $W.m^{-2}$. The samples were mounted in a cold finger of a closed-cycle helium cryostat, and the temperature was controlled in a range from 14 K to RT.

The data analysis and interpretation of the results presented in Chapters 3 and 4 using the PL technique were performed by Prof. Teresa Monteiro team from Departamento de Física and I3N from Universidade de Aveiro.

F. Photoelectrochemical Analysis

The photoelectroactivity of the ZnO electrodes was evaluated in an aqueous solution of 0.05 M Na_2SO_3 (pH ~ 9.5). The working electrode was illuminated through the backside (glass substrate) and a quartz window of the three-electrode cell. The irradiance source was a UV-enhanced mercury-xenon arc lamp (EmArc 200 W Ushio Lighting-Edge Technologies) housed in a Lot Oriel Apex light source and focused with a lens. The placement of the lens and the working electrode was adjusted to homogeneously illuminate the working electrode active area. The estimated irradiance was ~500 $mW.cm^{-2}$.

Photovoltammograms were obtained by scanning the applied potential between -1.0 V and 1.0 V vs Ref. at 2 $mV.s^{-1}$ using an EG&G Princeton Applied Research potentiostat/galvanostat Model PAR 263 with data acquisition via software. To eliminate the effect of the dark current, illumination was chopped at 0.1 Hz (Oriel Instruments chopper).

Photocurrent-time curves were obtained by applying 0.4 V vs Ref. and chopping the illumination at 0.025 Hz. The acquisition time was 3 min. Given the relatively short duration of these photocurrent measurements, the electrolyte was deaerated with N_2 flux for 15 min beforehand.

The open-circuit photovoltage transients under dark and illuminated conditions were recorded according to the time profile of 60 min in the dark, followed by 60 min illuminated and finally 10 min in the dark. The electrolyte here was continuously deaerated with N_2 flux.

2.6.2. Solar cell characterisation

Current-Voltage Measurements (I-V curves)

The I-V characteristics of the perovskite solar cells were measured under a xenon arc lamp simulator equipped with an AM 1.5 G spectral filter (Sun 2000, ABET Technologies). The intensity was adjusted to provide 1 sun (100 $mW.cm^{-2}$) using a calibrated silicon solar cell. The I-V curves were measured using a Keithley 2400 sourcemeter unit and were recorded by scanning the potential from higher than the open-circuit voltage to zero (i.e., "reverse mode") at approximately 300 $mV.s^{-1}$. Before the measurements, a voltage of about 1.25 V was applied to the devices for 1 min.

For all the I-V curves recorded, the photocurrents were converted into current densities, *J*, by dividing the current by the active cell area, making all the results comparable. A representative plot of current densities against the applied voltage to form an I-V curve is shown in Figure 2.8.

The power conversion efficiency of the devices, *PCE* or η, was calculated from I-V curves according to the following expression [14]:

$$PCE = \frac{J_{sc} \times V_{oc} \times FF}{P_{in}} \tag{2.4}$$

where J_{sc} is the short circuit current density obtained from the y-axis intercept (when represented in current density values), V_{oc} is the open-circuit voltage obtained from the x-axis intercept, *FF* is the fill factor which is a measure of ideality, a P_{in} is the solar incident power. The *FF* was calculated using the maximum power point (P_{max}), J_{sc} and V_{oc} according to equation 2.5.

$$FF = \frac{J_m \times V_m}{J_{sc} \times V_{oc}} = \frac{P_{max}}{J_{sc} \times V_{oc}} \times 100\ \% \tag{2.5}$$

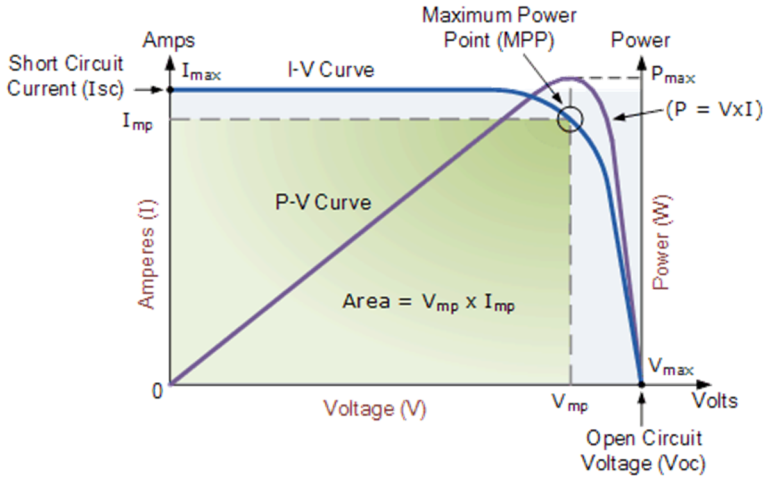

Figure 2.8 - Example of a typical I-V curve of a solar cell showing the associated parameters measured from it and the corresponding plot of power vs voltage from which the maximum power point (P_{max}) is obtained [15].

2.7. References

[1] T. Frade, D. Siopa, A.F. Martins, J.F.C. Carreira, J. Rodrigues, N. Ben Sedrine, M.R. Correia, T. Monteiro, R. Tena-Zaera, A. Gomes, Optoelectronic Characterization of ZnO Nanorod Arrays Obtained by Pulse Electrodeposition, J. Electrochem. Soc. 165 (2018) D595–D603. doi:10.1149/2.0131813jes.

[2] S. Panigrahi, D. Basak, Core-shell TiO2@ZnO nanorods for efficient ultraviolet photodetection, Nanoscale. 3 (2011) 2336–2341. doi:10.1039/c1nr10064e.

[3] M. Liu, M.B. Johnston, H.J. Snaith, Efficient planar heterojunction perovskite solar cells by vapour deposition, Nature. 501 (2013) 395–398. doi:https://doi.org/10.1038/nature12509.

[4] D.A. Aikens, Electrochemical methods, fundamentals and applications, 2nd Ed., Wiley, New York, 2009. doi:10.1021/ed060pa25.1.

[5] I. Rodriguez-Torres, G. Valentin, F. Lapicque, Electrodeposition of zinc--nickel alloys from ammonia-containing baths, J. Appl. Electrochem. 29 (1999) 1035–1044. doi:10.1023/A:1003610617785.

[6] K. Gelderman, L. Lee, S.W. Donne, Flat-Band Potential of a Semiconductor: Using the Mott–Schottky Equation, J. Chem. Educ. 84 (2009) 685–688. doi:10.1021/ed084p685.

[7] A.W. Bott, Electrochemistry of Semiconductor, Curr. Sep. 3 (1998) 87–91. doi:10.4139/sfj1950.29.43.

[8] I. Mora-Seró, F. Fabregat-Santiago, B. Denier, J. Bisquert, R. Tena-Zaera, J. Elias, C. Lévy-Clément, Determination of carrier density of ZnO nanowires by electrochemical techniques, Appl. Phys. Lett. 89 (2006) 203117. doi:10.1063/1.2390667.

[9] E.T. McAdams, A. Lackermeier, J.A. McLaughlin, D. Macken, J. Jossinet, The linear and non-linear electrical properties of the electrode-electrolyte interface, Biosens. Bioelectron. 10 (1995) 67–74. doi:https://doi.org/10.1016/0956-5663(95)96795-Z.

[10] D.M. Hercules, Electron Spectroscopy: Applications for Chemical Analysis, J. Chem. Educ. 81 (2004) 1751. doi:10.1021/ed081p1751.

[11] L.P. BERUBE, G. LESPERANCE, A quantitative method of determining the degree of texture of zinc electrodeposits, J. Electrochem. Soc. 136 (1989) 2314–2315. doi:10.1149/1.2097318.

[12] J.I. Pankove, Optical Processes in Semiconductors, Dover Publications, 2012.

[13] M.A.B. Peres, Caracterização óptica de amostras de ZnO, Universidade de Aveiro, 2007.

[14] Basic Characteristics and Characterization of Solar Cells, in: Mater. Concepts Sol. Cells, WORLD SCIENTIFIC (EUROPE), 2017: pp. 3–43. doi:doi:10.1142/9781786344496_0001.

[15] Alternative Energy Tutorials, Sol. Cell I-V Charact. (n.d.). http://www.alternative-energy-tutorials.com/energy-articles/solar-cell-i-v-characteristic.html (accessed 8 April 2019).

Chapter III

TiO_2 anatase intermediary layer acting as a template for ZnO pulsed electrodeposition

3.1. Introduction

In the last decade, ZnO has attracted much attention for optical and electronic applications due to its excellent properties, such as high electron mobility (200 $cm^2.V^{-1}.s^{-1}$), high exciton binding energy (60 meV), direct bandgap n-type semiconductor (~ 3.3 eV), non-toxicity, and is a low-cost material [1–3].

Several morphologies can be obtained for ZnO, depending on the growth conditions. The 1D ZnO nanostructures such as nanorods, nanowires or nanotubes, should be the most favourable as electron collecting layers because they combine direct electron transport pathways with large surface areas [4,5]. The 1D ZnO nanostructures can be prepared by a variety of processes, e.g. sputtering [6], chemical vapour deposition (CVD) [7], atomic layer deposition (ALD) [8], metal-organic chemical vapour deposition (MOCVD) [9], sol-gel synthesis [10,11], spray pyrolysis [12], and electrodeposition [13,14]. Due to the a) low temperatures involved (< 100 ºC), b) growth orientation control of ZnO thin films, and c) scalability and hence economic viability, electrodeposition has attracted significant attention for the formation of 1D ZnO nanostructures [15,16].

There are several reports about the orientation control of ZnO thin films prepared by electrodeposition [4,17]. Previous studies using the electrodeposition technique employed a constant potential/current, and ZnO films with hexagonal single-crystal columns were attained, which is the most typical morphology obtained by electrodeposition [18–20]. However, the application of a constant potential/current has limitations when tuning some features of ZnO films. Pulsed electrodeposition, for example, has the advantage of promoting nucleation, enabling the formation of fine crystals, which can be achieved by the opportunity of adjusting pulse parameters independently over a wide range. The result is the additional diffusion of reacting species, which plays an important role during electrodeposition [15,21,22]. Consequently, it should be possible to further optimise the films to the desired morphologies by controlling pulse parameters. Most reports in the literature use dissolved oxygen as the oxidant [194] for the electrolyte composition, although electrodeposition of ZnO from nitrate-based electrolytes has also been extensively studied [18,23]. When

compared to the use of O_2 [16,24] or H_2O_2 [25], the use of nitrate-based electrolytes has the advantage of reducing the need for convection and the addition of an extra oxidant.

The substrate onto which the electrodeposition occurs is also a fundamental parameter that defines film growth morphology. For example, for photovoltaic applications, the substrate tends to be a transparent conducting oxide (*e.g.* FTO or ITO). However, it can be modified with intermediate (or buffer) layers to model ZnO film growth [26–29].

Using a TiO_2 thin layer as a template, ZnO electrodeposition in one or two steps, *i.e.*, with or without a ZnO seed-layer, seems to allow better control of the nucleation step, which is a crucial factor for ZnO vertical growth [30]. However, before the work here presented, the use of TiO_2 as an intermediate layer for pulsed electrodeposition of ZnO nanorods has never been reported.

This chapter is divided into three main sections. The first section, entitled "Understanding the deposition process", will introduce the process of ZnO nanorod growth on FTO and modified substrates by identifying the different stages of the deposition process, from the formation of the initial seeds to the well-aligned arrays of nanorods at the end of the process, using cyclic voltammetry (CV) and scanning electron microscopy (SEM). The second section, "Growth modulation by substrate conditioning", will focus on the several factors that affect the nanorod growth process, namely the inclusion of a ZnO seed-layer and a TiO_2 intermediate layer. The final section, named "Evaluation of ZnO nanorods properties", will analyse how the modified surface substrates affect some ZnO characteristics, such as crystallinity, optical properties, and photoelectrochemical behaviour. The results shown in this chapter have been published as a full paper in a peer-reviewed journal [31].

3.2. Understanding the deposition process

The mechanism of ZnO formation by electrodeposition using nitrate-based electrolytes initiates with an electrochemical reduction of NO_3^- ions followed by a chemical formation of $Zn(OH)_2$ and subsequent dehydration to ZnO, equation 3.1 and 3.2 [18,23]:

$$NO_3^- + H_2O + 2e^- \rightarrow NO_2^- + 2OH^- \quad (3.1)$$

$$Zn^{2+} + 2OH^- \rightarrow Zn(OH)_2 \rightarrow ZnO + H_2O \quad (3.2)$$

The cyclic voltammograms shown in Figure 3.1 was recorded for pristine and modified FTO substrates in the same solution and temperature as used for the electrodeposition of ZnO films (seed-layer formation or nanorod growth). During the negative sweep, an abrupt increase of the cathodic current density was observed at potentials more negative than -0.6 V, which can be attributed to the reduction of NO_3^- ions (Eq. 3.1). At -1.0 V, the potential imposed on the cathodic pulse during nanorod growth, the recorded current density follows the sequence FTO < FTO/TiO_2 < FTO/TiO_2/ZnO_SL < FTO/ZnO_SL. This trend is probably due to the surface morphology and accessibility of active sites for the electrochemical reaction. To better understand this sequence, all the substrates were analysed by SEM, Figure 3.2.

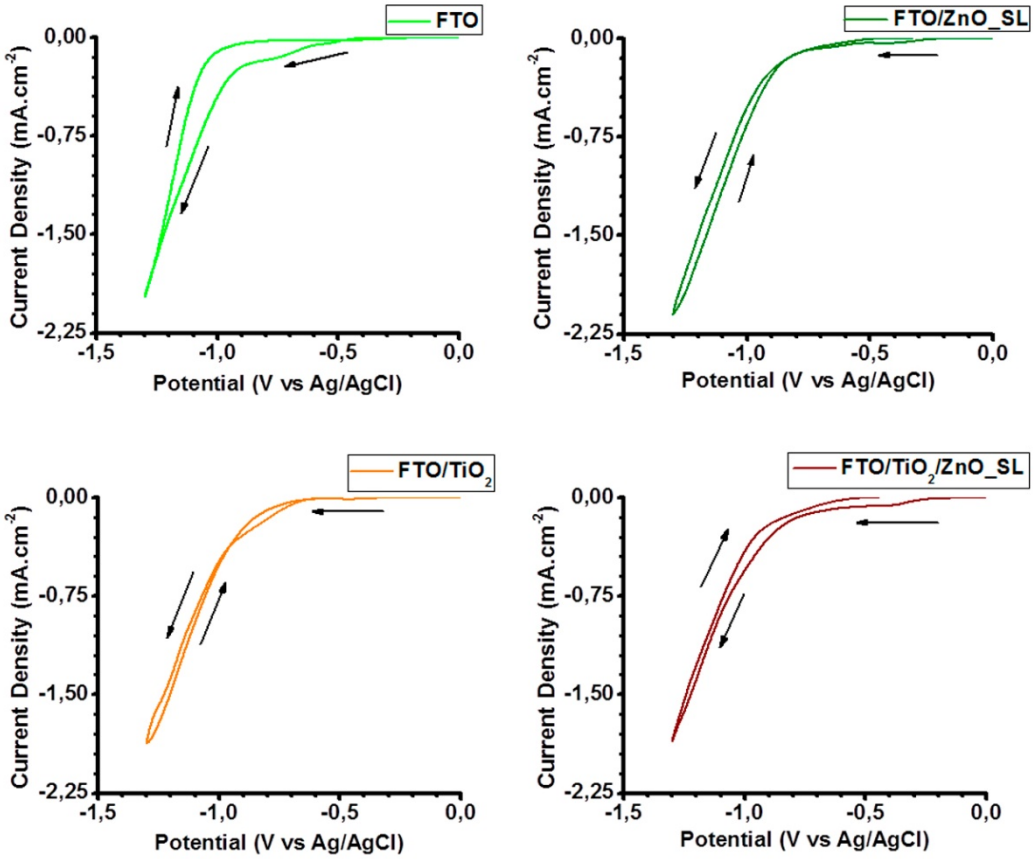

Figure 3.1 - Schematic Cyclic voltammograms (first cycle) recorded for FTO and modified substrates in an aqueous solution containing 10 mM $Zn(NO_3)_2$ and 5 mM KCl at 70 ºC. ν = 10 mV.s^{-1}.

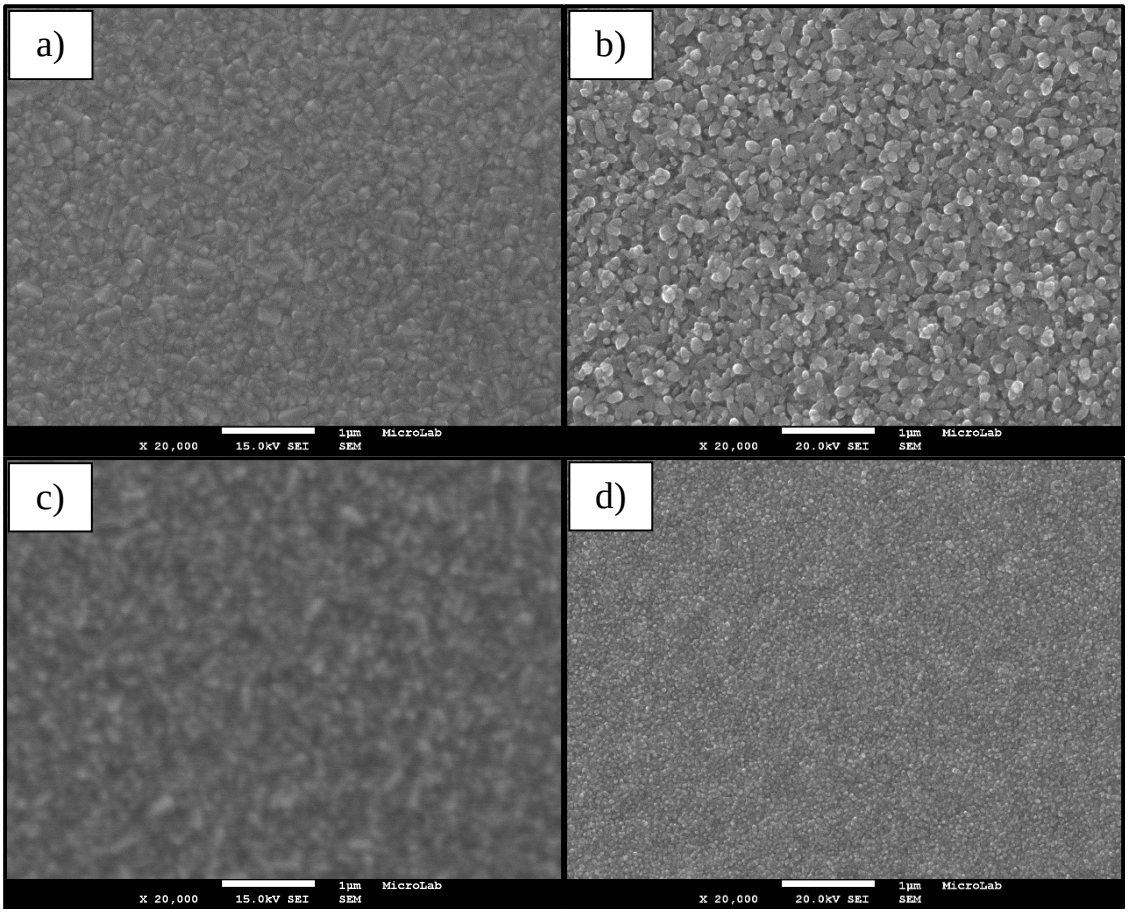

*Figure 3.2 - Representative SEM micrographs of **a)** FTO and **c)** TiO_2-coated FTO substrates and respective electrodeposited ZnO seed-layer **b)** and **d)**.*

The FTO surface is somewhat rough (Figure 3.2a)) compared to the TiO_2-coated FTO surface, which is smoother (Figure 3.2c)), resulting in an electrodeposited seed-layer on TiO_2-coated FTO significantly different in morphology than that electrodeposited directly on FTO (Figure 3.2d) and b), respectively). In addition, the ZnO seed-layer electrodeposited directly on the FTO substrate forms larger grains, likely due to the large grain structure of the FTO that plays a significant role in the mechanism that regulates the deposition. On the other hand, the ZnO seed-layer electrodeposited on the TiO_2 layer has a considerably smoother topography, possibly due to the more compact nature of the underlying TiO_2, as shown in the AFM image, Figure 3.3.

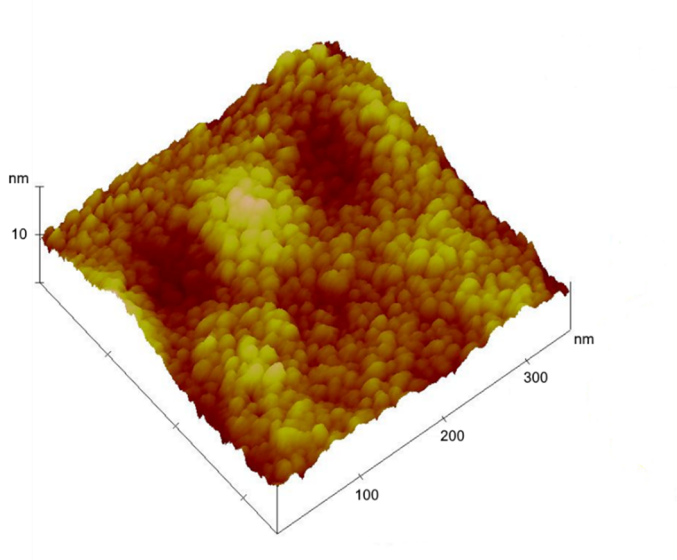

Figure 3.3 - Representative 3D-AFM image for TiO_2-coated FTO substrate.

In the cyclic voltammograms presented in Figure 3.1, the line crossing of the voltammetric response in the anodic and cathodic scans in all the studied systems indicates a nucleation process corresponding to the formation of ZnO grains. The SEM micrographs of the respective films after three voltammetric cycles confirmed their formation, Figure 3.4. Furthermore, it is quite visible the different morphologies obtained depending on the modification of FTO substrate, with an uncontrolled growth of ZnO directly in FTO (Figure 3.4 a)), creating large and poorly oriented ZnO nanorods that become smaller (Figure 3.4 b)), and well distributed on all the substrate surface (Figure 3.4 c) and d)), which is in accordance with the type of substrate topography where the ZnO is growing.

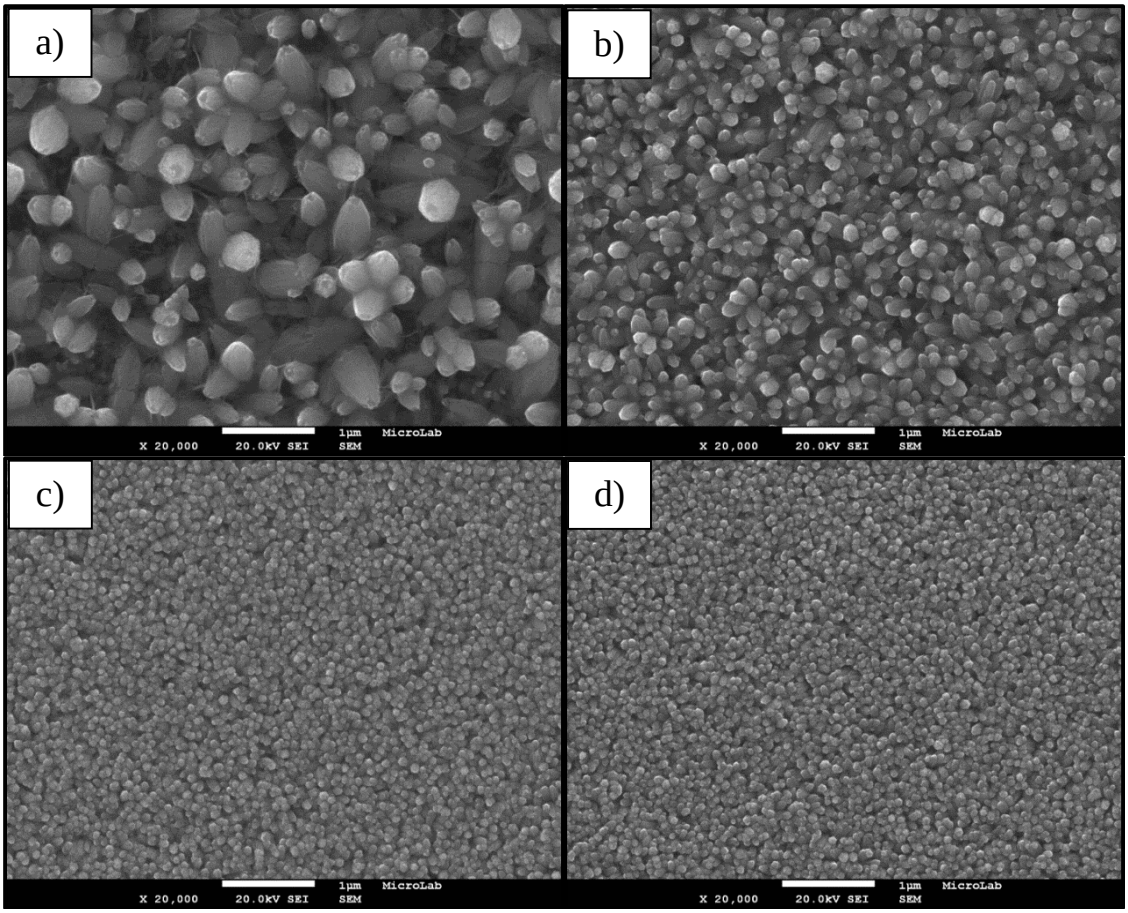

*Figure 3.4 - Representative SEM micrographs of **a)** FTO, **b)** FTO/ZnO_SL, **c)** FTO/TiO_2, and **d)** FTO/TiO_2/ZnO_SL substrates after three cycles of cyclic voltammetry in a solution containing 10 mM $Zn(NO_3)_2$ and 5 mM KCl at 70 ºC.*

3.3. Growth modulation by substrate conditioning

Figure 3.5 shows the representative SEM micrographs of electrodeposited ZnO nanorods on pristine and modified FTO substrates. These samples were prepared by applying a potentiostatic square wave for 60 min, where each cycle consisted of 0.25 s at -1.0 V *vs* Ref. and 1 s at 0.0 V (pulse profile C). The inclusion of a ZnO seed-layer on the FTO increases the number of nanorods per unit area, with reduced average diameter, compared to those grown directly on FTO (Figure 3.5 a) and b)). When a TiO_2 intermediate layer is formed over the FTO substrate, not only this effect is enhanced, but so is the vertical alignment of the nanorods (Figure 3.5 c) and d)). Using a modified FTO/TiO_2/ZnO_SL substrate reduces the average nanorod diameter by half (*ca.* 80 nm to 40 nm) and increases nanorod density by about 7 times (*ca.* 25 to 165 μm^{-2}) when compared to the unmodified FTO substrate.

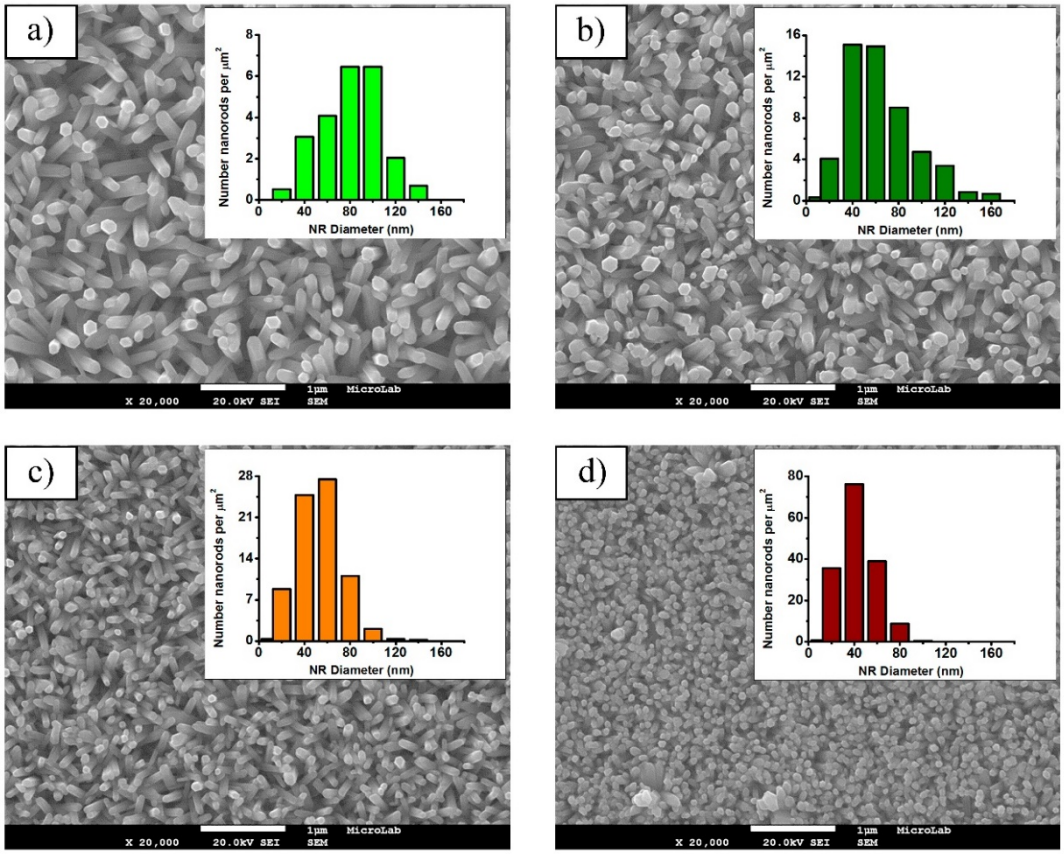

Figure 3.5 - Representative SEM micrographs of electrodeposited ZnO nanorods (pulse profile C for 60 min.) on ***a)*** *FTO,* ***b)*** *FTO/ZnO_SL,* ***c)*** *FTO/TiO_2, and* ***d)*** *FTO/TiO_2/ZnO_SL substrates. Inset: Histograms of the estimated number of nanorods per area as a function of the diameter.*

The resulting current transients from the pulsed potentiostatic deposition for all the studied conditions tended to similar shapes towards the end of the deposition (Figure 3.6). For samples where deposition occurred onto modified FTO substrates, the shapes always showed capacitive anodic and cathodic current spikes with subsequent exponential decays. This can be because of intra-bandgap states in TiO_2 and ZnO acting as electron traps [32,33]. Initially, this is not observed for deposition directly on FTO but becomes evident as ZnO material is deposited. Towards the end of the deposition, the transients show that the faradaic cathodic charge passed increased in the following order: FTO < FTO/ZnO_SL < FTO/TiO_2 < FTO/TiO_2/ZnO_SL. This increment suggests that more material is deposited in this order. This is supported by the top view and cross-sectional SEM micrographs (Figure 3.5 and

Figure 3.7, respectively), where it is shown a higher nanorod density and more closely packed and narrowed nanorods, respectively. However, a more significant charge does not result in longer nanorods. On the contrary, the thickness of the nanorods tends to decrease from ca. 800 nm for FTO/ZnO NRs layers to ca. 600 nm for FTO/TiO_2/ZnO_SL/ZnO NRs layers (Figure 3.7).

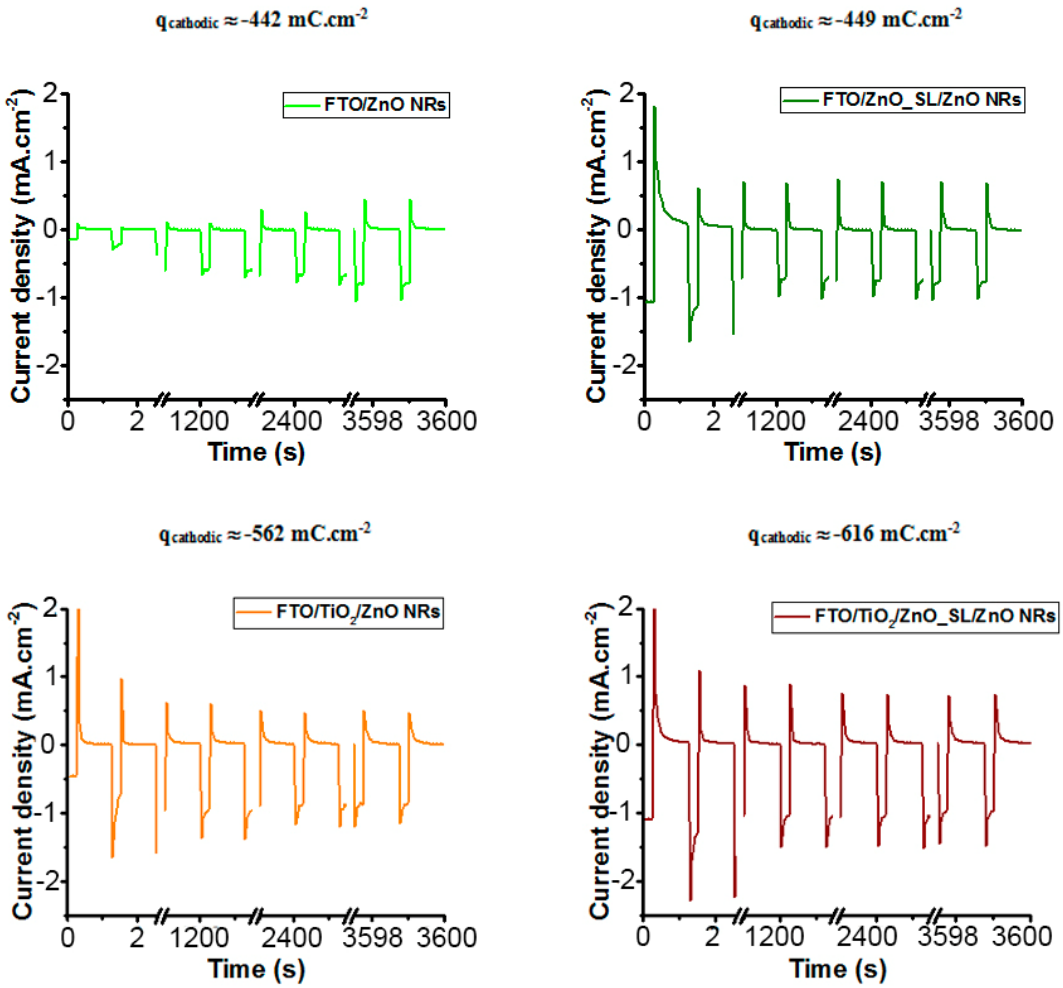

Figure 3.6 - Pulsed potentiostatic transients obtained during electrodeposition of ZnO nanorods.

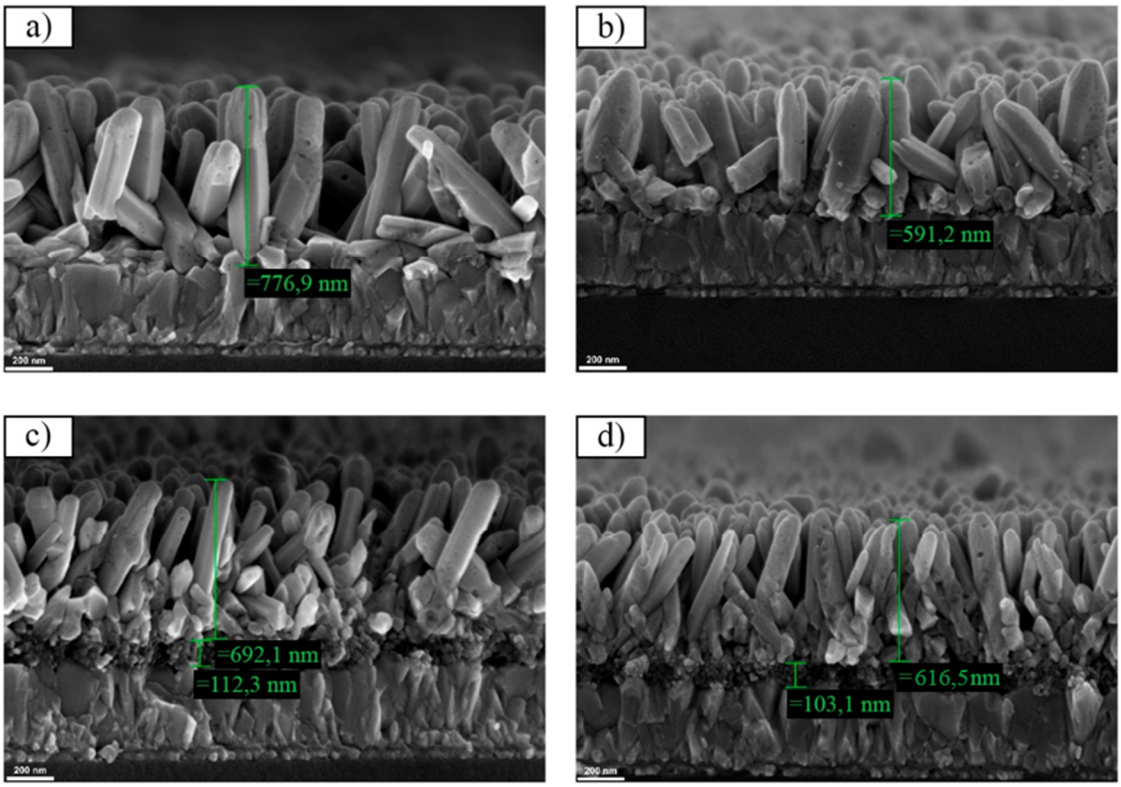

*Figure 3.7 - Representative SEM cross-section micrographs of electrodeposited ZnO nanorods grown on **a)** FTO, **b)** FTO/ZnO_SL, **c)** FTO/TiO_2, and **d)** FTO/TiO_2/ZnO_SL substrates. The layer thickness for spin-coated TiO_2 was estimated at ~100 nm, and the underlying FTO was estimated at ~300 nm.*

The X-ray diffraction (XRD) patterns presented in Figure 3.8 for all the ZnO films studied are in line with the hexagonal wurtzite crystalline structure (space group $P6_3mc$) for ZnO (JCPDS Card No. 36-1451). The relative texture coefficients (RTC) for the electrodeposited ZnO nanorods were calculated and presented in Table 3.1, establishing that the (002) plan is the preferential orientation. The RTC_{002} increases in the following order: FTO/ZnO NRs < FTO/TiO_2/ZnO NRs < FTO/ZnO_SL/ZnO NRs < FTO/TiO_2/ZnO_SL/ZnO NRs, reaching almost 100 % for the last one. These results agree with what was observed in the SEM micrographs, suggesting a more ordered ZnO nanorod growth. In addition, the TiO_2 crystalline structure was not possible to detect due to its low thickness.

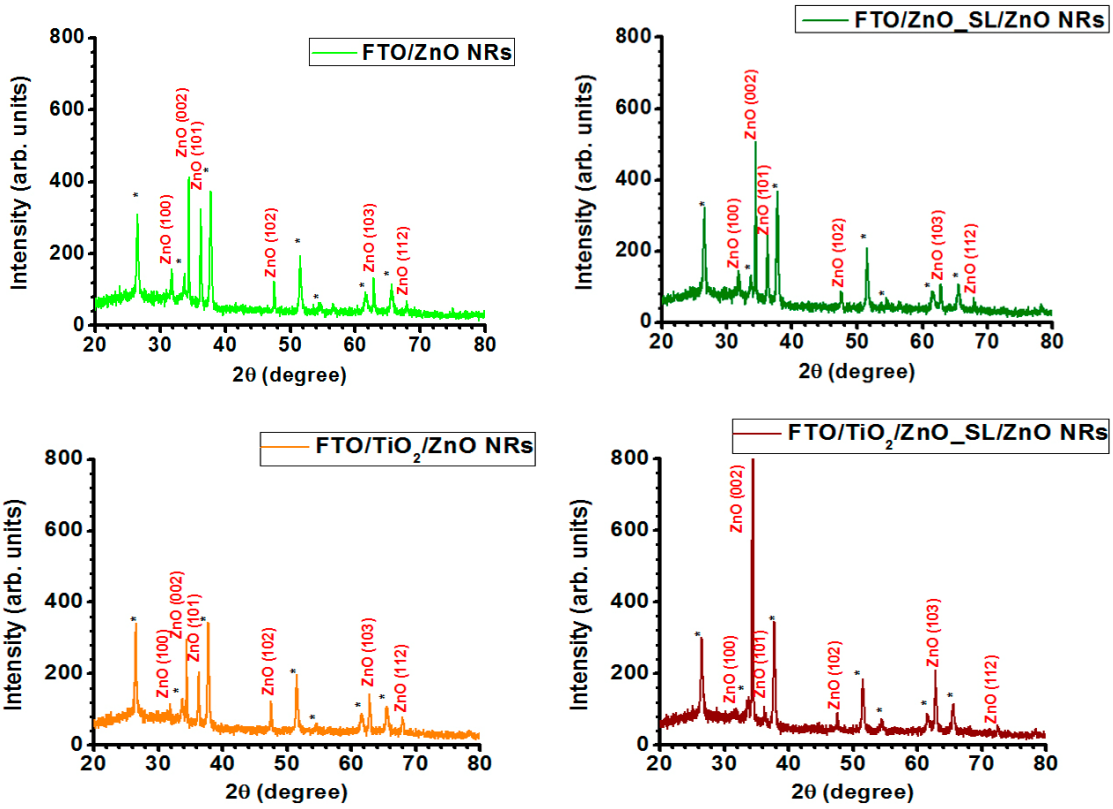

*Figure 3.8 - XRD patterns obtained from electrodeposited ZnO nanorods grown on pristine and modified FTO substrates. *corresponds to the FTO diffraction pattern.*

Table 3.1 - Relative texture coefficient (RTC_{hkl}) of pulsed electrodeposited ZnO nanorods growth on FTO and modified surface substrates.

Sample	**RTC_{100} (%)**	**RTC_{002} (%)**	**RTC_{101} (%)**
FTO/ZnO NRs	8.6	69.9	21.5
FTO/ZnO_SL/ZnO NRs	7.6	78.4	14.0
FTO/TiO_2/ZnO NRs	5.0	76.5	18.5
FTO/TiO_2/ZnO_SL/ZnO NRs	1.0	98.5	0.5

To assess the crystalline quality of the samples, Raman spectroscopy was performed. For the ZnO crystalline structure, group theory predicts (for the Γ point of the Brillouin zone) the following optical phonons: $A_1 + E_1 + 2B_1 + 2E_2$. The B_1 modes are silent, while A_1 and E_1 are polar modes and split into transverse (TO) and longitudinal (LO) optical vibration [34]. Therefore, six active Raman modes are expected.

Figure 3.9 shows the Raman spectra of the ZnO nanorods grown on FTO and FTO/TiO_2/ZnO_SL templates. For comparison, the spectra of glass, FTO and FTO/TiO_2 are also shown. The Raman spectrum of the glass is responsible for the background observed in all spectra. According to the literature [35], the FTO spectrum exhibits two main broad resonances at 561 and 630 cm^{-1} (identified in red in the figure). The typical vibrational modes of TiO_2 in the anatase crystalline phase [36] were identified for the FTO/TiO_2 template (in blue in the figure). For the ZnO nanorods, the expected vibrational frequencies for the hexagonal wurtzite ZnO structure [37] are clearly seen (identified in black) and are indicated in Table 3.2. For the ZnO nanorods grown on the FTO/TiO_2/ZnO_SL substrate, the vibrational modes for TiO_2 were also observed.

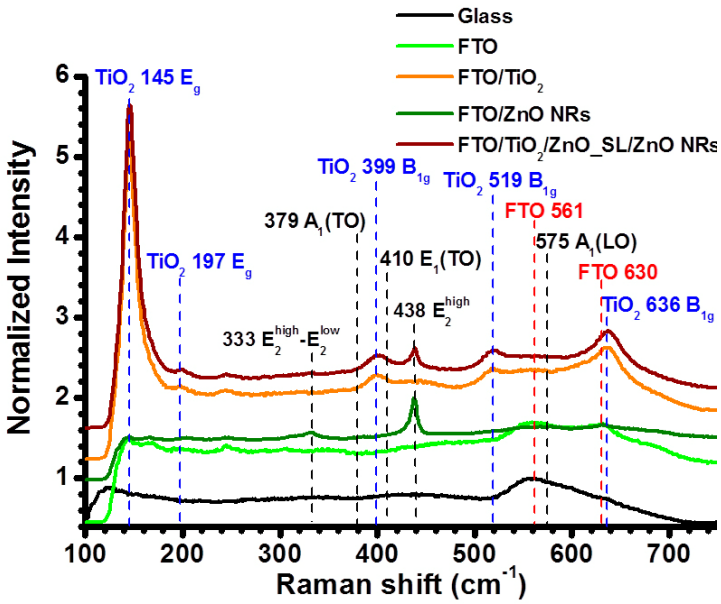

Figure 3.9 - Raman spectra of the studied samples using a 442 nm wavelength laser as the excitation source. The spectra were obtained in backscattering geometry. ZnO vibrational modes were identified in black, FTO substrate in red, and TiO_2 in blue.

Table 3.2 - Vibrational frequencies recorded in this work for ZnO and from Ref. [37]*, as well as their symmetry.*

Frequency (cm^{-1})		
This work	**Ref.** [37]	**Symmetry**
333	333	$E_2^{high} - E_2^{low}$
379	378	$A_1(TO)$
410	410	$E_1(TO)$
438	438	E_2^{high}
575	574	$A_1(LO)$

3.4. Evaluation of ZnO nanorods properties

The optical and photoelectrochemical properties of the ZnO nanorods were analysed by absorption spectroscopy, photoluminescence, and linear photovoltammetry.

The optical bandgap of each studied sample was obtained from Tauc plots shown in Figure 3.10, which follows the sequence of FTO/ZnO NRs, FTO/ZnO_SL/ZnO NRs, FTO/TiO_2/ZnO NRs, and FTO/TiO_2/ZnO_SL/ZnO NRs. This increase may be explained by observing that the films respectively present an increasing nanorod number, *i.e.* there is a more significant fraction of absorbing material per unit of volume. The samples exhibit an absorption onset near 3.2 eV with a steeper gradient for higher energies. The bandgap energy for ZnO nanorods grown directly on FTO or seed-layer coated FTO is 3.26 and 3.27 eV, respectively. For ZnO nanorods grown on TiO_2 coated FTO substrates or subsequently coated with a ZnO seed-layer, the bandgap energy is 3.27 and 3.28 eV, respectively. In both cases, the estimated values agree with the reported 3.3 eV direct bandgap of ZnO at RT [38].

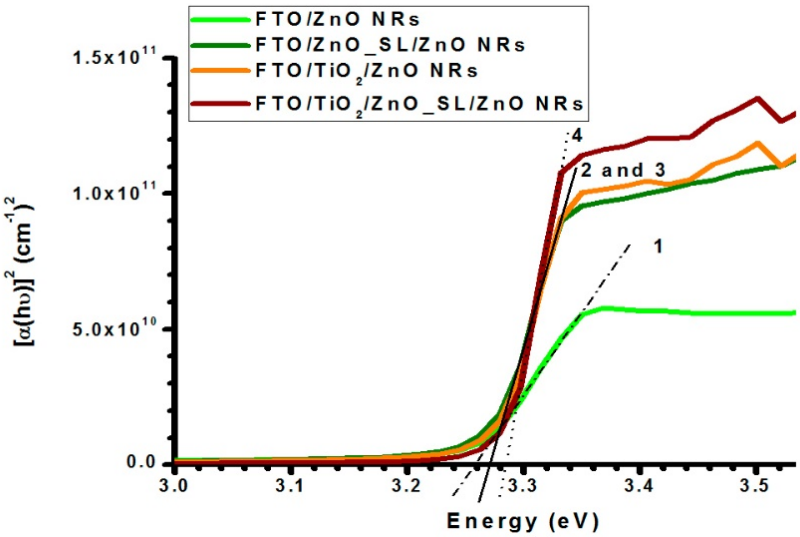

Figure 3.10 - Tauc plots for electrodeposited ZnO nanorods grown on FTO and modified surface substrates. The line numbered (1) (2) (3) and (4) are the extrapolation lines for FTO/ZnO NRs, FTO/ZnO_SL/ZnO NRs, FTO/TiO_2/ZnO NRs, and FTO/TiO_2/ZnO_SL/ZnO NRs, respectively.

Figure 3.11 depicts the normalized RT photoluminescence (PL) results obtained for the ZnO nanorods grown on FTO and FTO/TiO_2/ZnO_SL substrates. For comparison, the PL spectra of glass, FTO and FTO/TiO_2 are also shown. The PL spectra of FTO and FTO/TiO_2 reveal that the main emission coming from the substrate is responsible for wide unstructured broad bands in the ultraviolet, yellow, and red spectral regions observed in all the sample's spectra. The features in the spectra of the ZnO nanorods grown on the distinct templates are evidence of optically active defects covering a wide spectra range. The emission peaked at ~3.28 eV (Figure 3.11 b)), which is an almost mirror image of the absorption, corresponds to the near band edge emission (NBE) of ZnO, typically associated with free exciton recombination and their longitudinal optical phonons (LO) replicas [38–40]. However, when we refer to nanostructured ZnO samples, surface defects could also influence the ultraviolet emission's peak position and spectral shape [41]. Besides this high energy transition, broad emission bands in the green, orange, and red regions were identified in the analysed samples. The main intensity peak was found to occur at ~1.8 eV (red emission peak), with a high energy shoulder in the green region ~2.5 eV for FTO/ZnO NRs samples. The measured broad luminescence bands in the ZnO nanostructures match those currently reported for bulk, thin

films and ZnO nanomaterials [38–40,42–44]. The chemical nature of the defects from where the green and red luminescence occurs has generated controversy in the literature. The most common explanation is that these PL bands are due to intrinsic defects. However, in the case of nanostructures, some of the broad emission bands have also been associated with the presence of surface-related defects. Pimentel et al. [45] reported the presence of such defects when evaluating the effect of solvent used in ZnO nanorod synthesis. This work observed that the yellow/red emission intensity was strongly sensitive to the laser irradiation time, suggesting that surface-mediated processes could be at the origin of the recombination process of the broad visible band.

The intensity ratio of the NBE/deep level recombination is generally used to measure sample optical quality. Despite the ZnO nanorods grown on FTO exhibiting a relative increase of the green emission, when compared with those grown on FTO/TiO_2/ZnO_SL templates, the intensity ratio of the NBE/deep level recombination is higher for the FTO/ZnO NRs, meaning that higher optical quality is reached for the nanostructures. The Raman results (Figure 3.9) reinforce this affirmation, where the ZnO vibrational modes are more intense for FTO/ZnO NRs samples than FTO/TiO_2/ZnO_SL/ZnO NRs. Focusing on FTO/TiO_2/ZnO_SL/ZnO NR samples, besides the contribution of the FTO substrate, an additional contribution of the anatase defects luminescence from the yellow band cannot be discarded, as TiO_2 is known to emit in this spectral region [46,47].

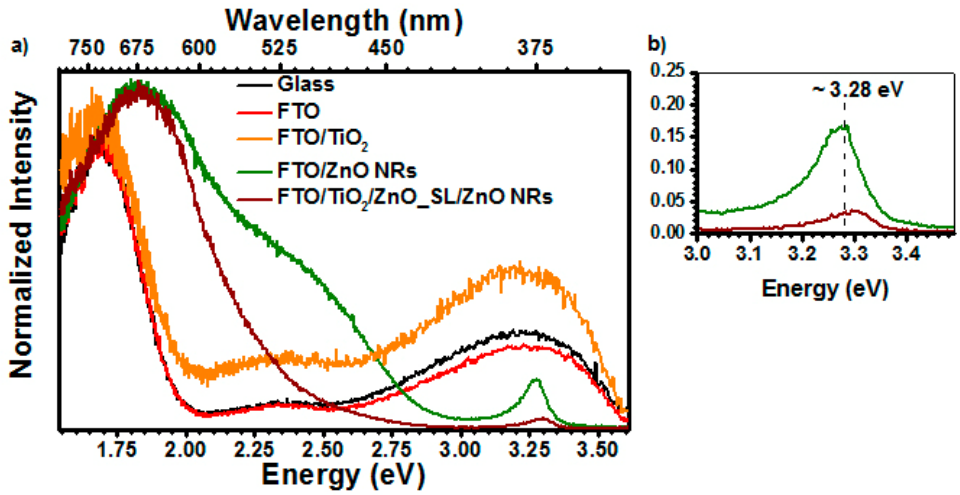

*Figure 3.11 - **a)** Normalized RT photoluminescence spectra of the studied samples with 325 nm wavelength excitation; **b)** detail of the emission in the UV region.*

The linear photovoltammograms shown in Figure 3.12 for FTO modified substrates in the absence and presence of ZnO nanorods are in agreement with those expected for nanocrystalline and single-crystal n-type electrodes under reverse bias [48]. In addition, no dark current flow is visible, except for potentials greater than -0.7 V (vs Ag/AgCl). This increment is attributed to the oxidation reaction of SO_3^{2-} species, equation 3.3:

$$SO_3^{2-} + 2OH^- \rightarrow SO_4^{2-} + H_2O + 2e^- \quad (3.3)$$

Under illumination, three broad regions can be distinguished. The first region refers to significantly negative potentials, where the photocurrent density is zero, implying no driving force for efficient electron-hole separation. The second region is related to intermediate potentials, where an increase in photocurrent is detected, suggesting that the driving force for charge separation depends on the applied bias. Finally, the third region is located at a more positive bias, where a photocurrent plateau is usually observed, meaning that the driving force is independent of applied bias.

Along with the morphological information of the film, the driving force for electron and hole flow is most likely a mixture of concentration gradient induced diffusion and electric field-induced drift. Firstly, the photoactivity of the films composed by a thin ZnO seed layer

or TiO_2 intermediate layer is comparable to those constituted by ZnO nanorods. Secondly, films not employing a TiO_2 intermediate layer demonstrate higher photocurrent densities. This seems to be against what is expected for films with a more desirable ZnO nanorod morphology (Figure 3.5). Thirdly, the films employing a TiO_2 intermediate layer demonstrate onset currents at more negative bias. There can be two reasons for this: 1) could be due to the relative position of the band edges of the layers, with the TiO_2 layer being the more negative of the materials in question [49–51]; 2) assuming that the driving force required for efficient charge separation is higher in the ZnO layers than in the TiO_2 layers [52].

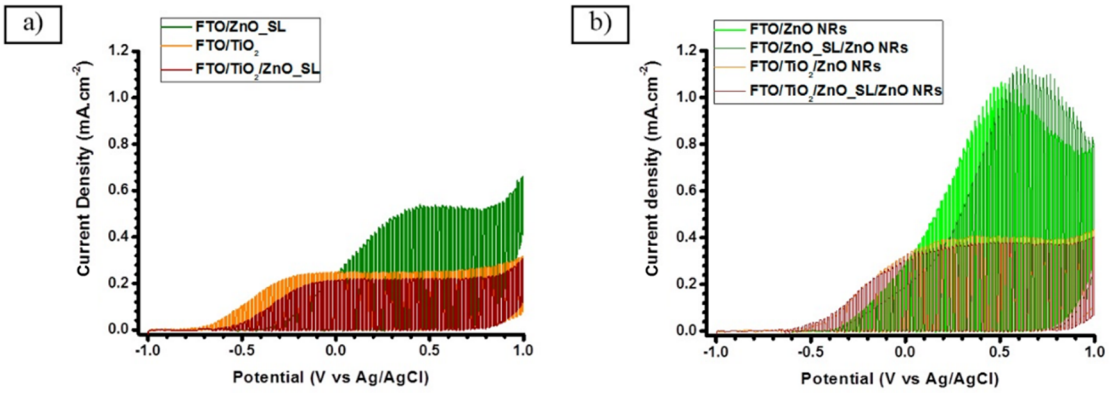

*Figure 3.12 - j-V curves of modified surface substrates **a)** and the corresponding pulsed electrodeposited ZnO nanorods **b)**, recorded in 50 mM Na_2SO_3 aqueous solution (pH ~ 9.5) under chopped illumination at 0.1 Hz. Scan rate of 2 $mV.s^{-1}$.*

Although the films employing ZnO, as a seed layer or nanorod layer without TiO_2 interlayer, generate higher photocurrent densities, they appear to be unstable, showing a peak in the photocurrent density with a subsequent decrease. To better understand the stability of the films, photocurrent transients were recorded by holding the potential at 0.4 V (vs Ag/AgCl), shown in Figure 3.13.

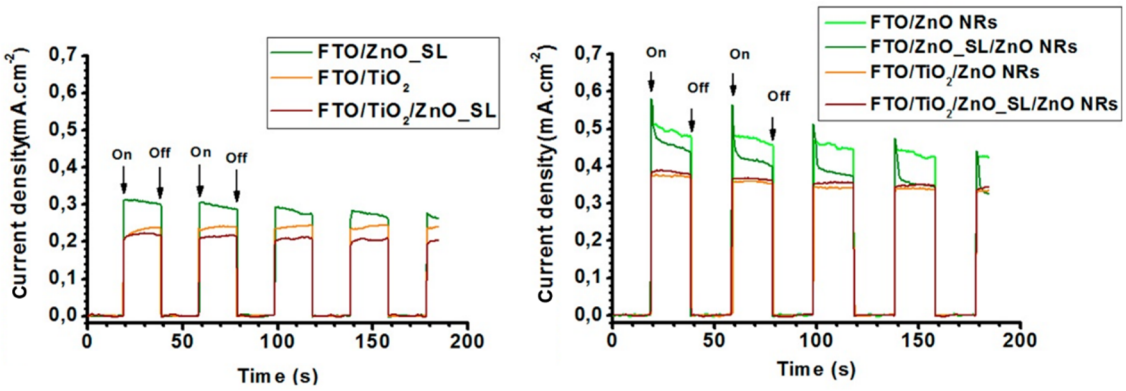

Figure 3.13 - Photocurrent transients of FTO modified surface substrates and the corresponding pulsed electrodeposited ZnO nanorods, obtained in 50 mM Na_2SO_3 aqueous solution (pH ~ 9.5) under chopped illumination at 0.025 Hz frequency, at 0.4 V vs Ag/AgCl applied potential.

The films employing a TiO_2 intermediate layer have a far squarer like and reproducible photocurrent transient. However, a decay in the photocurrent intensity is still observed for all the films employing both TiO_2 and ZnO layers. The decrease in photoactivity may be attributed to the photo-dissolution of ZnO [53–55]. A proposed mechanism is that the residual photogenerated holes on ZnO surfaces attack the Zn—O bonds and dissociate Zn^{2+} from ZnO surface [56], equations 3.4-3.6:

$$ZnO_{(s)} + hv \rightarrow ZnO_{(s)} + h^+ + e^- \quad (3.4)$$

$$h^+ + e^- \rightarrow hv \text{ or } \Delta \qquad \text{recombination} \quad (3.5)$$

$$ZnO_{(s)} + 2h^+ \rightarrow Zn^{2+}_{(aq.)} + \frac{1}{2}O_2 \qquad \text{ZnO photo-dissolution} \quad (3.6)$$

where $ZnO_{(s)}$ is a solid ZnO film, hv is a photon absorbed by the ZnO, h^+ and e^- are the photo-generated hole and electron carriers on the ZnO film surface, and $Zn^{2+}_{(aq.)}$ are Zn^{2+} ions in an aqueous solution.

Three reasons are proposed to explain why films employing the TiO_2 intermediate layer seem to be more chemically stable with time and under illumination.

The first one may be due to the crystalline structure of the ZnO. Films with a TiO_2 intermediate layer have a higher RTC_{002} and suppressed some of the green intra-bandgap defect states that can act as hole traps catalysing ZnO photo-dissolution.

The second reason may be due to the band alignment of the individual layers. For example, if the TiO_2 bands are more negative than the ZnO bands, then photogenerated electrons in the ZnO layer would be unable to be collected and contribute to the photocurrent because of the barrier created by the more negative conduction band edge of the TiO_2 layer. In essence, photogenerated electron-hole pairs in the ZnO layer would recombine, preventing the holes from participating in the photodissolution of the ZnO.

The third possible reason may be related to the light absorption process. The lamp's spectrum used for the illumination has an effective irradiance up to ~5 eV (down to ~250 nm). At these energies, the photon penetration depth is approximately 50 to 100 nm, which is in the order of the thickness of the TiO_2 intermediate and ZnO seed layers. Since the illumination was through the substrate side, films employing a TiO_2 intermediate layer have a portion of the absorbable (UV) photons absorbed in the TiO_2 layer and not subsequently by the ZnO. Furthermore, the subsequent layers deposited on the TiO_2 should allow direct contact between the electrolyte and the TiO_2 layer, promoting hole collection at the electrolyte interface and hence the photocurrent generation, without the harmful effects of the presence of holes at the ZnO surface.

The films employing the ZnO layers without the TiO_2 intermediate layer showed greater photocurrent densities due to more efficient electron-hole pair separation. Since there is no TiO_2 layer depriving the ZnO of absorbable photons, the consequence is an electron-hole generation that occurs within the ZnO. In addition, the observed morphologies of the ZnO seed and nanorod layers (Figure 3.2 and Figure 3.5) suggest a greater surface|electrolyte interface area, where minority carrier collection occurs. Also, minority carrier diffusion lengths in anatase TiO_2 are normally reported to be significantly smaller than ZnO [57,58]. Therefore, a more significant fraction of electron-hole pair generation may occur in regions whose distance is smaller than the minority carrier diffusion length, resulting in higher internal quantum efficiencies and hence greater photocurrent densities.

Figure 3.14 shows the photovoltage transients of the ZnO nanorods grown on FTO modified substrates, which exhibit a behaviour expected for n-type semiconductors, with a negative photopotential occurring upon illumination. The measured photopotential indicates

conduction band edge energy, whereby equilibrium is reached when the Fermi level resides close to the conduction band edge. However, considering that the recombination kinetics are not slow, a smaller shift in photopotential occurs. In general, a ~300 mV difference in the potential obtained for films employing a TiO_2 compared to those that do not is observed. These results are in line with the observed photocurrent onset potential shift, suggesting that either the band edges are more negative or electron-hole pair recombination is less pronounced in films employing a TiO_2 intermediate layer.

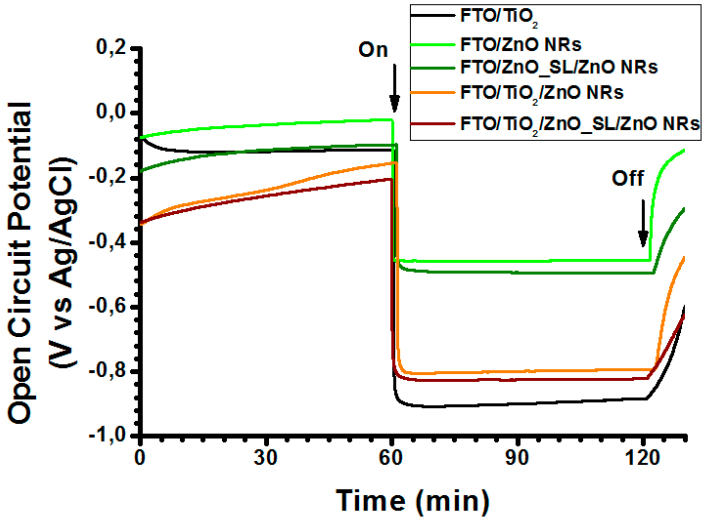

Figure 3.14 - E_{oc} transients of TiO_2-coated FTO substrate and ZnO nanorods grown on pristine and modified FTO substrates.

3.5. Chapter Summary

The results demonstrate that ZnO nanorods were successfully prepared by pulsed electrodeposition, and the modification of the surface substrate affects the ZnO nanorod characteristics.

From the voltammetric studies, it can be concluded that ZnO grains were formed during the potential negative sweep, at which the reduction of NO_3^- occurs, and SEM micrographs confirmed that their dimensions depend on the modified substrate used.

SEM images and XRD results revealed misoriented vertically aligned ZnO nanorods with improved orientation when a TiO_2 intermediate layer was applied as a template. These also demonstrated a decrease in nanorod diameter and an increase in the number of nanorods per unit area. Raman results confirmed the hexagonal wurtzite structure of the ZnO nanorods. Additionally, for samples containing TiO_2, the vibrational modes on the anatase structure were identified.

The RT PL analyses reveal the presence of the near band edge recombination and deep level emission in both FTO/ZnO NR and FTO/TiO_2/ZnO_SL/ZnO NR samples. The intensity ratio of the near band edge emission/deep level emission is higher in the FTO/ZnO NR samples, indicating higher optical properties of these samples. It should be emphasized that the green emission is almost suppressed in samples with TiO_2 intermediate layer. The optical bandgap, estimated from the absorption spectra, is 3.27 eV. This value is in line with the reported values in ZnO literature.

Photoelectrochemical measurements confirmed the n-type photoactivity behaviour of the films. However, they all demonstrated instability (at different degrees) under illumination, likely due to photo-dissolution.

For application in solar cells, the morphology of the films is encouraging as an n-type selective contact with a high surface area and oriented structure.

3.6. References

[1] P. Yang, H. Yan, S. Mao, R. Russo, J. Johnson, R. Saykally, N. Morris, J. Pham, R. He, H.-J. Choi, Controlled Growth of ZnO Nanowires and Their Optical Properties, Adv. Funct. Mater. 12 (2002) 323–331. doi:10.1002/1616-3028(20020517)12:5<323::AID-ADFM323>3.0.CO;2-G.

[2] Xia, J. B., Zhang, X. W., Electronic structure of ZnO wurtzite quantum wires, Eur. Phys. J. B. 49 (2006) 415–420. doi:10.1140/epjb/e2006-00093-1.

[3] S. Baruah, J. Dutta, Hydrothermal growth of ZnO nanostructures, Sci. Technol. Adv. Mater. 10 (2009) 013001. doi:10.1088/1468-6996/10/1/013001.

[4] C. Levy-Clement, R. Tena-Zaera, M.A. Ryan, A. Katty, G. Hodes, CdSe-Sensitized p-CuSCN/nanowire n-ZnO heterojunctions, Adv. Mater. 17 (2005) 1512–1515. doi:10.1002/adma.200401848.

[5] C. V. Manzano, D. Alegre, O. Caballero-Calero, B. Alén, M.S. Martín-González, Synthesis and luminescence properties of electrodeposited ZnO films, J. Appl. Phys. 110 (2011) 043538. doi:10.1063/1.3622627.

[6] S. Eisermann, A. Kronenberger, M. Dietrich, S. Petznick, A. Laufer, A. Polity, B.K. Meyer, Hydrogen and nitrogen incorporation in ZnO thin films grown by radio-frequency (RF) sputtering, Thin Solid Films. 518 (2009) 1099–1102. doi:10.1016/J.TSF.2009.05.050.

[7] K.-S. Kim, H.W. Kim, Synthesis of ZnO nanorod on bare Si substrate using metal organic chemical vapor deposition, Phys. B Condens. Matter. 328 (2003) 368–371. doi:10.1016/S0921-4526(02)01954-3.

[8] J.-M. Huang, C.-S. Ku, H.-Y. Lee, C.-M. Lin, S.-Y. Chen, Growth of high-quality epitaxial ZnO films on (10–10) sapphire by atomic layer deposition with flow-rate interruption method, Surf. Coatings Technol. 231 (2013) 323–327. doi:10.1016/J.SURFCOAT.2012.05.067.

[9] A. Rivera, J. Zeller, A. Sood, M. Anwar, A Comparison of ZnO Nanowires and Nanorods Grown Using MOCVD and Hydrothermal Processes, J. Electron. Mater. 42 (2013) 894–900. doi:10.1007/s11664-012-2444-4.

[10] L. Znaidi, Sol–gel-deposited ZnO thin films: A review, Mater. Sci. Eng. B. 174 (2010)

18–30. doi:10.1016/J.MSEB.2010.07.001.

[11] V. Kumar, N. Singh, R.M. Mehra, A. Kapoor, L.P. Purohit, H.C. Swart, Role of film thickness on the properties of ZnO thin films grown by sol-gel method, Thin Solid Films. 539 (2013) 161–165. doi:10.1016/J.TSF.2013.05.088.

[12] P. Nunes, B. Fernandes, E. Fortunato, P. Vilarinho, R. Martins, Performances presented by zinc oxide thin films deposited by spray pyrolysis, Thin Solid Films. 337 (1999) 176–179. doi:10.1016/S0040-6090(98)01394-7.

[13] B.N. Illy, A.C. Cruickshank, S. Schumann, R. Da Campo, T.S. Jones, S. Heutz, M.A. McLachlan, D.W. McComb, D.J. Riley, M.P. Ryan, Electrodeposition of ZnO layers for photovoltaic applications: controlling film thickness and orientation, J. Mater. Chem. 21 (2011) 12949–12957. doi:10.1039/C1JM11225B.

[14] T. Pauporté, E. Jouanno, F. Pellé, B. Viana, P. Aschehoug, Key Growth Parameters for the Electrodeposition of ZnO Films with an Intense UV-Light Emission at Room Temperature, J. Phys. Chem. C. 113 (2009) 10422–10431. doi:10.1021/jp9010179.

[15] C. Dunkel, F. Lüttich, H. Graaf, T. Oekermann, M. Wark, Investigation of the pulsed electrochemical deposition of ZnO, Electrochim. Acta. 80 (2012) 60–67. doi:10.1016/J.ELECTACTA.2012.06.113.

[16] S. Peulon, D. Lincot, Cathodic electrodeposition from aqueous solution of dense or open-structured zinc oxide films, Adv. Mater. 8 (1996) 166–170. doi:10.1002/adma.19960080216.

[17] M. Izaki, T. Omi, Characterization of Transparent Zinc Oxide Films Prepared by Electrochemical Reaction, J. Electrochem. Soc. 144 (1997) 1949–1952. doi:doi: 10.1149/1.1837727.

[18] M.R. Khajavi, D.J. Blackwood, G. Cabanero, R. Tena-Zaera, New insight into growth mechanism of ZnO nanowires electrodeposited from nitrate-based solutions, Electrochim. Acta. 69 (2012) 181–189. doi:10.1016/J.ELECTACTA.2012.02.096.

[19] R. Tena-Zaera, J. Elias, G. Wang, C. Lévy-Clément, Role of Chloride Ions on Electrochemical Deposition of ZnO Nanowire Arrays from O2 Reduction, J. Phys. Chem. C. 111 (2007) 16706–16711. doi:10.1021/jp073985g.

[20] D. Siopa, A. Gomes, Nucleation and Growth of ZnO Nanorod Arrays onto Flexible

Substrates, J. Electrochem. Soc. 160 (2013) D476–D484. doi:doi: 10.1149/2.088310jes.

[21] K. Nomura, N. Shibata, M. Maeda, Orientation control of zinc oxide films by pulsed current electrolysis, J. Cryst. Growth. 235 (2002) 224–228. doi:10.1016/S0022-0248(01)01773-0.

[22] N.P. Klochko, G.S. Khrypunov, Y.O. Myagchenko, E.E. Melnychuk, V.R. Kopach, E.S. Klepikova, V.M. Lyubov, A. V Kopach, Controlled Growth of one-dimensional zinc oxide nanostructures in the pulsed electrodeposition mode, Semiconductors. 46 (2012) 825–831. doi:10.1134/S1063782612060127.

[23] M. Wadowska, T. Frade, D. Siopa, K. Lobato, A. Gomes, ZnO nanostructured films electrodeposited at room temperature, ECS Electrochem. Lett. 2 (2013) D40–D42. doi:10.1149/2.009307eel.

[24] J. Elias, R. Tena-Zaera, C. Levy-Clement, Effect of the chemical nature of the anions on the electrodeposition of ZnO nanowire arrays, J. Phys. Chem. C. 112 (2008) 5736–5741. doi:10.1021/jp7120092.

[25] T. Pauporte, D. Lincot, Hydrogen peroxide oxygen precursor for zinc oxide electrodeposition I. Deposition in perchlorate medium, J. Electrochem. Soc. 148 (2001) C310–C314.

[26] J. Elias, R. Tena-Zaera, C. Lévy-Clément, Electrodeposition of ZnO nanowires with controlled dimensions for photovoltaic applications: Role of buffer layer, Thin Solid Films. 515 (2007) 8553–8557. doi:10.1016/J.TSF.2007.04.027.

[27] J. Lang, X. Li, J. Yang, Q. Han, Y. Yan, M. Gao, D. Wang, L. Yang, X. Liu, R. Wang, S. Yang, The effect of ZnO buffer layer on structural and optical properties of ZnO nanorods, Cryst. Res. Technol. 46 (2011) 691–696. doi:10.1002/crat.201100024.

[28] S. Sanchez, R. Salazar, C. Levy-Clement, V. Ivanova, ZnO Buffer Layers and Nanowires Electrodeposition for Extremely Thin Absorber Solar Cells, ECS Trans. 33 (2011) 183–190. doi:10.1149/1.3553360.

[29] T. Frade, M.E.M. Jorge, B. Fernandez, R. Pereiro, A. Gomes, A Possible Growth Mechanism for ZnO-TiO2 Composite Nanostructured Films Prepared by Electrodeposition, J. Electrochem. Soc. 161 (2014) D125–D133.

doi:10.1149/2.102403jes.

[30] A.-F. Kanta, A. Schrijnemakers, A. Decroly, Electrochemical characterisations of ZnO nanowires for dye-sensitised solar cells, Mater. Des. 95 (2016) 481–485. doi:10.1016/j.matdes.2016.01.069.

[31] T. Frade, K. Lobato, J.F.C. Carreira, J. Rodrigues, T. Monteiro, A. Gomes, TiO2 anatase intermediary layer acting as template for ZnO pulsed electrodeposition, Mater. Des. 110 (2016) 18–26. doi:10.1016/j.matdes.2016.07.122.

[32] S. Kohtani, A. Kawashima, H. Miyabe, Reactivity of Trapped and Accumulated Electrons in Titanium Dioxide Photocatalysis, Catal. . 7 (2017). doi:10.3390/catal7100303.

[33] F. Caballero-Briones, J.A. Barón-Miranda, C. Guarneros-Aguilar, O. Calzadilla, F. Sanz, Influence of pulse frequency on the morphology, structure and optical properties of ZnO films prepared by pulsed electrodeposition, Mater. Res. Express. 6 (2019) 86464. doi:10.1088/2053-1591/ab2554.

[34] C.A. Arguello, D.L. Rousseau, S.P.S. Porto, First-Order Raman Effect in Wurtzite-Type Crystals, Phys. Rev. 181 (1969) 1351–1363. doi:10.1103/PhysRev.181.1351.

[35] M. Berruet, C.J. Pereyra, G.H. Mhlongo, M.S. Dhlamini, K.T. Hillie, M. Vázquez, R.E. Marotti, Optical and structural properties of nanostructured ZnO thin films deposited onto FTO/glass substrate by a solution-based technique, Opt. Mater. (Amst). 35 (2013) 2721–2727. doi:10.1016/J.OPTMAT.2013.08.018.

[36] W. Ma, Z. Lu, M. Zhang, Investigation of structural transformations in nanophase titanium dioxide by Raman spectroscopy, Appl. Phys. A. 66 (1998) 621–627. doi:10.1007/s003390050723.

[37] R. Cuscó, E. Alarcón-Lladó, J. Ibáñez, L. Artús, J. Jiménez, B. Wang, M.J. Callahan, Temperature dependence of Raman scattering in ZnO, Phys. Rev. B. 75 (2007) 165202–165211. doi:10.1103/PhysRevB.75.165202.

[38] U. Ozgur, Y.I. Alivov, C. Liu, A. Teke, M.A. Reshchikov, S. Dogan, V. Avrutin, S.J. Cho, H. Morkoc, A comprehensive review of ZnO materials and devices, J. Appl. Phys. 98 (2005) 041301 (1–103). doi:10.1063/1.1992666.

[39] B.K. Meyer, H. Alves, D.M. Hofmann, W. Kriegseis, D. Forster, F. Bertram, J.

Christen, A. Hoffmann, M. Straßburg, M. Dworzak, U. Haboeck, A. V Rodina, Bound exciton and donor–acceptor pair recombinations in ZnO, Phys. Status Solidi. 241 (2004) 231–260. doi:10.1002/pssb.200301962.

[40] T. Monteiro, A.J. Neves, M.C. Carmo, M.J. Soares, M. Peres, J. Wang, E. Alves, E. Rita, U. Wahl, Near-band-edge slow luminescence in nominally undoped bulk ZnO, J. Appl. Phys. 98 (2005) 013502 (1–6). doi:10.1063/1.1946200.

[41] A.B. Djurišić, Y.H. Leung, Optical Properties of ZnO Nanostructures, Small. 2 (2006) 944–961. doi:10.1002/smll.200600134.

[42] M. Peres, S. Magalhães, M.R. Soares, M.J. Soares, L. Rino, E. Alves, K. Lorenz, M.R. Correia, A.C. Lourenço, T. Monteiro, Disorder induced violet/blue luminescence in rf-deposited ZnO films, Phys. Status Solidi C. 10 (2013) 662–666. doi:10.1002/pssc.201200873.

[43] J. Rodrigues, M. Peres, M.R.N. Soares, A.J.S. Fernandes, N. Ferreira, M. Ferro, A.J. Neves, T. Monteiro, F. Costa, ZnO Nano/Microstructures Grown by Laser Assisted Flow Deposition, J. Nano Res. 18 (2012) 129–137. doi:10.4028/www.scientific.net/JNanoR.18-19.129.

[44] M.A. Reshchikov, H. Morkoç, B. Nemeth, J. Nause, J. Xie, B. Hertog, A. Osinsky, Luminescence properties of defects in ZnO, Phys. B Condens. Matter. 401–402 (2007) 358–361. doi:10.1016/J.PHYSB.2007.08.187.

[45] A. Pimentel, J. Rodrigues, P. Duarte, D. Nunes, F.M. Costa, T. Monteiro, R. Martins, E. Fortunato, Effect of solvents on ZnO nanostructures synthesized by solvothermal method assisted by microwave radiation: a photocatalytic study, J. Mater. Sci. 50 (2015) 5777–5787. doi:10.1007/s10853-015-9125-7.

[46] H. Tang, H. Berger, P.E. Schmid, F. Lévy, G. Burri, Photoluminescence in TiO2 anatase single crystals, Solid State Commun. 87 (1993) 847–850. doi:10.1016/0038-1098(93)90427-O.

[47] H. Tang, H. Berger, P.E. Schmid, F. Lévy, Optical properties of anatase (TiO2), Solid State Commun. 92 (1994) 267–271. doi:10.1016/0038-1098(94)90889-3.

[48] T. Berger, D. Monllor-Satoca, M. Jankulovska, T. Lana-Villarreal, R. Gómez, The Electrochemistry of Nanostructured Titanium Dioxide Electrodes, ChemPhysChem. 13

(2012) 2824–2875. doi:10.1002/cphc.201200073.

[49] J. Li, N. Wu, Semiconductor-based photocatalysts and photoelectrochemical cells for solar fuel generation: a review, Catal. Sci. Technol. 5 (2015) 1360–1384. doi:10.1039/C4CY00974F.

[50] V. Stevanović, S. Lany, D.S. Ginley, W. Tumas, A. Zunger, Assessing capability of semiconductors to split water using ionization potentials and electron affinities only, Phys. Chem. Chem. Phys. 16 (2014) 3706–3714. doi:10.1039/C3CP54589J.

[51] Y. Xu, M.A.A. Schoonen, The absolute energy positions of conduction and valence bands of selected semiconducting minerals, Am. Mineral. 85 (2000) 543–556. doi:10.2138/am-2000-0416.

[52] Radim Beranek, (Photo)electrochemical Methods for the Determination of the Band Edge Positions of TiO2-Based Nanomaterials, Adv. Phys. Chem. 2011 (2011) 786759 (20 pages). doi:https://doi.org/10.1155/2011/786759.

[53] P. Spathis, I. Poulios, The corrosion and photocorrosion of zinc and zinc oxide coatings, Corros. Sci. 37 (1995) 673–680. doi:10.1016/0010-938X(95)80001-8.

[54] B. Neppolian, H.. Choi, S. Sakthivel, B. Arabindoo, V. Murugesan, Solar/UV-induced photocatalytic degradation of three commercial textile dyes, J. Hazard. Mater. 89 (2002) 303–317. doi:10.1016/S0304-3894(01)00329-6.

[55] S. Lathasree, A.N. Rao, B. SivaSankar, V. Sadasivam, K. Rengaraj, Heterogeneous photocatalytic mineralisation of phenols in aqueous solutions, J. Mol. Catal. A Chem. 223 (2004) 101–105. doi:10.1016/J.MOLCATA.2003.08.032.

[56] J. Han, W. Qiu, W. Gao, Potential dissolution and photo-dissolution of ZnO thin films, J. Hazard. Mater. 178 (2010) 115–122. doi:10.1016/J.JHAZMAT.2010.01.050.

[57] L. Chernyak, E. Flitsiyan, M. Shatkhin, Z. Dashevsky, Studies of Electron Trapping in ZnO Semiconductor, ECS Trans. 28 (2010) 3–11. doi:10.1149/1.3377093.

[58] T. Luttrell, S. Halpegamage, J. Tao, A. Kramer, E. Sutter, M. Batzill, Why is anatase a better photocatalyst than rutile? - Model studies on epitaxial TiO2 films, Sci. Rep. 4 (2014) 4043. https://doi.org/10.1038/srep04043.

Chapter IV

Optoelectronic characterization of ZnO nanorod arrays obtained by pulsed electrodeposition

4.1. Introduction

The fields of application of ZnO depend on the physical properties, which are strongly affected by its morphological characteristics, such as shape, surface density, size and vertical alignment. As previously shown, ZnO nanorods are interesting to apply in solar cells due to their direct electron transport pathways and large surface/volume ratio [1,2]. Therefore, it is crucial to have a growth/synthesis process that provides control of the orientation, size, and surface density of the ZnO nanorods. In addition, deep knowledge of the defects will also be required since this is linked to the material's performance.

Electrodeposition of ZnO nanorods has been studied in the last decades by employing mostly constant current/potential in different solutions [3–7]. However, applying a constant current/potential has limitations, as was reported by Manzano *et al.* [8]. These authors synthesized ZnO films at a constant potential, using nitrate and peroxide solutions, and detected that some OH^- becomes trapped in the structure during the deposition [8]. Pulsed electrodeposition has the advantage of promoting nucleation and the formation of fine crystals [9].

Furthermore, it is possible to control the properties of ZnO films by choosing adequate pulse conditions, as these parameters can be regulated independently over a wide range. There are only two parameters in the continuous electrodeposition: applied potential/current density and deposition time. However, in pulsed electrodeposition, other parameters can be considered, such as pulse deposition time (t_{on}) and rest time (t_{off}), that defines the percentage of the total time of a cycle, the duty cycle, and the frequency, which is defined as the reciprocal of the cycle time [10]. For example, for the same applied potential/current, the deposition rate in pulsed electrodeposition could be the same as in the continuous electrodeposition if the duty cycle of 33-50% is taken as the minimum value [11], and limiting the maximum frequency of 500 Hz [12].

Several FTO-modified substrates were used in the previous chapter to prepare ZnO nanorods by pulsed electrodeposition. The films' morphological, structural and photoelectrochemical analysis revealed that a TiO_2 intermediate layer improved the vertical alignment, increased the spatial density, decreased the diameter, and increased the stability of the ZnO nanorods towards photo-dissolution.

In this chapter, using the optimized substrate conditions (FTO/TiO_2/ZnO_SL), ZnO nanorods were prepared by potentiostatic pulsed electrodeposition by changing some

parameters, such as cycle time (*T*), pulse frequency (*f*), and duty cycle. Furthermore, the role of the growth parameters and heat treatment on the optical and electrical ZnO properties was investigated and discussed by using optical spectroscopic techniques (absorption, Raman, steady-state photoluminescence (PL), PL excitation (PLE) and time-resolved PL (TRPL)) and electrochemical impedance spectroscopy (EIS). The results shown within this chapter have been published as a full paper in a peer-reviewed journal [13].

4.2. Effect of the pulse parameters on ZnO nanorods optoelectronic properties

Considering a possible application in photovoltaics, a pre-defined cathodic charge density of 425 $mC.cm^{-2}$ was considered to ensure a film thickness of around 200-300 nm since short-length ZnO nanorods were reported results in better photovoltaic performances due to less recombination processes [14]. Cross-section SEM micrographs analyses were performed to confirm the film thicknesses, as shown in Figure 4.1. It is evident that the film thickness is correlated with the duty cycle, increasing from Profile C < Profile A < Profile B, i.e., from 20 % to 25 %, up to 33 % of duty cycle, respectively. This means that as long as the ratio between t_{on} and t_{off} increases, the film thickness also increases.

Figure 4.2 (left) shows the pulse current-time transients obtained during electrodeposition of ZnO nanorods on FTO/TiO_2/ZnO_SL substrates. The current transients observed from the different applied pulse profiles present similar shapes. During the cathodic pulse (E_{on}), hydroxyl ions are formed at the electrode interface, followed by the reduction of nitrate ions, which react with Zn^{2+} ions present in the electrolyte, resulting in the ZnO deposition on the substrate through dehydration of $Zn(OH)_2$. On the other hand, the rest potential pulse (E_{off}), corresponding to a zero-current state, allows refreshing the concentration of the electrolytic species at the interface, leading to a consistent growth of nanorods.

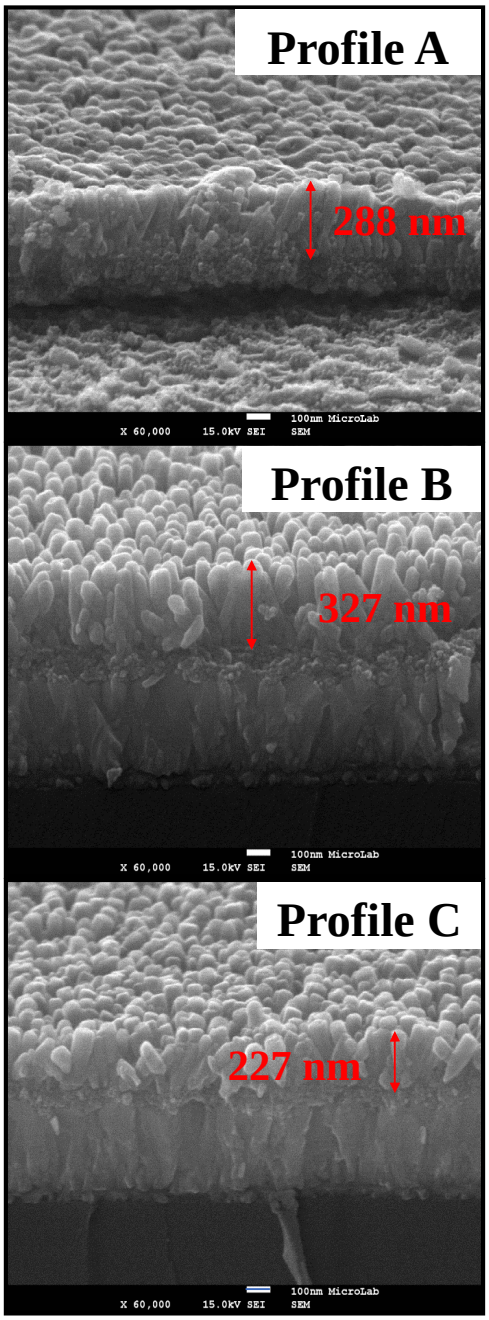

Figure 4.1 - Representative cross-section SEM micrographs of electrodeposited ZnO thin films prepared by applying different pulse profiles after annealing at 450 ºC for 1 h. Profiles A, B, and C correspond to 25.0 %, 33.3 %, and 20.0 % of duty cycle, respectively.

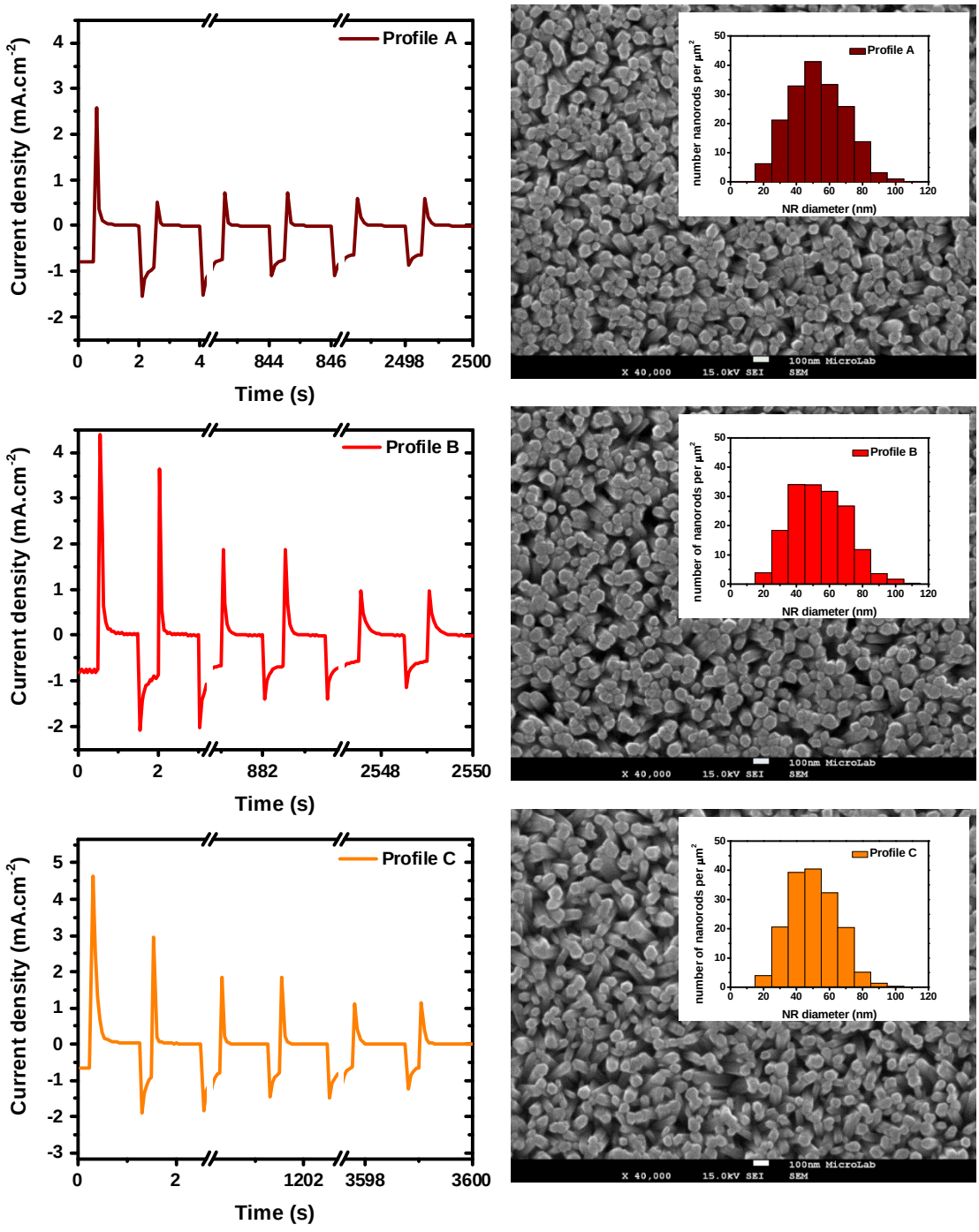

Figure 4.2 - Current transients recorded for pulsed electrodeposition ZnO nanorods arrays on FTO/TiO_2/ZnO_SL substrates by applying different pulse profiles (left) and the respective SEM top-view micrographs of the resulting deposits (right). Inset: Histograms of the estimated number of nanorods per area as a function of the diameter for the ZnO nanorods obtained for each profile. Profiles A, B, and C correspond to 25.0 %, 33.3 %, and 20.0 % of duty cycle, respectively.

For a better appraisal of the beginning of the deposition, the first 10 seconds of the current transients, recorded for all the applied pulse profiles, are shown in Figure 4.3, displaying similar initial cathodic current density. Since the substrate (Figure 3.2 d)) and the pulse potential (E_{on}) are the same in all the applied conditions, a similar response is expected until

complete coverage of the substrate with small grains [15,16]. The initial cathodic charge density obtained for each profile is directly related to the deposition time (t_{on}), being smaller for a shorter deposition time. According to N. Ibl [12], the diffusion layer does not have time to extend very far into the solution at short pulse deposition time. Also, M. Stumpp *et al.* [17] assumed that when t_{off} is larger than t_{on}, the concentration of reactant ions such as NO^{3-} and Zn^{2+} at the electrode surface is completely regenerated during the pause. Considering profile C, despite the t_{off}/t_{on} ratio being the highest of all the applied profiles, which would allow the total regeneration of the surface concentrations during the rest time, the t_{on} used is small enough for the capacitive current becomes relevant. Indeed, a considerable fraction of the measured charge must be accounted to the double layer charging that does not correspond to any faradaic process. In short pulses, this contribution is significant, affecting to a substantial extent the value of the measured charge (capacitive + faradaic). This practical constraint forces the use of a longer deposition time to obtain the same cathodic (faradaic) charge density as with the other profiles. This problem is not so substantial for longer t_{on} values since the double charge layer does not have a relative contribution when short times are employed. On the other hand, the pulse parameters of profile C allow better control of the growth of well-defined ZnO nanorods with a hexagonal shape and with lower coalescence than when the other profiles are applied (Figure 4.2). The histograms of the distribution of ZnO nanorod diameters according to the applied pulse profile are shown in the inset of Figure 4.2. In general, the diameter average is around 50 nm, being slightly smaller for profile C, with a diameter average of 40 nm, pointing out slower lateral growth of the nanorods due to the mass transport limited processes [18,19]. Also, the heterogeneity of ZnO diameters is reduced with the duty cycle, meaning that the heterogeneity of ZnO diameters decreases from profile B > profile A > profile C.

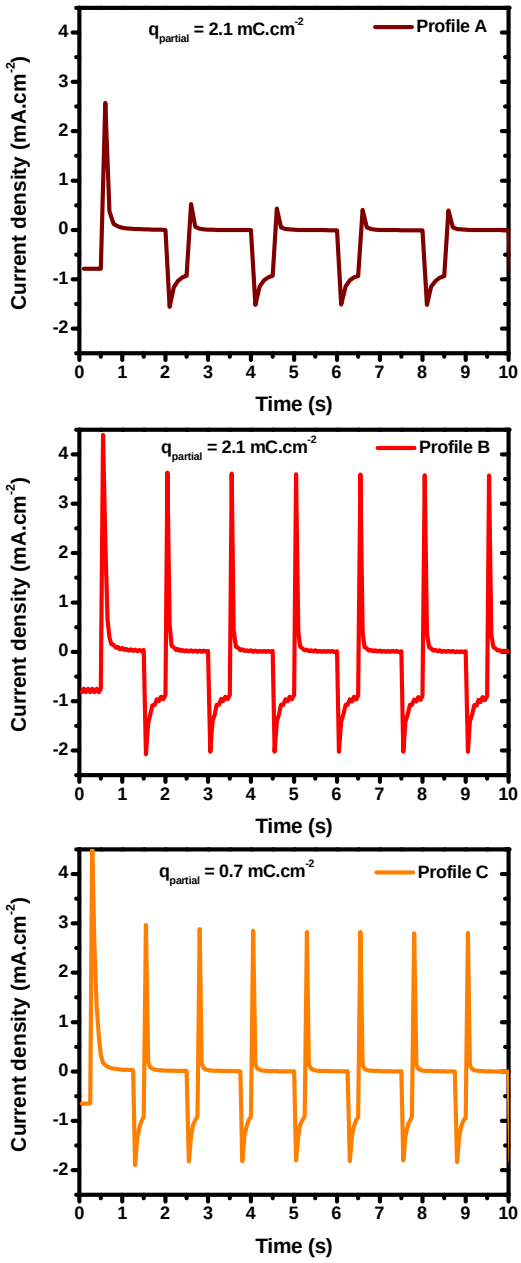

Figure 4.3 - Current transients obtained for pulsed electrodeposition of ZnO nanorods on FTO/TiO_2/ZnO_SL substrates by applying different pulse profiles (first 10 s of electrodeposition). Profiles A, B, and C correspond to 25.0 %, 33.3 %, and 20.0 % of duty cycle, respectively.

The XRD patterns presented in Figure 4.4a) show a sharp XRD reflection peak detected at ~ 34.4°, suggesting that the growth of the ZnO nanorods is along the *c*-axis normal to the substrate, with good crystallinity of the hexagonal wurtzite crystalline structure (JCPDS Card No. 36-1451), which agrees with the SEM micrographs. N. P. Klochko *et al.* [20] observed similar behaviour for pulsed electrodeposition of ZnO at different pulse frequencies. It is important to mention that no significant changes in XRD patterns of ZnO thin films were

observed before and after heat treatment, Figure 4.4b). It was impossible to detect the TiO_2 crystalline structure due to its low thickness.

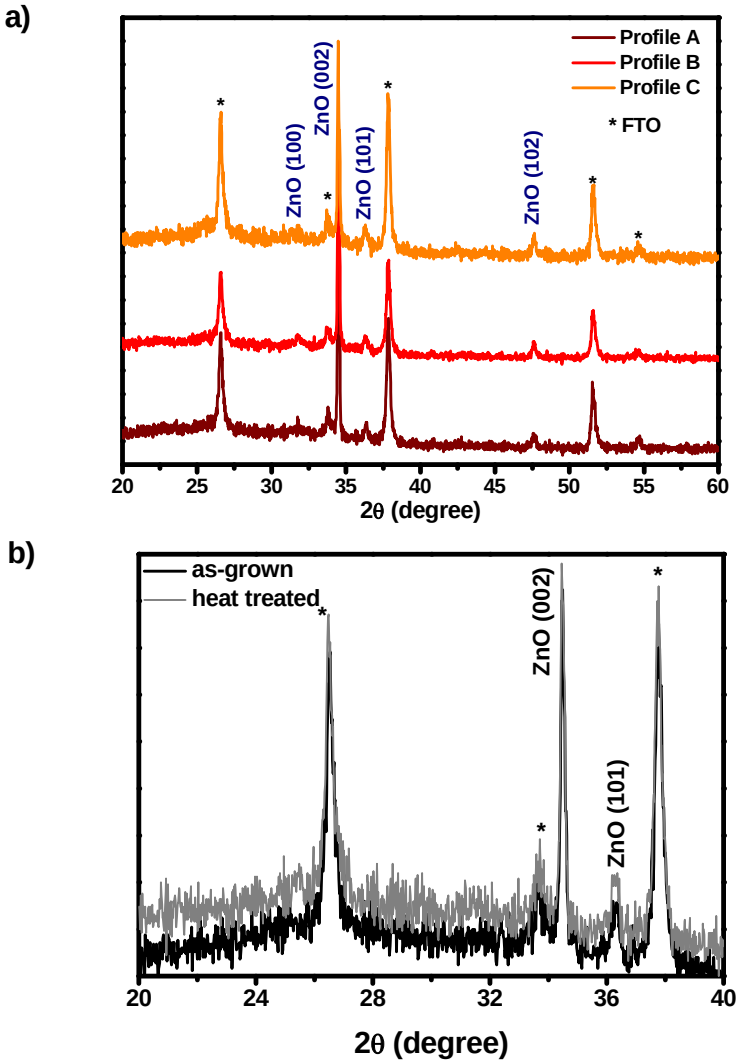

*Figure 4.4 - **a)** XRD patterns obtained for electrodeposited ZnO nanorods grown on FTO/TiO_2/ZnO_SL substrates by applying different potential pulse profiles, after annealing at 450 °C for 1h; **b)** XRD patterns illustrating the effect of the annealing treatment (profile C has been used for the electrodeposition process). Profiles A, B, and C correspond to 25.0 %, 33.3 %, and 20.0 % of duty cycle, respectively.*

Table 4.1 shows the effect of pulse profile on structural parameters of the electrodeposited ZnO thin films after heat treatment. A representative wurtzite ZnO structure is shown in Figure 4.5.

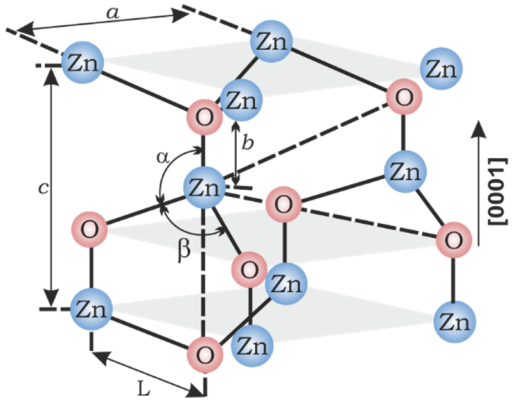

Figure 4.5 - Schematic representation of a wurtzite ZnO structure with lattice constants a, b and c, bond length Zn-O, L, and bond angles α and β (109.47° in ideal crystal).

Table 4.1 - Structural parameters of the pulsed electrodeposited ZnO thin films, after heat treatment. Profiles A, B, and C correspond to 25.0 %, 33.3 %, and 20.0 % of duty cycle, respectively.

Profile	***a* (Å)**	***c* (Å)**	***V* (Å³)**	***c/a***	**XRD (002) peak position (°)**	**Stress (σ) (GPa)**	**L (Å)**
A	3.25	5.20	47.61	1.60	34.47	0.22	1.98
B	3.24	5.20	47.25	1.60	34.47	0.24	1.97
C	3.24	5.20	47.10	1.61	34.47	0.24	1.97
JCPDS (36-1451)	3.25	5.20	47.20	1.60	34.42		1.98

The lattice constants a and c for hexagonal ZnO structure, obtained after heat treatment, agree with the reported ones in JCPDS Card No. 36-1451. However, the position of (002) peaks (see Table 4.1) is slightly shifted to higher 2θ values than those reported in JCPDS standard data. This shift of XRD peak (002) towards higher angles could be due to the release of intrinsic strain. The strain along the *c*-axis (ε) is given by the following equation [21],

$$\varepsilon = \frac{c_{film} - c_{bulk}}{c_{bulk}} \tag{4.1}$$

where c_{film} is the lattice parameter of the film and c_{bulk} (5.205 Å) [22] is the strain-free lattice parameter of the ZnO thin films. It is well known that the intrinsic strain in thin films can be due to impurities and defects in the lattice [23]. The stress (σ) of the ZnO nanorods films was estimated using the following formula [23],

$$\sigma = -233 \times 10^9 \left(\frac{c_{film} - c_{bulk}}{c_{bulk}}\right) \quad (4.2)$$

The stress values for the different ZnO films are given in Table 4.1. Positive stress means that the nanorods are in a state of compressive stress, *i.e.*, structure compression due to the rearrangement of atoms in ZnO. A possible factor that can generate compressive stress in ZnO nanorods is the presence of zinc interstitials, causing lattice disorder [24]. Fang *et al.* [25] reported similar stress behaviour of ZnO films by variation of the post-annealing temperature. Furthermore, an increase in the residual stress promotes the decrease in the bond length of the Zn-O, L [26].

The crystalline quality of the samples was further assessed by Raman spectroscopy. The Raman spectra presented in Figure 4.6 for all the as-grown and annealed samples exhibit the expected vibrational frequencies for the hexagonal wurtzite ZnO structure [27]. In addition, vibrational modes due to the FTO substrate [28] and anatase TiO_2 were also detected [29,30].

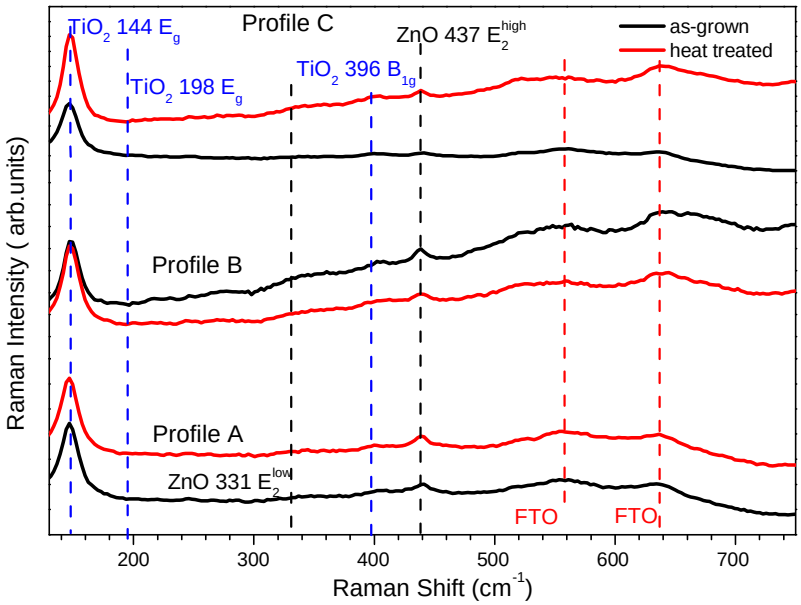

Figure 4.6 - Raman spectra of the studied samples using a 442 nm laser line as the excitation source. ZnO vibrational modes were identified in black, FTO substrate in red and TiO_2 in blue. Profiles A, B, and C correspond to 25.0 %, 33.3 %, and 20.0 % of duty cycle, respectively.

Figure 4.7 shows the RT absorption spectra of the as-deposited and heat-treated ZnO nanorods obtained with the A, B and C pulse profiles. Independently of the used profile, all the as-grown samples exhibit similar absorption. A pronounced onset absorption is observed near 3.15 eV, followed by a steeper increase in the absorption, reaching a maximum at

~3.5 eV. The measured spectra indicate a high energy shift of the ZnO bandgap when a comparison is made with the RT reported value for the nondegenerate semiconductor of ~3.3 eV [31,32]. This finding suggests that the as-deposited ZnO nanorods are heavily-doped, resulting in a band filling responsible for high energy bandgap shift due to the Burstein-Moss effect [33]. After heat treatment, noticeable changes are identified in the absorption spectra. Particularly, a low energy shift of the absorption band maximum to ~3.3 eV is promoted, which agrees with the ZnO bandgap energy [31,32], as shown in the Tauc plots presented in Figure 4.8 b). Such behaviour indicates that a carrier reduction is privileged through the annealing process of the ZnO nanorods. In both cases, a wide absorption tail extending to lower energies is measured, likely due to a wide distribution of energetic states below the bandgap of ZnO.

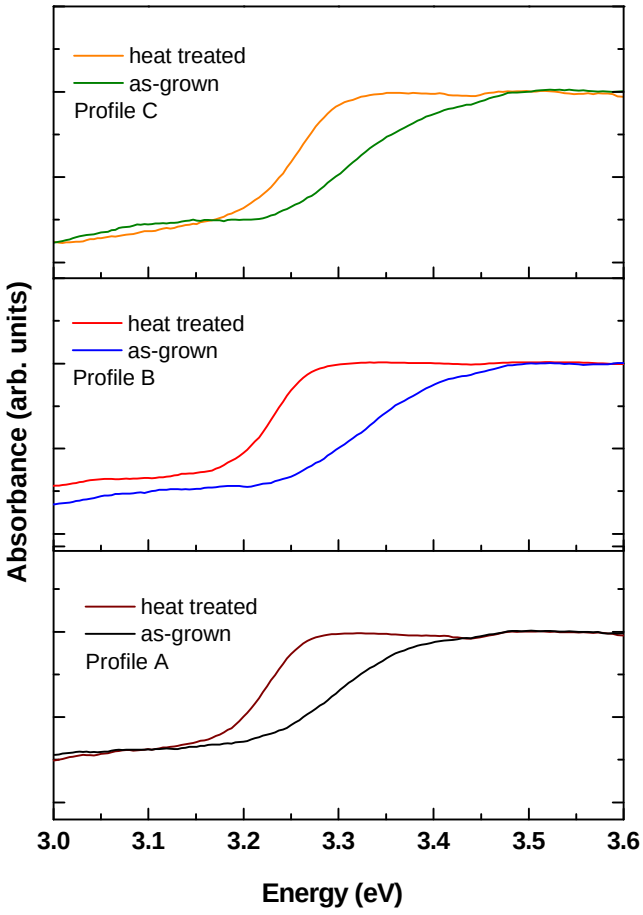

Figure 4.7 - RT absorption spectra of the as-grown and heat-treated electrodeposited ZnO nanorods using the pulse profiles A, B and C. Profiles A, B, and C correspond to 25.0 %, 33.3 %, and 20.0 % of duty cycle, respectively.

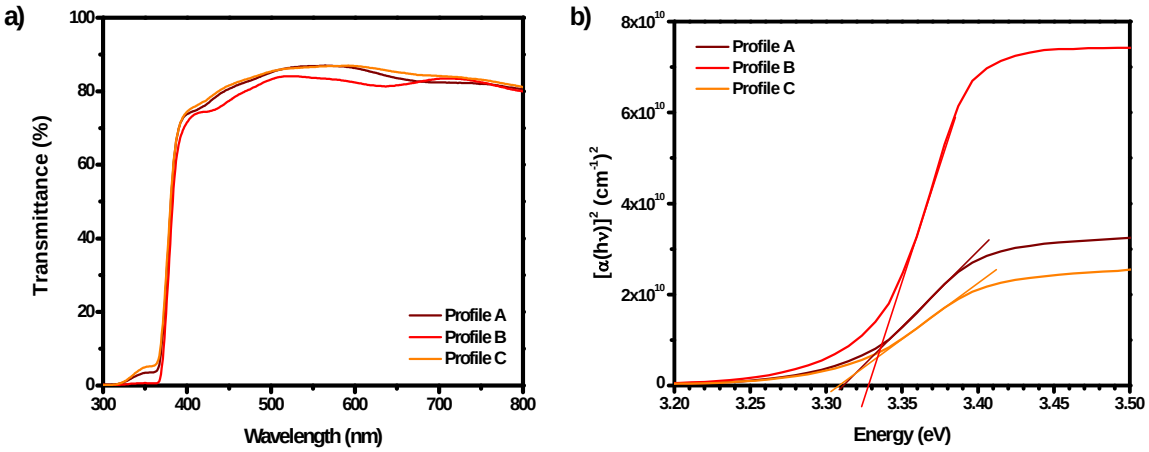

*Figure 4.8 - **a)** Optical transmittance and **b)** Tauc plots for electrodeposited ZnO nanorods on FTO/TiO_2/ZnO_SL substrates, prepared at different pulse profiles after annealing at 450 ℃ for 1 h. Profiles A, B, and C correspond to 25.0 %, 33.3 %, and 20.0 % of duty cycle, respectively.*

The transparency of the annealed electrodeposited ZnO nanorods was verified from the optical transmittance spectra shown in Figure 4.8 a). In addition, the RT optical energy bandgap of such ZnO nanostructures was determined from optical absorption spectra. Figure 4.8 b) shows the Tauc plots for the heat-treated pulse electrodeposited ZnO nanorods. The E_g was found to be 3.31, 3.33, and 3.31 eV for samples obtained by profiles A, B, and C, respectively, which is in fair agreement with the reported ~3.3 eV direct bandgap of ZnO at RT [31,32].

The RT PL spectra of the ZnO nanorods obtained at different pulse profiles are displayed in Figure 4.9, showing optically active defects covering a wide spectral range. Besides the near band edge (NBE) recombination in the UV spectral region, broad emission bands spreading from the visible to the near-infrared were measured. Typically, the NBE spectral region corresponds to an overlap of free and bound exciton transitions [31–38], although surface defects are also known to influence the peak position and spectral shape of this emission [36]. On the other hand, broad emission bands are currently identified in ZnO samples [31,32,34–38]. The chemical nature of the defects responsible for those broad bands has generated controversy in literature, being its dependence on the intrinsic defects the most used explanation. However, in the case of nanostructures, some of the broad emission bands have been associated with the presence of surface-related defects, which, in turn, are dependent on the synthesis/growth processes [39,40]. In the samples analysed here, a comparison among the spectra of the as-grown nanorods allows one to observe that the peak intensity of the NBE is higher than the peak intensity of the broad bands. The highest ratio occurs for the nanorods produced with pulse profile B, and therefore we have chosen the

electrodeposited samples with this profile for further in-depth analysis. Moreover, and independently of the applied pulse profile, a comparison between the as-grown and heat-treated nanorods reveals that the full width at half maximum (FWHM) of the NBE peak decreases after the thermal annealing, indicating an optical quality improvement of the ZnO nanorods. Such results agree with the RT absorption spectra discussed above, where the ~3.3 eV ZnO bandgap was reached after annealing. The narrowing of the NBE recombination is accompanied by a decrease of its intensity, likely due to a lower concentration of shallow defects, which contribute to the UV emission. Additionally, the heat-treatment enhances the intensity ratio of broad emission bands/NBE and induces changes in their spectral shape, probably due to new thermally promoted or rearranged defects. Remarkable maxima at ~1.9 eV and ~2.4 eV are present in the heat-treated ZnO nanorods (*e.g.* see the sample with profile B in Figure 4.9).

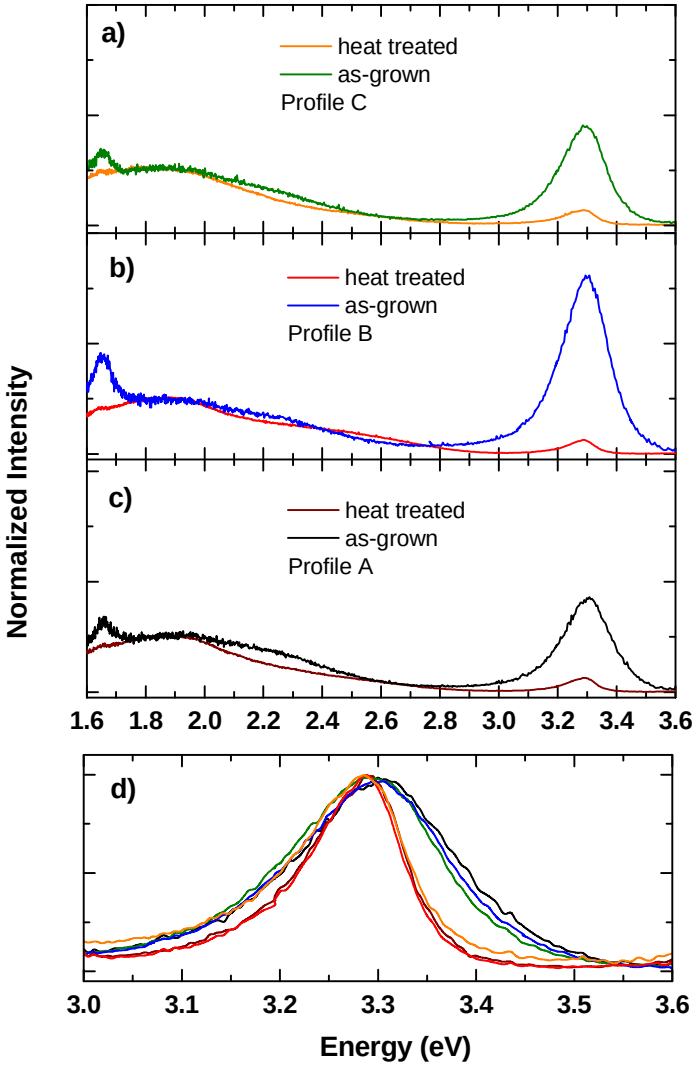

*Figure 4.9 - RT normalized PL at 1.9 eV for the as-grown and heat-treated ZnO nanorods deposited with **a)** profile C, **b)** profile B, **c)** profile A. **d)** RT normalized PL at 3.3 eV for the as-grown and heat-treated ZnO nanorods. Profiles A, B, and C correspond to 25.0 %, 33.3 %, and 20.0 % of duty cycle, respectively.*

The chosen ZnO nanorods were studied in detail to understand this behaviour. Figure 4.10 shows the normalized (to the band edge at 3.3 eV) RT PL and PLE spectra for both as-grown and heat-treated samples.

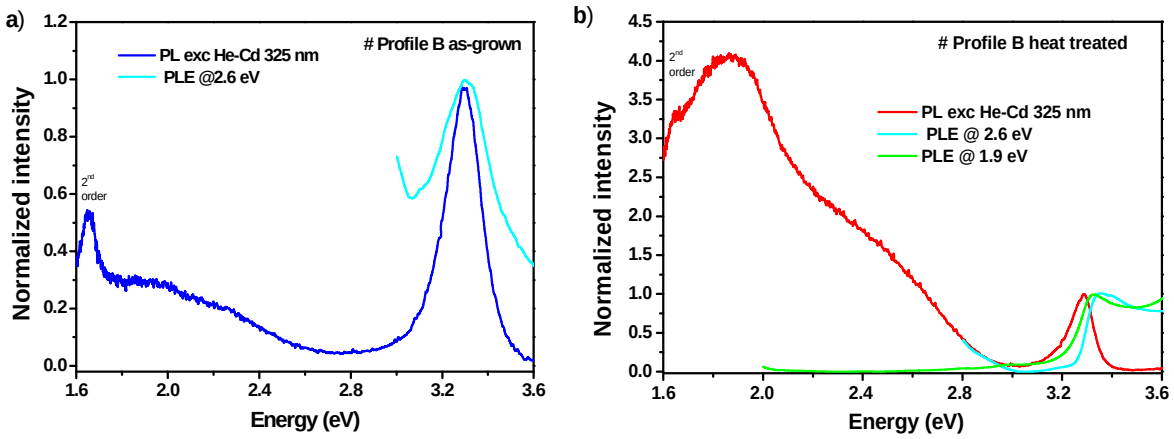

Figure 4.10 - RT PL and PLE spectra from ZnO nanorods prepared using pulse profile B (33.3 % of duty cycle): ***a)*** *as-grown,* ***b)*** *heat-treated.*

As previously noticed, the as-grown and heat-treated samples show differences in the NBE spectral region. Particularly a narrowing of the FWHM of the high energy UV luminescence and an inversion of the relative intensity of deep level emission/UV band. The PL spectra of both samples do not overlap with the one of the glass/FTO [15] and, therefore, this contribution can be discarded, being the main emission originated from the ZnO and/or TiO_2 lattices and/or surface-related defects. For the as-grown films, when the PLE is monitored at the deep level recombination bands, the excitation maximum was superimposed with the ZnO NBE emission sample. Such behaviour indicates that the main population of the deep luminescence is strongly localized at ~3.33 eV and arises from the exciton excitation. For higher energies, a fast decrease in the excitation efficiency is observed, which can be accounted for by additional nonradiative centres that promote the capture of carriers with such energies, hampering their participation in the excitation process.

In contrast, for the heat-treated sample, the PLE monitored either at the red or green luminescence reveals that the emission bands are populated through a continuous tail of states inside the ZnO bandgap. Moreover, a steeper excitation is observed in the ZnO bandgap region, slightly shifted to higher energies when the PL is monitored at the green band maximum. In contrast with the as-grown samples, the heat-treated nanorods the PLE spectra show almost a mirror image of the ZnO excitonic transition, and the population of the red and green bands can be promoted through higher excited states (Figure 4.10b)).

The presence of distinct optically active defects in the produced samples was further analysed by transient spectroscopy. Figure 4.11 depicts the TRPL spectra of the heat-treated ZnO nanorods prepared using profile B for a 325 nm excitation using a pulsed Xe lamp as the source. By comparing the TRPL measured for the shorter sample delay (SD) with the steady-

state PL spectra, it can be seen that the UV emission has a lifetime faster than the 50 μs since the recombination is not observed by TRPL. Focusing the attention on the deep level recombination, it should be noticed from Figure 4.11a) that no spectral correspondence occurs between the steady-state green (~2.4 eV) and red (1.9 eV) PL bands with the yellow/orange one (2.0 eV) observed by TRPL. Therefore, the data are consistent with the overlapping of three emitting centres, two of them with faster decays (green and red) and a slower emission peaked at 2.0 eV. Despite the fact that the yellow/orange emission could arise from anatase TiO_2 [30], the absence of the TiO_2 edge absorption in the absorption spectrum (Figure 4.7) of the heat-treated sample makes this hypothesis unlikely. As such, it is fair to assume that the emission peaked at 2.0 eV arises from the ZnO host. This is further corroborated by the detection of an extending tail of energy states close to the ZnO band edges, together with previously reported works, pointing out the presence of a yellow/orange emission in ZnO peaked at the same energy position and with a similar spectral shape as the one here observed [31,39]. Figure 4.11b) illustrates the RT TRPL spectra, showing the yellow/orange emission intensity behaviour with different time delays, evidencing that this optical centre has a lifetime in the range of tens or hundreds of μs.

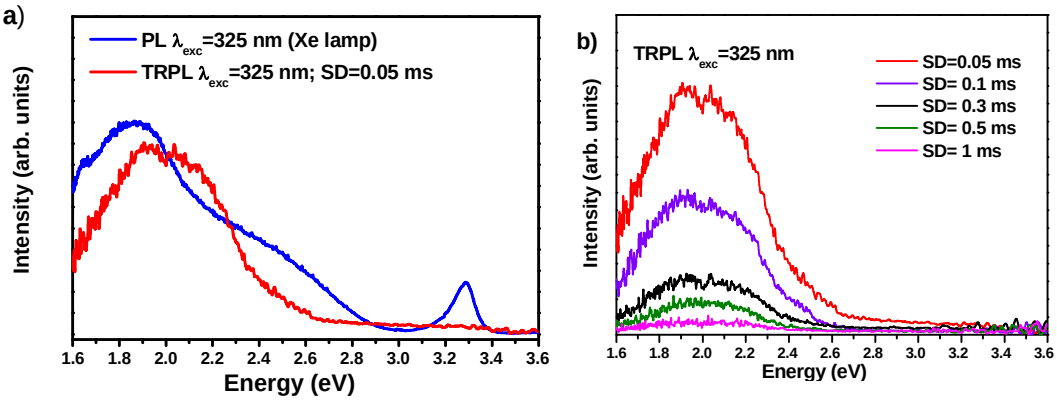

*Figure 4.11 - RT comparison of **a)** steady-state PL (blue line) and TRPL (red line) spectra of heat-treated ZnO nanorods prepared using profile B (33.3 % of duty cycle) and **b)** TRPL spectra acquired using 325 nm photons from a pulsed Xe lamp as excitation, using different sample delays (SD) for a time window of 0.2 ms.*

In order to further evaluate the samples' optical response, high-resolution PL spectra were measured at low temperature for both the as-grown and heat-treated samples, as depicted in Figure 4.12. Following the behaviour identified at RT, it was observed that the as-grown sample has a wider FWHM of the UV band, likely due to the unfold of the overlapped high energy recombination processes such as free (FX) and donor bound excitons (D^0X), 3.31 eV line and their phonon replicas. On the contrary, after annealing, the sample evidences a

narrower FWHM of the UV band, exhibiting defined shoulders that were tentatively assigned to the standard optical centre of the ZnO host in the mentioned spectral range. An additional remark should be made regarding the deep level emission bands observed at low temperatures. Figure 4.12a) shows that the red bands in the as-grown and heat-treated samples have different maxima. The first one is peaked at ~1.9 eV while the latter is peaked at ~1.7 eV, meaning that different defects are present in the two samples. On the other hand, as discussed before, the recombination processes in the as-grown samples are blue-shifted, in line with their higher bandgap energy. Moreover, as mentioned, the annealed nanorods an additional yellow/orange band was identified by the TRPL. Therefore, the observed energy shift between the peak position of the red bands in the as-grown and annealed samples can also be accounted for the relative intensity of the red, yellow and green-emitting centres, meaning that the same defects centres may be present in both samples but with different distribution and concentration.

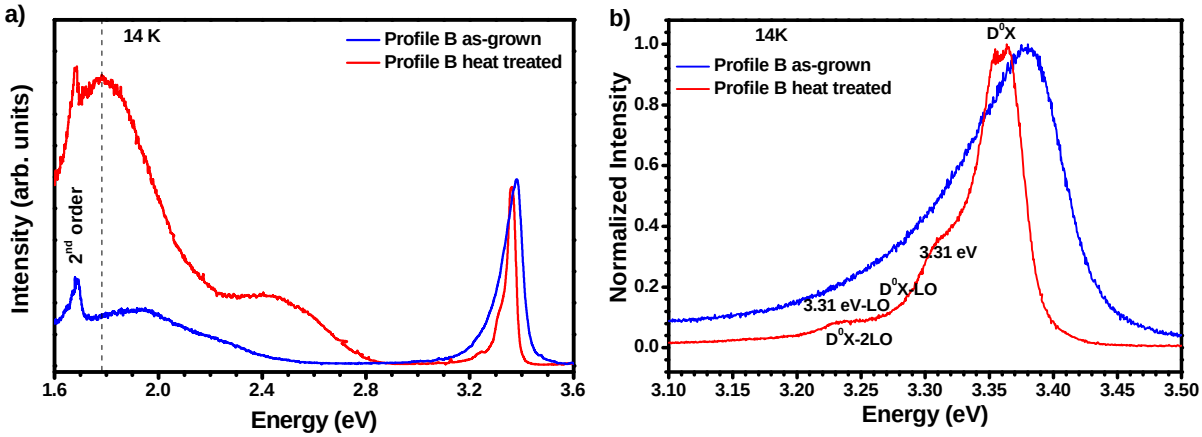

Figure 4.12 - ***a)*** *14 K PL spectra of the as-grown and heat-treated ZnO nanorods, excited with a 325 nm He-Cd laser line.* ***b)*** *High-resolution spectra of the UV region.*

Figure 4.13 and Figure 4.14 depict the temperature-dependent PL spectra of the selected samples. Figure 4.13b) and Figure 4.14b) highlight the temperature dependence behaviour of the band edge recombination. The evolution of its peak position as a function of the temperature was fitted using a semi-empirical expression equivalent to the Bose-Einstein model according to Pässler *et al.* [41,42],

$$E_g(T) = E_g(T=0) - \frac{\alpha\Theta}{exp\left(\frac{\Theta}{T}\right)-1} \tag{4.3}$$

where T stands for the absolute temperature and Θ corresponds to the effective phonon temperature. The experimental data and best fit to the NBE peak position are displayed in Figure 4.15. However, as the NBE is due to an overlap of emitting centres (FX, D^0X, and 3.31 eV), the fit can only be understood as a general trend of the main recombination rather than the individual behaviour of each optical defect. As a general trend, the peak position of the UV band suffers a redshift with increasing temperature because of the bandgap shrinkage, as expected. For comparison purposes, the peak position shift with the temperature of the FX_A measured in ZnO bulk samples [43] was included in the Figure. Furthermore, the overall luminescence intensity (either from the NBE or from the deep level emission) decreases for higher temperatures due to nonradiative processes, which compete with the radiative ones, as shown in Figure 4.13 and Figure 4.14. Distinct quenching mechanisms of the defects that compose the broad bands explain the observed high energy shift of the red emission with increasing temperatures, as seen for the heat-treated ZnO nanorods arrays (Figure 4.14 a)).

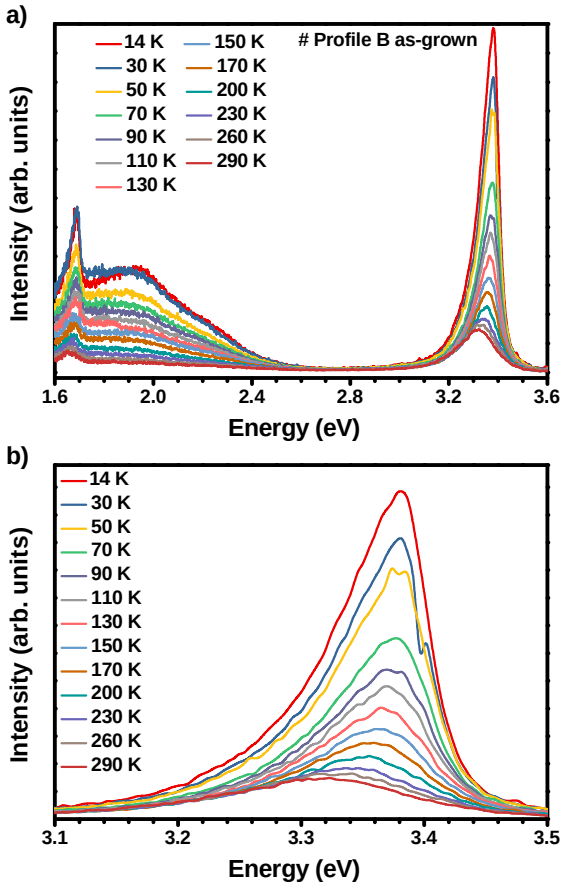

*Figure 4.13 - **a)** Temperature-dependent PL spectra for the as-grown ZnO samples, prepared using profile B (33.3 % of duty cycle) and excited with a 325 nm wavelength radiation. **b)** Detail of the emission in the UV region.*

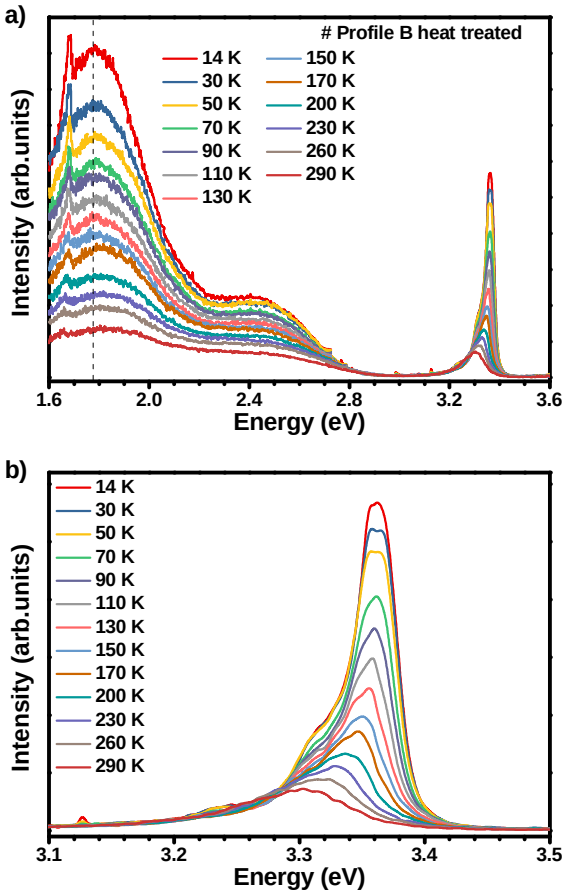

*Figure 4.14 - **a)** Temperature-dependent PL spectra for the heat-treated ZnO samples, prepared using profile B (33.3 % of duty cycle) and excited with a 325 nm wavelength radiation. **b)** Detail of the emission in the UV region.*

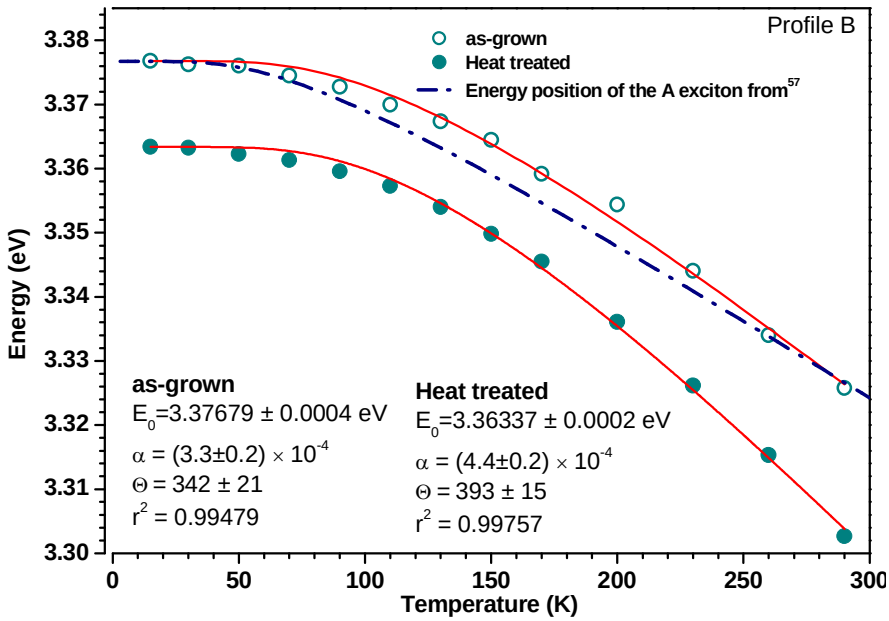

Figure 4.15 - Peak position as a function of the temperature of the NBE recombination for the as-grown (empty circles) and heat-treated (full circles) ZnO nanorods. Full lines correspond to the best fit to experimental values according to eq. (4.4). The dashed-dot line represents the peak position of the A free exciton in a bulk crystal [43]. *E_0 is the energy gap at 0 K, α is the slope of the curve, and Θ is the effective phonon temperature.*

EIS was carried out to obtain more information related to the electrical properties of the pulse electrodeposited ZnO nanorods arrays. The Mott-Schottky relation (Eq. 4.4) was used to calculate flatband potential (V_{FB}) and donor density (N_D) of the ZnO thin films [44,45],

$$\frac{1}{C^2} = \frac{2}{q\varepsilon_0\varepsilon_{ZnO}A^2N_D}(V + V_{FB}) \quad (4.4)$$

where ε_0 is the permittivity of free space (8.85×10^{-14} F.cm^{-1}), ε_{ZnO} is the dielectric constant of ZnO (ε_{ZnO} = 10 for ZnO nanowires [16]), q is the electron charge (1.6×10^{-19} C), A is the geometric surface area (0.196 cm^2), and C is the space charge capacitance at potential V_{ZnO}, which is the potential difference across the ZnO space-charge region. The slope of the linear $1/C^2$ vs applied potential (V) was used to calculate N_D according to equation 4.5, and the flatband potential can be obtained from the intercept of the linear portion of the Mott-Schottky plot on the potential axis,

$$slope = \frac{2}{q\varepsilon_0\varepsilon_{ZnO}A^2N_D} \quad (4.5)$$

Figure 4.16 shows the Mott-Schottky plots of the as-grown and heat-treated pulse electrodeposited samples. A linear variation of $1/C^2$ with applied potential between -0.4 and 0.2 V is observed for all the plots of as-grown ZnO nanorods arrays, while for heat-treated ZnO nanorods, the range is between 0.0 and 0.6 V, indicating in all the cases that the ZnO nanorods obey to the Mott-Schottky behaviour [46]. The positive slope obtained for all ZnO samples reveals n-type conductivity. Additionally, different slope values were observed depending on the pulse profile to obtain the ZnO nanorod arrays, as seen in Table 4.2. The donor density values shown in the table are in line with what has been reported in the literature [47,48], namely values of the order of 10^{19} cm^{-3} for as-deposited samples with a slight decrease for annealed samples, showing ZnO carrier concentrations ranging between 10^{17} and 10^{18} cm^{-3}. These results are in good accordance with the above discussed Burstein-Moss band filling and the corresponding high energy bandgap of the heavily-doped as-grown samples (Figure 4.7). Annealing in air at 450 °C induces a reduction of the donor density of the ZnO nanorods independently of the applied pulse profile, which may be attributed to a lower content of defects that mainly act as shallow electron donors. The decrease of the carrier concentration for the heat-treated ZnO nanorods arrays agrees with the measured

bandgap redshift in the absorption spectra and the observation of an extending tail of energy states close to the ZnO band edges. The reduction of the N_D may be due to (i) a change in morphology and crystal structure, (ii) a decrease of intrinsic point defects, like Zn atoms (Zn_i) and oxygen vacancies (V_o), and/or (iii) a change of impurities [49]. Previous studies [50] showed no changes in the morphology of as-deposited and heat-treated ZnO nanorods, corroborating the SEM images and XRD data, which also did not show significant changes after annealing at 450 °C for 1h. A decrease in V_o due to the effective incorporation of O atoms is quite likely since the annealing was carried out in air [51]. Also, since ZnO is n-type doped, the most probable impurity incorporated is hydrogen H^+ (H_i) as a shallow donor.

Focusing on as-deposited ZnO nanorods arrays, it seems that N_D decreases with the heterogeneity of nanorod diameter. Specifically, the nanorods prepared using profile C, which shows less heterogeneity of nanorod diameter (range of 40-50 nm) (Figure 4.2), present a lower N_D value than the ones obtained for the samples prepared using profile B (range of 40-70 nm). Furthermore, this decrease in N_D values is accompanied by a reduction in the flatband potential, which corresponds to the height of double Schottky barriers. Similar results were reported by Klochko group [52], where increasing the ZnO nanorod diameter from 30-50 nm to 70-190 nm increased the N_D values from 10^{14} to 10^{17} cm^{-3}. However, the annealed ZnO nanorods arrays show a reverse effect, increasing the N_D values and decreasing the flatband potentials with the pulse frequency. According to the literature, less positive flatband potential suggests a larger band bending, resulting in an enhanced charge separation, whereas an increase in carrier density can be attributed to a more significant presence of surface states [53].

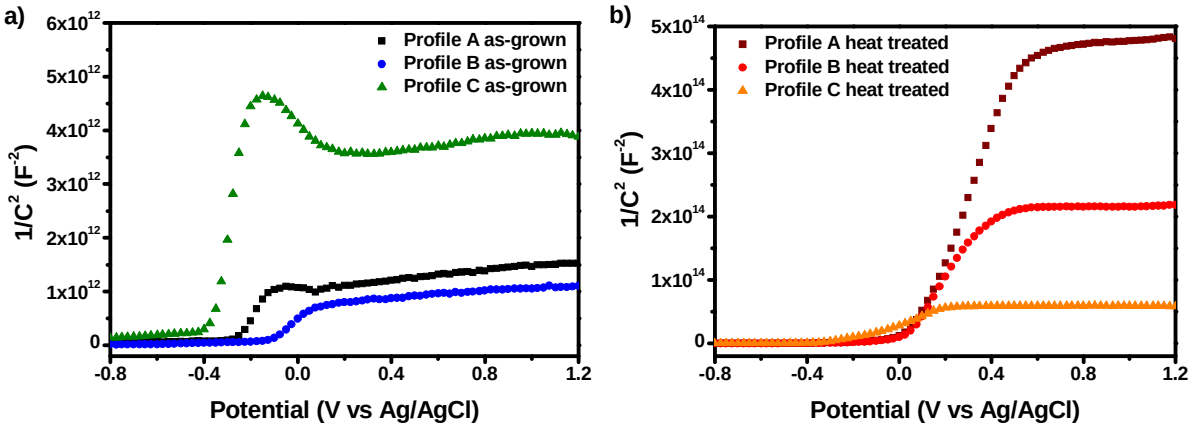

*Figure 4.16 - Mott-Schottky plots of electrodeposited ZnO nanorods arrays at different pulse profiles, in 0.1 M $LiClO_4$ in propylene carbonate for **a)** as-grown and **b)** heat-treated samples. The measurements were recorded at 5 kHz with an AC amplitude signal of 20 mV over the range of potential applied.*

Table 4.2 – Mott-Schottky parameters estimated for the pulse electrodeposited ZnO nanorod arrays.

Profile		N_D (cm^{-3})	V_{FB} (V vs Ag/AgCl)
Profile A	**as-grown**	4.67×10^{19}	-0.29
	heat treated	3.41×10^{17}	0.06
Profile B	**as-grown**	9.45×10^{19}	-0.15
	heat treated	6.14×10^{17}	0.00
Profile C	**as-grown**	1.13×10^{19}	-0.39
	heat treated	2.74×10^{18}	-0.24

4.3. Chapter Summary

The results presented within this chapter demonstrate that the electrodeposition conditions at which ZnO nanorod arrays are prepared to have an impact on its optoelectronic properties.

The morphological characterization of ZnO films revealed that the applied pulse parameters of profile C allowed better control of the growth of well-defined ZnO nanorods with lower coalescence and high homogeneity of nanorod diameters. From the structural characterisation point-of-view, no significant changes in the crystal structure were observed for as-deposited and heat-treated ZnO independently of the applied pulse profile.

The RT absorption, PL, TRPL, and PLE studies identified distinct defects exhibited in the as-grown and heat-treated samples. In particular, the absorption spectra of the as-grown samples evidence a Burstein-Mott effect on the ZnO bandgap energy, in line with their character of heavily-doped n-type semiconductor as measured by electrochemical impedance spectroscopy. In addition, the ZnO carrier concentration and the barrier height at the grain boundary (V_{FB}) seem to be related to the applied pulse conditions.

After annealing, with the decrease of the carrier concentration, the samples exhibit a steeper absorption ~3.3 eV, as expected for nondegenerate ZnO. Additionally, a spreading of energetic states is detected inside the ZnO bandgap. The as-grown and heat-treated samples exhibit near band edge recombination and deep level emission. The peak intensity of the former is higher in the as-grown ZnO nanorods arrays and reversed upon annealing. Moreover, the heat-treatment promotes a higher optical quality of the ZnO nanorods, as

evidenced by the sharpness of the absorption edge and the narrowing of the full width at half maximum of the ultraviolet emission. Combined spectroscopic techniques reveal that the broad emission bands overlap three emitting centres in the red, yellow and green spectral regions, with the yellow emission showing a longer decay time.

Since the electrodeposition usually provides high donor density ZnO, the reported characterisation protocol and conclusions may significantly impact further understanding the optoelectronic properties of electrodeposited ZnO nanostructures and/or thin films in general.

4.4. References

[1] R. Pietruszka, B.S. Witkowski, S. Gieraltowska, P. Caban, L. Wachnicki, E. Zielony, K. Gwozdz, P. Bieganski, E. Placzek-Popko, M. Godlewski, New efficient solar cell structures based on zinc oxide nanorods, Sol. Energy Mater. Sol. Cells. 143 (2015) 99–104. doi:10.1016/J.SOLMAT.2015.06.042.

[2] S.H. Ko, D. Lee, H.W. Kang, K.H. Nam, J.Y. Yeo, S.J. Hong, C.P. Grigoropoulos, H.J. Sung, Nanoforest of Hydrothermally Grown Hierarchical ZnO Nanowires for a High Efficiency Dye-Sensitized Solar Cell, Nano Lett. 11 (2011) 666–671. doi:10.1021/nl1037962.

[3] R. Chander, A.K. Raychaudhuri, Electrodeposition of aligned arrays of ZnO nanorods in aqueous solution, Solid State Commun. 145 (2008) 81–85. doi:10.1016/J.SSC.2007.09.031.

[4] H. Kim, J.Y. Moon, H.S. Lee, Growth of ZnO nanorods on various substrates by electrodeposition, Electron. Mater. Lett. 5 (2009) 135–138. doi:10.3365/eml.2009.09.135.

[5] T. Singh, D.K. Pandya, R. Singh, Effect of supporting electrolytes on the growth and optical properties of electrochemically deposited ZnO nanorods, Opt. Mater. (Amst). 35 (2013) 1493–1497. doi:10.1016/J.OPTMAT.2013.03.015.

[6] T. Shinagawa, M. Izaki, Morphological evolution of ZnO nanorod arrays induced by a pH-buffering effect during electrochemical deposition, RSC Adv. 4 (2014) 30999–31002. doi:10.1039/C4RA04342A.

[7] S.N. Sarangi, Controllable growth of ZnO nanorods via electrodeposition technique: towards UV photo-detection, J. Phys. D. Appl. Phys. 49 (2016) 355103. doi:10.1088/0022-3727/49/35/355103.

[8] C. V. Manzano, D. Alegre, O. Caballero-Calero, B. Alén, M.S. Martín-González, Synthesis and luminescence properties of electrodeposited ZnO films, J. Appl. Phys. 110 (2011) 043538. doi:10.1063/1.3622627.

[9] M.D. Reyes Tolosa, J. Orozco-Messana, L.C. Damonte, M.A. Hernandez-Fenollosa, ZnO Nanoestructured Layers Processing with Morphology Control by Pulsed Electrodeposition, J. Electrochem. Soc. 158 (2011) D452–D455. doi:10.1149/1.3593004.

[10] M.S. Chandrasekar, M. Pushpavanam, Pulse and pulse reverse plating—Conceptual, advantages and applications, Electrochim. Acta. 53 (2008) 3313–3322.

doi:10.1016/J.ELECTACTA.2007.11.054.

[11] D. Landolt, Fundamental aspects of alloy plating, 2001.

[12] N. Ibl, Some theoretical aspects of pulse electrolysis, Surf. Technol. 10 (1980) 81–104. doi:10.1016/0376-4583(80)90056-4.

[13] T. Frade, D. Siopa, A.F. Martins, J.F.C. Carreira, J. Rodrigues, N. Ben Sedrine, M.R. Correia, T. Monteiro, R. Tena-Zaera, A. Gomes, Optoelectronic Characterization of ZnO Nanorod Arrays Obtained by Pulse Electrodeposition, J. Electrochem. Soc. 165 (2018) D595–D603. doi:10.1149/2.0131813jes.

[14] D. Bi, G. Boschloo, S. Schwarzmüller, L. Yang, E.M.J. Johansson, A. Hagfeldt, Efficient and stable CH3NH3PbI3-sensitized ZnO nanorod array solid-state solar cells, Nanoscale. 5 (2013) 11686–11691. doi:10.1039/C3NR01542D.

[15] T. Frade, K. Lobato, J.F.C. Carreira, J. Rodrigues, T. Monteiro, A. Gomes, TiO2 anatase intermediary layer acting as template for ZnO pulsed electrodeposition, Mater. Des. 110 (2016) 18–26. doi:10.1016/j.matdes.2016.07.122.

[16] I. Mora-Seró, F. Fabregat-Santiago, B. Denier, J. Bisquert, R. Tena-Zaera, J. Elias, C. Lévy-Clément, Determination of carrier density of ZnO nanowires by electrochemical techniques, Appl. Phys. Lett. 89 (2006) 203117. doi:10.1063/1.2390667.

[17] M. Stumpp, T.H.Q. Nguyen, C. Lupo, D. Schlettwein, Interplay of Different Reaction Pathways in the Pulsed Galvanostatic Deposition of Zinc Oxide, Electrochim. Acta. 169 (2015) 367–375. doi:10.1016/J.ELECTACTA.2015.04.038.

[18] R. Tena-Zaera, J. Elias, C. Lévy-Clément, I. Mora-Seró, Y. Luo, J. Bisquert, Electrodeposition and impedance spectroscopy characterization of ZnO nanowire arrays, Phys. Status Solidi. 205 (2008) 2345–2350. doi:10.1002/pssa.200779426.

[19] M.R. Khajavi, D.J. Blackwood, G. Cabanero, R. Tena-Zaera, New insight into growth mechanism of ZnO nanowires electrodeposited from nitrate-based solutions, Electrochim. Acta. 69 (2012) 181–189. doi:10.1016/J.ELECTACTA.2012.02.096.

[20] N.P. Klochko, G.S. Khrypunov, Y.O. Myagchenko, E.E. Melnychuk, V.R. Kopach, E.S. Klepikova, V.M. Lyubov, A. V Kopach, Controlled Growth of one-dimensional zinc oxide nanostructures in the pulsed electrodeposition mode, Semiconductors. 46 (2012) 825–831. doi:10.1134/S1063782612060127.

[21] R. Ghosh, D. Basak, S. Fujihara, Effect of substrate-induced strain on the structural, electrical, and optical properties of polycrystalline ZnO thin films, J. Appl. Phys. 96 (2004) 2689–2692. doi:10.1063/1.1769598.

[22] E. Şenadim, H. Kavak, R. Esen, The effect of annealing on structural and optical properties of ZnO thin films grown by pulsed filtered cathodic vacuum arc deposition, J. Phys. Condens. Matter. 18 (2006) 6391–6400. doi:10.1088/0953-8984/18/27/021.

[23] Y.G. Wang, S.P. Lau, H.W. Lee, S.F. Yu, B.K. Tay, X.H. Zhang, K.Y. Tse, H.H. Hng, Comprehensive study of ZnO films prepared by filtered cathodic vacuum arc at room temperature, J. Appl. Phys. 94 (2003) 1597–1604. doi:10.1063/1.1592007.

[24] S.K. Shrama, N. Saurakhiya, S. Barthwal, R. Kumar, A. Sharma, Tuning of structural, optical, and magnetic properties of ultrathin and thin ZnO nanowire arrays for nano device applications, NANOSCALE Res. Lett. 9 (2014) 122 (1–17). doi:10.1186/1556-276X-9-122.

[25] Z.B. Fang, Z.J. Yan, Y.S. Tan, X.Q. Liu, Y.Y. Wang, Influence of post-annealing treatment on the structure properties of ZnO films, Appl. Surf. Sci. 241 (2005) 303–308. doi:10.1016/J.APSUSC.2004.07.056.

[26] M.S. Kim, T.H. Kim, D.Y. Kim, D.-Y. Lee, S.-O. Kim, J.-Y. Leem, Effects of annealing atmosphere and temperature on properties of ZnO thin films on porous silicon grown by plasma-assisted molecular beam epitaxy, Electron. Mater. Lett. 8 (2012) 123–129. doi:10.1007/s13391-012-1089-z.

[27] R. Cuscó, E. Alarcón-Lladó, J. Ibáñez, L. Artús, J. Jiménez, B. Wang, M.J. Callahan, Temperature dependence of Raman scattering in ZnO, Phys. Rev. B. 75 (2007) 165202–165211. doi:10.1103/PhysRevB.75.165202.

[28] M. Berruet, C.J. Pereyra, G.H. Mhlongo, M.S. Dhlamini, K.T. Hillie, M. Vázquez, R.E. Marotti, Optical and structural properties of nanostructured ZnO thin films deposited onto FTO/glass substrate by a solution-based technique, Opt. Mater. (Amst). 35 (2013) 2721–2727. doi:10.1016/J.OPTMAT.2013.08.018.

[29] W. Ma, Z. Lu, M. Zhang, Investigation of structural transformations in nanophase titanium dioxide by Raman spectroscopy, Appl. Phys. A. 66 (1998) 621–627. doi:10.1007/s003390050723.

[30] M.P.F. Graça, C. Nico, M. Peres, M.A. Valente, T. Monteiro, Study of the Optical and Dielectric Properties of TiO2 Nanocrystals Prepared by the Pechini Method, J. Nanosci. Nanotechnol. 12 (2012) 8600–8606. doi:10.1166/jnn.2012.6819.

[31] Ü. Özgür, Y.I. Alivov, C. Liu, A. Teke, M.A. Reshchikov, S. Doğan, V. Avrutin, S.-J. Cho, H. Morkoç, A comprehensive review of ZnO materials and devices, J. Appl. Phys. 98 (2005) 041301. doi:10.1063/1.1992666.

[32] B.K. Meyer, H. Alves, D.M. Hofmann, W. Kriegseis, D. Forster, F. Bertram, J. Christen, A. Hoffmann, M. Straßburg, M. Dworzak, U. Haboeck, A. V Rodina, Bound exciton and donor–acceptor pair recombinations in ZnO, Phys. Status Solidi. 241 (2004) 231–260. doi:10.1002/pssb.200301962.

[33] J.I. Pankove, Optical Processes in Semiconductors, Dover Publications, 2012.

[34] A.B. Djurišić, Y.H. Leung, Optical Properties of ZnO Nanostructures, Small. 2 (2006) 944–961. doi:10.1002/smll.200600134.

[35] M. Peres, S. Magalhães, M.R. Soares, M.J. Soares, L. Rino, E. Alves, K. Lorenz, M.R. Correia, A.C. Lourenço, T. Monteiro, Disorder induced violet/blue luminescence in rf-deposited ZnO films, Phys. Status Solidi C. 10 (2013) 662–666. doi:10.1002/pssc.201200873.

[36] J. Rodrigues, M. Peres, M.R.N. Soares, A.J.S. Fernandes, N. Ferreira, M. Ferro, A.J. Neves, T. Monteiro, F. Costa, ZnO Nano/Microstructures Grown by Laser Assisted Flow Deposition, J. Nano Res. 18 (2012) 129–137. doi:10.4028/www.scientific.net/JNanoR.18-19.129.

[37] M.A. Reshchikov, H. Morkoç, B. Nemeth, J. Nause, J. Xie, B. Hertog, A. Osinsky, Luminescence properties of defects in ZnO, Phys. B Condens. Matter. 401–402 (2007) 358–361. doi:10.1016/J.PHYSB.2007.08.187.

[38] T. Monteiro, A.J. Neves, M.C. Carmo, M.J. Soares, M. Peres, J. Wang, E. Alves, E. Rita, U. Wahl, Near-band-edge slow luminescence in nominally undoped bulk ZnO, J. Appl. Phys. 98 (2005) 013502 (1–6). doi:10.1063/1.1946200.

[39] A. Pimentel, J. Rodrigues, P. Duarte, D. Nunes, F.M. Costa, T. Monteiro, R. Martins, E. Fortunato, Effect of solvents on ZnO nanostructures synthesized by solvothermal method assisted by microwave radiation: a photocatalytic study, J. Mater. Sci. 50 (2015) 5777–5787. doi:10.1007/s10853-015-9125-7.

[40] C.H. Ahn, Y.Y. Kim, D.C. Kim, S.K. Mohanta, H.K. Cho, A comparative analysis of deep level emission in ZnO layers deposited by various methods, J. Appl. Phys. 105 (2009) 013502. doi:10.1063/1.3054175.

[41] R. Pässler, E. Griebl, H. Riepl, G. Lautner, S. Bauer, H. Preis, W. Gebhardt, B. Buda, D.J. As, D. Schikora, K. Lischka, K. Papagelis, S. Ves, Temperature dependence of exciton peak energies in ZnS, ZnSe, and ZnTe epitaxial films, J. Appl. Phys. 86 (1999) 4403–4411. doi:10.1063/1.371378.

[42] R. Pässler, F. Blaschta, E. Griebl, K. Papagelis, B. Haserer, T. Reisinger, S. Ves, W.

Gebhardt, Temperature and Composition Dependence of Exciton Peak Positions and Band Gap Energies of Zn1—xMgx(≤0.19)Se Epitaxial Films, Phys. Status Solidi. 204 (1997) 685–699. doi:10.1002/1521-3951(199712)204:2<685::AID-PSSB685>3.0.CO;2-1.

[43] C. Boemare, T. Monteiro, M.J. Soares, J.G. Guilherme, E. Alves, Photoluminescence studies in ZnO samples, Phys. B Condens. Matter. 308–310 (2001) 985–988. doi:10.1016/S0921-4526(01)00854-7.

[44] C. Yilmaz, U. Unal, Effect of Zn(NO3)2 concentration in hydrothermal–electrochemical deposition on morphology and photoelectrochemical properties of ZnO nanorods, Appl. Surf. Sci. 368 (2016) 456–463. doi:10.1016/J.APSUSC.2016.01.253.

[45] H. Mandal, S. Shyamal, P. Hajra, B. Samanta, P. Fageria, S. Pande, C. Bhattacharya, Improved photoelectrochemical water oxidation using wurtzite ZnO semiconductors synthesized through simple chemical bath reaction, Electrochim. Acta. 141 (2014) 294–301. doi:10.1016/J.ELECTACTA.2014.06.013.

[46] D. Siopa, S. Serio, M.E. Melo Jorge, A.S. Viana, A. Gomes, ZnO Seed Layers Prepared by DC Reactive Magnetron Sputtering to be Applied as Electrodeposition Substrates, J. Electrochem. Soc. 163 (2016) H697–H704. doi:10.1149/2.0741608jes.

[47] R. Tena-Zaera, J. Elias, C. Lévy-Clément, C. Bekeny, T. Voss, I. Mora-Seró, J. Bisquert, Influence of the Potassium Chloride Concentration on the Physical Properties of Electrodeposited ZnO Nanowire Arrays, J. Phys. Chem. C. 112 (2008) 16318–16323. doi:10.1021/jp804563a.

[48] W.-D. Zhang, L.-C. Jiang, J.-S. Ye, Photoelectrochemical Study on Charge Transfer Properties of ZnO Nanowires Promoted by Carbon Nanotubes, J. Phys. Chem. C. 113 (2009) 16247–16253. doi:10.1021/jp905500n.

[49] H. Liu, G. Piret, B. Sieber, J. Laureyns, P. Roussel, W. Xu, R. Boukherroub, S. Szunerits, Electrochemical impedance spectroscopy of ZnO nanostructures, Electrochem. Commun. 11 (2009) 945–949. doi:10.1016/J.ELECOM.2009.02.019.

[50] O. Lupan, T. Pauporté, L. Chow, B. Viana, F. Pellé, L.K. Ono, B. Roldan Cuenya, H. Heinrich, Effects of annealing on properties of ZnO thin films prepared by electrochemical deposition in chloride medium, Appl. Surf. Sci. 256 (2010) 1895–1907. doi:10.1016/J.APSUSC.2009.10.032.

[51] Z.L. Wang, Zinc oxide nanostructures: growth, properties and applications, J. Phys. Condens. Matter. 16 (2004) R829--R858. doi:10.1088/0953-8984/16/25/r01.

[52] V.R. Kopach, K.S. Klepikova, N.P. Klochko, G.S. Khrypunov, V.E. Korsun, V.M. Lyubov, M. V Kirichenko, A. V Kopach, Structure and properties of nanostructured ZnO arrays and ZnO/Ag nanocomposites fabricated by pulsed electrodeposition, Semiconductors. 51 (2017) 335–343. doi:10.1134/S1063782617030125.

[53] B. Mukherjee, W. Wilson, V. (Ravi) Subramanian, TiO2 nanotube (T_NT) surface treatment revisited: Implications of ZnO, TiCl4, and H2O2 treatment on the photoelectrochemical properties of T_NT and T_NT–CdSe, Nanoscale. 5 (2013) 269–274. doi:10.1039/C2NR31660A.

Chapter V

Influence of the ZnO deposition media on the $CH_3NH_3PbI_3$ formation time and thermal stability

5.1. Introduction

Over the last decade, the metal halide perovskites have emerged as a new material with great potential for efficient solar energy conversion. Since their first report in 2009, where methylammonium lead halide perovskites were used as sensitizers in photovoltaic devices [1], the energy conversion efficiencies have increased dramatically from the initial 3.8 % to the record certified efficiencies of 25.2 %, which have recently been reported in the literature [2]. Therefore, these materials have potential competitors with the best solar technologies, including crystalline silicon [3].

The most reported material used in perovskite solar cells (PSCs) is $CH_3NH_3PbI_3$ [4], for which has been studied different methodologies of synthesis [5], architectures [6], ETL and HTL materials [7]. Considering the metal oxides that have been reported in PSCs, TiO_2 nanostructure films are the most widely used due to their good electron mobility, which is essential to achieve high photovoltaic performance. However, the high annealing temperatures that TiO_2 films require preclude their future applicability on flexible plastic substrates. Therefore, ZnO is a viable alternative to TiO_2 since it has physical properties similar to TiO_2, and its structure can be easily obtained at a low temperature of synthesis.

Many reports of ZnO as an ETL in PSCs have emerged [8], revealing some issues that require further attention, namely the thermal instability of the perovskite film coated on top of the ZnO layer [9]. It was found that the dark brown perovskite film, when deposited on top of the ZnO layer, turned yellow after a few minutes during the perovskite' annealing process, indicating a fast degradation of the $CH_3NH_3PbI_3$ film when the temperature exceeded 90 °C [9,10].

In this chapter, the use of ZnO compact films on perovskite cells will be investigated. The research will be focused on how the deposition condition of ZnO films, more precisely the deposition media (aqueous, ionic liquid or organic), affects the long-term stability of ZnO-based PSCs. These results will allow optimising the conditions of the perovskite' annealing process when applied on ZnO nanorod arrays. All the ZnO-based PSCs results will be compared to those obtained with TiO_2 compact films.

5.2. Effect of the ZnO deposition conditions on the $CH_3NH_3PbI_3$ formation

Four different ZnO thin films were prepared using different methods, namely spray-pyrolysis, electrodeposition and spin-coating. Furthermore, each technique used different media, i.e., spray-pyrolysis method used aqueous media (hereafter "ZnOsp"), electrodeposition method used ionic liquid media (hereafter "ZnOil), and spin-coating method used organic media with (hereafter "$ZnONP_{ac}$") and without the addition of acid (hereafter "ZnOnp"). In Figure 5.1, top-view SEM micrographs of the different ZnO thin films. For comparison, a thin compact TiO_2 layer was also studied. All the thin films were transparent and uniform to the naked eye. In general, it is well known that growth morphology depends on the growth method and media. It has been reported that interactions with the substrate and among the growing particles play an important role in the nucleation and first growth stage [11]. The ZnOsp thin films show a high density of nano-aggregates forms on the substrate, causing some surface roughness that may be due to the FTO coated substrate. Similar results were reported for ZnO thin films fabricated by spray pyrolysis using zinc acetate precursor solution at different growth temperatures [12]. The ZnOil thin films exhibit a smooth surface constituted of close-packed agglomerates with a round-top shape of 100-200 nm in diameter. The adsorption of the IL moieties onto the ZnO surfaces, hindering the grain growth, may be the origin of the relatively smaller grains [13]. The synthesis method of the ZnO nanoparticles seems to affect the ZnO thin film morphology prepared by the spin-coating technique. The ZnOnp thin films showed a smooth grain-like surface morphology constituted of small nanoparticle aggregates. Though, the $ZnONP_{ac}$ thin films appear to be porous, exhibiting some micro-cracks. Generally, the thickness and morphology of the coatings prepared by spin-coating depend on the speed at which solution spreads, concentration, viscosity and surface tension of the respective solution, temperature and relative humidity [14].

Figure 5.1 illustrates the surface and cross-section SEM micrographs of perovskite film deposited on TiO_2 and ZnO thin films. In general, the surface morphology of perovskite films is similar, exhibiting dense-packed grains with sizes of about 100 ~ 500 nm, except on ZnOil and $ZnONP_{ac}$ thin films, which present smaller grain sizes. Moreover, as shown in Figure 5.1, from cross-section SEM micrographs, void-free perovskite layers with 400 ~ 500 nm of thickness on ZnO films and 500 ~ 600 nm on TiO_2 film were observed. One of the advantages of using a two-step coating method to prepare $CH_3NH_3PbI_3$ layers is full coverage of the semiconductor layer used as electron transport material (ETM) compared with the one-step spin-coating method [15]. Several parameters influence the perovskite morphology due to

different crystallization mechanisms, namely the annealing process, precursor solvent, anti-solvent treatment, and additives to the perovskite solution [16]. The annealing process has two principal functions on the perovskite formation: (1) driving the interdiffusion of PbI_2 and MAI precursors to form perovskite, and (2) inducing the recrystallization and grain growth in the formed perovskite films. Furthermore, the annealing time plays a vital role in the crystalline grain size, i.e., the crystalline grain size increases gradually with the thermal annealing time, reducing the grain boundaries [17]. However, long annealing times may lead to chemical stability issues yielding to the decomposition process of perovskite [18].

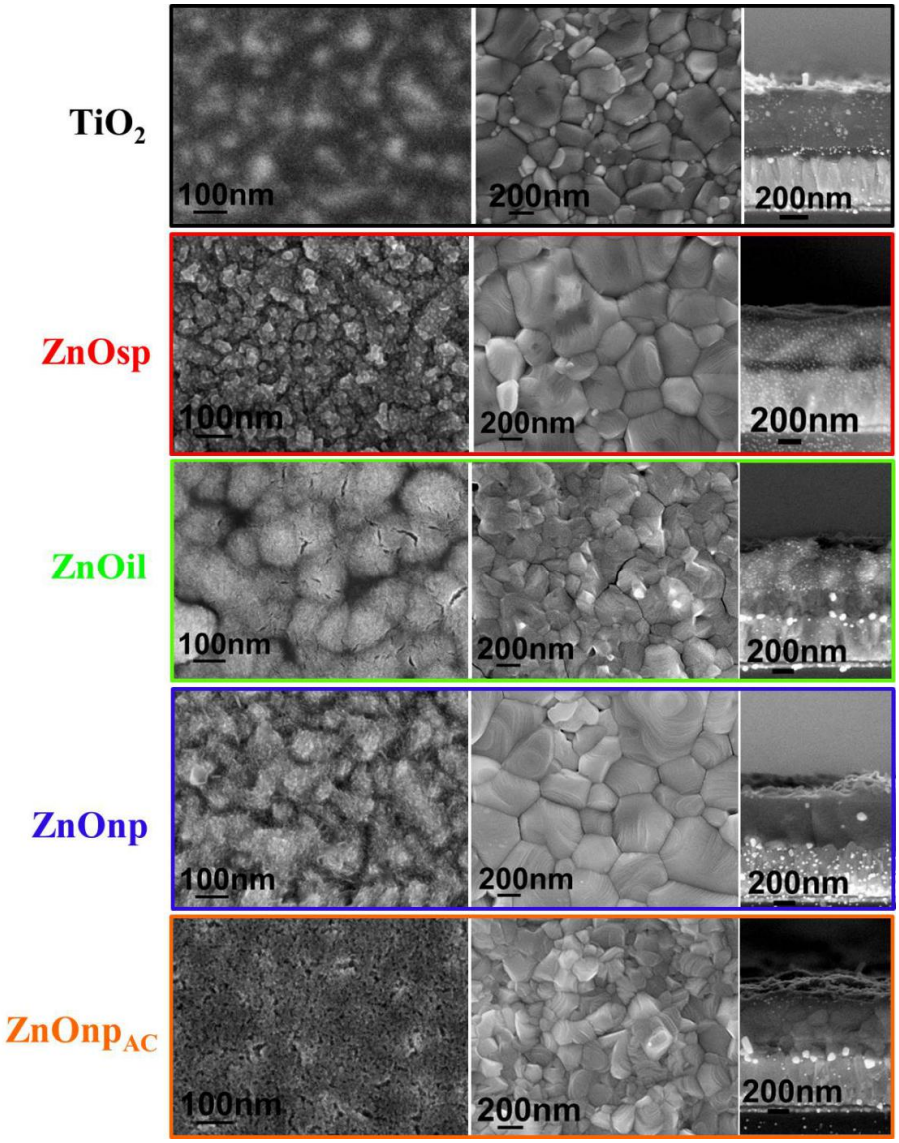

Figure 5.1 - Top-view SEM micrographs of the TiO_2 and ZnO thin films before (left) and after coating with the perovskite film (centre) and the respective cross-section SEM micrographs (right). The nomenclature sp, il, np, and np_{AC} means spray pyrolysis, electrodeposition in ionic liquid, spin-coated nanoparticles film, and spin-coated nanoparticles film with acid, respectively.

The influence of the annealing time on the chemical stability of the perovskite film was then evaluated. Figure 5.2 shows the visual monitoring of perovskite films on TiO_2 and ZnO films annealed at 100 ºC at different times. It has already been reported that $CH_3NH_3PbI_3$ film on TiO_2 layers is chemically stable after annealing at 100 ºC for a long time [19]. However, the $CH_3NH_3PbI_3$ perovskite film on ZnO films turns from dark brown to yellow, varying from minutes to hours depending on the ZnO processing method and media. This behaviour has been widely reported for ZnO-based perovskite solar cells in which $CH_3NH_3PbI_3$ crystals severely decompose into PbI_2 during the annealing process when in direct contact with the ZnO layer [9,10]. The origin of such decomposition may be due to the basic nature of the ZnO surface [20] and/or by the presence of surface hydroxyl groups and residual acetate ligands on the ZnO surface [9].

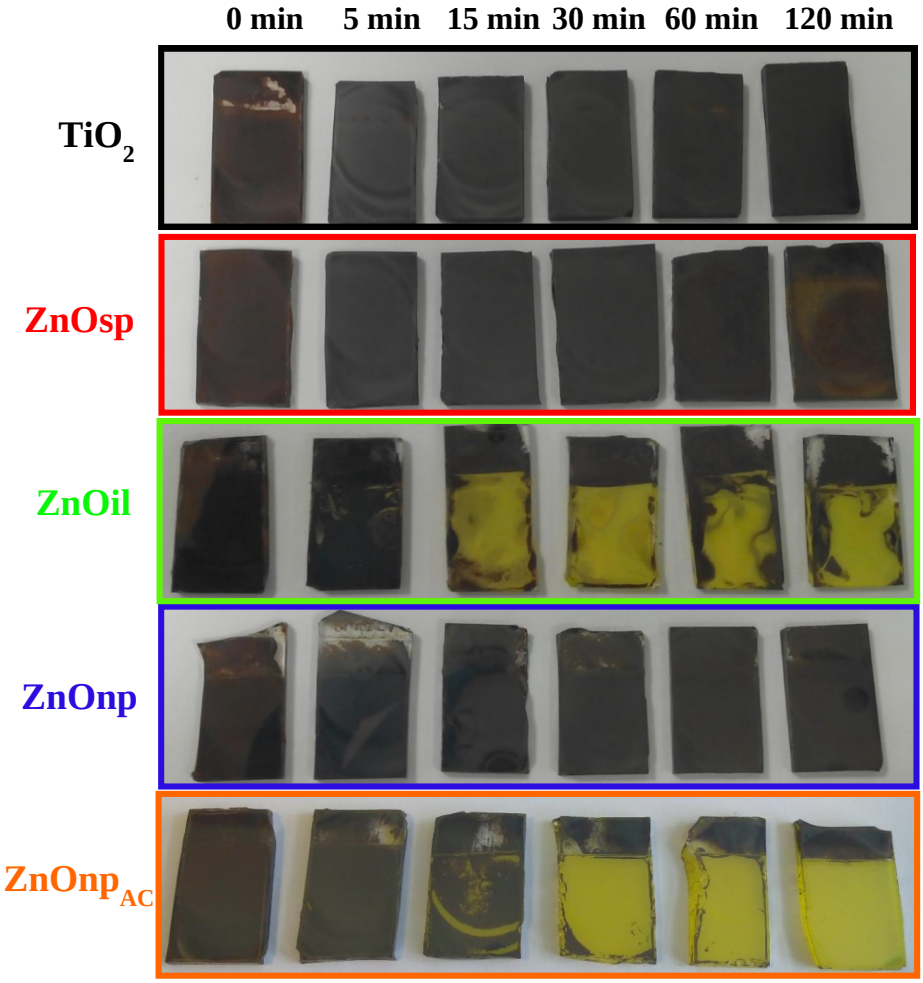

Figure 5.2 - Photographs of $CH_3NH_3PbI_3$ films deposited on TiO_2 and ZnO thin films and heated at 100 ºC for the indicated time. The nomenclature sp, il, np, and np_{AC} means spray pyrolysis, electrodeposition in ionic liquid, spin-coated nanoparticles film, and spin-coated nanoparticles film with acid, respectively.

The thermal stability of $CH_3NH_3PbI_3$ perovskite films deposited on ZnO films at 100 ºC has been further characterized by XRD measurements in Figure 5.3. The diffractograms of as-deposited $CH_3NH_3PbI_3$ films on TiO_2 and ZnO films present two main diffraction peaks at ~12.7 º and ~14.0 º which were assigned to the PbI_2 and $MAPbI_3$ reflections, respectively. Additionally, the diffraction peak at ~14.0 º can be integrated into two different diffraction peaks, (002) and (110) planes of the $MAPbI_3$ tetragonal phase [21]. After 5 min of annealing time, the reflection peak related to PbI_2 decreases mainly for perovskite films deposited on ZnO films and increases the intensity of the diffraction peak at ~14.0 º assigned to (100) plan of $MAPbI_3$ cubic phase [22]. After 15 min, depending on the ZnO processing method and media, the PbI_2 peak increased intensity. The peak related to $MAPbI_3$ decreased, and in some cases, has become absent, like happened for the perovskite layer on ZnOil film. As the annealing time increases, the PbI_2 peak happened to be the main reflection being evidence of fast degradation of the perovskite layer deposited on ZnO. J. Zhang *et al.* [23] reported that in the case of ZnO underlayers, the perovskite annealing must be short to avoid the decomposition reaction and PbI_2 formation, as described in the following equation,

$$CH_3NH_3PbI_3 \xrightarrow{100\,°C,\ ZnO} PbI_2 + CH_3NH_2 \uparrow + HI \uparrow \quad (5.1)$$

On the other hand, the perovskite layers deposited on ZnOnp films seemed to be chemical stable at least 60 min of thermal annealing, presenting a similar behaviour as the perovskite layers on TiO_2 films.

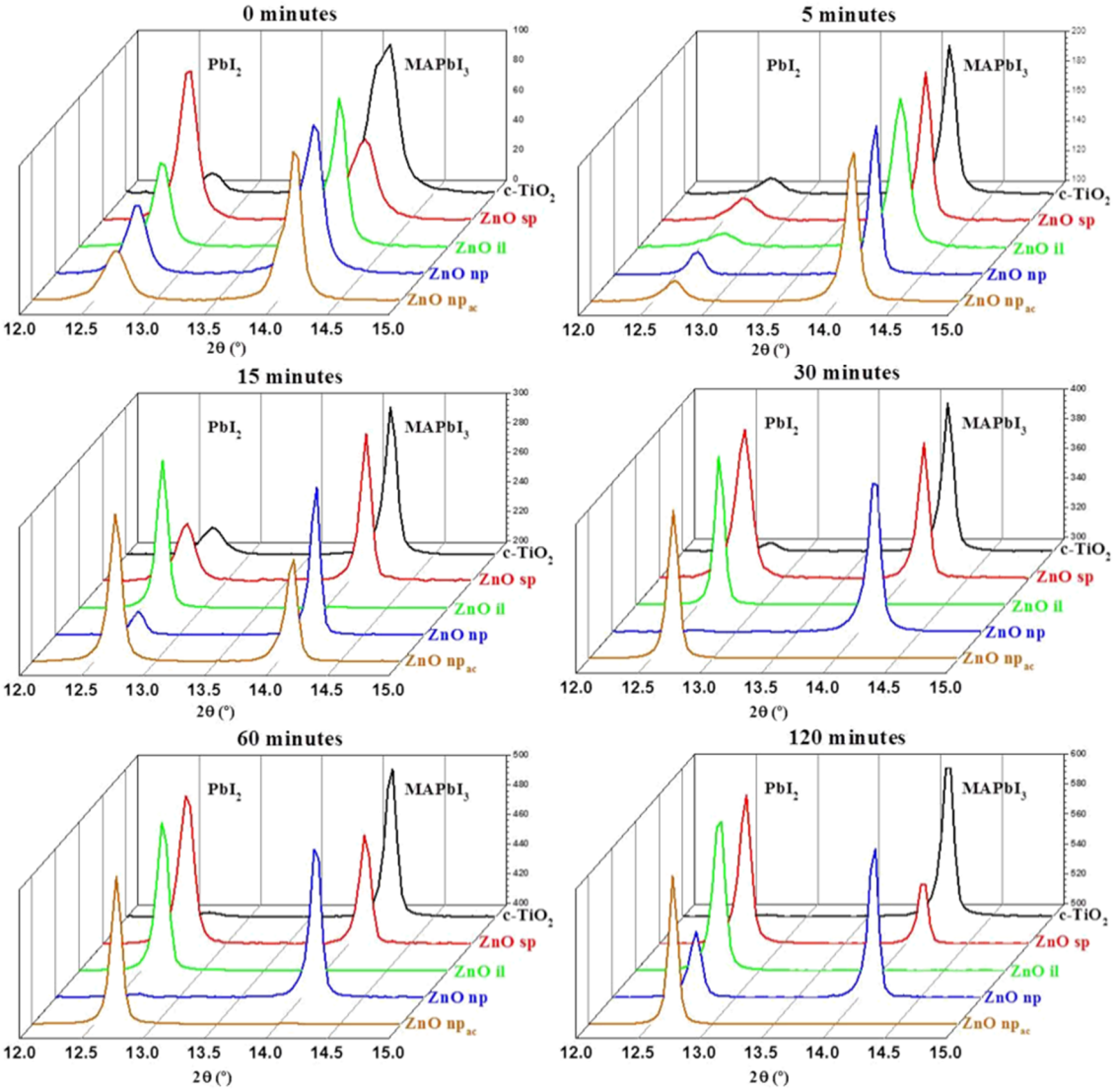

Figure 5.3 - X-ray diffraction patterns of $CH_3NH_3PbI_3$ films deposited on TiO_2 and ZnO thin films and heated at 100 ℃ for the indicated time. The nomenclature sp, il, np, and np_{AC} means spray pyrolysis, electrodeposition in ionic liquid, spin-coated nanoparticles film, and spin-coated nanoparticles film with acid, respectively.

To further understand what causes the decomposition of perovskite films on ZnO underlayers with thermal annealing, we investigated the chemical structure of ZnO film surfaces by X-ray photoelectron spectroscopy (XPS).

The survey spectra for ZnO thin films prepared in different deposition media in the full binding-energy (BE) range 0-1200 eV are presented in Figure 5.4. All the peak intensities were normalised to the high resolution of Zn2p peaks. The XPS spectra of all the ZnO samples revealed apart of the typical Auger electron lines ZnKLL, the core level lines Zn2p, O1s, Zn3s, Zn3p, and Zn3d that proves the presence of ZnO material. Moreover, a contribution of carbon contamination at ZnO thin films surface was observed, as confirmed by the presence of XPS C1s lines at BE ~286 eV [24]. More in detail, the ZnOil sample also

revealed an F contamination by the presence of XPS F1s and FKLL lines [25], which could be due to the remains of the electrolytic bath used in its preparation. Also, the ZnOnp sample contains an Sn contamination by the presence of XPS Sn3d and Sn4d lines that indicate that the Sn was oxidized [26]. However, this Sn contamination detected on the ZnOnp sample may not be surface contamination but instead, the detection of the SnO_2 from the FTO substrate, since the ZnOnp layer was not continuous on all the area analysed by XPS, as can be seen by SEM analysis in Figure 5.1.

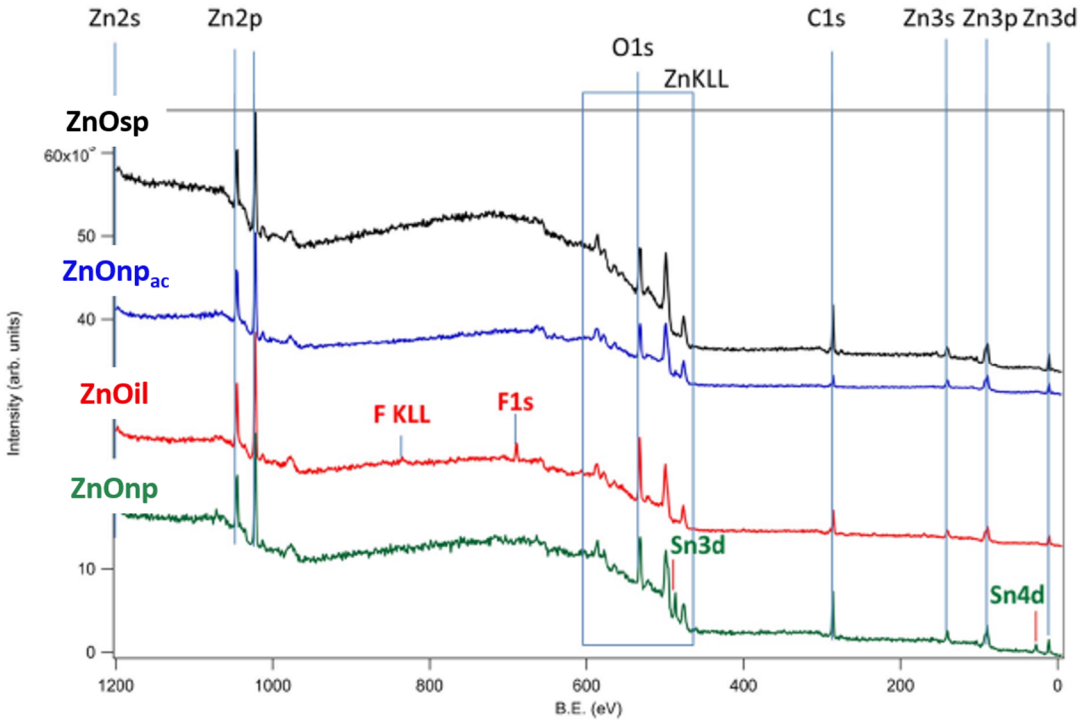

Figure 5.4 - XPS wide survey spectra of various ZnO thin films prepared by different deposition media, namely ZnOsp, ZnOil, $ZnOnp_{ac}$, and ZnOnp obtained in aqueous, ionic liquid, and organic media with and without the addition of acid, respectively.

Figure 5.5 shows the XPS profiles of Zn2p of all the ZnO thin film samples comparatively to an XPS profile of ZnO single crystal as a reference. The Zn2p spectra show a sharp and symmetric peak at BE around 1023 eV, associated with the Zn species in the completely oxidised state [27]. This affirmation was confirmed by the Zn2p spectra of all the ZnO samples that appeared at the same BE as the ZnO single crystal reference.

Figure 5.6 shows the XPS spectra of O1s of all the ZnO samples, and the O1s peak shows an asymmetric shape, which can be deconvoluted into two subpeaks at BE around 531 and 533 eV. The subpeak at lower BE can be ascribed to O atoms of the Zn-O bond [28]. On the other hand, the subpeak at high BE can be associated with Zn hydroxides (Zn-OH), the main

component in the ZnOil sample [29]. In general, the intensities of the different O1s peaks are similar, with a 25 % discrepancy.

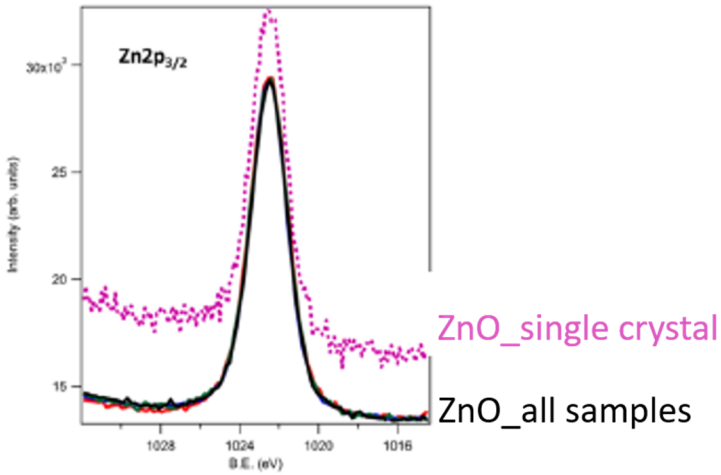

Figure 5.5 - XPS spectra of $Zn2p_{3/2}$ of all the studied ZnO thin film samples compared with ZnO single crystal.

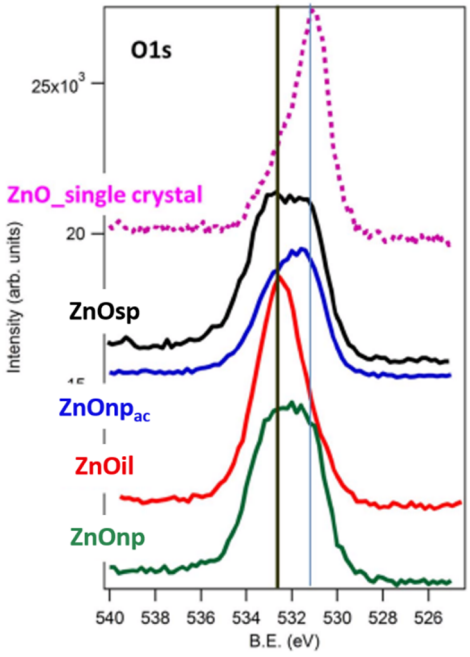

Figure 5.6 - XPS spectra of O1s of various ZnO thin films prepared by different deposition media, namely ZnOsp, ZnOil, $ZnOnp_{ac}$, and ZnOnp obtained in aqueous, ionic liquid, and organic media with and without the addition of acid, respectively, compared with ZnO single crystal.

Considering the main contaminant, the presence of C, it is crucial to understand the origin of this contamination and how it will affect the performance of these thin films on PSCs. Figure 5.7 a) shows the main C1s peak for all the ZnO samples, where the C1s core lines are centred around 286 eV, although there are clear shifts between them. It is also evident that the

amount of C differs substantially, depending on the ZnO sample. The O/C ratio for the ZnO samples decreased in the following order: 3.5, 3, 1.1, and 1.0 for the $ZnOnp_{ac}$, ZnOil, ZnOnp, and ZnOsp, respectively. According to the literature, the main C1s peak is commonly attributed to air contaminants, mainly hydrocarbons, that usually presented BE centred around 285 eV [30]. The shifts toward higher BE indicate the presence of extra components or C-O bonds, such as C-O or C=O species [30]. By analysing the XPS spectra in full scan, Figure 5.7 b), an additional peak at BE around 289.5 eV was observed for ZnOil and $ZnOnp_{ac}$ samples. The BE position is typically associated with carboxyl or carbonate groups [31,32].

Additionally, the ZnOil sample shows a peak at BE around 293 eV, which can be ascribed to C-F bonds. This is in agreement with the F1s peak (Figure 5.7 c)) that appears at 689.6 eV, which is compatible with CF_2=CF_2 species [33]. The origin of these C-O and C-F contaminations could be from the compounds used to synthesise the $ZnOnp_{ac}$ and ZnOil samples.

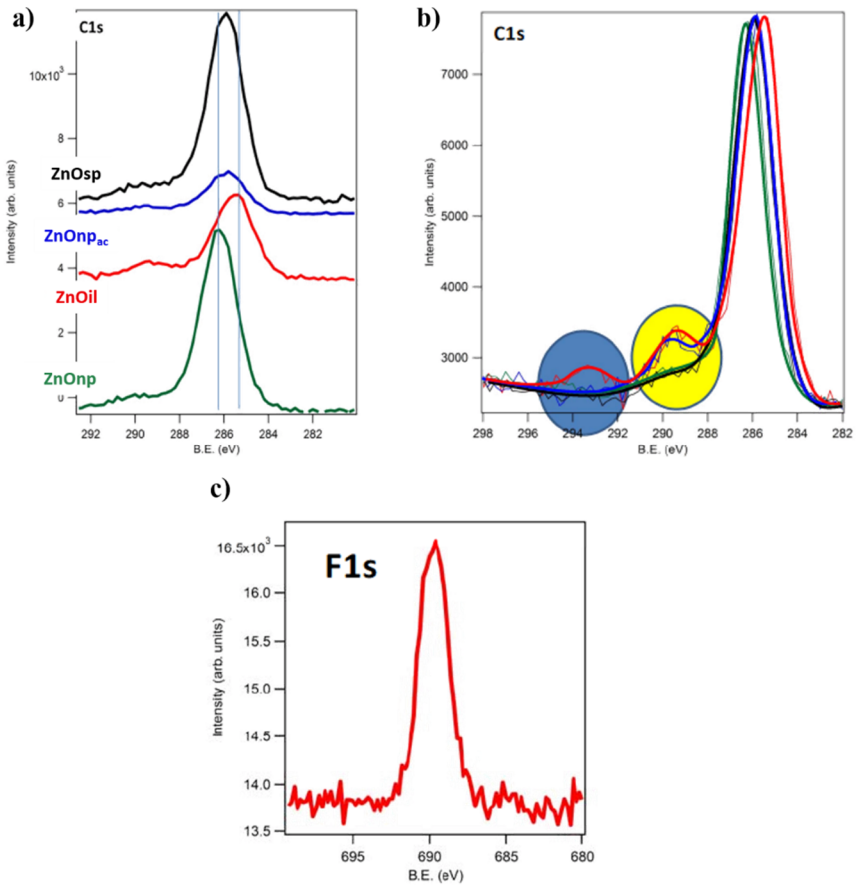

*Figure 5.7 - XPS spectra of C1s of various ZnO thin films prepared by different deposition media, namely ZnOsp, ZnOil, $ZnOnp_{ac}$, and ZnOnp obtained in aqueous, ionic liquid, and organic media with and without the addition of acid, respectively. The main peak is represented in **a)** and a full scan in **b)**. **c)** XPS spectrum of F1s of the ZnO_oil sample.*

Correlating the XPS data with the visual aspect and the XRD spectra, the faster degradation of the perovskite films is evident when deposited on ZnO thin films in which carboxyl/carbonate groups were detected, namely the $ZnOnp_{ac}$ and ZnOil thin films. This faster degradation of the perovskite films will compromise the PSC performance.

5.3. Effect of the ZnO deposition method on the performance of $CH_3NH_3PbI_3$ devices

The photovoltaic (PV) parameters of the best FTO/TiO_2 and FTO/ZnO/$CH_3NH_3PbI_3$/Spiro-OMeTAD/Au devices as a function of the perovskite' annealing time are depicted in Figure 5.8 and Table 5.1. The presented results considered an active area of 0.07 cm^2 and are an average of the three best devices. The corresponding PV values were obtained from *I-V* curves measured at the reverse mode (from the open-circuit voltage (V_{oc}) to the short-circuit current (J_{sc})) under the illumination of AM 1.5 G simulated Sunlight.

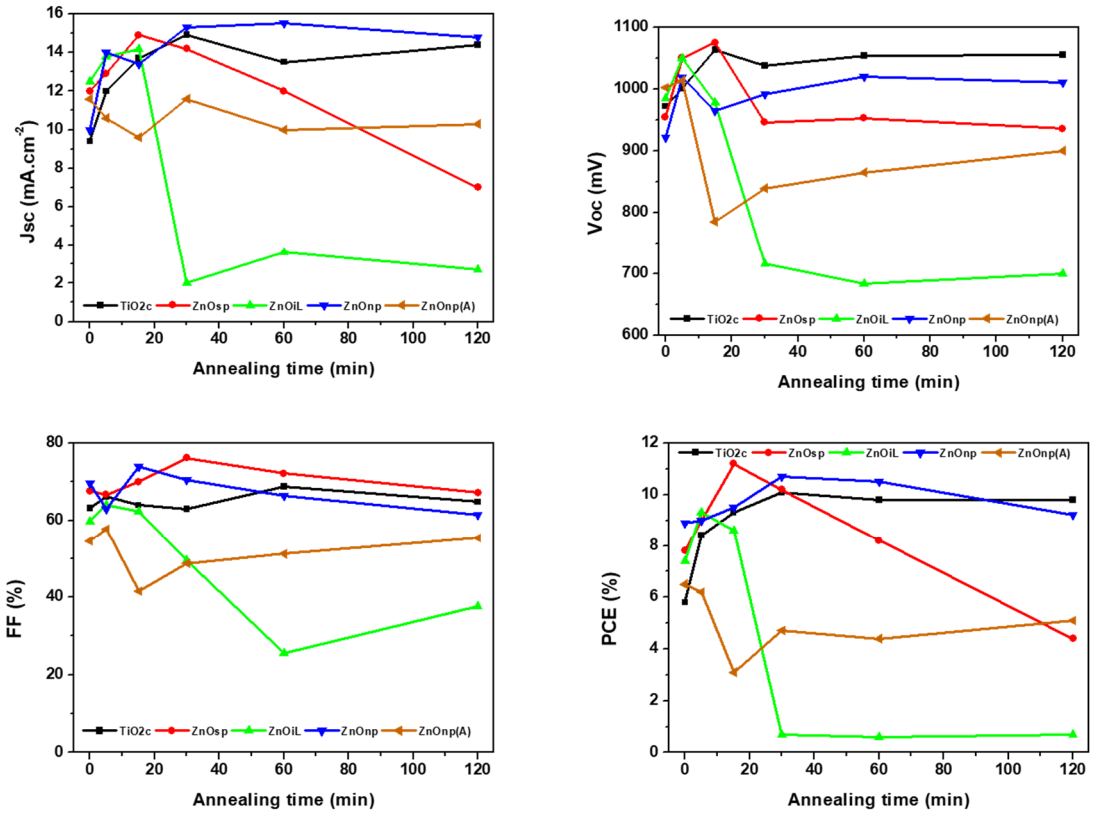

Figure 5.8 - Effect of $CH_3NH_3PbI_3$ thin films on photovoltaic parameters, short-circuit current density (J_{sc}), open-circuit voltage (V_{oc}), fill factor (FF), and power conversion efficiency (PCE) versus the perovskite's annealing time. The annealing temperature was constant at 100 ℃. The nomenclature sp, il, np, and np_{AC} means spray pyrolysis, electrodeposition in ionic liquid, spin-coated nanoparticles film, and spin-coated nanoparticles film with acid, respectively.

Table 5.1 - Photovoltaic performance parameters of the best $CH_3NH_3PbI_3$ devices.

A) TiO_2 compact

Annealing time (min)	J_{SC} (mA cm^{-2})	V_{OC} (mV)	*FF* (%)	*PCE* (%)
0	9.4	972	63.1	5.8
5	12.0	1001	66.1	8.4
15	13.7	1063	63.9	9.3
30	14.9	1038	63.0	10.1
60	13.5	1054	68.8	9.8
120	14.4	1055	64.8	9.8

B) ZnO spray-pyrolysis

Annealing time (min)	J_{SC} (mA cm^{-2})	V_{OC} (mV)	*FF* (%)	*PCE* (%)
0	12.0	955	67.6	7.8
5	12.9	1050	66.7	9.0
15	14.9	1075	70.0	11.2
30	14.2	946	76.1	10.2
60	12.0	953	72.2	8.2
120	7.0	936	67.2	4.4

C) ZnO nanoparticles

Annealing time (min)	J_{SC} (mA cm^{-2})	V_{OC} (mV)	*FF* (%)	*PCE* (%)
0	10.0	921	69.7	8.9
5	14.0	1019	63.0	9.0
15	13.4	965	73.9	9.5
30	15.3	991	70.5	10.7
60	15.5	1020	66.3	10.5
120	14.8	1011	61.4	9.2

D) ZnO ionic liquid

Annealing time (min)	J_{SC} (mA cm^{-2})	V_{OC} (mV)	*FF* (%)	*PCE* (%)
0	12.5	985	59.8	7.4
2.5	13.1	1059	61.7	8.6
5	13.8	1049	64.1	9.3
15	14.2	978	62.2	8.6
30	2.0	716	49.6	0.7
60	3.6	683	25.6	0.6
120	2.7	700	37.7	0.7

E) ZnO nanoparticles (acid)

Annealing time (min)	J_{SC} (mA cm^{-2})	V_{OC} (mV)	*FF* (%)	*PCE* (%)
0	11.6	1002	54.6	6.5
2.5	13.0	981	60.3	7.7
5	10.6	1014	57.7	6.2
15	9.6	785	41.5	3.1
30	11.6	839	48.7	4.7
60	10.0	865	51.2	4.4
120	10.3	900	55.4	5.1

The PV parameters for optimized conditions of $CH_3NH_3PbI_3$ devices are presented in Table 5.2. The PCE of the devices with TiO_2 layers increased with the annealing time until reaching a constant value of around 10 % after 30 min of annealing. However, the PCE depended on the ZnO preparation method and media for devices with ZnO layers. The devices of $CH_3NH_3PbI_3$ films deposited on ZnOsp layers showed an increase of PCE up to a maximum of 11.2 % for 15 min of annealing, decreasing after that. On the other hand, the devices with $ZnOnp_{ac}$ and ZnOil layers showed that the PCE decreases after only 2.5 to 5 min of annealing, obtaining a PCE maximum of 7.7 and 9.3 %, respectively. However, the devices with ZnOnp layers presented similar results to those with TiO_2 layers, increasing PCE up to 10.7 % after 30 min of annealing and decreasing only after 120 min. The perovskite morphology can explain the difference in PCE. The small grain size obtained for perovskite

crystals deposited on ZnOil and $ZnONp_{ac}$ layers produced many grain boundaries that generated recombination of photocurrent that may affect the overall device performance. It was also reported previously that the presence of a certain amount of PbI_2 phase passivates the perovskite layer, reducing the recombination effects on ETM/perovskite interface, leading to improved carrier performance of devices [34], which was observed for perovskite layer deposited on TiO_2 and ZnOsp layers. The main reason for the decrease of J_{sc} and V_{oc} values in the ZnOsp, $ZnONp_{ac}$ and ZnOil-based perovskite devices is the decomposition of the perovskite film into PbI_2, which has lower light absorption and is relatively electrically insulating [10] and was proved by the increase of PbI_2 diffraction peak with the annealing time. However, the improved V_{oc} values suggest that the electron transport layers successfully extracted carriers from the perovskite due to their intimate contact verified by cross-section SEM micrographs. In conclusion, the ZnO based solar cells from methanolic suspensions of capping agent-free ZnO nanoparticles appear to be an excellent candidate to compete with TiO_2 based solar cells.

Table 5.2 – Photovoltaic performance parameters for optimized conditions of $CH_3NH_3PbI_3$ devices.

Device	Annealing time (min)	J_{SC} (mA cm^{-2})	V_{OC} (mV)	*FF* (%)	η (%)
TiO_2/$CH_3NH_3PbI_3$/Spiro-OMeTAD	30	14.9	1038	63.0	10.1
ZnOsp/$CH_3NH_3PbI_3$/Spiro-OMeTAD	15	14.9	1075	70.0	11.2
ZnOil/$CH_3NH_3PbI_3$/Spiro-OMeTAD	5	13.8	1049	64.1	9.3
ZnONp/$CH_3NH_3PbI_3$/Spiro-OMeTAD	30	15.3	991	70.5	10.7
$ZnONp_{ac}$/$CH_3NH_3PbI_3$/Spiro-OMeTAD	2.5	13.0	981	60.3	7.7

5.4. Chapter Summary

In this chapter, the use of ZnO thin films on perovskite solar cells has been presented. ZnO nanostructures prepared by different deposition media were tested to evaluate if the ZnO nature influences the thermal stability of $CH_3NH_3PbI_3$ perovskite.

A correlation between the photovoltaic performance and the XRD patterns of the perovskite films has been found. The presence of a large amount of PbI_2 due to perovskite decomposition compromises photovoltaic performance. However, according to the presented results here, the formation of small amounts the PbI_2 can be beneficial to cell performance.

It seems that some chemical groups attached to the ZnO surface may affect the perovskite film crystallization, and consequently, the thermal stability of the ZnO/perovskite interface. For example, the perovskite films deposited on ZnOil and $ZnONp_{ac}$ thin films showed a faster degradation in which carboxyl groups were detected. This means that minimising the presence of surface functionalities on the ZnO surface can prevent the degradation process, increasing the long-term stability of these cells.

Overall, the problem of perovskite instability on ZnO is a significant obstacle and compromises its practical application. Efforts might, therefore, be made to understand if, besides the interfacial groups attached to the ZnO surface, the ETM morphology is also an issue that contributes to the ZnO/perovskite instability.

5.5. References

[1] A. Kojima, K. Teshima, Y. Shirai, T. Miyasaka, Organometal Halide Perovskites as Visible-Light Sensitizers for Photovoltaic Cells, J. Am. Chem. Soc. 131 (2009) 6050–6051. doi:10.1021/ja809598r.

[2] N.-G. Park, Research Direction toward Scalable, Stable, and High Efficiency Perovskite Solar Cells, Adv. Energy Mater. 10 (2020) 1903106. doi:https://doi.org/10.1002/aenm.201903106.

[3] M.A. Green, Y. Hishikawa, E.D. Dunlop, D.H. Levi, J. Hohl-Ebinger, M. Yoshita, A.W.Y. Ho-Baillie, Solar cell efficiency tables (Version 53), Prog. Photovoltaics Res. Appl. 27 (2019) 3–12. doi:10.1002/pip.3102.

[4] M.K. Assadi, S. Bakhoda, R. Saidur, H. Hanaei, Recent progress in perovskite solar cells, Renew. Sustain. Energy Rev. 81 (2018) 2812–2822. doi:10.1016/J.RSER.2017.06.088.

[5] N.-G. Park, Methodologies for high efficiency perovskite solar cells, NANO Converg. 3 (2016). doi:10.1186/s40580-016-0074-x.

[6] G.A. Al-Dainy, S.E. Bourdo, V. Saini, B.C. Berry, A.S. Biris, Hybrid Perovskite Photovoltaic Devices: Properties, Architecture, and Fabrication Methods, Energy Technol. 5 (2017) 373–401. doi:10.1002/ente.201600486.

[7] H.S. Jung, N.-G. Park, Perovskite Solar Cells: From Materials to Devices, Small. 11 (2015) 10–25. doi:10.1002/smll.201402767.

[8] J. Luo, Y. Wang, Q. Zhang, Progress in perovskite solar cells based on ZnO nanostructures, Sol. Energy. (2018). doi:10.1016/j.solener.2018.01.035.

[9] J. Yang, B.D. Siempelkamp, E. Mosconi, F. De Angelis, T.L. Kelly, Origin of the Thermal Instability in CH3NH3PbI3 Thin Films Deposited on ZnO, Chem. Mater. 27 (2015) 4229–4236. doi:10.1021/acs.chemmater.5b01598.

[10] Y. Cheng, Q.-D. Yang, J. Xiao, Q. Xue, H.-W. Li, Z. Guan, H.-L. Yip, S.-W. Tsang, Decomposition of Organometal Halide Perovskite Films on Zinc Oxide Nanoparticles, ACS Appl. Mater. Interfaces. 7 (2015) 19986–19993. doi:10.1021/acsami.5b04695.

[11] F.C.M. van de Pol, F.R. Blom, T.J.A. Popma, R.f. planar magnetron sputtered ZnO films I: Structural properties, Thin Solid Films. 204 (1991) 349–364. doi:10.1016/0040-6090(91)90074-8.

[12] Ü. Alver, A. Kudret, S. Tekerek, Spray pyrolysis deposition of ZnO thin films on FTO coated substrates from zinc acetate and zinc chloride precursor solution at different growth temperatures, J. Phys. Chem. Solids. 72 (2011) 701–704.

doi:10.1016/J.JPCS.2011.02.017.

[13] E. Azaceta, R. Tena-Zaera, R. Marcilla, S. Fantini, J. Echeberria, J.A. Pomposo, H. Grande, D. Mecerreyes, Electrochemical deposition of ZnO in a room temperature ionic liquid: 1-Butyl-1-methylpyrrolidinium bis(trifluoromethane sulfonyl)imide, Electrochem. Commun. 11 (2009) 2184–2186. doi:10.1016/J.ELECOM.2009.09.026.

[14] M. Smirnov, C. Baban, G.I. Rusu, Structural and optical characteristics of spin-coated ZnO thin films, Appl. Surf. Sci. 256 (2010) 2405–2408. doi:10.1016/J.APSUSC.2009.10.075.

[15] J.H. Im, H.S. Kim, N.G. Park, Morphology-photovoltaic property correlation in perovskite solar cells: One-step versus two-step deposition of CH3NH3PbI3, APL Mater. 2 (2014). doi:10.1063/1.4891275.

[16] B.-E. Cohen, L. Etgar, Parameters that control and influence the organo-metal halide perovskite crystallization and morphology, Front. Optoelectron. 9 (2016) 44–52. doi:10.1007/s12200-016-0630-3.

[17] C. Bi, Y. Shao, Y. Yuan, Z. Xiao, C. Wang, Y. Gao, J. Huang, Understanding the formation and evolution of interdiffusion grown organolead halide perovskite thin films by thermal annealing, J. Mater. Chem. A. 2 (2014) 18508–18514. doi:10.1039/C4TA04007D.

[18] A. Dualeh, P. Gao, S. Il Seok, M.K. Nazeeruddin, M. Grätzel, Thermal Behavior of Methylammonium Lead-Trihalide Perovskite Photovoltaic Light Harvesters, Chem. Mater. 26 (2014) 6160–6164. doi:10.1021/cm502468k.

[19] H. Zhou, Q. Chen, G. Li, S. Luo, T. Song, H.-S. Duan, Z. Hong, J. You, Y. Liu, Y. Yang, Interface engineering of highly efficient perovskite solar cells, Science (80-.). 345 (2014) 542–546. doi:10.1126/science.1254050.

[20] M. Kosmulski, Chemical Properties of Material Surfaces, Taylor & Francis, 2001. https://books.google.pt/books?id=l1c9ngEACAAJ.

[21] T. Oku, Crystal Structures of CH3NH3PbI3 and Related Perovskite Compounds Used for Solar Cells, in: L.A. Kosyachenko (Ed.), Sol. Cells, IntechOpen, Rijeka, 2015. doi:10.5772/59284.

[22] S. Luo, W. Daoud, Crystal structure formation of CH3NH3PbI3-xClx perovskite, Materials (Basel). 9 (2016) 123. doi:10.3390/ma9030123.

[23] J. Zhang, T. Pauporté, Effects of Oxide Contact Layer on the Preparation and Properties of CH3NH3PbI3 for Perovskite Solar Cell Application, J. Phys. Chem. C. 119 (2015) 14919–14928. doi:10.1021/acs.jpcc.5b02984.

[24] D. PARK, Y. TAK, J. KIM, K. YONG, LOW-TEMPERATURE SYNTHESIZED ZnO NANONEEDLES: XPS AND PL ANALYSIS, Surf. Rev. Lett. 14 (2007) 1061–1065. doi:10.1142/S0218625X07010639.

[25] J.F. Moulder, W.F. Stickle, P.E. Sobol, K.D. Bomben, Handbook of x-ray photoelectron spectroscopy: A reference book of standard spectra for identification and interpretation of XPS data, 18th ed., Physical Electronics Division, Perkin-Elmer Corp., Eden Prairie, Minnesota, 1992.

[26] M. Kwoka, B. Lyson-Sypien, A. Kulis, D. Zappa, E. Comini, Surface Properties of SnO2 Nanowires Deposited on Si Substrate Covered by Au Catalyst Studies by XPS, TDS and SEM, Nanomaterials. 8 (2018) 738. doi:10.3390/nano8090738.

[27] X. Wang, K. Huo, F. Zhang, Z. Hu, P.K. Chu, H. Tao, Q. Wu, Y. Hu, J. Zhu, Structural Regulation and Optical Properties of One-Dimensional ZnO Nanomaterials in Situ Grown from and on Brass Substrates, J. Phys. Chem. C. 113 (2009) 170–173. doi:10.1021/jp808679q.

[28] X.-J. Yang, X.-Y. Miao, X.-L. Xu, C.-M. Xu, J. Xu, H.-T. Liu, Structure, X-ray photoelectron spectroscopy and photoluminescence properties of highly ordered ZnO microrods, Opt. Mater. (Amst). 27 (2005) 1602–1605. doi:https://doi.org/10.1016/j.optmat.2004.05.007.

[29] J. Duchoslav, R. Steinberger, M. Arndt, D. Stifter, XPS study of zinc hydroxide as a potential corrosion product of zinc: Rapid X-ray induced conversion into zinc oxide, Corros. Sci. 82 (2014) 356–361. doi:https://doi.org/10.1016/j.corsci.2014.01.037.

[30] G. Greczynski, L. Hultman, C 1s Peak of Adventitious Carbon Aligns to the Vacuum Level: Dire Consequences for Material's Bonding Assignment by Photoelectron Spectroscopy, ChemPhysChem. 18 (2017) 1507–1512. doi:https://doi.org/10.1002/cphc.201700126.

[31] D.R. Dreyer, S. Park, C.W. Bielawski, R.S. Ruoff, The chemistry of graphene oxide, Chem. Soc. Rev. 39 (2010) 228–240. doi:10.1039/B917103G.

[32] L.L. Skovbjerg, D. V Okhrimenko, J. Khoo, K.N. Dalby, T. Hassenkam, E. Makovicky, S.L.S. Stipp, Preferential Adsorption of Hydrocarbons to Nanometer-Sized Clay on Chalk Particle Surfaces, Energy & Fuels. 27 (2013) 3642–3652. doi:10.1021/ef301832b.

[33] Y.-G. Lei, K.-M. Ng, L.-T. Weng, C.-M. Chan, L. Li, XPS C 1s binding energies for fluorocarbon–hydrocarbon microblock copolymers, Surf. Interface Anal. 35 (2003) 852–855. doi:https://doi.org/10.1002/sia.1615.

[34] Q. Chen, H. Zhou, T.-B. Song, S. Luo, Z. Hong, H.-S. Duan, L. Dou, Y. Liu, Y. Yang, Controllable Self-Induced Passivation of Hybrid Lead Iodide Perovskites toward High Performance Solar Cells, Nano Lett. 14 (2014) 4158–4163. doi:10.1021/nl501838y.

Chapter VI

$ZnO@TiO_2$ core-shell nanostructures for solar cell applications

6.1. Introduction

In the previous chapters, attempts were made to optimise film growth conditions in order to obtain well-aligned ZnO nanostructures and understand what issues may cause the ZnO/perovskite instability.

In terms of ZnO-containing PSCs, one approach to reduce the recombination processes is to coat a stable material with a wider bandgap onto the 1D ZnO nanostructure surface, creating a core-shell nanostructure [1]. In the last decades, several shell materials have been studied to coat ZnO, TiO_2 or SnO_2 films, namely insulating or semiconducting oxides, such as Nb_2O_5, Al_2O_3, SiO_2, ZrO_2, MgO, TiO_2, SnO_2, and ZnO [2–7]. Theoretically, an oxide shell can suppress recombination by i) increasing the physical separation between injected electrons and holes at the interface ETM/perovskite layer, ii) forming a tunnelling barrier, or iii) passivating surface recombination centres of the ETM [8].

One of the most cited articles that refer to the use of ZnO-based core-shell nanostructures applied in DSSCs is from P. Yang group [9]. Two oxide shell materials, amorphous Al_2O_3 and TiO_2 anatase were coated on ZnO nanowire arrays. Their interpretation is that the Al_2O_3 shell acts as an insulating barrier reducing recombination and the TiO_2 shell suppresses recombination by passivating the ZnO surface recombination sites. Furthermore, the DSSCs with ZnO-TiO_2 core-shell nanowires substantially improve the overall conversion efficiency, increasing V_{OC} and fill factor, using only a few nanometers of shell thickness [9].

Researchers have chosen TiO_2 as a potential shell material due to its high overall conversion efficiency. Additionally, a TiO_2 shell will form an energy barrier at the electrode surface, preventing recombination and degradation processes, and may also create a synergic photo-generation with separation of the charge carriers between the TiO_2 shell and in the ZnO core, leading to an improvement of all solar cell parameters [8,10].

The 1D $ZnO@TiO_2$ core-shell nanostructures have been reported in DSSCs applications, and there is an improvement in the conversion efficiencies compared with the bare ZnO nanostructures [11].

According to what has been studied and evaluated in the previous chapter, in this chapter, the preparation of $ZnO@TiO_2$ core-shell nanostructures will be explored to minimize the stability issues of perovskite solar cells.

This chapter is divided into three main sections. The first section (TiO_2 shell preparation: spin-coating versus solvothermal technique) will evaluate which approach to synthesise the

TiO_2 layer can better coat the ZnO NRs surface. The second section (Optimization of TiO_2 shell by solvothermal method) will focus on several factors that affect the formation of a TiO_2 layer on the ZnO surface, namely the synthesis temperature, the duration of the synthesis, and the addition of additives, such as acetylacetone, in different concentrations. The final section (Evaluation of ZnO@TiO_2 core-shell nanorods in solar cells performance) is dedicated to the analysis of the performance of dye-sensitised solar cells and perovskite solar cells using pulsed electrodeposited ZnO NRs (in optimised conditions following Chapters 3 and 4) and the ZnO@TiO_2 core-shell nanorods, as developed in this chapter.

6.2. TiO_2 shell preparation: spin-coating versus solvothermal technique

Different techniques have been reported for the growth of TiO_2 shell on ZnO surface based on physical [12] and chemical methods [10,11,13–15]. While physical processes allow the production of high-quality and single-crystalline nanostructures, their processing under harsh conditions, namely high-temperature-synthesis and ultra-high vacuum in some cases, restricts its application to some substrates and makes the process costly. On the other hand, chemical methods may not have these drawbacks and can produce nanomaterials of different shapes and structures at low temperatures and using low-cost equipment [16].

The sol-gel method is widely used to prepare homogeneous nanomaterials due to its high versatility, simplicity and low processing temperature. In terms of creating a TiO_2 shell on ZnO nanorods surface, Panigrahi *et al.* [15] used the spin-coating technique since it is an easy and quite practical procedure [17]. Based on this method, with strict control of the operational parameters, it was possible to apply this deposition technique to deposit the TiO_2 coating layer, ensuring that the TiO_2 thin layer coverers the ZnO nanorods uniformly.

Another route that has been employed to prepare TiO_2 nanomaterials is hydrothermal synthesis, which allows controlling the particle size and phase composition by tuning some parameters such as temperature, duration of the process, solution concentration and pH [18]. In addition, some authors report the use of an acidic pathway to synthesise TiO_2 anatase [19,20]. However, this is unfeasible because of the instability of ZnO in acidic media. Therefore, this subsection studied a solvothermal method to prepare TiO_2 anatase thin layer without compromising the ZnO structure stability.

Figure 6.1 shows a comparison of the results gathered from the application of spin-coating and solvothermal techniques used to create a TiO_2 shell on ZnO nanorods surface. Through SEM micrographs (Figure 6.1 a1) and b1)), visible differences of TiO_2 shell morphology are

shown. The applied conditions of the formulated sol-gel solution via spin-coating technique were unable to create a TiO_2 shell on each ZnO nanorod. Instead, a thin layer was formed on top of the nanorods (Figure 6.1 a1)). On the other hand, the solvothermal treatment allowed a TiO_2 porous structure to form, increasing the ZnO nanorod roughness (Figure 6.1 b1)).

The EDS spectra, Figure 6.1 a2) and b2), allowed to qualitatively identify the deposited TiO_2 using both deposition methods. It is evident a presence of Ti signal in both samples, being this signal assembles to the TiO_2 thin layer coating the FTO substrate that was used as a template in the growth of ZnO nanorods, as previously discussed in Chapter 3.

Figure 6.1 c), a3) and b3) shows the TEM micrographs of ZnO nanorod before and after TiO_2 deposition by spin-coating and solvothermal treatment, respectively. The lack of stability of the TiO_2 layer deposited by spin-coating shows heterogeneity in the dimensions of TiO_2 nanoparticles formed and completely detached from the ZnO nanorod. A slight decrease in ZnO nanorod thickness was also observed for the TiO_2 spin-coating samples (ZnO nanorod thickness was around 70 nm, Figure 6.1 c)), which could be due to the slightly acidic pH of the sol-gel solution (about 6) that may have caused instability in the ZnO structure. However, for the TiO_2 solvothermal samples, the ZnO structure appeared to be intact, and a TiO_2 adherent layer was formed, which validated the solvothermal method for the preparation of the TiO_2 shell.

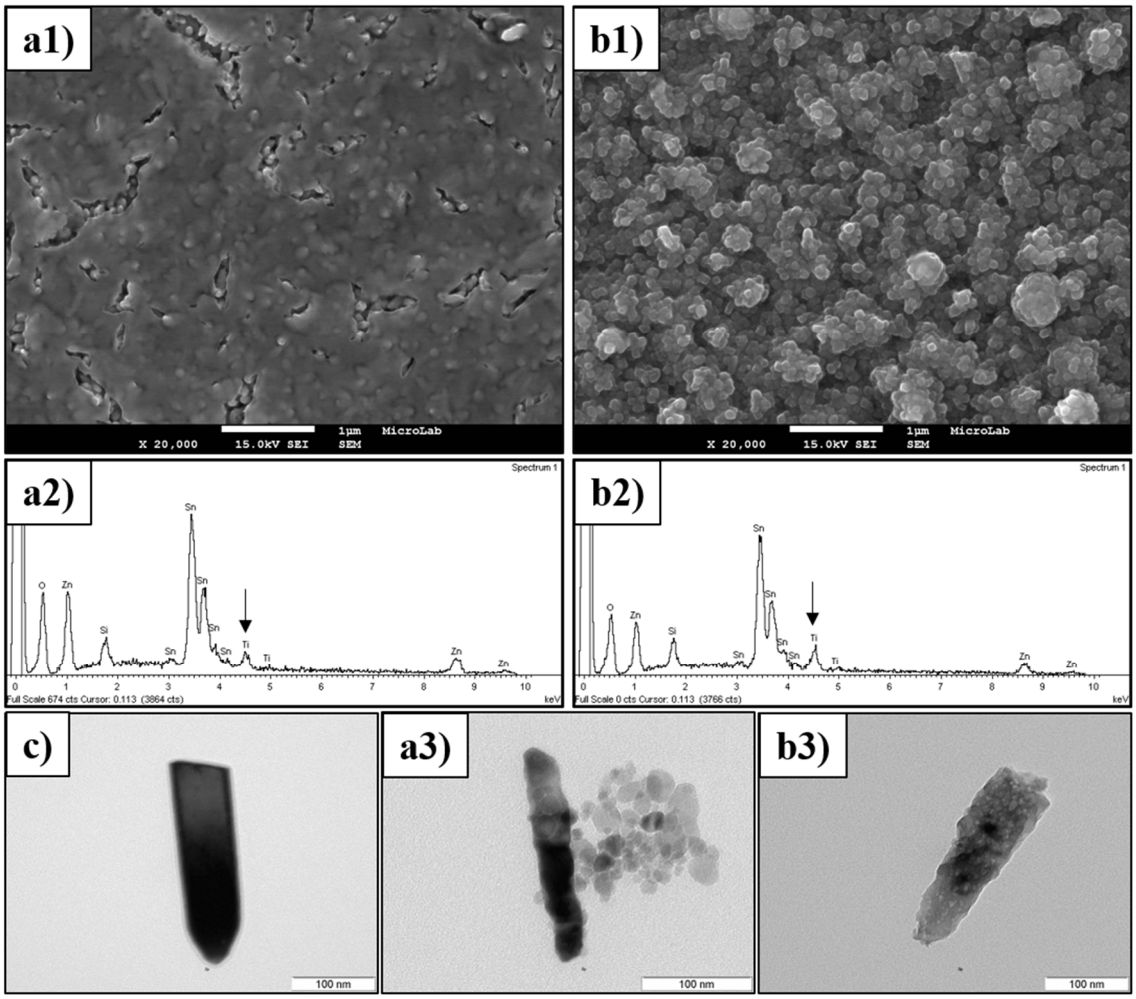

*Figure 6.1 - **C**omparison of **a)** spin-coating and **b)** solvothermal techniques used to prepare TiO_2 shell on ZnO nanorod surface: 1) SEM micrographs, 2) EDS spectra, and 3) TEM micrographs. **c)** TEM micrograph of a ZnO nanorod.*

The TiO_2 can acquire different crystalline polymorphic structures such as anatase (tetragonal), rutile (tetragonal), and brookite (orthorhombic), which give them unique properties [21–23]. Anatase has been the first structure option for photovoltaic purposes due to its low cost, environmentally friendly nature, high transparency, tailorable electronic, and compatibility with perovskite in terms of energy level when applied as ETM in PSCs [24]. Structural characterisation was carried out on ZnO@TiO_2 core-shell samples to evaluate the formation of TiO_2 anatase on the shell. Figure 6.2 shows the diffractograms of as-deposited ZnO NRs before and after the deposition of the TiO_2 shell through spin-coating and solvothermal methods. The XRD patterns for the as-deposited ZnO samples were in line with ZnO's hexagonal wurtzite crystalline structure (JCPDS 36-1451). After applying the deposition procedures to prepare ZnO@TiO_2 core-shell nanostructures, an additional peak at 25.3 ° was observed for solvothermal treatment, attributed to (101) plan of the hexagonal crystalline structure of anatase (JCPDS 21-1272). This additional information reinforces the

choice of the solvothermal approach to prepare the ZnO@TiO_2 core-shell nanostructures. It should be noted that in the TiO_2 formation by solvothermal method, there is not a strict on-time control of the development of the reactions resulting in the formation of clusters. Therefore, some parameters need to be adjusted to optimise the deposition of the TiO_2 shell, and this study will be discussed in the following subsections.

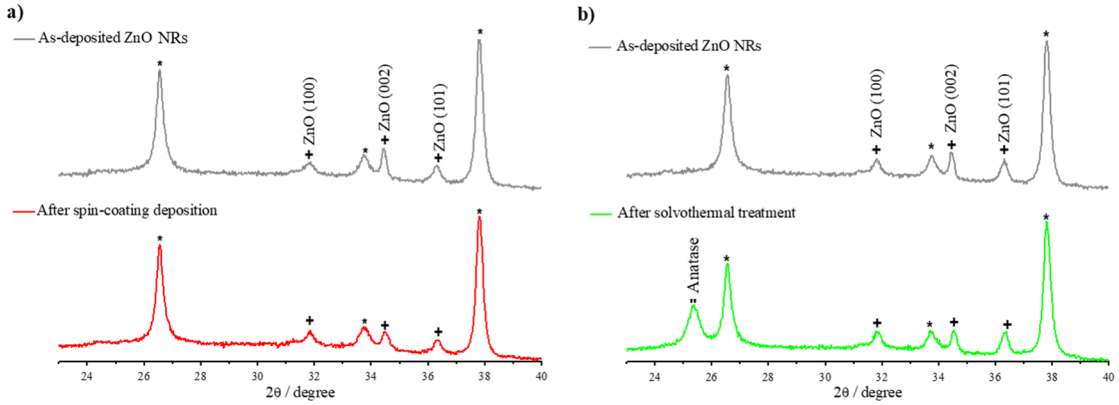

*Figure 6.2 - XRD patterns obtained to as-deposited ZnO nanorods (NRs) before and after **a)** spin-coating deposition of the sol-gel solution and **b)** solvothermal treatment to prepare a TiO_2 shell on ZnO nanorod surface.* corresponds to the FTO substrate diffraction pattern.*

6.3. Optimisation of TiO_2 shell by solvothermal method

The solvothermal method is an alternative to other wet chemical methods which allows, through adjusting several experimental parameters, namely the temperature at which the synthesis takes place, pressure, duration of the synthesis, and the nature of the solution components, either solvent or reagents [25], to control the size of TiO_2 nanoparticles that are formed, as well as the shaping of thin films.

The difference between the solvothermal and hydrothermal methods, usually used to prepare TiO_2 nanoparticles, is the absence of water that hydrolyses the titanium precursor and hence the TiO_2 formation [26]. Although this process has been studied in the last decades, the occurrence of hydrolysis and condensation reactions simultaneously results in a wide variety of species that are sometimes difficult to identify, apart from occurring the formation of clusters of nanoparticles difficult to disperse [27].

In the following subsections, temperature dependence, the addition of acetylacetone as an additive, and the reaction time will be discussed in detail.

6.3.1. Reaction temperature

According to the literature, to obtain TiO_2 nanoparticles in the anatase crystalline phase, the commonly used reaction temperatures range lies between 150 °C to 200 °C [28].

Figure 6.3 shows a comparison of ZnO@TiO_2 core-shell nanostructures prepared by the solvothermal method at 150 °C and 180 °C, using a precursor solution of 10 mM TTIP in isopropanol. Previously, it was found that 24 hours of solvothermal treatment may increase the TiO_2 particle size and, consequently, the thickness of the TiO_2 shell. Therefore, for a solvothermal treatment at 150 °C for 6 h (Figure 6.3 a)), small grain size TiO_2 are prepared, resulting in a better distribution of the shell over the ZnO nanorods. However, for a higher temperature of 180 °C (Figure 6.3 b)), the TiO_2 grain size increased considerably to the point where the nanoparticles agglomerated. According to the literature, the reaction temperature strongly affects the nanoparticle size, doubling in size for T > 150 °C [28,29].

The crystallization of TiO_2 anatase starts at 120 °C in isopropanol. Up to 200 °C, the only crystalline phase present is anatase, which means that the majority of the atomic percentages of Ti detected in both EDS spectra are TiO_2 in the anatase phase [30]. The ability to process the anatase phase at low temperatures has the advantage of requiring less energy in the preparation. In addition, lower temperatures tend to form finer grains with larger specific surface areas [31].

Despite the low temperature of 150 °C appearing to be enough to create a TiO_2 shell on the ZnO nanorod, further adjustments need to be made to ensure that the coating takes place individually and between nanorods. In the next subsection, the effect of adding an additive will be discussed.

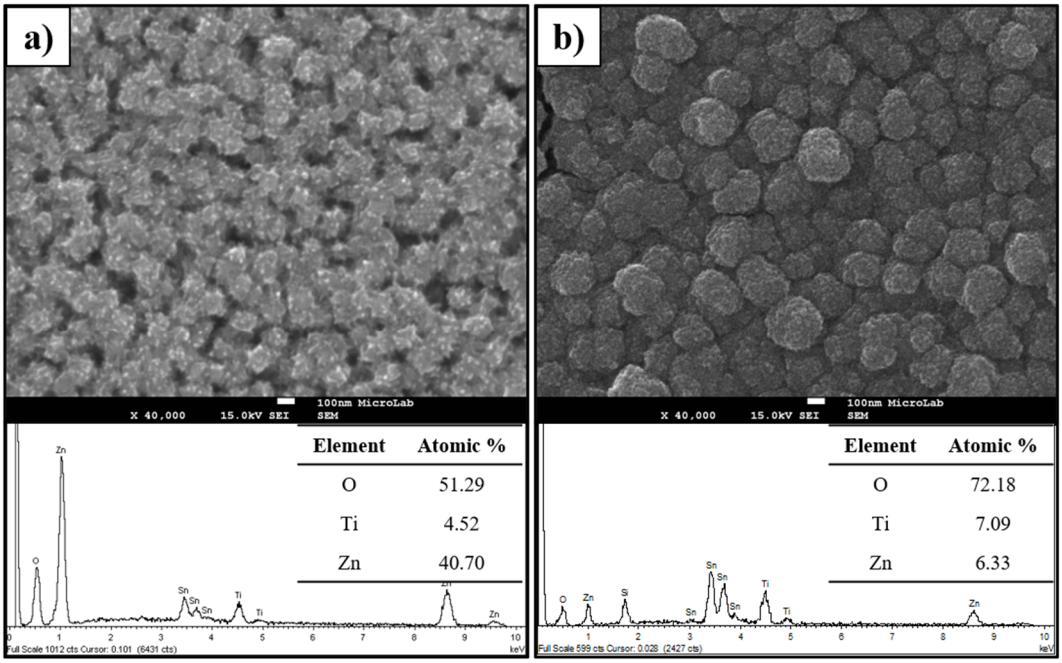

*Figure 6.3 - SEM micrographs and the respectively EDS spectra of ZnO@TiO₂ core-shell nanostructures prepared by solvothermal method at **a)**150 ℃ and **b)**180 ℃ for 6 h. Both samples were calcinated at 450 ℃ for 2 h (1 ℃/min of heating rate). The atomic percentages presented are only for the main elements (oxygen (O), titanium (Ti), and zinc (Zn)).*

6.3.2. Addition of additives: effect of acetylacetone concentration

For better control of the hydrolysis-condensation processes of the metal alkoxides (e.g. titanium (IV) isopropoxide (TTIP)), a chelating agent can be added to the alkoxide precursor solution, modifying the ligand structure and thereby suppressing its hydrolysis reaction [32]. Acetylacetone (ACAC) has been used as a chelating agent and can be exhibited in two tautomeric forms: keto form and enol form, as shown in Figure 6.4. The keto form is stable in aqueous solutions, and the enol form in organic solutions. The reaction between TTIP and ACAC is based on an alcoholic condensation according to the reaction mechanism shown in Figure 6.5 [33].

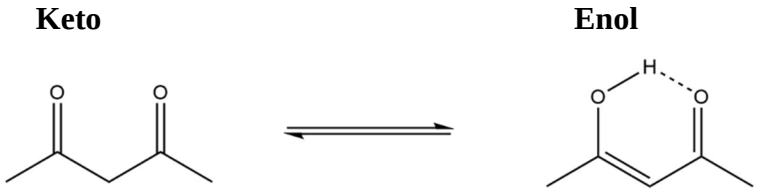

Figure 6.4 - Tautomeric forms of acetylacetone (ACAC).

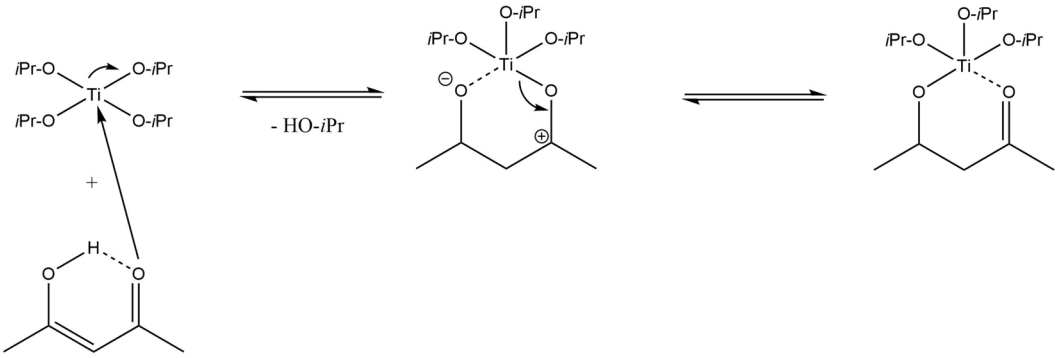

Figure 6.5 - Scheme of the proposed reaction mechanism between TTIP and ACAC.

First, the ACAC coordinates with the Ti metal centre, deprotonation occurs with a loss of isopropanol, and an enolate complex is formed [33]. This complex may react to obtain Ti-(OH) species that will form Ti-O-Ti bonds (Figure 6.6) or undergo a new condensation reaction with another molecule of ACAC (Figure 6.7).

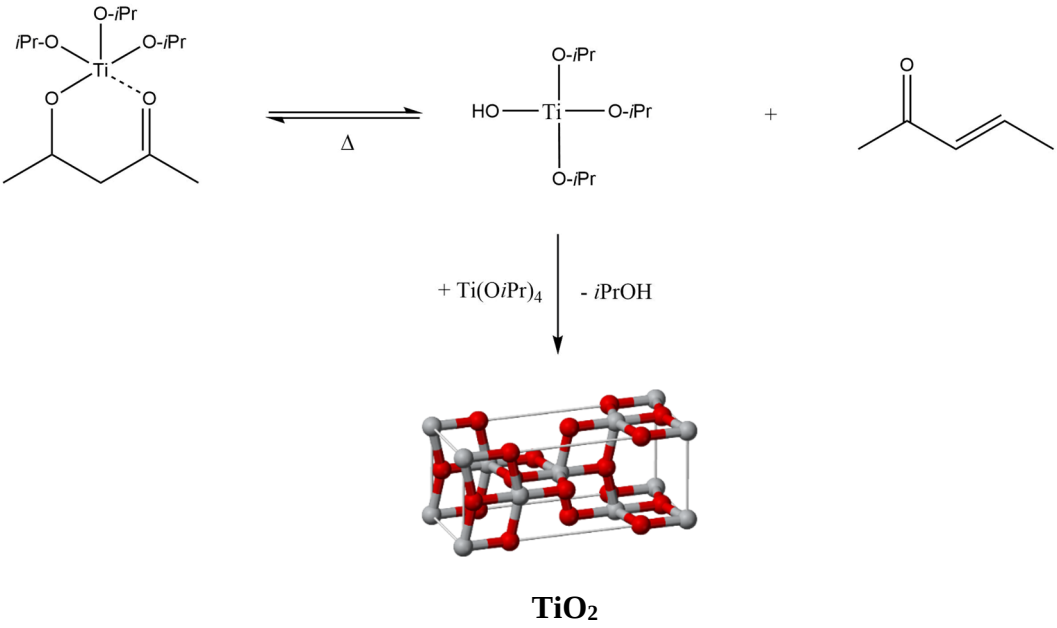

Figure 6.6 - Proposed mechanism of TiO_2 formation through enolate precursor.

Figure 6.7 - Enolate precursors according to TTIP and ACAC proportions.

It is known that ageing the TiO_2 gels increases the crystallinity of the anatase phase [34]. In this sense, ZnO@TiO_2 nanorod core-shell nanostructures were prepared using a precursor solution of 10 mM TTIP in isopropanol with 20 μL ACAC in a 1:1 molar ratio, respectively, which were aged for 24 h inside a closed vessel isolated from sunlight. After ageing the precursor solution and without ageing, solvothermal treatments at 150 °C for 6 h were performed. To better evaluate the shell formation, the solvothermal treatments were performed on FTO/ZnO_NRs samples with 100-120 nm of NR diameter, where nanorods are well spaced apart.

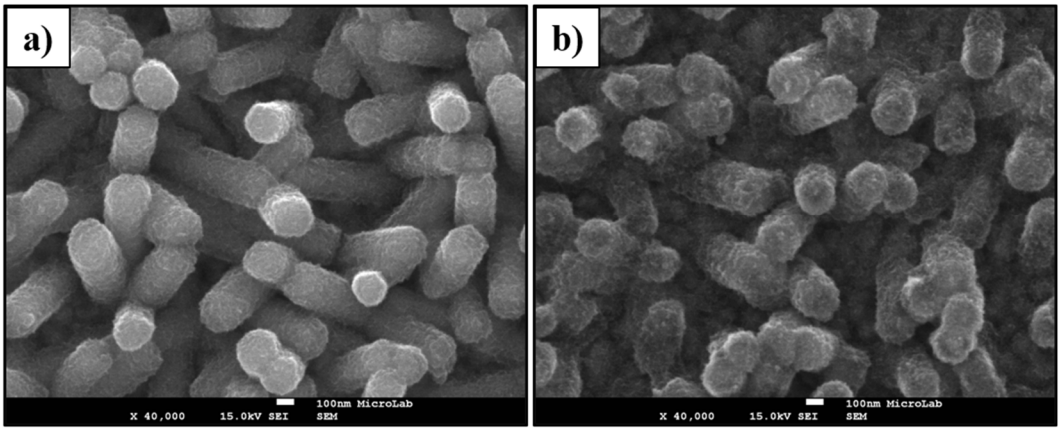

*Figure 6.8 - Top-section representative SEM micrographs of ZnO@TiO$_2$ core-shell nanostructures prepared by the solvothermal method, at 150 ℃ for 6 h, with **(a)** and without **(b)** ageing the precursor solution. Both samples were calcinated at 450 ℃ for 2 h (1 ℃/min of heating rate).*

Figure 6.8 shows the morphology of ZnO@TiO_2 core-shell nanostructures after calcination at 450 °C for 1h. It seems the precursor solution with ACAC added allowed a formation of a uniform TiO_2 shell with a small grain size, independently of whether it was aged or not, since a TiO_2 shell is seen to cover the ZnO nanorod surface individually. However, when looking at cross-section SEM micrographs, Figure 6.9, a total dissolution of the ZnO nanorods were observed for the aged solution prepared samples. It was also possible to estimate the TiO_2 shell thickness, being around 30-50 nm for all samples prepared with and without ageing the precursor solution. Also, Table 6.1 confirmed the ZnO dissolution when a decrease in the Zn atomic percentage of the aged solution-based samples is observed, comparatively to the unaged solution-based samples.

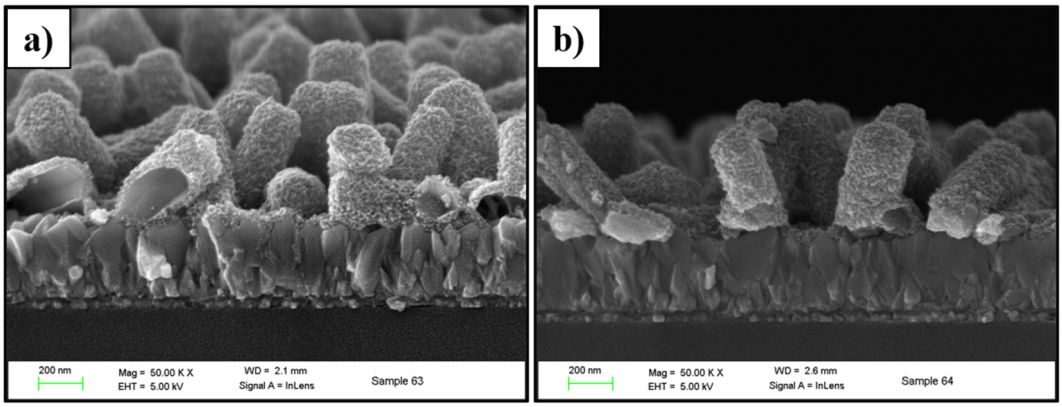

*Figure 6.9 - Cross-section representative SEM micrographs of ZnO@TiO₂ core-shell nanostructures prepared by the solvothermal method, at 150 ℃ for 6 h, with **(a)** and without **(b)** ageing the precursor solution. Both samples were calcinated at 450 ℃ for 2 h (1 ℃/min of heating rate).*

Table 6.1 - EDS data of ZnO@TiO₂ core-shell nanostructures prepared by solvothermal technique with or without an aged precursor solution.

Element	Atomic %	
	Aged solution-based sample	unaged solution-based sample
O	74.07	68.81
Ti	2.84	3.07
Zn	2.04	13.48
Si	4.90	2.42
Sn	16.15	12.22

This dissolution of the ZnO nanorods may be due to the pH of the precursor solution during the solvothermal process. Therefore, the pH before and after ageing of the precursor solution and after solvothermal treatment were probed. It was found that the precursor solution before the ageing step had a pH of 9. After 24 h of ageing, the pH decreased to 7, and at the end of the solvothermal treatment, the pH was 5.5. Since an acidic pH favours selective etching, it seems the etching of the ZnO nanorods starts on the (001) polar plane comprised of either O^{2-} or Zn^{2+} [35]. Illy *et al.* also found that the dissolution rate is slow at pH 4 and above, allowing good control of nanotube dimensions [35]. In the next subsection, the TiO_2 shell growth and the ZnO dissolution phenomena are evaluated, using different reaction times of the shell coating production on FTO/TiO_2/ZnO NRs arrays.

Since the precursor solution's ageing was not beneficial for the ZnO nanorod structure, the effect of different amounts of acetylacetone on the precursor solution proceeded without the ageing step.

To obtain good coverage of ZnO NRs with a thin TiO_2 layer by solvothermal treatment without dissolving the ZnO core, different precursor solutions were used, by adding 5 to

20 μL of ACAC to 50 mL of a 10 mM TTIP (in isopropanol) solution, without the ageing step (initial pH 8). The solvothermal treatments were performed at 150 °C for 6 h.

Figure 6.10 shows that the addition of acetylacetone on the precursor solution directly affects the formation of a TiO_2 layer, keeping the ZnO nanorod morphology intact. It seems that small amounts of acetylacetone (Figure 6.10 b)) did not allow the formation of TiO_2 nanoparticles for the same temperature and time of synthesis. However, as the amount of acetylacetone added increased (Figure 6.10 c)), a TiO_2-coated thin layer on the ZnO surface started to form until the whole ZnO nanorod surface was covered (Figure 6.10 d) and e)). The EDS data (Table 6.2) confirmed the presence of TiO_2 by increasing the atomic percentage of Ti after the solvothermal treatment of ZnO NRs. Also, a decrease in the atomic percentage of Zn was detected. Furthermore, the pH of the precursor solution after solvothermal treatment decreased to 7.1 and 6.8 when 5 or 10 μL and 15 or 20 μL of ACAC were added, respectively. The slightly acidic pH (pH 6.8) of the precursor solution after the solvothermal treatment may have caused some etching of ZnO nanorods, resulting in a decrease of the ZnO available percentage [36].

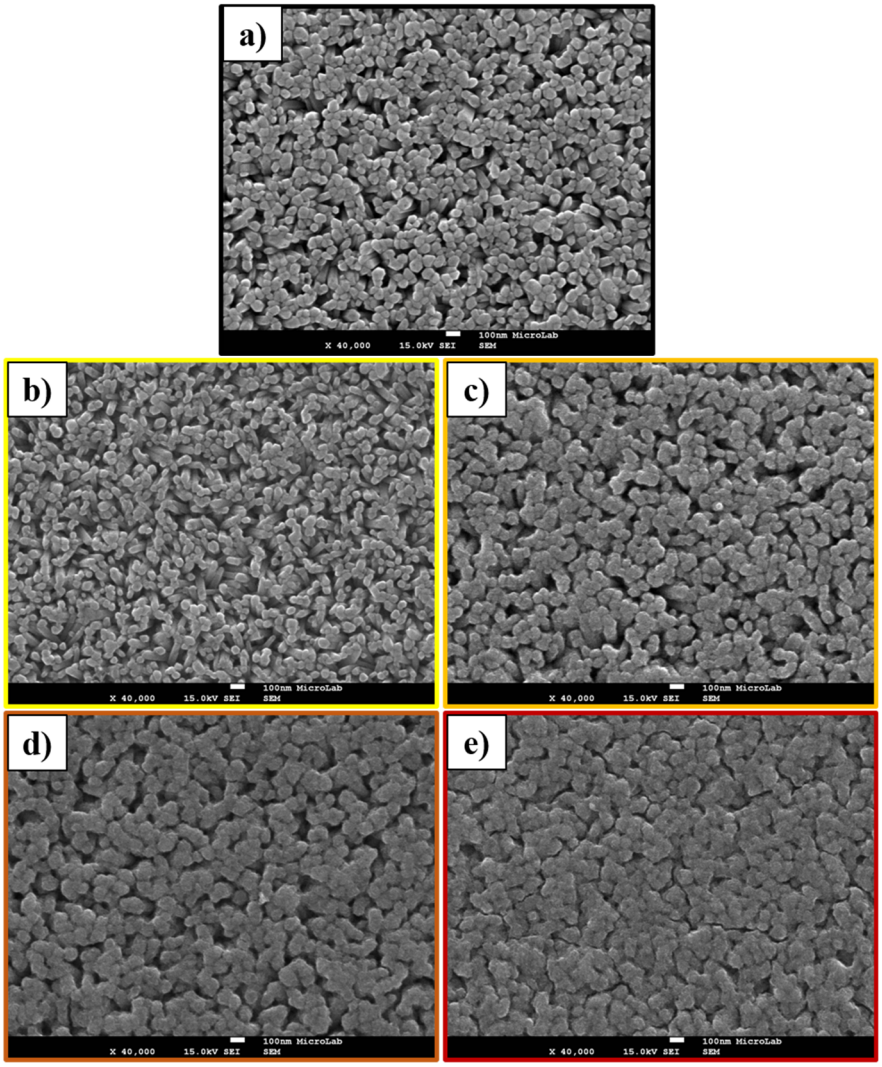

*Figure 6.10 - Representative SEM micrographs of **a)** as-deposited ZnO and after solvothermal treatment using a precursor solution composed by 10 mM TTIP in isopropanol and **b)** 5 μL, **c)** 10 μL, **d)** 15 μL, or **e)** 20 μL of acetylacetone, at 150 ℃ for 6 h. All the samples were calcinated at 450 ℃ for 2 h (1 ℃/min of heating rate).*

Table 6.2 - EDS data of as-deposited ZnO and ZnO@TiO₂ core-shell nanorods, using different amounts of acetylacetone added to the precursor solution of the solvothermal treatment.

Element	Atomic %				
	As-deposited ZnO	5 μL	10 μL	15 μL	20 μL
O	61.40	61.90	63.84	68.55	68.57
Ti	2.08	3.33	3.47	3.28	3.31
Zn	28.19	24.72	21.49	15.43	13.49

The photoelectroactivity of the ZnO and ZnO@TiO_2 core-shell NR electrodes was evaluated through the photocurrent response of the films, being the results shown in Figure 6.11. The obtained photovoltammograms exhibited an expected response for nanocrystalline n-type semiconductor electrodes [37]. There is no dark current flow in all the potential

scanned ranges, meaning that no oxidation reactions occurred at high potential values. The photocurrent onset of ZnO NRs films started at -0.30 V, but the ZnO@TiO_2 core-shell NRs films exhibit photocurrent onsets at more negative biases, revealing a 200 mV difference when 20 μL ACAC were used. This negative shift can be attributed to the values of band edge position of the TiO_2 layers, which are reported to be more negative than that of the ZnO [38].

Considering the generated photocurrents, an increase of photocurrent densities occurs accordingly with the amount of ACAC added in the solvothermal treatment, reaching the highest value when 15 μL of ACAC were used, decreasing when a higher amount of ACAC was used. This highest photocurrent density may be due to the optimal conditions of the TiO_2 shell, namely thickness and homogeneity, that, in synergy with the ZnO core, allowed an effective separation of photogenerated charge carriers [39]. On the other hand, when a higher amount of ACAC was added, according to SEM micrographs (Figure 6.10 e)), the TiO_2 layer deposited on the ZnO surface was thick enough to create a layer on top of ZnO nanorods and cover all the nanorod interspaces, increasing the charge transfer path, thus triggering higher recombination and lower separation of charge carriers, which resulted in a decrease of the photocurrent density [40]. Additionally, the ZnO@TiO_2 core-shell films prepared using 15 or 20 μL of ACAC showed a photocurrent density plateau, which means that the driving force used for efficient electron-hole separation was independent of applied bias, and also that these core-shell films were stable at more positive biases.

In conclusion, it seems that the addition of 15 μL of ACAC to the solvothermal precursor solution, without the ageing step, created the optimal conditions to obtain ZnO@TiO_2 core-shell nanorods. The application of these core-shell nanostructures as an electron transport material on perovskite solar cells will be discussed in subsection 6.4.

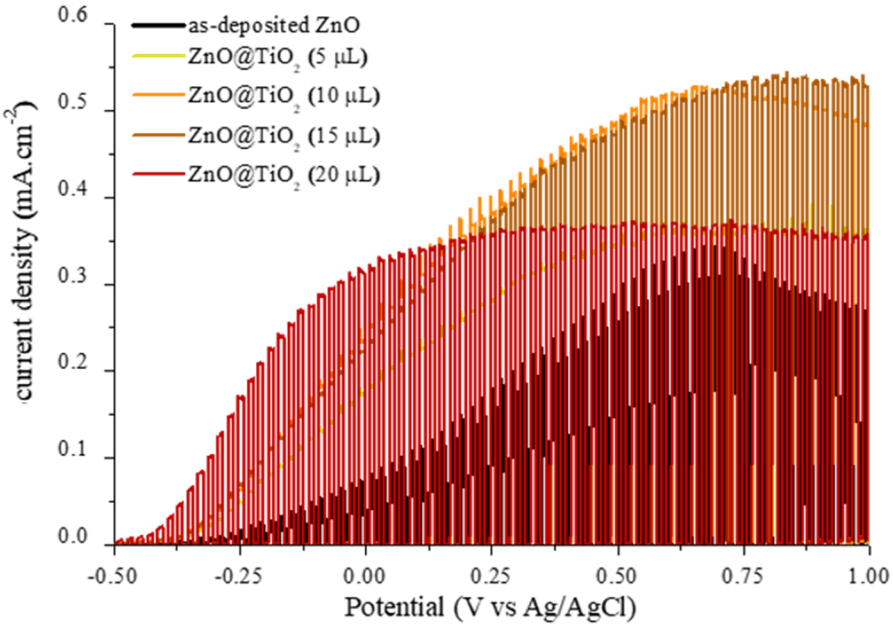

Figure 6.11 - j-V curves of as-deposited ZnO NRs and ZnO@TiO₂ core-shell NRs, prepared by solvothermal treatment using a precursor solution with different amounts of acetylacetone added. Obtained in 50 mM Na_2SO_3 aqueous solution (pH 9.5), under chopped illumination at 0.1 Hz. Scan rate of 2 mV.s^{-1}.

6.3.3. Reaction time

During the ageing study of the precursor solution, even though the TiO_2 layer formed was uniform, the main issue was the acidic pH of the solution. Therefore, to better understand at which point the pH of the precursor solution changes, the solvothermal treatment was carried out on ZnO nanorods, with different processing times, measuring the pH of the precursor solution before and after the core-shell synthesis. The FTO/TiO_2/ZnO_sl/ZnO_NRs electrodes were used for this study since they will be subsequently applied in perovskite solar cells.

Figure 6.12 shows the top-view SEM micrographs of as-deposited ZnO nanorods and after 30, 60, 180, and 240 min of solvothermal treatment. After 30 and 60 min of solvothermal treatment, no visible morphological changes in the ZnO structure were observed, nor was a TiO_2 thin layer formed on the ZnO nanorod surface. It seems that the formation of TiO_2 nanoparticles only started after 180 min of solvothermal treatment with an aged precursor solution, but at the same time, the ZnO nanorod structure began to collapse.

The XRD patterns of ZnO nanorods obtained before and after the solvothermal treatment shown in Figure 6.13 confirmed the decrease of ZnO diffraction planes intensities after solvothermal treatment, compared to as-deposited ZnO XRD patterns.

According to what has been reported, depending on the TiO_2 shell thickness, two situations would be expected: 1) if the TiO_2 shell was too thin, no changes in the ZnO and/or FTO XRD peak intensities should be observed; 2) if the TiO_2 shell was too thick and compact, all the

ZnO and FTO peak intensities should decrease. However, neither of these situations were observed, but a third situation is related to the ZnO structure dissolution with solvothermal treatment. Comparatively to as-deposited ZnO XRD patterns, after 30 and 60 min of solvothermal treatment, the ZnO XRD peaks slightly reduced intensity (~10 % decrease in intensity of the diffraction peak related to the (002) plane of the ZnO wurtzite structure). As the reaction time increased, this decrease in the ZnO peaks intensity became more pronounced, with ~ 40 % and ~50 % decrease in (002) peak intensity, after 180 and 240 min of solvothermal treatment, respectively. A decrease in FTO XRD peak intensities was also expected if this decline was related to TiO_2 shell formation on the ZnO nanorod surface. However, this decrease was not observed, remaining the same as the FTO XRD peak intensities after solvothermal treatment.

A possible explanation for this may be the pH solution after solvothermal treatment. Before starting the solvothermal reaction, without ACAC solution volume, the precursor solution presented a pH value of ~7. After the ACAC addition, the pH value increased to ~7.5. The ageing step decreased the pH value again to ~7, which is considered “ideal” for the ZnO structure stability. As soon as the solvothermal treatment starts, the pH solution decreases to 5 after just 30 min, thus remaining the same regardless of the reaction time. At this pH value, the ZnO suffers dissolution that will be gradually extended to all the nanorod structures after long exposure, in line with the SEM data. Without the ageing step, after 30 min or 240 min of solvothermal treatment, the precursor solution kept the same pH value of ~7.

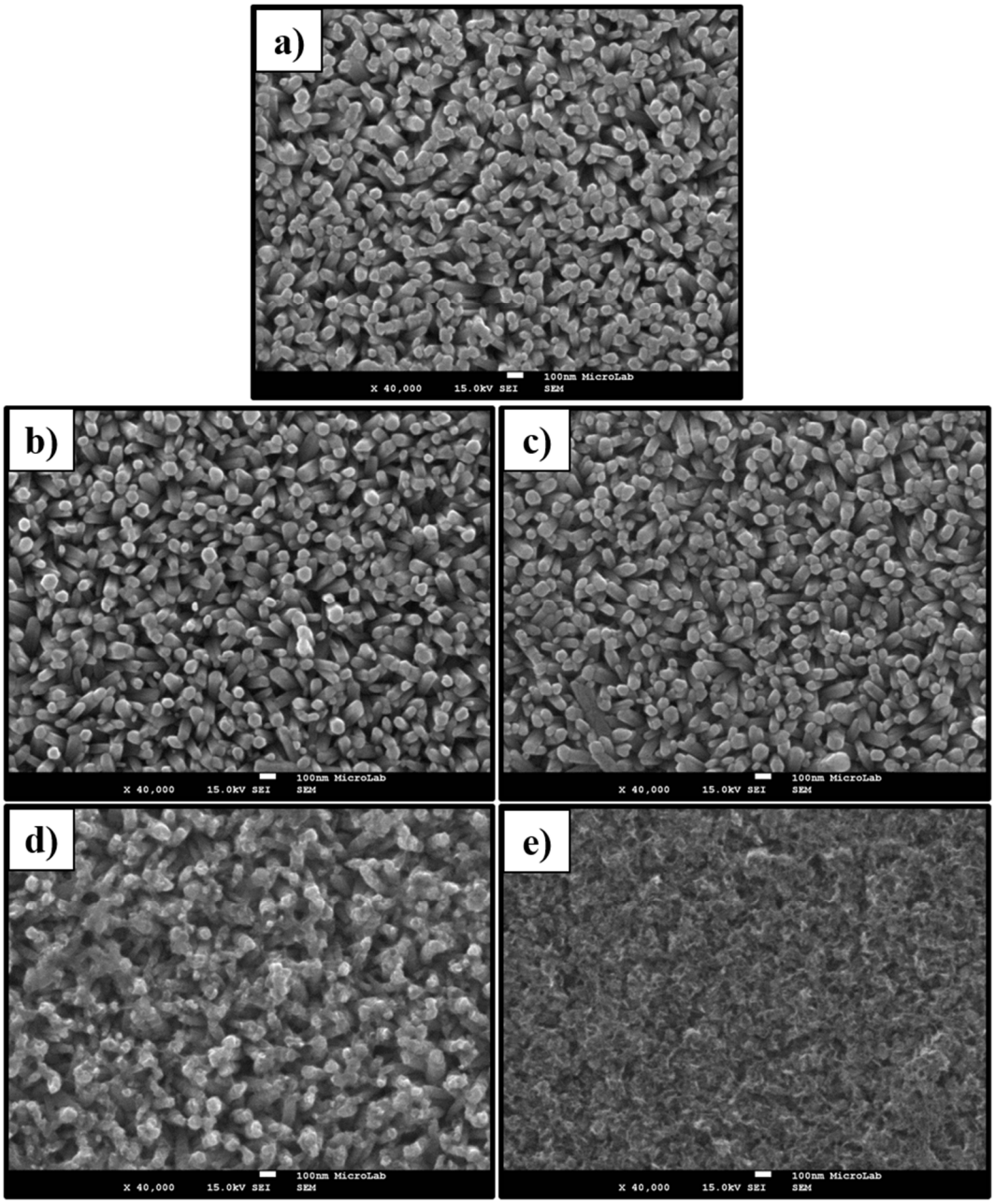

*Figure 6.12 - Representative SEM micrographs of **a)** as-deposited ZnO NRs and after solvothermal treatment at 150 ℃ for **b)** 30 min, **c)** 60 min, **d)** 180 min, and **e)** 240 min, using an aged precursor solution (10 mM TTIP in isopropanol and 20 μL ACAC). All the samples were calcinated at 450 ℃ for 2 h (1 ℃/min of heating rate).*

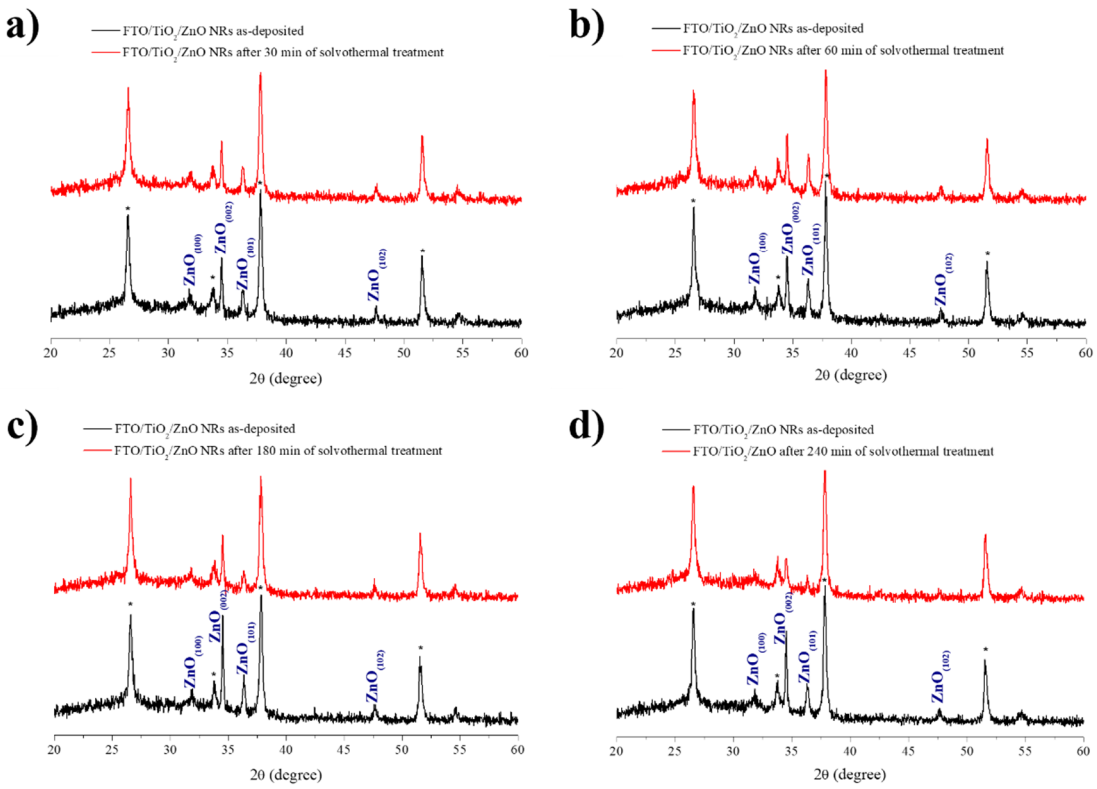

*Figure 6.13 - XRD spectra obtained to as-deposited ZnO NRs before and after **a)** 30 min, **b)** 60 min, **c)** 180 min, **d)** 240 min of solvothermal treatment to prepare a TiO_2 shell on ZnO NR surface. *Corresponds to the FTO substrate diffraction pattern.*

Therefore, ageing the precursor solution was not viable to obtain a TiO_2 shell on FTO/TiO_2/ZnO_sl/ZnO_NRs films since the ZnO structure was not chemically stable in the acidic pH solution during solvothermal treatment.

6.4. Evaluation of ZnO@TiO₂ core-shell nanorods in solar cells performance

The optimised ZnO@TiO_2 core-shell nanostructures were evaluated as an electron transport material (ETM) in perovskite solar cells, more precisely in methylammonium lead iodide-based perovskite solar cells ($MAPbI_3$-based PSCs).

Before their application in PSCs, a cross-section SEM analysis was performed, and the resulting SEM micrographs are shown in Figure 6.14. The cross-section SEM micrographs of ZnO films showed vertically orientated nanorods (Figure 6.14a)), 350-400 nm long and 80-120 nm diameter. The cross-section SEM micrographs of ZnO@TiO_2 core-shell films (Figure 6.14 b)) showed TiO_2 nanoparticles deposited on ZnO nanorods, confirmed by EDS analysis (Table 6.3) without covering all the available surface, which may be an issue when applied as

ETL on PSCs, due to recombination processes that might occur, as well as the thermal instability of $MAPbI_3$ layer when in direct contact with ZnO, as it was discussed in Chapter 5.

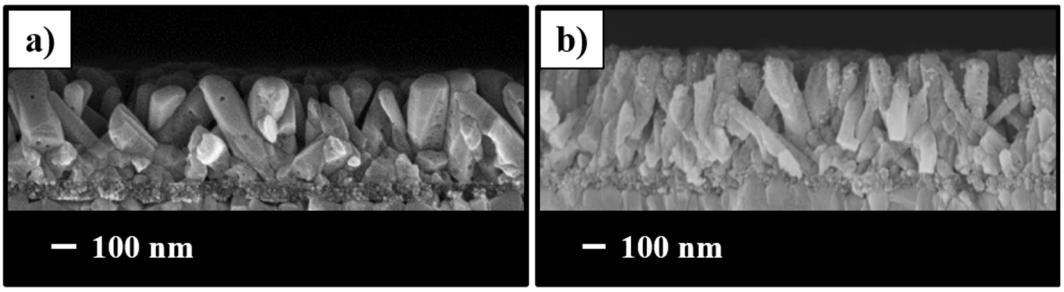

*Figure 6.14 - Cross-section representative SEM micrographs of **a)** ZnO NRs and **b)** ZnO@TiO₂ core-shell NRs films used as ETM on perovskite solar cells.*

Table 6.3 - EDS data of ZnO NRs and ZnO@TiO₂ core-shell NRs films used as ETM on perovskite solar cells.

Element	Atomic %	
	ZnO_NR	**ZnO@TiO₂_NR**
O	47.62	43.40
Ti	---	14.42
Zn	52.38	42.18

Figure 6.15 shows the cross-section SEM micrographs of ZnO and ZnO@TiO_2 core-shell films applied on a PSC setup, namely FTO/TiO_2/ZnO_SL/ZnO or ZnO@TiO_2/$MAPbI_3$/Spiro-OMeTAD/Au. It seems that the $MAPbI_3$ layer deposited on both studied ETLs fills the gaps between the nanorods and creates a layer of 220-240 nm and 125-150 nm thickness above the ZnO nanorods and ZnO@TiO_2 core-shell nanorods, respectively. On the other hand, the affinity of $MAPbI_3$ perovskite material for TiO_2 may have allowed the insertion of perovskite in the gaps of ZnO@TiO_2 core-shell NRs, higher than that verified in the gaps of pure ZnO NRs, decreasing the thickness of the perovskite layer on top of the ETL [41]. Furthermore, the space between the nanorods was too small to guarantee full coverage of the ZnO and ZnO@TiO_2 surfaces with the $MAPbI_3$ perovskite layer, decreasing the available active area for carrier transport. It has also been noticed that the perovskite layer on the top of the ZnO nanorod had high roughness and more grain boundaries to those of the perovskite layer covering the ZnO@TiO_2 NRs, which may lead to the formation of recombination centres for charge carriers.

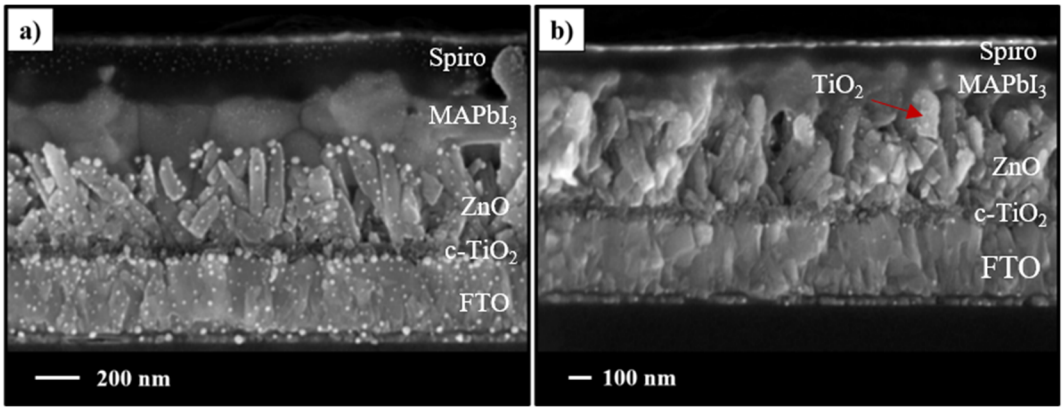

Figure 6.15 - Cross-section representative SEM micrographs of ***a)*** *FTO/TiO₂/ZnO_sl/ZnO_NR/MAPbI₃/Spiro-OMeTAD/Au and* ***b)*** *FTO/TiO₂/ZnO_sl/ZnO@TiO₂_NR/MAPbI₃/Spiro-OMeTAD/Au. The white spots on left micrography is the gold sputtering for SEM analysis.*

Preliminary photovoltaic performance parameters of the studied perovskite-based solar cells are presented in Table 6.4. The presented results considered an operational area was 0.07 cm^2 with a circular configuration and are representative of the three best devices measured. Firstly, the as-obtained efficiencies are low. The cells employing the TiO_2 have a higher open-circuit voltage (ca. 100mV), greater short-circuit current density (2 to 3 times greater) and slightly better fill-factors (increasing from about 30 % to 40 %). Nonetheless, efficiencies are very low compared to literature reported values for similar devices. Comparative devices have efficiencies in the range of 5 % to 8 % for ZnO NRs and ZnO@TiO_2 NRs devices, respectively [41]. Furthermore, complete coverage of the ZnO nanorod with the TiO_2 shell can eliminate the direct contact between ZnO and the perovskite absorber, lowing the charge recombination at the ZnO/perovskite interface. As a result, the overall charge recombination of the PSC is suppressed due to the TiO_2 shell, improving the cell efficiency considerably [41].

Table 6.4 - Photovoltaic performance parameters of MAPbI₃ devices.

Device	J_{sc} **(mA.cm^{-2})**	V_{OC} **(mV)**	***FF*** **(%)**	η **(%)**	$\eta_{average}$ **(%)**
ZnO_NR	3.9	768	26.6	0.8	1.0 ± 0.1
	4.6	766	32.2	1.1	
	4.6	738	33.4	1.1	
ZnO@TiO₂_NR	8.3	888	42.8	3.2	3.4 ± 0.2
	9.3	877	43.9	3.6	
	8.6	878	45.2	3.4	

6.5. Chapter Summary

The results within this chapter showed a way to obtain ZnO@TiO_2 core-shell nanostructures by choosing a coating technique that can be cost-effective (requires low temperatures and has few steps).

Three main parameters were selected to improve the thickness, morphology, and uniformity of the TiO_2 shell: the reaction temperature, the reaction time, and the use of an additive. The reaction temperature has a direct influence on the crystallinity of the shell. To ensure that only the anatase phase is present in the TiO_2 shell, a temperature of 150 ºC was chosen. Also, at this temperature, it allowed better control of the morphology and roughness of the TiO_2 layer. By evaluating the influence of the reaction time, it was possible to ascertain that the TiO_2 nanoparticles needed at least 180 min to be formed. The acetylacetone was the chelating agent selected to control the grain size of the TiO_2 layer and thereby create a uniform layer that could cover the entire surface of the ZnO nanorod. Before adding the acetylacetone to the precursor solution, an additional ageing step was considered since it improved the coverage of ZnO nanorods with a TiO_2 shell. However, after adding an amount of acetylacetone, the acidic pH of the precursor solution during the solvothermal treatment dissolved the ZnO nanorods.

The optimised ZnO@TiO_2 core-shell nanorods were employed in a mesoscopic perovskite solar cell architecture, using the methylammonium lead triiodide perovskite as the absorbing layer. The procedures employed in this case for preparing these devices require development. Nonetheless, the preliminary results with the inclusion of a TiO_2 shell point to improving PSC devices based on ZnO ETLs.

6.6. References

[1] C.M. Pelicano, I. Raifuku, Y. Ishikawa, Y. Uraoka, H. Yanagi, Hierarchical core–shell heterostructure of H2O-oxidized ZnO nanorod@Mg-doped ZnO nanoparticle for solar cell applications, Mater. Adv. 1 (2020) 1253–1261. doi:10.1039/D0MA00313A.

[2] A. Zaban, S.G. Chen, S. Chappel, B.A. Gregg, Bilayer nanoporous electrodes for dye sensitized solar cells, Chem. Commun. (2000) 2231–2232. doi:10.1039/B005921H.

[3] E. Palomares, J.N. Clifford, S.A. Haque, T. Lutz, J.R. Durrant, Control of Charge Recombination Dynamics in Dye Sensitized Solar Cells by the Use of Conformally Deposited Metal Oxide Blocking Layers, J. Am. Chem. Soc. 125 (2003) 475–482. doi:10.1021/ja027945w.

[4] K. Tennakone, J. Bandara, P.K.M. Bandaranayake, G.R.A. Kumara, A. Konno, Enhanced Efficiency of a Dye-Sensitized Solar Cell Made from MgO-Coated Nanocrystalline SnO2, Jpn. J. Appl. Phys. 40 (2001) L732–L734. doi:10.1143/jjap.40.l732.

[5] R.R. Knauf, B. Kalanyan, G.N. Parsons, J.L. Dempsey, Charge Recombination Dynamics in Sensitized SnO2/TiO2 Core/Shell Photoanodes, J. Phys. Chem. C. 119 (2015) 28353–28360. doi:10.1021/acs.jpcc.5b10574.

[6] Y. Zhou, C. Xia, X. Hu, W. Huang, A.A. Aref, B. Wang, Z. Liu, Y. Sun, W. Zhou, Y. Tang, Dye-sensitized solar cells based on nanoparticle-decorated ZnO/SnO2 core/shell nanoneedle arrays, Appl. Surf. Sci. 292 (2014) 111–116. doi:https://doi.org/10.1016/j.apsusc.2013.11.095.

[7] N. Rajamanickam, S.S. Kanmani, K. Jayakumar, K. Ramachandran, On the possibility of ferromagnetism and improved dye-sensitized solar cells efficiency in TiO2/ZnO core/shell nanostructures, J. Photochem. Photobiol. A Chem. 378 (2019) 192–200. doi:https://doi.org/10.1016/j.jphotochem.2019.04.042.

[8] Y. Diamant, S. Chappel, S.G. Chen, O. Melamed, A. Zaban, Core–shell nanoporous electrode for dye sensitized solar cells: the effect of shell characteristics on the electronic properties of the electrode, Coord. Chem. Rev. 248 (2004) 1271–1276. doi:https://doi.org/10.1016/j.ccr.2004.03.003.

[9] M. Law, L.E. Greene, A. Radenovic, T. Kuykendall, J. Liphardt, P. Yang, ZnO−Al2O3 and ZnO−TiO2 Core−Shell Nanowire Dye-Sensitized Solar Cells, J. Phys. Chem. B. 110 (2006) 22652–22663. doi:10.1021/jp0648644.

[10] S. Hernández, V. Cauda, A. Chiodoni, S. Dallorto, A. Sacco, D. Hidalgo, E. Celasco, C.F. Pirri, Optimization of 1D ZnO@TiO2 Core–Shell Nanostructures for Enhanced

Photoelectrochemical Water Splitting under Solar Light Illumination, ACS Appl. Mater. Interfaces. 6 (2014) 12153–12167. doi:10.1021/am501379m.

[11] X. Ji, W. Liu, Y. Leng, A. Wang, Facile Synthesis of ZnO@TiO2 Core-Shell Nanorod Thin Films for Dye-Sensitized Solar Cells, J. Nanomater. 2015 (2015) 647089. doi:10.1155/2015/647089.

[12] L.E. Greene, M. Law, B.D. Yuhas, P. Yang, ZnO−TiO2 Core−Shell Nanorod/P3HT Solar Cells, J. Phys. Chem. C. 111 (2007) 18451–18456. doi:10.1021/jp077593l.

[13] X. Yan, C. Zou, X. Gao, W. Gao, ZnO/TiO2 core–brush nanostructure: processing, microstructure and enhanced photocatalytic activity, J. Mater. Chem. 22 (2012) 5629–5640. doi:10.1039/C2JM15477C.

[14] J. Qiu, Z. Jin, Z. Liu, X. Liu, G. Liu, W. Wu, X. Zhang, X. Gao, Fabrication of TiO2 nanotube film by well-aligned ZnO nanorod array film and sol–gel process, Thin Solid Films. 515 (2007) 2897–2902. doi:https://doi.org/10.1016/j.tsf.2006.08.023.

[15] S. Panigrahi, D. Basak, Core-shell TiO2@ZnO nanorods for efficient ultraviolet photodetection, Nanoscale. 3 (2011) 2336–2341. doi:10.1039/c1nr10064e.

[16] S. Marouf, A. Beniaiche, H. Guessas, A. Azizi, S. Marouf, A. Beniaiche, H. Guessas, A. Azizi, Morphological, Structural and Optical Properties of ZnO Thin Films Deposited by Dip Coating Method, Mater. Res. 20 (2016) 88–95. doi:10.1590/1980-5373-mr-2015-0751.

[17] J. Griffin, H. Hassan, E. Spooner, Spin Coating: Complete Guide to Theory and Techniques, Ossila.Com. (2021). https://www.ossila.com/pages/spin-coating (accessed 27 April 2021).

[18] K.A. Malinger, A. Maguer, A. Thorel, A. Gaunand, J.-F. Hochepied, Crystallization of anatase nanoparticles from amorphous precipitate by a continuous hydrothermal process, Chem. Eng. J. 174 (2011) 445–451. doi:https://doi.org/10.1016/j.cej.2011.08.065.

[19] A. Testino, I.R. Bellobono, V. Buscaglia, C. Canevali, M. D'Arienzo, S. Polizzi, R. Scotti, F. Morazzoni, Optimizing the Photocatalytic Properties of Hydrothermal TiO2 by the Control of Phase Composition and Particle Morphology. A Systematic Approach, J. Am. Chem. Soc. 129 (2007) 3564–3575. doi:10.1021/ja067050+.

[20] Y.V. Kolen'ko, B.R. Churagulov, M. Kunst, L. Mazerolles, C. Colbeau-Justin, Photocatalytic properties of titania powders prepared by hydrothermal method, Appl. Catal. B Environ. 54 (2004) 51–58. doi:https://doi.org/10.1016/j.apcatb.2004.06.006.

[21] T. Leijtens, B. Lauber, G.E. Eperon, S.D. Stranks, H.J. Snaith, The Importance of

Perovskite Pore Filling in Organometal Mixed Halide Sensitized TiO2-Based Solar Cells, J. Phys. Chem. Lett. 5 (2014) 1096–1102. doi:10.1021/jz500209g.

[22] J.-W. Lee, T.-Y. Lee, P.J. Yoo, M. Grätzel, S. Mhaisalkar, N.-G. Park, Rutile TiO2-based perovskite solar cells, J. Mater. Chem. A. 2 (2014) 9251–9259. doi:10.1039/C4TA01786B.

[23] M. Shahiduzzaman, S. Visal, M. Kuniyoshi, T. Kaneko, S. Umezu, T. Katsumata, S. Iwamori, M. Kakihana, T. Taima, M. Isomura, K. Tomita, Low-Temperature-Processed Brookite-Based TiO2 Heterophase Junction Enhances Performance of Planar Perovskite Solar Cells, Nano Lett. 19 (2019) 598–604. doi:10.1021/acs.nanolett.8b04744.

[24] T. Luttrell, S. Halpegamage, J. Tao, A. Kramer, E. Sutter, M. Batzill, Why is anatase a better photocatalyst than rutile? - Model studies on epitaxial TiO2 films, Sci. Rep. 4 (2014) 4043. https://doi.org/10.1038/srep04043.

[25] G. Demazeau, Solvothermal reactions: an original route for the synthesis of novel materials, J. Mater. Sci. 43 (2008) 2104–2114. doi:10.1007/s10853-007-2024-9.

[26] N.Y. Turova, E.P. Turevskaya, V.G. Kessler, M.I. Yanovskaya, The Chemistry of Metal Alkoxides, Springer, Boston, 2002. doi:10.1007/b113856.

[27] M. In, C. Sanchez, Growth versus Cyclization in the Early Stages of the Polycondensation of Metal Alkoxides, J. Phys. Chem. B. 109 (2005) 23870–23878. doi:10.1021/jp052410l.

[28] W. Li, M. Body, C. Legein, O.J. Borkiewicz, D. Dambournet, Solvothermal Temperature Drives Morphological and Compositional Changes through Dehydroxyfluorination in Anatase Nanoparticles, Eur. J. Inorg. Chem. 2017 (2017) 192–197. doi:https://doi.org/10.1002/ejic.201601160.

[29] G.C. Collazzo, S.L. Jahn, N.L. V. Carreño, E.L. Foletto, Temperature and reaction time effects on the structural properties of titanium dioxide nanopowders obtained via the hydrothermal method, Brazilian J. Chem. Eng. 28 (2011) 265–272. doi:10.1590/S0104-66322011000200011.

[30] X.M. Wang, P. Xiao, Morphology tuning in nontemplated solvothermal synthesis of titania nanoparticles, J. Mater. Res. 21 (2006) 1189–1203. doi:DOI: 10.1557/jmr.2006.0146.

[31] R.K. Wahi, Y. Liu, J.C. Falkner, V.L. Colvin, Solvothermal synthesis and characterization of anatase TiO2 nanocrystals with ultrahigh surface area, J. Colloid Interface Sci. 302 (2006) 530–536. doi:https://doi.org/10.1016/j.jcis.2006.07.003.

[32] J.-H. You, K.-Y. Hsu, Influence of chelating agent and reaction time on the swelling process for preparation of porous TiO2 particles, J. Eur. Ceram. Soc. 30 (2010) 1307–1315. doi:https://doi.org/10.1016/j.jeurceramsoc.2009.10.011.

[33] M. Niederberger, G. Garnweitner, Organic Reaction Pathways in the Nonaqueous Synthesis of Metal Oxide Nanoparticles, Chem. – A Eur. J. 12 (2006) 7282–7302. doi:https://doi.org/10.1002/chem.200600313.

[34] H.-I. Hsiang, S.-C. Lin, Effects of aging on the phase transformation and sintering properties of TiO2 gels, Mater. Sci. Eng. A. 380 (2004) 67–72. doi:https://doi.org/10.1016/j.msea.2004.03.045.

[35] B.N. Illy, B. Ingham, M.F. Toney, I. Nandhakumar, M.P. Ryan, Understanding the Selective Etching of Electrodeposited ZnO Nanorods, Langmuir. 30 (2014) 14079–14085. doi:10.1021/la503765a.

[36] J. Hüpkes, J.I. Owen, S.E. Pust, E. Bunte, Chemical etching of zinc oxide for thin-film silicon solar cells, Chemphyschem. 13 (2012) 66–73. doi:10.1002/cphc.201100738.

[37] C.M.V.B. Almeida, M. Nuñez, Progress in Electrochemistry Research, New York, 2005.

[38] Y. Xu, M.A.A. Schoonen, The absolute energy positions of conduction and valence bands of selected semiconducting minerals, Am. Mineral. 85 (2000) 543–556. doi:10.2138/am-2000-0416.

[39] K. Jeong, P.R. Deshmukh, J. Park, Y. Sohn, W.G. Shin, ZnO-TiO2 Core–Shell Nanowires: A Sustainable Photoanode for Enhanced Photoelectrochemical Water Splitting, ACS Sustain. Chem. Eng. 6 (2018) 6518–6526. doi:10.1021/acssuschemeng.8b00324.

[40] Y.-F. Xu, H.-S. Rao, X.-D. Wang, H.-Y. Chen, D.-B. Kuang, C.-Y. Su, In situ formation of zinc ferrite modified Al-doped ZnO nanowire arrays for solar water splitting, J. Mater. Chem. A. 4 (2016) 5124–5129. doi:10.1039/C5TA10563C.

[41] M. Zhong, L. Chai, Y. Wang, Core-shell structure of ZnO@TiO2 nanorod arrays as electron transport layer for perovskite solar cell with enhanced efficiency and stability, Appl. Surf. Sci. 464 (2019) 301–310. doi:10.1016/J.APSUSC.2018.09.080.

Chapter VII

Final Conclusions and Future Work

7.1. Final Conclusions

In this thesis, the production of new ZnO core-shell nanostructures and their application in solar cells has been presented. Overall, the pulsed electrodeposition of ZnO is a promising technique for the fast and well-aligned production of ZnO nanorods under mild conditions. We showed that the nanorod morphology and optoelectronic properties could be tuned by adding an extra layer deposited onto the bare FTO substrate or, as expected, by altering the electrical parameters governing the electrodeposition. This approach resulted in promising 1D ZnO nanostructures that can be applied in solar cells. Furthermore, given the inherent instability of perovskite films when in direct contact with ZnO, the creation of a TiO_2 shell deposited on the ZnO to act as a barrier between the ZnO and perovskite film was explored. Core-shell ZnO@TiO_2 were obtained, but application in full devices resulted in poor devices, yet was promising at this preliminary stage.

TiO_2 anatase intermediary layer acting as a template for ZnO pulsed electrodeposition

In Chapter 3, the pulsed electrodeposition technique was successfully applied to grow ZnO nanorods. Additionally, by modifying the FTO substrate surface, it was found that the ZnO nanorod characteristics were affected.

The growth of the ZnO nanorods was evaluated through voltammetric studies, morphological and structural characterisation. It was found that, during the cathodic sweep, at values where the reduction of NO_3^- occurs, ZnO grains are initially formed, being their dimensions dependent on the modified substrate used. Furthermore, SEM images and XRD results reveal misoriented vertically aligned ZnO nanorods with improved orientation when a TiO_2 anatase intermediate layer was applied as a buffer, with a decrease in the nanorod diameter and an increase in the number of nanorods per unit of area.

Although the photoluminescence analyses indicated a higher optical quality for the FTO/ZnO NR films, the green emission is almost suppressed when a TiO_2 anatase intermediate layer is employed due to luminescence defects of TiO_2 on the yellow region.

The photoelectrochemical characterisation of the ZnO thin films confirmed their n-type photoactivity behaviour, ideal for solar cells application. However, all demonstrated instability (to a greater or lesser degree) under illumination, possibly due to photo-dissolution.

Optoelectronic characterization of ZnO nanorod arrays obtained by pulsed electrodeposition

In Chapter 4, the optoelectronic properties of the ZnO nanorod prepared by pulsed electrodeposition were evaluated according to the pulse conditions applied.

The profile at which the t_{off}/t_{on} ratio is the highest of all the applied profiles seemed to allow better control of the growth of well-defined ZnO nanorods, with lower coalescence degree and higher homogeneity of nanorod diameters.

No significant changes in the ZnO crystal structure were observed for the heat-treated samples comparatively with the as-grown samples. However, with further studies of the optoelectronic properties of the as-grown and heat-treated samples, it was possible to identify distinct defects through PL and EIS techniques. In particular, the absorption spectra of the as-grown samples show a Burstein-Mott effect on the ZnO bandgap energy, in line with their character of a heavily-doped n-type semiconductor as measured by electrochemical impedance spectroscopy. The ZnO carrier concentration and the barrier height at the grain boundary (V_{FB}) seem to be related to the applied pulse conditions. A decrease of the carrier concentration occurred after the heat-treatment of the samples, exhibiting a steeper absorption ~3.3 eV, as expected for nondegenerate ZnO. Additionally, a spreading of energetic states is detected inside the ZnO bandgap. The as-grown and heat-treated samples exhibit near band edge recombination and deep level emission. The peak intensity of the former is higher in the as-grown ZnO nanorods arrays and reversed upon annealing. Moreover, the heat-treatment promotes a higher optical quality of the ZnO nanorods, as evidenced by the sharpness of the absorption edge and the narrowing of the full width at half maximum of the ultraviolet emission.

The use of combined spectroscopic techniques reveals that the broad emission bands are an overlap of three emitting centres in the red, yellow and green spectral regions, with the yellow emission showing a longer decay time.

Influence of the ZnO deposition media on the $CH_3NH_3PbI_3$ formation time and thermal stability

In Chapter 5, the ZnO nature as a concern for the thermal stability of $MAPbI_3$ perovskite was evaluated. For this, different deposition media were tested to prepare ZnO thin films to be used as ETMs on perovskite solar cells.

A correlation between the photovoltaic performance and the XRD patterns of the perovskite films has been found. A large amount of PbI_2 resulting from perovskite decomposition compromises the photovoltaic efficiency.

Also, it seems that the presence of carboxyl groups attached to the ZnO surface may affect the perovskite film crystallization, and consequently, the thermal stability of the ZnO/perovskite interface. The perovskite films deposited on ZnO thin films, prepared in ionic liquid and acidic organic media, showed faster degradation in which these groups were detected. This means that to prevent the degradation process and increase the long-term stability of these cells, some surface functionalities need to be avoided.

The problem of perovskite instability on ZnO compromises its practical application. One explored solution was the introduction of a passivation layer to prevent direct contact between the perovskite and the ZnO surface, as a formation of a TiO_2 shell coating the ZnO nanorods.

ZnO@TiO_2 core-shell nanostructures for solar applications

In Chapter 6, ZnO@TiO_2 core-shell nanostructures were prepared by coating the electrodeposited ZnO films with a thin TiO_2 layer.

Three main solvothermal parameters were studied: synthesis temperature, duration, and composition. Firstly, the temperature of 150 °C was selected as the reaction temperature to ensure that the shell was pure TiO_2 anatase phase. Secondly, to allow the formation of TiO_2 nanoparticles to create a thin layer on the ZnO nanorod surface, treatment time was found to be at least 180 min. Finally, to control TiO_2 particle size, acetylacetone was used as a chelating agent and thus formed a uniform layer that covered the entire surface of the ZnO nanorods. An additional ageing step of the precursor solution has been considered to improve the coverage of the ZnO nanorods with a TiO_2 shell. However, due to the acidic pH of the precursor solution during the solvothermal treatment, the undesirable dissolution of the ZnO structure occurred.

The optimised ZnO@TiO_2 core-shell nanorods were applied as ETM on perovskite solar cells. Despite the preliminary results of the device's performance, it appears that the presence of TiO_2 had a positive impact on device performance.

7.2. Future Work

The research presented in this thesis provided many insights into the ZnO nanorod growth by pulsed electrodeposition and into the production of ZnO-based core-shell nanostructures and their application on perovskite solar cells. However, it is obvious that there is significant scope for future work.

One approach that could be considered is the field of application of the well-aligned ZnO nanorods. The photoelectrochemical and optoelectronic properties of these ZnO nanorod arrays suggest good qualities to be applied in photoelectrochemical catalysis. This area has been explored in previous works and has shown the excellent potential of research.

Since the ZnO as an ETM on $CH_3NH_3PbI_3$ solar cells leads to several problems of perovskite instability due to its chemical nature or even the chosen morphology to apply in devices, the introduction of a passivation layer to prevent direct contact between the perovskite and the ZnO surface should be contemplated, which will improve the structural stability of perovskite thin films. To guarantee full coverage of the ZnO nanorod surface with the TiO_2 coated layer, efforts need to be made in order to optimise the synthesis conditions. Other alternatives could be the use of ZnSe semiconductor as a shell layer due to its direct bandgap of 2.67 eV that allows applications in optoelectronic devices [1], or even the use of ZnS since it is a wide bandgap (3.7 eV) semiconductor material and has shown to be efficient for photodegradation of organic pollutants [2].

An alternative to the current hybrid organic-inorganic perovskite materials, such as $CH_3NH3PbI_3$, is the inorganic perovskite materials, where the $CH_3NH_3^+$ is replaced by monovalent Cs^+ ions, thereby increasing the stability of PSCs [3]. In this case, higher efficiencies can be expected.

7.3. References

[1] C. Cai, Y.-F. Xu, H.-Y. Chen, X.-D. Wang, D.-B. Kuang, Porous ZnO@ZnSe nanosheet array for photoelectrochemical reduction of CO2, Electrochim. Acta. 274 (2018) 298–305. doi:https://doi.org/10.1016/j.electacta.2018.04.108.

[2] Sunaina, S. Devi, S.T. Nishanthi, S.K. Mehta, A.K. Ganguli, M. Jha, Surface photosensitization of ZnO by ZnS to enhance the photodegradation efficiency for organic pollutants, SN Appl. Sci. 3 (2021) 689. doi:10.1007/s42452-021-04643-z.

[3] M. Yue, J. Su, P. Zhao, Z. Lin, J. Zhang, J. Chang, Y. Hao, Optimizing the Performance of CsPbI3-Based Perovskite Solar Cells via Doping a ZnO Electron Transport Layer Coupled with Interface Engineering, Nano-Micro Lett. 11 (2019) 91. doi:10.1007/s40820-019-0320-y.